



HAL
open science

Numerical simulation of atmospheric dispersion : application for interpretation and data assimilation of pollution optical measurements

Jheyson Mejia Estrada

► **To cite this version:**

Jheyson Mejia Estrada. Numerical simulation of atmospheric dispersion : application for interpretation and data assimilation of pollution optical measurements. Other. Université de Lyon, 2022. English. NNT : 2022LYSEC012 . tel-03739279

HAL Id: tel-03739279

<https://theses.hal.science/tel-03739279>

Submitted on 27 Jul 2022

HAL is a multi-disciplinary open access archive for the deposit and dissemination of scientific research documents, whether they are published or not. The documents may come from teaching and research institutions in France or abroad, or from public or private research centers.

L'archive ouverte pluridisciplinaire **HAL**, est destinée au dépôt et à la diffusion de documents scientifiques de niveau recherche, publiés ou non, émanant des établissements d'enseignement et de recherche français ou étrangers, des laboratoires publics ou privés.



ÉCOLE
CENTRALE LYON

N° d'ordre NNT : 2022LYSEC0012

THESE de DOCTORAT DE L'UNIVERSITE DE LYON
opérée au sein de l'École centrale de Lyon

Ecole Doctorale N° 162
Mécanique - Energétique - Génie Civil - Acoustique

Spécialité de doctorat : Mécanique des fluides

Soutenue publiquement le 31/03/2022, par :

Jheyson Brayam MEJIA ESTRADA

**Numerical simulation of atmospheric
dispersion: application for the
interpretation and assimilation of pollution
optical measurements**

Devant le jury composé de :

SALIZZONI, Pietro	Professeur	École Centrale de Lyon	Président du jury
CALMET, Isabelle	Maître de Conférences (HDR)	École Centrale de Nantes	Rapporteuse
PARENTE, Alessandro	Professeur	Univ. Libre de Bruxelles	Rapporteur
LACOME, Jean-Marc	Ingénieur de Recherche	INERIS	Examineur
TURBELIN, Grégory	Maître de Conférences	Univ. d'Évry	Examineur
SOULHAC, Lionel	Professeur	INSA Lyon	Directeur de thèse
DONNAT, Ludovic	Ingénieur de Recherche	TotalEnergies	Encadrant de thèse

Acknowledgements

This PhD project was developed thanks to the collaboration between the Laboratoire de Mécanique des Fluides et d'Acoustique (LMFA) in the École Centrale de Lyon and the Laboratoire Qualité de l'Air (LQA) of TotalEnergies. I would like to thank both laboratories for the opportunity to work in the research sector and for their help in achieving the aims of the thesis.

Je tiens à remercier mon directeur de thèse Professeur Lionel SOULHAC. Grâce à son soutien et son aide, nous avons pu mener à bien ce projet. J'ai beaucoup appris sur la dispersion atmosphérique et le monde de la recherche grâce à nos échanges. Je remercie également Perrine CHARVOLIN-VOLTA et Guillevic LAMAISON pour leur aide dans les différentes étapes de la thèse.

Je suis tout aussi reconnaissant à mon encadrant de thèse Ludovic DONNAT pour son aide précieuse et pour l'opportunité de travailler également dans le secteur industriel. Je voudrais remercier aussi Olivier DUCLAUX et l'équipe LQA pour leur soutien et leur hospitalité.

I would like to thank the defense jury made up of Prof. Isabelle CALMET, Prof. Alessandro PARENTE, Eng. Jean-Marc LACOME and Prof. Grégory TURBELIN for their time and the very useful comments and suggestions.

My gratitude goes also to my colleagues of the team AIR and of the LMFA. In particolare, vorrei ringraziare il Professore Pietro SALIZZONI per il suo supporto e per i diversi scambi che abbiamo avuto durante il dottorato. Poi, ci tengo a ringraziare enormemente Andrea MAFFIOLI per il suo aiuto con gli spettri e per la sua amicizia. Ugualmente, sono molto grato a Cristina VIDALI e Sofia FELLINI per il loro aiuto e la loro amicizia. I thank Matteo, Michel, Livia, Fabio, Joy, Marcia, Fateh, Chi Vuong, Thierry, Mehdi, Giovanni, Pietro CINGI, Raffaello and all the people I shared special moments with during my PhD.

Quisiera agradecer a mi familia por creer siempre en mí.

El último y más especial agradecimiento es para Lucile, quien siempre me animó y siempre se mantuvo cerca de mí en los momentos más difíciles.

Abstract

Nowadays the control and surveillance of gas and particles emitted into the atmosphere is done more through optical systems, e.g. multi-spectral cameras, LIDARS, satellites images, etc. Optical instruments allow the measurement of pollutant concentration in the plume. It is believed that, in the future, optical instruments at high frequency resolution should work with or replace the current fixed and punctual monitoring networks. So they could contribute to a major technological leap in detecting substances in the atmosphere.

In the industrial sector, the use of optical measurements could contribute to:

- A better knowledge of industrial sites.
- Management of the future regulatory controls, made through remote sensing addressed to measure COV and methane.
- Improvement of physical representability of dispersion models employed for prevention of major risks.
- An approach validated for critical environmental events.
- Recognition of emission sources.

Current work is focused on the enhancement and interpretation of the results of optical measurements thanks to the numerical modelling of atmospheric dispersion. In order to make the most of the new experimental data, characterised by a high sampling frequency and a strong level of fluctuations, a robust direct simulation approach is required. It has to be able to capture not only the mean state of turbulent flow and of plume dispersion but also its higher moments, which better characterise the non-linear and instantaneous behaviour.

The strategy of the present work is based on a gradual increment of complexity. Before dealing with the atmospheric dispersion and modelling methods to simulate higher moments, we treat the study of the Atmospheric Boundary Layer (ABL) and its simplest modelling strategy, such as the RANS model. Working with them, we have been faced with one big source of uncertainties: the boundary conditions, e.g. inflow profiles, ground roughness and others. The proper setting of boundary conditions enable to reduce numerical errors and correctly interpreted the final results. Although decades of studies, this issue is still open due to the extremely complexity of the ABL. Even the simple case of a Surface Boundary Layer (SBL) in neutral conditions can present difficulties due to the appropriate application of boundary conditions and the equilibrium of the coefficients of the turbulence models. Some cases from the literature are reproduced to understand the problem and apply the solutions suggested. This allowed to become familiar with cases encountered later on.

Subsequently we pass to investigate the LES approach to model the SBL in neutral conditions together with the dispersion of a passive scalar and the related boundary conditions. The previous steps contribute to the development of a LES methodology employed to simulate numerically the atmospheric dispersion of a passive scalar. The development of the methodology has identified some physical and numerical criteria that could condition the validity and the accuracy of the approach adopted. In fact, the application of the criteria to simulate a wind

tunnel experiment, conducted in the Laboratoire de Mécanique des Fluides et d'Acoustique of the École Centrale de Lyon, was useful to validate the LES methodology. The validation turned out to be more complex than expected because compromises were necessary to violate the fewest criteria. In this context, our methodology was validated with the appropriate interpretation of the results.

Finally, all the acquired knowledge is used to simulate a real scenario, i.e. a test case of the TotalEnergies Anomaly Detection Initiatives (TADI) project, an experiment organised by TotalEnergies with the participation of different optical instruments manufacturers and developers. The numerical results are conceived in such way as to be able to interpret and assimilate the optical measurements. In particular using multi-spectral camera SIMAGAZ.

Résumé

Actuellement le contrôle et la surveillance des émissions de gaz et particules émises dans l'atmosphère s'effectuent de plus en plus par des systèmes optiques, comme les images des caméras multispectrales, LIDARS, satellite, etc. Ces instruments optiques permettent la mesure des polluants dans le panache. À l'avenir, les instruments optiques à haute résolution de fréquence devraient fonctionner avec ou remplacer les réseaux de surveillance fixes et ponctuels actuels. Ils pourraient donc contribuer à un saut technologique majeur dans la détection de substances dans l'atmosphère.

Dans le milieu industriel, l'exploitation de mesures optiques pourrait contribuer à :

- Une meilleure connaissance des émissions des sites industriels.
- La maîtrise des futurs contrôles réglementaires par « remote sensing » comme la mesure des COV et de méthane.
- Une amélioration de la représentativité des modèles de dispersion utilisés en prévention des risques majeurs.
- Une approche validée en cas d'évènement environnemental majeur.
- Identification et caractérisation des sources d'émission.
- Éviter les fuites et les catastrophes environnementales.

Le travail actuel port sur la valorisation et l'interprétation des résultats de mesures optiques grâce à la modélisation numérique de la dispersion atmosphérique. Afin de tirer le meilleur parti des nouvelles données expérimentales, caractérisées par une fréquence d'échantillonnage élevée et un niveau élevé de fluctuations, une approche de simulation directe robuste est requise. L'approche doit pouvoir capter non seulement l'état moyen de l'écoulement turbulent et de dispersion du panache mais aussi ses moments supérieurs, qui caractérisent mieux le comportement non linéaire et instantané.

La stratégie du travail est basée sur une augmentation progressive de la complexité. Avant d'aborder la dispersion atmosphérique et les méthodes de modélisation pour simuler des moments plus élevés, nous traitons l'étude de la Couche Limite Atmosphérique (CLA) et sa stratégie de modélisation la plus simple, comme le modèle RANS. Même le cas simple d'une Couche Limite de Surface (CLS) dans des conditions neutres peut présenter des difficultés en raison de l'application appropriée des conditions aux limites et de l'équilibre des coefficients des modèles de turbulence. Quelques cas de la littérature sont reproduits pour comprendre le problème et appliquer les solutions proposées. Cela a permis de familiariser avec des cas rencontrés par la suite.

Par la suite, nous passons à l'étude de l'approche LES pour modéliser la CLS dans des conditions neutres avec la dispersion d'un scalaire passif et les conditions aux limites associées. Les étapes précédentes contribuent au développement d'une méthodologie LES utilisée pour simuler numériquement la dispersion atmosphérique d'un scalaire passif. Le développement de la méthodologie a permis d'identifier certains critères physiques et numériques qui pourraient

conditionner la validité et la précision de l'approche adoptée. En fait, l'application des critères pour simuler une expérience en soufflerie, menée dans le Laboratoire de Mécanique des Fluides et d'Acoustique de l'École Centrale de Lyon, a été utile pour valider la méthodologie LES. La validation s'est avérée plus complexe que prévu car des compromis ont été nécessaires pour violer le moins de critères. Dans ce contexte, notre méthodologie a été validée avec l'interprétation appropriée des résultats.

Enfin, toutes les connaissances acquises sont utilisées pour simuler un scénario réel, c'est-à-dire un cas test du projet TotalEnergies Anomaly Detection Initiatives (TADI), une expérience organisée par TotalEnergies avec la participation de différents fabricants et développeurs d'instruments optiques. Les résultats numériques sont conçus de manière à pouvoir interpréter et assimiler les mesures optiques. Notamment à l'aide de la caméra multispectrale SIMAGAZ.

Contents

Acknowledgements	3
Abstract	5
Résumé	7
Contents	9
List of Figures	13
General Introduction	19
Problem introduction and solution strategy proposed	19
Work strategy for the development of the simulation methodology	23
1 State of the Art of Dispersion in the ABL	25
1.1 Physics of dispersion in the atmospheric boundary layer	25
1.1.1 Introduction to the atmospheric boundary layer	25
1.1.2 Similarity theory for the ABL	28
1.1.3 General flow equations in the context of the ABL	31
1.1.4 Wall-bounded turbulent shear flow	34
1.1.5 Atmospheric dispersion state of the art	42
1.2 Simulation tools	50
1.2.1 Numerical modeling of the ABL	50
1.2.2 Numerical approach for atmospheric dispersion	52
1.2.3 Numerical models for atmospheric dispersion	55
2 RANS Methodology for the Neutral Boundary Layer	61
2.1 Overview of a RANS simulation approach for the SBL	61
2.1.1 RANS conservation equations	61
2.1.2 Reynolds stresses	63
2.1.3 The closure problem	64
2.1.4 Turbulent kinetic energy	64
2.1.5 Turbulent closure models	65
2.1.6 The $k-\epsilon$ model	67
2.1.7 The Richards and Hoxey (R&H) approach	68
2.1.8 Boundary conditions	70
2.1.9 Mean scalar equation	73
2.2 RANS literature issues, improvements and comparison	75
2.2.1 Irvine case	75
2.2.2 Blocken case	80
2.2.3 Hargreaves and Wright case	83
2.3 Conclusions	88

3	LES Methodology for Dispersion in the Neutral SBL	89
3.1	LES simulation approach for dispersion in the neutral SBL	89
3.1.1	LES filtering	90
3.1.2	LES conservation equations	91
3.1.3	Smagorinsky model	94
3.1.4	Subgrid Kinetic Energy model	98
3.1.5	WALE model	99
3.1.6	Overview of the boundary conditions	99
3.1.7	Inlet boundary condition	101
3.1.8	Rough wall model for LES simulations	103
3.1.9	Schumann wall model	106
3.1.10	Mason and Callen model	107
3.1.11	Thomas and Williams model	108
3.1.12	Xie model	109
3.1.13	Passive scalar equation	110
3.2	Nironi experiment and LES methodology inputs	111
3.2.1	Nironi neutral boundary layer experiment	111
3.2.2	Boundary layer characteristics	114
3.2.3	Concentration field characteristics	121
3.3	Computational settings	126
3.3.1	Domains	126
3.3.2	Meshes	129
3.3.3	Equations and solver	133
3.3.4	Boundary and initial conditions	135
3.3.5	Numerical schemes	136
3.3.6	Conclusions	137
3.4	LES methodology, sensitivity study and results	138
3.4.1	Sensitivity study	141
3.4.2	Wind field comparison and validation	152
3.4.3	Concentration field comparison and validation	156
3.5	Conclusions	162
4	TADI: Real Scenario Case	165
4.1	Experiment description and case selection	165
4.1.1	Case selection	166
4.1.2	Optical instrument	169
4.2	LES simulation	172
4.2.1	Application of the LES methodology	172
4.2.2	Simulation results	177
4.3	Data interpretation and assimilation	180
4.3.1	Methodology for the source emission estimation from optical measurements	180
4.3.2	Evaluation of the methodology	183
4.4	Conclusions	184
	Conclusions and perspectives	185
	Conclusions	185
	Perspectives	186
	Appendix A	187
A.1	Wall function for rough surfaces	187
A.2	WALE model development	190

Bibliography

List of Figures

2	Optical instruments, from left to right: Hyperspectral Camera, multispectral camera and LIDAR.	21
3	TADI site	23
1.1	Subdivision of the ABL. From Establishment of an Atmospheric Flow Laboratory Project ; last access: January 18 th , 2022.	26
1.2	Reproduction of horizontal wind speed spectrum of Van der Hoven (1957) at Brookhaven National Laboratory. From: Martin-Martínez et al. (2012)	28
1.3	Measured drag coefficient for a boundary layer over a flat plate. From: Kundu et al. (2012b)	35
1.4	Sketch of a flat-plate boundary layer.	35
1.5	Profiles of the viscous shear stress and Reynolds shear stress in turbulent channel flow at two low Reynolds numbers: $Re = 56000$ (dashed line) and $Re = 13750$ (solid line). From DNS data of Kim et al. (1987)	37
1.6	Sketch illustrating the various wall regions and layers defined in terms of z^+ and z/δ , for a turbulent channel flow ($Re_\tau = 1 \times 10^4$). From: (Pope, 2000c).	39
1.7	Typical form of the plume in the neutral condition of the atmosphere. The shape is almost coning. From: (Cancelli et al., 2006)	44
1.8	The standard deviation σ_X of dispersion from a point source thanks to the Langevin model, i.e. Eq. (1.64). From: (Pope, 2000c)	46
1.9	Evolution of the horizontal standard deviation σ_y as a function of the downwind distance from the source, (Briggs, 1973).	49
1.10	Evolution of the vertical standard deviation σ_z as a function of the downwind distance from the source, (Briggs, 1973).	49
2.1	A sketch of an apparatus similar to that used by Uberoi (1956) , to study the effect of axisymmetric mean straining on grid turbulence. From (Pope, 2000c).	66
2.2	Inlet profiles	71
2.3	ESDU profiles. From: (Tian et al., 2018)	71
2.4	2D domain for the Irvine case.	76
2.5	CS1 case profiles computed using OpenFOAM.	78
2.6	CS1 case profiles computed using Fluent.	78
2.7	CS2 case profiles computed using Fluent.	78
2.8	CS3 case profiles computed using OpenFOAM.	79
2.9	CS3 case profiles computed using Fluent.	79
2.10	2D domain for the Blocken case.	81
2.11	Blocken et al. (2007) results	82
2.12	Blocken case simulation computed using OpenFOAM.	82
2.13	First 2D domain for the Hargreaves case.	84
2.14	Second 2D domain for the Hargreaves case.	85
2.15	From right to left, plots of \bar{u} , turbulent kinetic energy k and turbulent dissipation rate ε for the Fluent simulation. From: (Hargreaves and Wright, 2007).	85

2.16	Evolution of velocity, turbulent kinetic energy and dissipation of turbulent kinetic energy profiles along 2D domain of 5 km and with z_{ref} of 6 m. Overall setting: Hargreaves and Wright (2007) . The intermediate profiles are at 1 km, 2.5 km and 4 km. The ground wall-function uses a standard roughness model (<i>nutkRoughWallFunction</i>), available in OpenFOAM v1812.	85
2.17	Evolution of velocity, turbulent kinetic energy and dissipation of turbulent kinetic energy profiles along 2D domain of 5 km and with z_{ref} of 6 m. The ground wall-function uses the correction suggested by Hargreaves and Wright (2007) . In OpenFOAM v1812: <i>nutkAtmRoughWallFunction</i>	86
2.18	Evolution of velocity, turbulent kinetic energy and dissipation of turbulent kinetic energy profiles along 2D domain of 5 km and with z_{ref} of 6 m. Overall setting: Hargreaves and Wright (2007) . The intermediate profiles are at 1 km, 2.5 km and 4 km. The ground wall-function uses a standard roughness model (<i>nutkRoughWallFunction</i>), available also in OpenFOAM v2.3.1.	86
2.19	Evolution of velocity, turbulent kinetic energy and dissipation of turbulent kinetic energy profiles along 2D domain of 5 km and with z_{ref} of 6 m. The ground wall-function uses the standard rough wall-function in Ansys Fluent 18.2.	87
2.20	Evolution of velocity, turbulent kinetic energy and dissipation of turbulent kinetic energy profiles along 2D domain of 5 km with a central smooth region and two rough regions. OpenFOAM v1812 simulation.	87
3.1	Inlet boundary condition sketch.	100
3.2	Precursor-successor method.	101
3.3	Cyclic-Dispersion Domain (CDD).	101
3.4	Evolution of the mean velocity for rural case ($z_0 = 0.23$ m). From right to left: Precursor Method (PM), Vortex Method (VM) and Spectral Synthesizer (SS). From: Vasaturo et al. (2018)	102
3.5	Evolution of the turbulent kinetic energy for rural case ($z_0 = 0.23$ m). From right to left: Precursor Method (PM), Vortex Method (VM) and Spectral Synthesizer (SS). From: Vasaturo et al. (2018)	103
3.6	Sketch to illustrate the wall modelling philosophy. (a) Inner layer resolved and (b) inner layer modeled. Image modified from Piomelli and Balaras (2002)	105
3.7	Explanation sketch: the eddies are almost dissipated before reaching the roughness elements while the mean velocity always exerts its influence.	109
3.8	The atmospheric wind tunnel of LMFA, AIR	112
3.9	Position of available wind profiles: 1) 6 m, 2) 8 m and 3) 10 m	113
3.10	Horizontal profiles of concentration. Six profiles was measured at: 1) 0.25 m, 2) 0.50 m, 3) 1.00 m, 4) 2.00 m, 5) 3.00 m and 6) 4.00 m from the source.	113
3.11	Vertical profiles of concentration. Six profiles was measured at: 1) 0.25 m, 2) 0.50 m, 3) 1.00 m, 4) 2.00 m, 5) 3.00 m and 6) 4.00 m from the source.	114
3.12	Reynolds shear stress $\overline{u'w'}$ for the three available profiles, which are respectively at 6.00 m, 8.00 m and 10.00 m from the beginning of the test section.	115
3.13	Streamwise mean velocity and Reynolds stress components ($\overline{u'w'}$ and $\overline{u'v'}$) profiles at 6.0 m from the beginning of the test section.	116
3.14	Nondimensional Reynolds shear stress for the three available profiles, which are respectively at 6.00 m, 8.00 m and 10.00 m from the beginning of the test section.	116
3.15	Mean velocity profiles at $x = 6$ m. The left figure (a) shows the Nironi experimental profile, the power-law profile and the 5 profiles used for the optimisation procedure with the Method 1. The right figure (b) employs a semi-logarithmic plot to compare the optimal profile (obtained with 6 points) and the Nironi experimental profile.	117

3.16	Streamwise turbulence intensity profile at $x = 6$ m. The left figure (a) shows the $\overline{u'^2}$ profile along the boundary layer. Whereas the right figure (b) illustrates the nondimensional profile $\overline{u'^2}$ and highlight the logarithmic region thanks to the “Log fit” curve.	118
3.17	Mean velocity profiles at $x = 8$ m. The left figure (a) shows the Nironi experimental profile, the power-law profile and the 5 profiles used for the optimisation procedure with the Method 1. The right figure (b) employs a semi-logarithmic plot to compare the optimal profile (obtained with 6 points) and the Nironi experimental profile.	118
3.18	Mean velocity profiles at $x = 10$ m. The left figure (a) shows the Nironi experimental profile, the power-law profile and the 5 profiles used for the optimisation procedure with the Method 1. The right figure (b) employs a semi-logarithmic plot to compare the optimal profile (obtained with 6 points) and the Nironi experimental profile.	119
3.19	Velocity field spectrum for experimental data at $x = 6.0$ m, $y = 0.0$ m and $z = 0.152$ m. Figure (a) shows the spectrum of u' , v' and w' . Moreover, it illustrates the $-5/3$ law and the bounds of the inertial subrange, delimited by k_c min and max. Figure (b) compensates the spectrum and help to delimit the bounds of the inertial subrange.	120
3.20	Horizontal profiles of nondimensional mean concentration at 6 distances downwind. The profiles are satisfactory fitted by a Gaussian distribution (Gauss Exp. – Eq. (3.65)). Profiles were measured at the source height $h_s = 0.152$ m.	123
3.21	Vertical profiles of nondimensional mean concentration at 6 distances downwind. Profiles were measured at the plume axis.	123
3.22	Horizontal profiles of nondimensional concentration standard deviation at 6 distances downwind. The profiles were measured at the source height $h_s = 0.152$ m.	124
3.23	Vertical profiles of nondimensional concentration standard deviation at 6 distances downwind. The profiles were measured at the plume axis.	124
3.24	In the left-hand side figure, the experimental plume spreads σ_y and σ_z downstream the source are illustrated, while the figure on the right shows the development of the experimental intensity of concentration fluctuations i_c , defined in Eq. (3.67).	125
3.25	Graphic scheme to define the longitudinal dimension of the domain. The green region represents the region that respects the constraint.	128
3.26	Graphic scheme to define the cross-section dimension of the domain. The green region represents the region that respects the constraint.	128
3.27	Mesh criteria.	132
3.28	Generic mesh for Nironi case.	133
3.29	Overview of the LES methodology.	140
3.30	Profile statistics: Mesh sensitivity – U_{bulk} and z_0 reference.	142
3.31	Profile statistics: Wall model sensitivity – U_{bulk} (+8% w.r.t. reference) and z_0 reference.	144
3.32	Profile statistics: U_{bulk} perturbed and z_0 fixed.	147
3.33	Profile statistics: U_{bulk} perturbed and $z_0 = 1.174 \times 10^{-4}$ m fixed.	148
3.34	Profile statistics: U_{bulk} perturbed and $z_0 = 1.230 \times 10^{-4}$ m fixed.	149
3.35	Profile statistics: $U_{bulk} = 3.843$ m/s fixed and z_0 perturbed.	151
3.36	Wind field statistics of the final case and comparison with the Nironi (2013) experimental data. The validation of the methodology occurs for $z < 0.2$ m, i.e. $z/\delta < 0.285$	153
3.37	Sketch of the Irwin spire and roughness influence on the development of the experimental boundary layer.	154

3.38	Velocity field spectrum for the case final comparison. Figure (a), (b) and (c) shows respectively the spectrum of u' , v' and w' . They illustrate also the $-5/3$ law and the cut-off wavenumber of the LES filter.	155
3.39	Crosswind profiles of nondimensional mean concentration for the m12_U5-z5 case. The profiles were measured and sampled at the source height $z/\delta = 0.217$. The numerical profiles were fitted with a Gaussian distribution of the type of Eq. (3.65).	157
3.40	Vertical profiles of nondimensional mean concentration for the m12_U5-z5 case. The profiles were measured and sampled on the plume axis. The numerical profiles were fitted with a Gaussian distribution of the type of Eq. (3.66).	158
3.41	(a) Plume spread in transversal and vertical directions for LES and experiment. (b) $\sigma_y, \sigma_z, \sigma_v$ and σ_w ratio between experiment and LES values.	158
3.42	Crosswind profiles of nondimensional concentration standard deviation for the m12_U5-z5 case. The profiles were measured and sampled at the source height $z/\delta = 0.217$	159
3.43	Vertical profiles of nondimensional concentration standard deviation for the m12_U5-z5 case. The profiles were measured and sampled on the plume axis.	159
3.44	Experimental and LES concentration signal (a) and spectrum of concentration fluctuations (b) on the plume center line for the case m12_U5-z5 and the wind tunnel experiment. The sampling position is $x = 4.00$ m (i.e. $x/\delta = 5.714$).	160
3.45	Comparison of numerical and experimental PDF plots at different distances from the source. The ordinate axis expresses a normalised PDF, given by $\text{PDF}/(N \Delta c^*)$, where Δc^* is the amplitude of concentration classes and N is the total number of classes on which the PDF is calculated. The plots show also the relation between the concentration fluctuation intensity i_c and the concentration PDF for the LES results.	161
4.1	TADI facility.	165
4.2	Plume in TADI site	167
4.3	Inverse of the Monin-Obukhov length to identify neutral atmospheric conditions.	168
4.4	Inverse of the Monin-Obukhov length for the test W40-05.	168
4.5	Test case W40-05 data. The left figure shows the LIDAR wind profile averaged over the 3 minutes and the logarithmic law that best fits it. In the right figure the wind rose obtained from LIDAR data is illustrated. The legend shows the color related to each wind field velocity class (expressed in [m/s]) employed by the wind rose.	169
4.6	Diagram of the image taken by an optical instrument.	170
4.7	Instantaneous CIC field (expressed in $\text{kg} \cdot \text{m}^{-2}$) for the TADI case, obtained through the SIMAGAZ camera, with a resolution of 320x256 pixels.	171
4.8	Sketch of the field of view of two cameras from above. Image from: Dinger et al. (2018)	172
4.9	Graphic scheme to define the longitudinal dimension of the TADI domain.	173
4.10	Graphic scheme to define the transverse dimension of the TADI domain.	173
4.11	Dimensions of the precursor and successor domain of the TADI case.	173
4.12	TADI test section.	174
4.13	TADI mesh criteria.	175
4.14	TADI mesh.	176
4.15	Wind field statistics of the TADI case. The mean velocity of the wind field is compared with the TADI experimental data obtained with LIDAR. In this case, the validation of the methodology occurs for $z < 10$ m, i.e. $z/\delta < 0.285$	178
4.16	CIC field for the LES simulation with a resolution of 50x40 pixels and expressed in kg/m^2	179

4.17	Relation between the profile of the cross-section integrated mass $\mathcal{M}_i(t)$ and the integrated mass m_{ij} image.	181
4.18	Relation between the profile of the cross-section integrated mass $\mathcal{M}_i(t)$ and the integrated mass m_{ij} image at a different time step.	182
4.19	Cross-section integrated mass for different times.	182
4.20	Images used to estimate the LES emission rate. The time step is 0.025 s.	183

General Introduction

Problem introduction and solution strategy proposed

Nowadays pollution has become a global concern. Pollution can assume many forms, ranging from organic compounds and other chemical substances to different types of energy. Therefore pollution is present in the air we breath, the water we drink, the soil we use to grow our food, the lit-up skies and even the increasing noise we hear every day. It can contribute to health problems, a lower quality of life and major disruptions and effects on wildlife and ecosystems. The severity of a pollutant for human health and ecosystems depends on its chemical nature, quantity or concentration and persistence. The specific damage generated by different pollutants is related not only to the environment it is in (i.e. air, water, soil) but also the mix of other pollutants that are present and the actual exposure (Gee *et al.*, 2013). Some evidences are highlighted by United-Nations-Environment-Programme (2017): the air quality is a problem nearly all around the world, water pollution is a major cause of death of children under five years age, nutrient over-enrichment of land and water is causing shifts in ecosystems and loss of biodiversity, plastic in the ocean is on the rise and there is no acceptable storage or disposal option for processing of older-generation nuclear fuel. Pollution is also impacting the way in which some major Earth system processes, such as the climate, are functioning (Diamond *et al.*, 2015; Steffen *et al.*, 2015).

Consequently, pollution has a huge economic impact. In 2013, the welfare costs related to air pollution in the world were estimated at about US\$ 5.11 trillion (Bank *et al.*, 2016). Another tangible example in the private sector concerns the 6 days eruption of Eyjafjallajökull in Iceland in April 2010. The volcanic ash ejected had generated important disruptions to aerial transport in most parts of Europe because of closure of airspace. The estimated loss of airlines' revenue was about US\$ 1.7 billion (Flight disruptions cost airlines \$1.7bn, says IATA, BBC News; last access: January 18th, 2022). Major accidental events, like the meltdown of the Fukushima Dai-ichi nuclear plant, could cause both economic damage and increased health risks due to residual radiation. In the previous example, the economic damage from the radiation contamination is well documented (Yamane *et al.*, 2011a,b). In Fukushima and Miyagi prefectures, it was remarked that an augmentation of $1 \mu\text{Sv/h}$ decreases the land price by 3.39% on average and the economic damage due to radiation is approximately US\$ 0.53 billion (Tanaka and Managi, 2016). However, research points out that the land price decline is only partially explained by increased levels of radiation. The population reduction indirectly influence the land price (Shin *et al.*, 2016). Not only major accidents but also small or moderate emissions (e.g. liquid or gas leak from pipes or industrial equipments) could cause damage to health and ecosystems or lead to the loss of huge valuable resources. Achieving harmony with nature also means obtaining a higher quality of life and better economic results.

Since the Industrial revolution, a new era has arisen, the Anthropocene, in which humans and our society have become a global geophysical force (Steffen *et al.*, 2007). Hence, it is possible to consider that human activities push Earth system outside the stable environmental state of the Holocene, with consequences that are detrimental or even catastrophic for large part of the world (Rockström *et al.*, 2009). Referring to air pollution, the massive scale of urbanisation, the

increase of traffic, the industrialisation and the energy consumption are the main causes of the air quality worsening. Therefore, the achievement of a sustainable development is fundamental to improve the health of people and of the planet. The United Nation's 2030 Agenda for Sustainable Development affirms its commitment to "ensure that all human beings can enjoy prosperous and fulfilling lives and that economic, social and technological progress occurs in harmony with nature" (Lee *et al.*, 2016). Moreover, the recent Paris Agreement aims to enhance the UN Framework Convention on Climate Change, adopted in New York on 9th May 1992, and to strengthen the global response to the treat of climate change, in the context of sustainable development and efforts to eradicate poverty (Paris-Agreement, 2015).

As previously illustrated, pollution can affect different areas of our society and at different scales of the whole planet. The different identified scales could be: planetary scale, continental scale, regional scale, urban scale, district scale, street scale and indoor scale. A direct consequence is that the stakeholders could vary from world institutions, like United Nations, to local communities arriving until every person on the planet. In between we also find protagonists who have been playing a fundamental role in today's society: industries. To reduce pollution, collaboration and coordinated action at international, national and local levels have to be maintained, in coordination with other environmental, climate and sectoral policies. Holistic solutions are fundamental.

Focusing on air pollution, in order to save lives and to improve economic well-being, computational models of air pollutant dispersion together with consolidated and new measurement techniques are being developed to understand, identify and predict the origins and consequences of these phenomena and accidents. In fact, effective action to reduce air pollution and its impact requires a good understanding of its sources, how pollutants are transported, how chemical composition changes over time and how pollutants affect humans, ecosystems, climate and subsequently society and economy (EEA, 2020). From a regulatory point of view, countries or communities have developed an extensive body of legislation which establishes health based standards and objectives for a number of pollutants present in the air, like those made by European Union (European-Parliament and Council-EU, 2008). The control of the standards are conducted by the data collected by fixed and punctual monitoring stations. In this scenario, numerical models complement the measurements by obtaining dispersion maps over larger and more detailed areas or by making predictions and scenario studies. Similar standards regulate the industries' emissions. Detailed knowledge of the environmental impact is important not only for regulatory reasons but also for accidents' prevention and mitigation, e.g. nuclear (Managi and Guan, 2017), refinery, petrochemical accidents (Balasubramanian and Louvar, 2002) and others.

Today fixed monitoring stations or networks of micro-sensors are commonly used to measure concentration of pollutants. These techniques constitute a robust and widely diffused technology. Nevertheless, nowadays the control and surveillance of gas and particles emitted into the atmosphere is done more through optical systems, e.g. hyper-spectral cameras, UV cameras, LIDARs, satellites images, etc (Dinger *et al.*, 2018). Some of them are illustrated in Figure 2. Optical instruments allow the measurement of pollutant concentration directly in the plume. It is believed that, in the future, optical instruments at high frequency resolution should work with or replace the current monitoring networks. So they could contribute to a major technological progress in the domain of atmospheric substance detection. The interest on this technology is related to the TADI project (TotalEnergies Anomaly Detection Initiatives; last access: January 18th, 2022), organised by TotalEnergies with the participation of different optical instruments manufacturers and developers, which provided us some key data from different types of cameras.

The TADI experiment is not the only experience of this kind. For example, the Camera Observation and Modelling of 4D Tracer Dispersion in the Atmosphere (COMTESSA; last access January 18th, 2022) project wants to elevate the theory and simulation of turbulent tracer dispersion in the atmosphere to a new level of performing completely novel high-resolution 4D

measurements. The sulphur dioxide (SO_2) was chosen as tracer. In fact, it might be assumed to be a passive tracer over short transport distances. Moreover, SO_2 strongly absorbs radiations in part of the UV spectrum and may this be detected by, for example, UV-sensitive cameras. Optical data could be used to improve the modelled concentration field or vice versa a numerical model may enhance the data interpretation (e.g. [Kylling *et al.* \(2020\)](#)).



Figure 2: Optical instruments, from left to right: Hyperspectral Camera, multispectral camera and LIDAR.

In view of this innovation, the development of a direct model for the dispersion of pollutants capable of capturing instantaneous fluctuations and provide higher momentum statistics is a must. From the numerical point of view, the impact of computational fluid dynamic (CFD) has taken advantage of the decrease of computational power cost thanks to the rapid and continuous development of computer technologies and the algorithmic improvements. In fact, a direct consequence is that today we can not only count on the continuous progress of new CPUs but also of GPUs, ([Muñoz-Esparza *et al.*, 2020](#)). Numerical simulations of turbulent flows, which until a few decades ago were confined to research environment, are currently used for the development and design of engineering tools and devices. It was already true almost 20 years ago, as remarked by [Piomelli and Balaras \(2002\)](#).

In the field of atmospheric dispersion, the new resources motivate the scientific community to go further. Despite the uncertainties related to the filter numerical implementation, boundary conditions, wall treatment and the higher computational cost, today the most convenient CFD prediction model for simulating atmospheric flows and dispersion is the large-eddy simulation (LES). Its applications include urban environment and critical applications such as the release of toxic gas substances (e.g. [Fossum *et al.* \(2012\)](#); [Nakayama and Nagai \(2009\)](#); [Nakayama *et al.* \(2013\)](#)). Although the model based on Reynolds-Averaged Navier-Stokes (RANS) equations is more commonly used, especially for engineering applications due to a reduced computational cost, no model of this type can provide accurate results without ad-hoc adjustments of the model parameters ([Wilcox, 2001](#)). The RANS equations are obtained by time- or ensemble-averaging of the Navier-Stokes equations to generate a set of transport equations for the averaged fields. It is possible to obtain higher moments statistics through specific equations for those moments. In fact, RANS equations require a closure model with associated assumptions. The effect of all the scales of motion needs to be modeled. This approach results counterproductive for the new challenges. In this regard, it is more convenient to simulate instantaneous field in order to obtain directly the higher moments statistics. This is the case of direct numerical simulation (DNS) and large-eddy simulation (LES). The first resolves all the scales of the motion and no modeling is used. Nevertheless, the computational cost is prohibitive for high Reynolds number flows, typical of atmospheric flows in engineering field. On the other hand, LES solves a very wide range of time and length scales, computing the energy-carrying eddies, while it models the smaller scales of motion. It provides a good compromise between computational cost and accuracy of the instantaneous fields, making it more attractive for our purposes.

In the context of prevention of minor and major accidents, the current thesis is linked to

the TADI project, which aims to offer a safety diagnostic application adapted to each situation. It wants to help operators to make the best decision with confidence and without exposing human lives and installations thanks to a clear synthesis of multiple information in real time. To achieve the objectives, a large experimental campaign was organised capable of comparing different measurement techniques, from well-known fixed stations to innovative optical and acoustic technologies.

Current work is focused on the interpretation and enhancement of the results of optical measurements thanks to the numerical modelling of atmospheric dispersion. In order to make the most of the new experimental data, characterised by a high sampling frequency and a strong level of fluctuations, a robust direct simulation approach is required. It has to be able to capture not only the mean state of turbulent flow and of plume dispersion but also its higher moments, which better characterise the non-linear and instantaneous behaviour.

Therefore, the aim of the research is to simulate numerically the atmospheric flow and the dispersion of pollutants over a complex built terrain, mainly in industrial sites. In particular, our simulations are concentrated in the reproduction of the unsteady behaviour typical of these phenomena. In fact, air motion in the lower part of the atmosphere is bounded by a solid surface of varying temperature and roughness. It responds quickly to surface radiation changes, and the air motion is nearly always turbulent. A pollutant released into this turbulent atmosphere and surrounded by a complex terrain experiences concentration fluctuations that are significant. In particular, the fluctuations are of high order of magnitude if the response is non-linear, for instance when cases of toxicity, flammability and odour detection are concerned ([Gant and Kelsey, 2012](#)), and if non-linear chemical reactions are involved ([de Arellano *et al.*, 2004](#)).

The campaign TADI provides us some key data from different types of cameras, e.g. LIDAR, multi- and hyper-spectral, infrared cameras and others. These data are useful to many applications such as a better understanding of the strengths and weaknesses of a coupled approach, which combines optical measurements and numerical models. Furthermore, the use of optical measurements could contribute to:

- A better knowledge of industrial sites.
- Management of the future regulatory controls, made through remote sensing addressed to measure COV and methane.
- Improvement of physical representability of dispersion models employed for prevention of major risks.
- An approach validated for critical environmental events.
- Identification and characterisation of emission sources.
- Avoid leaks and environmental disasters.

The strategy of the present work is based on a gradual increment of complexity. Before dealing with the atmospheric dispersion and LES modelling, we treat the study of the Atmospheric Boundary Layer (ABL) and its simplest modelling strategy, such as the RANS model. Working with them, we have been faced with one big source of uncertainties: the boundary conditions, e.g. inflow profiles, ground roughness, etc. The proper setting of boundary conditions enable to reduce numerical errors and correctly interpret the final results. Although decades of studies, this issue is still open due to the extreme complexity of the ABL. Later we pass to investigate LES models and ABL in neutral conditions together with the dispersion of a passive scalar and the related boundary conditions. The previous steps contribute to the development of the methodology employed to simulate numerically the atmospheric flow and the dispersion of pollutants over a complex terrain. The final methodology is validated thanks to wind tunnel experiments ([Nironi *et al.*, 2015](#)). Finally, all the acquired knowledge is used to simulate a real scenario, i.e. the TADI experiment, and to compare and assimilate the optical measurements.



Figure 3: TADI site

Work strategy for the development of the simulation methodology

As pointed out in the current section, the first step to simulate a dispersion phenomena is to have a robust direct simulation approach for calculating numerically the atmospheric boundary layer flow.

Explicitly simulation of the concentration probability density function (p.d.f.) and its higher moments in real conditions and at very high Reynolds numbers typical of atmospheric flows is possible through the Lagrangian or Eulerian p.d.f. method (also known as micro-mixing method) (Leuzzi *et al.*, 2012) or the Large-Eddy Simulation method (Philips *et al.*, 2013; Ardeshiri *et al.*, 2020). The experience of the LMFA (Laboratoire de Mécanique des Fluides et d'Acoustique) research group in the CFD field, the accessibility to considerable computational resources and the curiosity to investigate new horizons have persuaded us to adopt the LES method. However, one of the first technical obstacle was represented by the choose of the CFD code. After a benchmark of the different codes available and commonly used by the atmospheric community, especially in the fields of microscale atmospheric flows and wind engineering, we have chosen the OpenFOAM code because it was planned to carry out large simulations that need to parallelize the calculations on many supercomputer nodes. In fact, CFD commercial licenses have been evaluated as an obstacle to our objectives and a drawback that should not be underestimated compared to open-source codes. On the other hand, OpenFOAM required a deeper understanding and support to be sought in the open-source community. However, this did not stop us from carrying out the first case studies using both OpenFOAM and Ansys Fluent.

Before to compute a LES simulation, a RANS simulation was preferable in order to handle with boundary and initial conditions (section 2.1). In fact the simulation of the ABL for microscale dispersion problems is still a challenge today. It is important to highlight that a good equilibrium between the boundary conditions and the conservation equations of turbulence is fundamental. Moreover, a convenient wall function determines the successful simulation of a rough wall typical of atmospheric flows, as we will see in practice in section 2.2.

More in-depth work was required to develop a wall model suitable for LES simulations (section 3.1). In the wall adjacent region, a wall model based on the mean flow is not always enough because it could be also required to consider its instantaneous part. Moreover, the LES closure model interacts differently near the wall than in the RANS case. Conversely, as well as RANS simulations, a constrain for LES wall model is the dimension of the cells adjacent to the wall in the direction normal to the surface. The idea that finer meshes lead to better LES simulations could be limited by the previous constrain. In fact, cells that are too small cannot reproduce the effect of turbulent eddies present in this region of the flow and treated in a Reynolds-average sense (Piomelli and Balaras, 2002). Furthermore, sometimes the source of

pollutants are situated close to the wall and have small dimensions. For low-Reynolds number, the source dimension could be smaller than the wall adjacent cells and it might be a problem if the required cells dimensions are too different. A good compromise between physical and numerical constraints determines the success of the simulation. These difficulties together with the methods to simulate the inlet flow represent the core of the methodology developed to simulate the atmospheric flow and the dispersion phenomenon. The complete setting of the validation case is illustrated in [section 3.3](#), while the methodology is presented in [section 3.4](#). The flow and the concentration field were compared with wind tunnel data ([section 3.2](#)) in order to validate the methodology and understand its limits ([section 3.4](#)).

Finally, it was possible to simulate a real scenario ([chapter 4](#)). After validation, the focus was on the available experimental data from the TADI experiment, described in [section 4.1](#). The identification of a test in neutral atmosphere conditions in the 2019 campaign made it possible to apply our methodology to simulate the atmospheric dispersion of pollutants over complex terrains, presented in [section 4.2](#). The final verification was conducted using the SIGMA gas camera images. The latter were compared with the images generated by the numerical methodology developed. The techniques of comparison and assimilation have the main objective of highlighting the performances of the numerical and experimental methodology and understanding how to better integrate them, as illustrated in [section 4.3](#).

The points presented in this section will be deepened throughout the entire thesis. The first part is concluded by the exposition of the physics of the atmospheric dispersion and how to model it ([section 1.1](#)). The simulation tools used to study atmospheric dispersion are also included in this part ([section 1.2](#)). Subsequently, the [chapter 2](#) and [chapter 3](#) are focused on the development of the RANS and LES methodology including our results and the validation of the final methodology. The second part includes also the treatment of RANS boundary conditions for a neutral ABL, taken particular attention to the wall function and inlet profiles. In this case, the RANS methodology is applied to revisit some cases from the literature and improve their resolutions ([section 2.2](#)). In a similar way, the third chapter investigates the LES boundary conditions, above all wall models and inlet flow generators ([section 3.1](#)). Moreover, it presents the wind tunnel experiment used to validate the methodology, the computational settings and the sensitivity studies and results of the validation ([section 3.2](#), [section 3.3](#) and [section 3.4](#)). The [chapter 4](#) part is entirely dedicated to the TADI experiment and the numerical simulation of it. The comparison and assimilation of optical data is also treated in this part. Finally the conclusions and perspectives are presented in the final chapter ([chapter 4.4](#)).

Chapter 1

State of the Art of Dispersion Phenomena in the Atmospheric Boundary Layer

1.1 Physics of dispersion in the atmospheric boundary layer

1.1.1 Introduction to the atmospheric boundary layer

In order to study the atmospheric dispersion, the knowledge of the atmospheric boundary layer and how to simulate it is fundamental.

According to [Stull \(2012\)](#), *the Atmospheric Boundary Layer (ABL) or Planetary Boundary Layer (PBL) could be defined as the part of the troposphere that is directly influenced by the presence of the earth's surface, and responds to surface forcing with a timescale of about one hour or less. The forcing includes the friction drag, the heat transfer, evaporation and transpiration, pollution emission and flow modification induced by terrain. The boundary layer thickness is quite variable in time and space ranging from hundreds of meters to a few kilometres. It is convenient to precise that this is the case of the ABL over earth's surface. Differently from the oceans, the variations in the nature and in the roughness of the earth's surface (i.e. countryside, more or less urbanised regions) are many and consequently modify the ABL. Furthermore, the flow over earth's surfaces are more sensible to daily cycles due to solar radiation. It is pointed out that only a small portion of solar radiation (almost 25 %) is directly absorbed by the atmosphere, while a part of the same order (29 %) is directly reflected, and the main part (almost 48 %) is transferred and then absorbed by the earth's surface. The absorption of this solar energy is the cause of the daily temperature variations of earth's surfaces, which modify the heat transfer between the ground and the ABL during the day. On the other hand, in the oceans the thermal structure of the ABL above it is less variable due to the important thermal capacity of the water which limits a lot the temperature variation at the ocean's surface.*

The lower part of the atmosphere is commonly divided into several layers with varying degrees of turbulent mixing and with distinct mechanisms of turbulence production. It is important to make convenient approximations in order to get simplified relationship between state and process variables because the forces that dominate the flow in each layer are different. The identification of the beginning or the end of layers is possible through the profiles of potential temperature, humidity, wind or trace gas of concentrations and the accuracy is improved thanks to observed patterns of time variations of these variables on the 24-h cycle. The existence of a vertical structure is a consequence of the gravity and of the strong influence of ground surface on the overlying atmosphere through momentum absorption and exchanges of energy and materials. Nevertheless, if the land cover is inhomogeneous, if the terrain is sloped, or if the flow is disturbed by synoptic weather events (e.g. cold front passage) or mesoscale phenomena (e.g. land-lake

breezes), some of the layers could be indistinct (Lee, 2018).

Although the structure of the ABL is not homogeneous in time or in space, for a first approximation it is common to consider it horizontally uniform (in statistical term) and to identify main different parts. The ABL is generally divided into 3 parts which are represented on the Figure 1.1. They are:

- **The Ekman layer or outer layer:** It is the upper part of the ABL. This layer marks the transition between the free atmosphere, where the air movements are given by the law of the geostrophic equilibrium and are only driven by the Coriolis force and an horizontal pressure gradient, and the lower part of the atmosphere where the wall effects of the ground or ocean surface begin to be important. Therefore, Ekman layer is the layer where there is a force balance between pressure gradient force, Coriolis force and turbulent drag.
- **Surface Boundary Layer (SBL) or surface layer:** Closer to the ground, it is possible to identify the SBL which is almost 10 % of the ABL and where the flow is not influenced by the Coriolis force, but it is driven by the friction and the heat transfer at ground. The similarity theory of Monin-Obukhov is generally applied (Monin and Obukhov, 1954). It introduces the concept of atmospheric stability to describe the vertical profile of velocity and temperature.
- **Canopy layer or urban canopy layer:** It is the layer attached to the ground surface. The canopy layer extends from the ground to the mean height of buildings or obstacles (i.e. trees, vegetation, etc). It is characterised by an extremely complex and inhomogeneous flow due to the amount of obstacles, the variable space between obstacles and their heights. In fact the interaction between the flow and the obstacles is of fundamental importance in this region. This is the reason why there is not a universal way to treat the air flow in this part of the atmosphere.

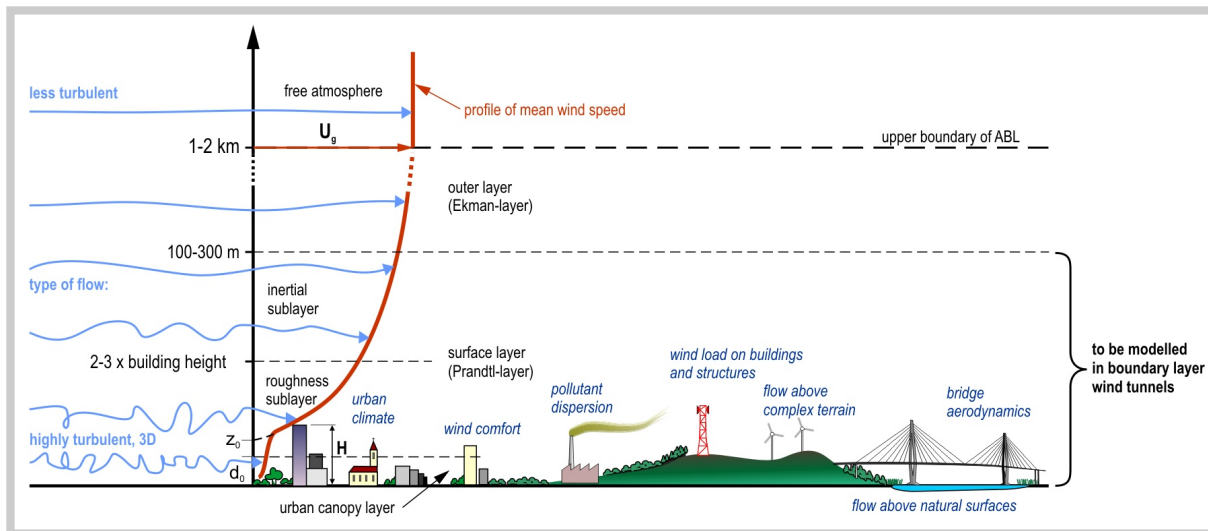


Figure 1.1: Subdivision of the ABL. From [Establishment of an Atmospheric Flow Laboratory Project](#); last access: January 18th, 2022.

The flow in the ABL is highly turbulent. A property of this turbulence is that it is decoupled from the large meteorological variations, which develop over several days. Analysing the spectral distribution of the kinetic energy of the wind speed, shown in Figure 1.2, it is pointed out that there exist a separation zone between the meteorological variations and the turbulent fluctuations (Soberanis and Mérida, 2015). This separation allow to treat or model independently the two scale ranges. For a time of the order of hours or minutes, it is possible to assume that the

meteorological variations are sufficiently slow to be considered constants and that the turbulent is fast enough to be parameterized by average operators.

As already mentioned, in the Ekman layer and free atmosphere, the wind flow is defined by the Coriolis, friction and pressure gradient forces. On the other hand, in the surface layer the Coriolis force is negligible, while the ground roughness becomes a more important parameter, influencing both the velocity profile and the angle of incidence of wind at the ground level according to the isobars. The roughness of the terrain conditions the depth of the ABL (i.e. the rougher the terrain and the higher the ABL). The parameter z_0 describes the roughness of the terrain (Nikuradse, 1933). It is called aerodynamic roughness length, or just roughness length. Its meaning will be explained in the subsection 1.1.2.

The forcing, like Earth's rotation and small or large variations in pressure and temperature, produces the wind. The latter represents the horizontal and vertical motion of the air in the atmosphere. The vertical movement of the air is affected by the atmospheric stability. The magnitude of the horizontal wind is far greater than the vertical movement of air. However, the influence of atmospheric stability on vertical movement is equally important because it could determine the behaviour of other physical phenomena such as the dispersion of pollutants. Stability is simply the resistance of the atmosphere to vertical motion. More precisely, it is the degree to which vertical motion is enhanced or suppressed in the atmosphere (Lee, 2018).

Atmospheric stability is described according to the effects of the environment on vertical motion. Each type can exist simultaneously in the atmosphere at different levels. The three types are:

- Unstable atmosphere, which enhance or encourage the vertical movement of air and is characterised by:

$$\partial\bar{\theta}/\partial z < 0$$

- Stable atmosphere, which suppress or limit vertical motion and is characterised by:

$$\partial\bar{\theta}/\partial z > 0$$

- Neutral atmosphere, which neither suppress nor enhance vertical motion and is characterised by:

$$\partial\bar{\theta}/\partial z = 0$$

The vertical gradient of the potential temperature $\partial\bar{\theta}/\partial z$ allows to know the state of the atmospheric stability. However, in this way, it is not possible to have a quantitative description of the stability. In fact, the combined effect of wind and thermal stratification can be captured only thanks to quantitative stability parameters. One such parameters is the Richardson number, which is the ratio between the thermal and the mechanical turbulent kinetic energy production terms. However, to deepen this topic, it was preferred to adopt the Monin-Obukhov similarity theory, as we will see in next subsection.

Based on theoretical considerations, it is possible to assume the boundary layer to have a depth proportional to u_*/f , where u_* is the friction velocity derived from the surface friction stress τ_w (Eq. (1.1)) and f is the Coriolis parameter equal to $2\Omega \sin \Phi$. In the latter relation, Ω is the earth's rotational speed and Φ the latitude. So the ABL height z_h , in the case of neutral stratification is expressed by Eq. (1.2).

$$\tau_w = \rho u_*^2 \tag{1.1}$$

$$z_h = C \left(\frac{u_*}{f} \right) \tag{1.2}$$

where a value of $C = 0.25$ provides boundary layer heights close to observed daytime heights.

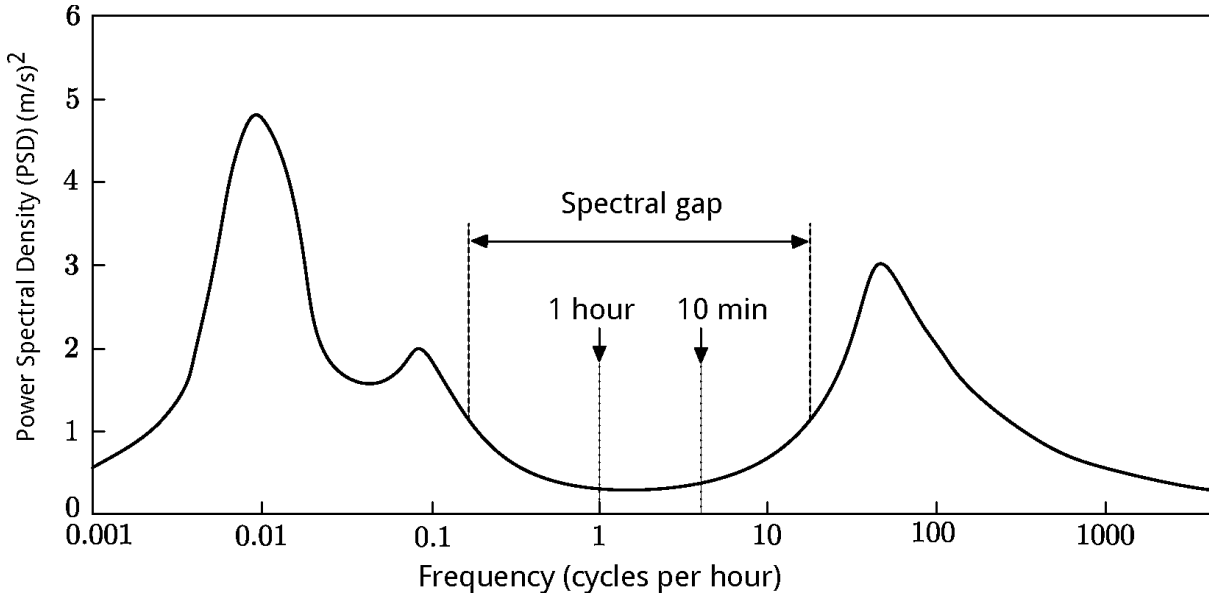


Figure 1.2: Reproduction of horizontal wind speed spectrum of [Van der Hoven \(1957\)](#) at Brookhaven National Laboratory. From: [Martin-Martínez *et al.* \(2012\)](#)

In the particular case of neutral ABL, which flows over a flat terrain, the horizontal mean velocity increases vertically with decreasing velocity gradient, and the turbulent shear stress decreases vertically. If only the lower part of the ABL is taken into account, the turbulent shear stress could be treated as almost constant and equal to the wall shear stress. Alternatively, if all ABL height is considered, shear stress should be variable along the height and vanish at the top of ABL ([Lee, 2018](#)).

Conform to previous considerations, the present study is focused on modeling the bottom part of the ABL, also known as surface boundary layer (SBL) or atmospheric surface layer, under neutral stability conditions. Nevertheless, the effects typical of the higher part of the ABL will be taken into account ([Gryning *et al.*, 2007](#)) through the use of characteristic profiles derived from experimental observations ([Tian *et al.*, 2018](#)), especially in RANS modeling. The application of our approach requires the analysis of small scale features like buildings and vegetation. Therefore, they will be treated in the proper manner.

1.1.2 Similarity theory for the ABL

For many boundary layer situations, the knowledge of the governing physics could be insufficient to derive laws based on first principles. Nevertheless, boundary layer observations often show consistent and repeatable characteristics, implying the possibility of developing empirical relationships for the variables of interest. Similarity theory provides a procedure to organise and group the variables to get the maximum advantage, and in turn provides guidelines on how to design experiments to gain more information and how to setup numerical models ([Stull, 2012](#)).

The similarity theory is an empirical method that describes the universal relationships between nondimensional variables thanks to the Buckingham π theorem ([Buckingham, 1914](#)). The most common classes of similarity scaling are Monin-Obukhov similarity, mixed-layer similarity, local similarity, local free convection and Rossby-number similarity. In the following part of the current subsection, the Monin-Obukhov similarity theory is presented.

Monin-Obukhov similarity theory

The most widely diffused approach to describe the nondimensional mean flow and mean temperature in the surface layer under non-neutral conditions as a function of the dimensionless height

parameter, named Obukhov length or Monin-Obukhov length L_{MO} , is the Monin-Obukhov similarity theory, (Monin and Obukhov, 1954). L_{MO} is the result of the combination of the turbulent vertical fluxes of heat and momentum, as illustrated by Eq. (1.3).

$$L_{MO} = -\frac{(\overline{-u'w'})^{\frac{3}{2}}}{\kappa \frac{g}{\theta_0} \overline{\theta'w'}} \quad (1.3)$$

where u' , w' , θ' are respectively the horizontal and vertical wind turbulent fluctuations and the potential temperature fluctuation. θ_0 is the mean potential temperature at ground level and κ is the von Kármán constant, usually equal to 0.4. Turbulent fluxes are hardly measurable, but they could be estimated thanks to two parameters: the friction velocity u_* and the turbulent heat flux q . Different methods exist to determine u_* and q using net radiation components and (potential) temperature gradient, which largely differ in the convective and in the stable boundary layer (Cimorelli *et al.*, 2005). The Monin-Obukhov length could be interpreted as the height from which the terms of production/dissipation of turbulent kinetic energy due to convective effects dominates over the terms of production/diffusion of turbulence due to shear.

A.S. Monin and A.M. Obukhov developed their famous similarity theory on the basis of the following findings (Foken, 2006):

- The essential experimental work at the Geophysical Main Observatory Leningrad, directed by scientists such as Lajchman, Budyko and others.
- The logarithmic wind profile (Prandtl, 1925).
- The zero-plane displacement (Paeschke, 1937).
- The Obukhov length (Obukhov, 1946).

In the SBL, the turbulent momentum and heat fluxes could be considered constants with respect to the height. If the wall temperature θ_0 , the constant momentum flux $\tau_0 = \tau_w$ and the constant heat flux q_0 are taken into account, it is possible to define the characteristic scales of velocity, temperature and length:

- Friction velocity:

$$u_* = \sqrt{\frac{\tau_0}{\rho}}$$

- Surface-layer temperature scale or dynamic temperature:

$$\theta_* = -\frac{q_0}{\rho C_p u_*}$$

- Monin-Obukhov length:

$$L_{MO} = \frac{u_*^3}{\kappa(g/\theta_0)\theta_*}$$

Here C_p is the heat capacity at pressure constant. The similarity theory of M-O states that all the turbulent variables, dimensionless according to their scales, could be expressed as a universal function of the variable $\zeta = z/L_{MO}$. So the vertical gradients of \bar{u} and $\bar{\theta}$ are:

$$\frac{\kappa z}{u_*} \frac{\partial \bar{u}}{\partial z} = \phi_m(\zeta) \quad (1.4)$$

$$\frac{\kappa z}{\theta_*} \frac{\partial \bar{\theta}}{\partial z} = \phi_h(\zeta) \quad (1.5)$$

In the case of a neutral atmosphere (i.e. $L_{MO} \rightarrow \infty$), the universal functions are constants and equal to 1. Nevertheless, in a stable and unstable atmosphere, they are defined thanks to their empirical relations, as for example (Dyer, 1974):

$$\phi_m(\zeta) = \sqrt{\phi_h(\zeta)} = (1 - 16\zeta)^{-\frac{1}{4}} \quad \text{if } L_{MO} < 0 \text{ (unstable)} \quad (1.6)$$

$$\phi_m(\zeta) = \phi_h(\zeta) = 1 + 5\zeta \quad \text{if } L_{MO} > 0 \text{ (stable)} \quad (1.7)$$

Consequently, for a neutral boundary layer, an idealised vertical profile of the mean flow is the logarithmic wind profile derived from the Prandtl's mixing length theory. The latter affirms that the horizontal component of mean flow is proportional to the logarithmic of the height, as shown by Eq. (1.8).

$$\frac{\bar{u}(z)}{u_*} = \frac{1}{\kappa} \ln \left(\frac{z}{z_0} \right) \quad (1.8)$$

Here, the mean velocity \bar{u} is normalised by the friction velocity u_* , derived from Eq. (1.1). Whereas the height z is compared to the roughness length z_0 , also known as aerodynamic roughness, and κ is the von Kármán constant. The roughness length z_0 allow to characterise different types of terrain surfaces, as shown by Table 1.1. This type of characterisation is mainly based on the effect the roughness has on the mean velocity. Nevertheless, Krogstad and Antonia (1994) argue that it is insufficient. In fact, their experimental results, as well as those from previous investigations (i.e. Krogstad *et al.* (1992)), indicate that a roughness characterisation in terms of turbulence structure would be worth pursuing in the future. The information in Table 1.1 represents a useful information for simulations but it would be important to carry out a more precise characterisation of the terrain surface, if possible.

Terrain surface characteristics	z_0 [m]
Water areas (lakes, open sea)	1×10^{-4}
Sand surfaces (smooth)	3×10^{-4}
Snow surfaces (smooth)	1×10^{-3}
Bare soil (smooth)	5×10^{-3}
Airport runway areas, mown grass	0.001 ÷ 0.01
Farmland with very few buildings, trees, etc	0.03
Farmland with open appearance	0.05
Farmland with closed appearance	0.10
Many trees and/or bushes	0.20
Shelter belts	0.30
Suburbs	0.50
City	1.00

Table 1.1: Order of magnitude of roughness lengths for different types of terrains (Troen and Lundtang Petersen, 1989).

As previously illustrated, the Monin-Obukhov similarity theory generalises the mixing length theory in non-neutral conditions by using “universal functions” of dimensionless height to characterise vertical distributions of mean flow and temperature. In fact, any height z can be provided with the dimensionless stability parameter z/L_{MO} . The universal functions describe the vertical profiles of wind and temperature as a function of z/L_{MO} for neutral, stable and unstable cases. Moreover, thanks to L_{MO} , it is possible to quantify the stability conditions. Table 1.2 presents the stability classes of Pasquill-Gifford and the respective values of L_{MO} . These values were estimated from a series of experiments (Hanna *et al.*, 1982).

Monin-Obukhov similarity theory represents a notable landmark of modern micrometeorology, providing a theoretical basis for micrometeorological experiments and measurement techniques (Foken, 2006). Numerous measurements and advanced computational fluid dynamics datasets have validated the theory. Although it showed some weakness, it still provides the most solid basis for all fields of atmospheric modeling (Garratt, 1980; Dyer *et al.*, 1982; Högström, 1990; Johansson *et al.*, 2001).

Stability class	Monin-Obukhov length [m]
A	$-2 < L_{MO} < -3$
B	$-4 < L_{MO} < -5$
C	$-12 < L_{MO} < -15$
D	$L_{MO} \rightarrow \infty$
E	$35 < L_{MO} < 75$
F	$8 < L_{MO} < 35$

Table 1.2: Typical values of the Monin-Obukhov length for each stability class of Pasquill-Gifford, (Pasquill, 1961; Gifford, 1976).

1.1.3 General flow equations in the context of the ABL

In this section, the generic equations that govern the dynamic of the ABL are presented. In addition, it is paid particular attention to the surface boundary layer (SBL). These are just the equations of fluid mechanics with the addition of some specific assumptions for the current cases. The different phenomena of the atmosphere are related to the energy and material fluxes. The fluxes are described by the fluid dynamics equations (or Navier-Stokes equations) that conserve the following physical quantities:

- the mass, expressed through the density ρ
- the momentum, where $\rho \mathbf{u}$ is the momentum per unit volume and $\mathbf{u} = (u, v, w) = (u_x, u_y, u_z) = (u_1, u_2, u_3)$
- the energy, E

Moreover, the momentum conservation introduces another unknown, the pressure P . It could be generally considered as a thermodynamic variable and related to density and temperature by an equation of state. The ideal gas law is capable to describe the state of gases in the boundary layer:

$$\frac{P}{\rho} = \mathcal{R} T \quad (1.9)$$

where \mathcal{R} is the gas constant for dry air ($\mathcal{R} = 287 \text{ J}\cdot\text{K}^{-1}\text{kg}^{-1}$) and T is the temperature of the system. However, for incompressible flows, there is no connection between pressure and density and a different understanding of pressure is required, as we will see below.

For the purposes of our research, it is needed to add a seventh physical quantity for the study of the desired pollutant. In fact, the pollutants considered in the thesis could be described by a passive scalar because they have characteristics similar to the air and/or do not influence the flow field (e.g. when the pollutant is very diluted in the air). It is important to highlight that we can add a passive scalar with its respective conservation equation for each pollutant to be analysed. Finally, an incompressible flow is adopted and the Coriolis force is negligible because we are interested to study the surface boundary layer (SBL).

Mass conservation

The continuity or mass conservation equation is expressed in Eq. (1.10).

$$\frac{\partial \rho}{\partial t} + \nabla \cdot (\rho \mathbf{u}) = 0 \quad (1.10)$$

If \mathcal{V} and \mathcal{L} are typical velocity and length scales for the boundary layer, then it can be shown that $(d\rho/dt)/\rho \ll \partial u_j/\partial x_j$ if the following conditions are met (Businger, 1982):

- $\mathcal{V} \ll 100 \text{ m/s}$, i.e. $\approx 0.3 C_s$.
- $\mathcal{L} \ll 12 \text{ km}$.
- $\mathcal{L} \ll C_s^2/g$.
- $\mathcal{L} \ll C_s/f$.

where C_s is the speed of sound and f is the frequency of any pressure waves that may occur. Since these conditions are generally respected by all turbulent motions smaller than mesoscale, Eq. (1.10) reduces to:

$$\nabla \cdot \mathbf{u} = 0 \quad (1.11)$$

Therefore, in the current thesis, it is possible to assume that the flow is characterised by constant-density (i.e. flow in which the density ρ is independent both of \mathbf{x} and of t) and that the velocity field is solenoidal.

Momentum conservation

The principle of momentum conservation is a direct consequence of Newton's second law of motion. It relates the fluid particle acceleration $D\mathbf{u}/Dt$ to the surface forces and body forces experienced by the fluid. In general, the surface forces, which are of molecular origin, are described by the stress tensor $\tau = \tau_{ij}(\mathbf{x}, t)$ – which is symmetric, i.e. $\tau_{ij} = \tau_{ji}$. Another surface force is the pressure gradient ∇P , while a common body force of interest is the gravity \mathbf{g} . These forces cause the acceleration of the fluid as pointed out by the momentum equation:

$$\frac{\partial \mathbf{u}}{\partial t} + \nabla \cdot (\mathbf{u} \otimes \mathbf{u}) = \frac{1}{\rho} \nabla \cdot \sigma + \mathbf{F} \quad (1.12)$$

where \mathbf{F} represent the sum of the volume forces (i.e. gravity, Coriolis force and others) and σ is the stress tensor, for a Newtonian fluid in an incompressible flow is:

$$\sigma = -P \mathbf{I} + \mu (\nabla \mathbf{u} + \nabla^t \mathbf{u}) = -P \mathbf{I} + \tau \quad (1.13)$$

\mathbf{I} is the identity tensor, P the pressure, μ the constant coefficient of viscosity and τ the viscous stress tensor. Recalling that the velocity is solenoidal (i.e. $\partial u_i/\partial x_i = 0$), it is observed that the Eq. (1.13) describes the stress as the sum of isotropic ($P\delta_{ij}$) and deviatoric contributions.

Exploiting the facts that ρ and μ are constants and the solenoidal field, the expression for the stress tensor (Eq. (1.13)) could be substituted inside the general momentum equation (Eq. (1.12)) to obtain the Navier-Stokes equations:

$$\frac{\partial u_j}{\partial t} + u_i \frac{\partial u_j}{\partial x_i} = -\frac{1}{\rho} \frac{\partial P}{\partial x_j} + \nu \frac{\partial^2 u_j}{\partial x_i \partial x_i} + F_j \quad (1.14)$$

It is possible to define a modified pressure:

$$p = \frac{P}{\rho}$$

In this way the Navier-Stokes equations are simplified:

$$\frac{\partial \mathbf{u}}{\partial t} + \nabla \cdot (\mathbf{u} \otimes \mathbf{u}) = -\nabla p + \nu \nabla^2 \mathbf{u} + \mathbf{F} \quad (1.15)$$

where ν is the kinematic viscosity, i.e. μ/ρ .

Energy conservation

The conservation of the total energy of the fluid E is given by the Eq. (1.16).

$$\frac{\partial(\rho E)}{\partial t} + \nabla \cdot (\rho E \mathbf{u}) = -\nabla \cdot (P \mathbf{u}) - \nabla \cdot \mathbf{q} + \nabla \cdot (\boldsymbol{\tau} \cdot \mathbf{u}) + \rho \mathbf{F} \cdot \mathbf{u} + \rho H \quad (1.16)$$

Here, the first right-hand term corresponds to the power of the pressure forces and the second term represent the conductive heat transfer, in which \mathbf{q} is the heat flux. The latter is related to temperature thanks to the Fourier law:

$$\mathbf{q} = -\lambda \nabla T$$

where λ is the thermal conductivity. The third term denotes the dissipation of mechanical energy by viscous friction. $\boldsymbol{\tau}$ is the tensor of viscous stresses. The fourth term is related to the power of volume forces. Finally, H represents the heat sources in the fluid.

Scalar conservation

In order to describe the conservation of a species' concentration in the atmosphere using an Eulerian approach, it is considered a scalar transported by an incompressible flow. Moreover, it is assumed that the dynamic and chemical behaviour of this scalar is passive, i.e. it exactly follows the movement of fluid particles and does not react with other species. If the passive scalar is denoted by c , the conservation of this variable is illustrated by:

$$\frac{\partial c}{\partial t} + \nabla \cdot (\mathbf{u} c) = \nabla \cdot (D_c \nabla c) + S_c \quad (1.17)$$

where D_c is the molecular diffusivity (or diffusion coefficient) of the passive scalar c and S_c corresponds to the source term. This equation represents the change of the concentration at a specified point as the sum of the advective flux, the diffusive flux and the source terms respectively. Gravitational influence could be added as an extra advection component. Nevertheless, turbulent diffusion is not represented in Eq. (1.17). In the following chapters and respective sections, dedicated to the RANS (subsection 2.1.1) and LES (subsection 3.1.2) approaches, we will discuss how this term is considered.

Simplifications and approximations

Under certain conditions the magnitude of some of the terms in the governing equations become smaller than the other terms and can be neglected. In these cases, the equations become simpler. In this way, many advances have been possible in atmospheric dynamics.

One simplification is called the *shallow motion approximation* (Mahrt, 1986). This approximation is valid if all the following conditions are true:

1. the vertical depth scale of density variations in the boundary layer is much shallower than the scale depth of the lower atmosphere. This latter scale depth is $\rho/(\partial\rho/\partial z) \approx 8$ km;
2. advection and divergence of mass at a fixed point approximately balance, leaving only slow or zero variations of density with time; and

3. the perturbation magnitudes of density, temperature and pressure are much less than their respective mean values.

A more stringent simplification, called the *shallow convection approximation*, needs to comply the conditions above plus:

4. the mean lapse rate ($\partial T/\partial z$) can be negative, zero, or even slightly positive. For the statically stable positive case, ($\partial T/\partial z \ll g/\mathcal{R}$, where $g/\mathcal{R} = 0.0345$ K/m; and
5. the magnitude of the vertical perturbation pressure gradient term must be of the same order or less than the magnitude of the buoyancy term in the equation of motion.

This latter condition establishes that vertical motion is limited by buoyancy, which is the origin of the term *shallow convection*.

We have applied condition (1) and (2) to yield the incompressible form of the continuity equation. The other conditions will be applied to yield further simplifications. One of them leads to the Boussinesq approximation. In fact, a prerequisite for the Boussinesq approximation is that the *shallow convection* conditions is satisfied. This approximation is useful when stable and unstable atmospheric conditions are treated. Nevertheless, the current thesis is focused on the neutral condition. For further details and for a more complete view, please consult [Stull \(2012\)](#).

1.1.4 Wall-bounded turbulent shear flow

This section brings another point of view regarding the atmospheric boundary layer. In addition, it treats more extensively the presence of the wall and its concrete and fundamental influence on the atmospheric flow. The concepts presented in the current subsection have been mainly taken from [Pope \(2000d\)](#) and [Kundu *et al.* \(2012a\)](#).

In the case of free turbulent shear flows at sufficiently higher Reynolds number (Re), these flows are independent of Re and a self-similar approach can be used. The latter implies that the flow could be defined by a single length-scale. Nevertheless, this simplifications are not valid when the flow is bounded by a surface. For these flows, the effect of viscosity is important in the region near the wall, where the turbulent fluctuations decay to zero. Further, the use of a second fundamental length scale, l_ν or δ_ν , is required in order to explain the physical phenomena close to the wall. As observed in [Figure 1.3](#), which represents the surface drag, the effect of viscosity is also felt at high Re. Differently from free turbulent shear flows, wall-bounded flows are not independent of Re when $\text{Re} \rightarrow \infty$.

The importance of wall-bounded turbulence is widely recognised in engineering applications and geophysical phenomena. It plays a fundamental role on regulating advective processes and on the exchange of mass, momentum and heat at the earth surface. Thus, the literature on this field is large. For instance, in addition to the already mentioned sources, the works of [Kline *et al.* \(1967\)](#) and [Adrian \(2007\)](#) are recommended. They discuss the vorticity structures in wall-bounded turbulence. Furthermore, the review articles of [George \(2006\)](#) and [Marusic *et al.* \(2010\)](#) are also remarked.

Between the wall-bounded turbulent shear flows, we focus on the turbulent boundary-layer flow that develops from uniform flow over a smooth flat plate. These flows are ruled by the boundary-layer approximation.

The boundary-layer approximation is based on the [Prandtl \(1905\)](#) hypothesis:

- For small values of viscosity, viscous forces are only important close to the solid boundaries (within the boundary layer) where no-slip condition needs to be satisfied. Everywhere else, they can be neglected.
- The thickness of the boundary layer approaches to zero as the viscous becomes smaller.

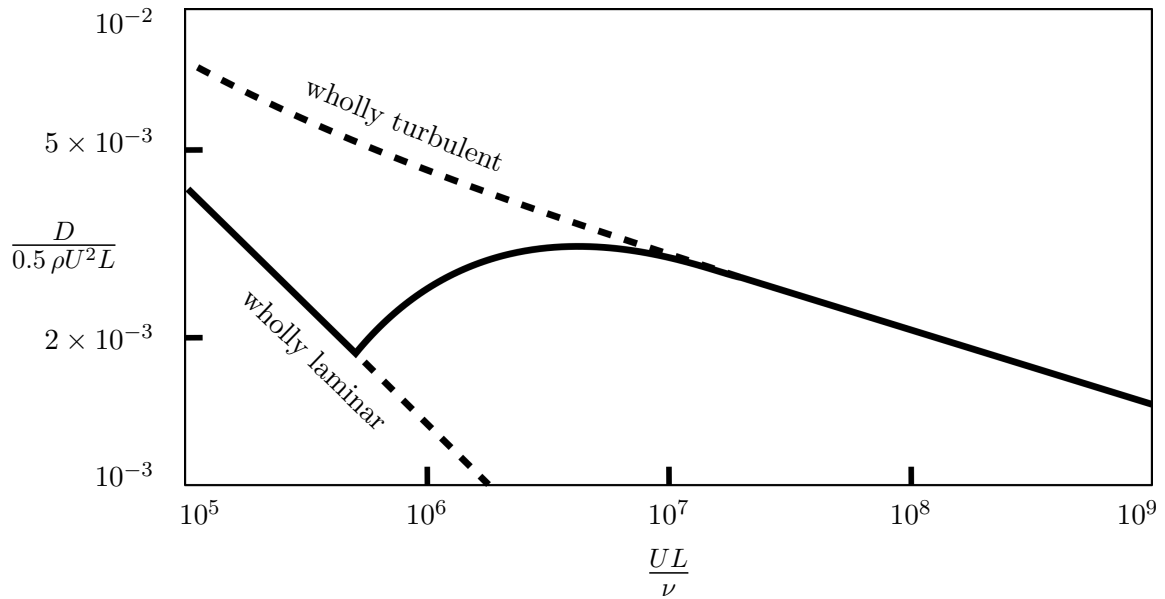


Figure 1.3: Measured drag coefficient for a boundary layer over a flat plate. From: Kundu *et al.* (2012b)

Therefore, the boundary layer approximation states that, for a sufficiently high Re , the flow over a surface can be divided into an outer region of inviscid flow unaltered by viscosity (most of the flow), and a region close to the surface where viscosity is fundamental (the boundary layer). In this way, the flow is divided into an inviscid portion and the boundary layer. We are particularly interested in the latter.

The simplest boundary layer (BL) to take into account is that which is formed when a uniform-velocity non-turbulent stream (u_0) flows over a smooth flat plate, as sketched in Figure 1.4. If compared with other wall-bounded turbulent flows, the main differences are three. Firstly, the BL develops continuously in the flow direction. It means that the BL thickness $\delta(x)$ increases with x . Then, wall shear stress $\tau_w(x)$ cannot be deduced a priori. Finally, the outer part of the flow is characterised by intermittency, which alternates turbulent and non-turbulent motion.

These differences does not influence the behaviour in the inner layer ($z/\delta < 0.1$), which is the same for all the wall-bounded turbulent flows previously cited.



Figure 1.4: Sketch of a flat-plate boundary layer.

Description of the flow

The coordinate system of the boundary layer flow is illustrated in Figure 1.4. The predominant direction of the flow is x . The statistics are independent of y direction. As stated above, the development of the BL implies that statistics depend on x and z coordinates. Therefore, the spanwise mean velocity is zero. Whereas the velocity components are respectively u , v and w .

The equation of Bernoulli relates the free-stream pressure $p_0(x)$ and velocity u_0 :

$$-p_0(x) + \frac{1}{2}\rho u_0(x)^2 = \text{constant} \quad (1.18)$$

Thus, the pressure gradient is given by:

$$-\frac{dp_0}{dx} = \rho u_0 \frac{du_0}{dx} \quad (1.19)$$

Accelerating flow ($du_0/dx > 0$) is related to a negative or favourable pressure gradient. On the other hand, decelerating flow implies a positive or adverse pressure gradient. The latter is so called because it could lead to a separation of the BL from the surface. Our attention is focused on the slightly negative pressure gradient, which is balanced by the shear stress.

The BL thickness $\delta(x)$ could be defined as *the value of z at which $\bar{u}(x, z)$ equals 99% of the free-stream velocity $u_0(x)$* . However, it might be affected by local variations or uncertainties in the streamwise mean velocity. On the other hand, a more reliable option can be to adopt an integral measure like the displacement thickness:

$$\delta^*(x) = \int_0^\infty \left(1 - \frac{\bar{u}}{u_0}\right) dz \quad (1.20)$$

or the momentum thickness:

$$\theta^*(x) = \int_0^\infty \frac{\bar{u}}{u_0} \left(1 - \frac{\bar{u}}{u_0}\right) dz \quad (1.21)$$

The momentum equations

Applying the BL equations, the flow develops in the x direction and the axial stress gradients are small with respect to the cross-stream gradients. The vertical mean momentum equation becomes:

$$\frac{1}{\rho} \frac{\partial \bar{p}}{\partial z} + \frac{\partial \overline{w^2}}{\partial z} = 0 \quad (1.22)$$

If it is integrated, it yields to:

$$\bar{p} + \rho \overline{w^2} = p_0(x) \quad (1.23)$$

In the case of $\overline{w^2}$ null at the wall, the wall pressure $p_w(x)$ equals the free-stream pressure $p_0(x)$.

In the BL approximation, the mean-axial momentum equation becomes:

$$\begin{aligned} \bar{u} \frac{\partial \bar{u}}{\partial x} + \bar{w} \frac{\partial \bar{u}}{\partial z} &= \nu \frac{\partial^2 \bar{u}}{\partial z^2} - \frac{\partial \overline{uw}}{\partial z} - \frac{1}{\rho} \frac{dp_0}{dx} \\ &= \frac{1}{\rho} \frac{\partial \tau}{\partial z} + u_0 \frac{du_0}{dx} \end{aligned} \quad (1.24)$$

where $\tau(x, z)$ is the total shear stress:

$$\tau(z) = \rho \nu \frac{d\bar{u}}{dz} - \rho \overline{u'w'} \quad (1.25)$$

At the wall, the convective terms are zero. It allows the balance between the shear stress and pressure gradients. In the case in which the pressure gradient is zero:

$$\frac{1}{\rho} \left(\frac{\partial \tau}{\partial z} \right)_{z=0} = \nu \left(\frac{\partial^2 \bar{u}}{\partial z^2} \right)_{z=0} = 0 \quad (1.26)$$

or non-zero:

$$\frac{1}{\rho} \left(\frac{\partial \tau}{\partial z} \right)_{z=0} = \nu \left(\frac{\partial^2 \bar{u}}{\partial z^2} \right)_{z=0} = -\frac{1}{\rho} \frac{dp_0}{dx} \quad (1.27)$$

Near-wall shear stress and wall regions

As observed in Eq. (1.25), the total shear stress is the result of the sum of the viscous stress $\rho \nu d\bar{u}/dz$ and the Reynolds stress $-\rho \overline{u'w'}$.

$$\tau_w \equiv \rho \nu \left(\frac{d\bar{u}}{dz} \right)_{z=0} \quad (1.28)$$

The profiles of the viscous and Reynolds shear stresses are shown in Figure 1.5. From the figure, it is important to highlight that the viscous stress dominates at the wall, while the Reynolds shear stress dominates in the free shear flow. In fact, in the latter region, the viscous stresses are negligibly small with respect to Reynolds stresses. Moreover, near the wall the velocity profiles depends on the Reynolds number because the viscosity is an influencing parameter, in contrast to the free shear flow situation.

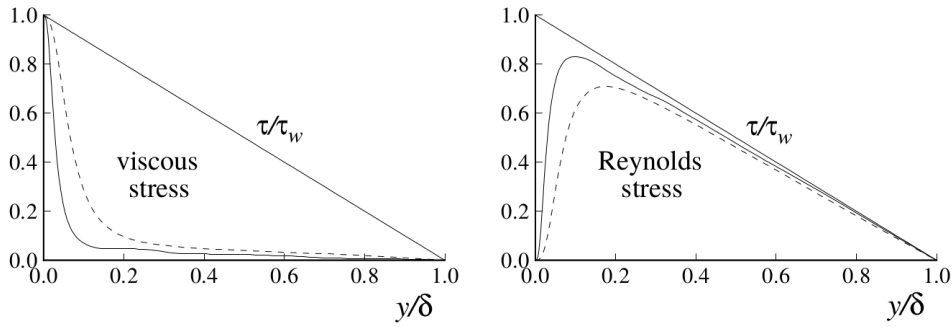


Figure 1.5: Profiles of the viscous shear stress and Reynolds shear stress in turbulent channel flow at two low Reynolds numbers: $Re = 56000$ (dashed line) and $Re = 13750$ (solid line). From DNS data of Kim *et al.* (1987).

The previous considerations highlight that the viscosity ν and the shear stress τ_w are fundamentals near the wall. Adding the density ρ to these quantities, two viscous scales are defined. These are the friction velocity:

$$u_\tau = u_* \equiv \sqrt{\frac{\tau_w}{\rho}} \quad (1.29)$$

and the viscous length scale:

$$\delta_\nu \equiv \nu \left(\frac{\rho}{\tau_w} \right) = \frac{\nu}{u_*} \quad (1.30)$$

Furthermore, the Reynolds number based on the viscous scales is identically unity, i.e. $u_* \delta_\nu / \nu = 1$. Whereas the friction Reynolds number Re_τ is defined as:

$$Re_\tau \equiv \frac{u_* \delta}{\nu} = \frac{\delta}{\delta_\nu} \quad (1.31)$$

The distance from the wall measured in viscous lengths - or wall units - is denoted by:

$$z^+ \equiv \frac{z}{\delta_\nu} = \frac{u_* z}{\nu} \quad (1.32)$$

Note that z^+ is similar to a local Reynolds number, so its magnitude can be expected to determine the relative importance of viscous and turbulent processes.

The subdivision of the stress contributions based on its viscous and turbulent origin allows to identify two different scaling laws for the wall-bounded turbulent flows. These laws are the *law of the wall* and the *velocity defect law*. The first is applied in the region, where the viscous effect matters. Furthermore, its length scale is z , i.e. the distance from the wall. It defines the *inner layer* region. The second law is valid where the flow becomes independent of the viscous effect. Whereas, its length scale is δ , i.e. the turbulent layer thickness. This region is commonly called *outer layer*. There is a third law, the *logarithmic law*, which is applied in the region where the inner and outer layers overlaps. This region is denoted as the *logarithmic region*. Here, the form of the mean streamwise velocity profile could be estimated from dimensional analysis.

In the near-wall flow, different regions or layers are defined on the basis of z^+ . In the viscous wall region, i.e. $z^+ < 50$, there is a direct effect of molecular viscosity on the shear stress. Moreover, in the viscous sublayer $z^+ < 5$, the Reynolds shear stress is negligible compared to viscous stress. On the other hand, in the outer layer, i.e. $z^+ > 50$, the direct effect of viscosity is negligible. In according with Prandtl hypothesis, as the Re of the flow increases, the fraction of the boundary layer occupied by the viscous wall region decreases.

The wall regions and layers are summarised in [Table 1.3](#) and [Figure 1.6](#). In the following part of this section, we pay particular attention to the inner layer and the logarithmic region. In fact, these layers of the wall region are fundamental to understand the wall functions and models used to achieve our scopes. For further details, please refer to the previously mentioned studies.

Region	Location	Properties
Inner layer	$z/\delta < 0.1$	\bar{u} determined by u_* and z^+ , independent of u_0 and δ .
Viscous wall region	$z^+ < 50$	The viscous contribution to the shear stress is important.
Viscous sublayer	$z^+ < 5$	The Reynolds shear stress is negligible compared with the viscous stress.
Outer layer	$z^+ > 50$	Direct effects of viscosity on \bar{u} are negligible.
Overlap region	$z^+ > 50, z/\delta < 0.1$	Region of overlap between inner and outer layers (at large Re numbers).
Log-law region	$z^+ > 30, z/\delta < 0.3$	The log-law is valid.
Buffer layer	$5 < z^+ < 30$	The region between the viscous sublayer and the log-law region.

Table 1.3: Wall regions and layers and their properties. From: ([Pope, 2000c](#)).

Mean velocity profiles

A boundary layer flow is completely defined by ρ , ν , δ and dp_w/dx , or equivalently by ρ , ν , δ and u_* . Consequently, there are two independent nondimensional groups that can be formed with the latter parameters (e.g. z/δ and $\text{Re}_\tau = u_*\delta/\nu$). Therefore, the mean velocity profile could be expressed as:

$$\bar{u} = u_* F_0 \left(\frac{z}{\delta}, \text{Re}_\tau \right) \quad (1.33)$$

where F_0 is a universal nondimensional functions that must be determined.

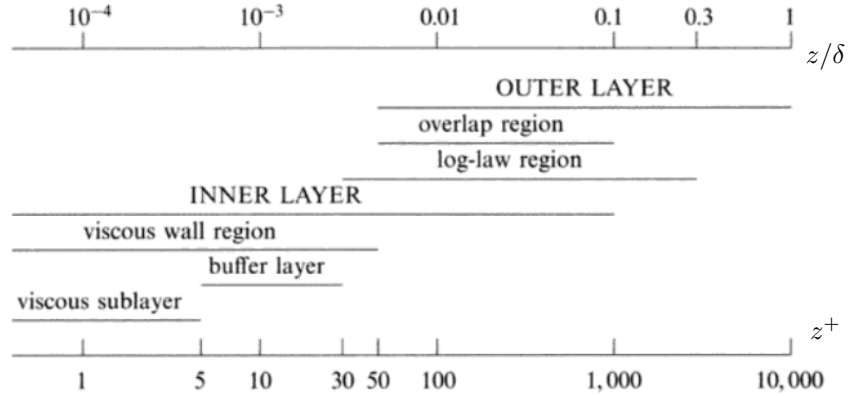


Figure 1.6: Sketch illustrating the various wall regions and layers defined in terms of z^+ and z/δ , for a turbulent channel flow ($\text{Re}_\tau = 1 \times 10^4$). From: (Pope, 2000c).

Although this way to determine the mean velocity profile seems natural, it is better to follow a different approach. Instead of considering \bar{u} , the velocity gradient $d\bar{u}/dz$ is considered, which is the dynamically important quantity. In fact, the viscous stress and the turbulence production are both determined by the velocity gradient. Similarly, on dimensional ground, $d\bar{u}/dz$ depends on two nondimensional parameters, so that it is possible to write:

$$\frac{d\bar{u}}{dz} = \frac{u_*}{z} \Phi\left(\frac{z}{\delta_\nu}, \frac{z}{\delta}\right) \quad (1.34)$$

where Φ is a universal nondimensional function. The choice of the parameters to scale z is due to their importance in the viscous wall region ($z^+ < 50$) and in the outer layer ($z^+ > 50$). Therefore, δ_ν and δ are respectively the chosen parameters. It yields to the following relation:

$$\left(\frac{z}{\delta_\nu}\right) \bigg/ \left(\frac{z}{\delta}\right) = \text{Re}_\tau \quad (1.35)$$

It illustrates that these two parameters contain the same information as z/δ and Re_τ .

The law of the wall

Prandtl (1925) postulated that, at high Re number, close to the wall (i.e. $z/\delta \ll 1$) there is an *inner layer* in which the mean velocity profile is determined by the viscous scales, independent of δ and u_0 . Mathematically, this implies that the function $\Phi(z/\delta_\nu, z/\delta)$ in Eq. (1.34) tends asymptotically to a function of z/δ_ν only, as z/δ tends to zero. Therefore, Eq. (1.34) becomes:

$$\frac{d\bar{u}}{dz} = \frac{u_*}{z} \Phi_{\text{I}}\left(\frac{z}{\delta_\nu}\right), \quad \text{for } \frac{z}{\delta} \ll 1 \quad (1.36)$$

where:

$$\Phi_{\text{I}}\left(\frac{z}{\delta_\nu}\right) = \lim_{z/\delta \rightarrow 0} \Phi\left(\frac{z}{\delta_\nu}, \frac{z}{\delta}\right) \quad (1.37)$$

Considering $z^+ \equiv z/\delta_\nu$ and u^+ defined by:

$$u^+ \equiv \frac{\bar{u}}{u_*} \quad (1.38)$$

Eq. (1.36) can alternatively be written as:

$$\frac{du^+}{dz^+} = \frac{1}{z^+} \Phi_I(z^+) \quad (1.39)$$

The integral of Eq. (1.39) is the *law of the wall*:

$$u^+ = f_w(z^+) \quad (1.40)$$

where:

$$f_w(z^+) = \int_0^{z^+} \frac{1}{z'} \Phi_I(z') dz' \quad (1.41)$$

The important point is not Eq. (1.41), but the fact that u^+ depends only on z^+ for $z/\delta \ll 1$.

For Reynolds numbers not too close to transition, there is abundant experimental verification that the function f_w is universal, not only for boundary layer flow, but also for pipe and channel flows. In fact, the form of the function $f_w(z^+)$ could be determined for small and large values of z^+ .

The viscous sublayer

The no-slip boundary condition, i.e. $\bar{u}_{z=0} = 0$, implies $f_w(0) = 0$. Whereas, the viscous stress law at the wall (Eq. (1.28)) imposes the derivative:

$$f'_w(0) = 1 \quad (1.42)$$

Thanks to these boundary conditions, the Taylor-series expansion for $f_w(z^+)$ for small z^+ is derived:

$$f_w(z^+) = z^+ + O(z^{+2}) \quad (1.43)$$

This is useful to state that the departures from the linear relation $u^+ = y^+$ are negligible in the viscous sublayer ($z^+ < 5$). Nevertheless, they are significant for $z^+ > 12$.

The logarithmic law

Commonly the inner layer is settled as $z/\delta < 0.1$. If a high Reynolds number is considered, the outer part of the inner layer would have large z^+ values. Therefore, in this case, the influence of the viscous is reduced. Considering Eq. (1.36), it is observed that $\Phi_I(z/\delta_\nu)$ no longer depends on ν . Therefore, its expression becomes:

$$\Phi_I = \frac{1}{\kappa}, \quad \text{for } \frac{z}{\delta} \ll 1 \text{ and } z^+ \gg 1 \quad (1.44)$$

It modifies also the mean velocity gradient expression, that is formulated as:

$$\frac{du^+}{dz^+} = \frac{1}{\kappa z^+} \quad (1.45)$$

The latter could be integrated to obtain:

$$u^+ = \frac{1}{\kappa} \ln(z^+) + B \quad (1.46)$$

where B is a constant. This is the logarithmic law of the wall due to [Von Kármán \(1930\)](#), or simply the *log law*, and κ is the von Kármán constant. According to [Pope \(2000c\)](#), there is some variation in the constant values of the log-law, but generally they are within 5% of $\kappa = 0.41$ and $B = 5.2$.

There is a transition region that separate the viscous sublayer ($z^+ < 5$) and the log-law region ($z^+ > 30$). It is called the buffer layer. Its bounds and graphical position are illustrated by [Table 1.3](#) and [Figure 1.6](#).

Rough surface

When the logarithmic law is derived, it is assumed that the flow in the inner layer is determined by the viscosity. The assumption is valid only for hydrodynamically smooth surfaces. In this case, the average height of the surface roughness elements is smaller than the thickness of the viscous sublayer. Contrarily for a hydrodynamically rough surface, the average height of surface roughness elements is greater than the viscous sublayer. An example, completely on our interest, is the atmospheric boundary layer where the trees, buildings and other near-ground obstacles behave as roughness elements. Each roughness element develops a wake and the shear stress is transmitted to the wall by the resulting drag on the roughness elements. Viscosity becomes irrelevant when the velocity distribution or the overall drag on the surface are determined. For this reason, the friction coefficients for a rough pipe and a rough flat surface results constant as $\text{Re} \rightarrow \infty$ (Nikuradse, 1933).

Close to the rough surface, the velocity distribution is still logarithmic. However, the intercept constant need to be fixed considering that the mean velocity $\bar{u}(z)$ is negligible within the roughness elements. It is possible to assume that the logarithmic-law is applied for $z > z_0$, where z_0 could be interpreted as a parameter representative of the effect of the roughness heights. Thanks to an approximate evaluation of the constant B in the logarithmic-law of Eq. (1.46), it is obtained Eq. (1.47).

$$u^+ = \frac{\bar{u}(z)}{u_*} = \frac{1}{\kappa} \ln \left(\frac{z}{z_0} \right) \quad (1.47)$$

Up to this point, we have presented the classical approach related to the study of wall-bounded turbulence, focused on the inertial sublayer or logarithmic region.

The mean velocity \bar{u} follows a logarithmic profile with distance from the wall z , as already illustrated by Eq. (1.46). In the latter equation, the coefficient B could be considered as a parameter that depends on the roughness of the surface, and is assumed to be constant for smooth-wall flows. Many approaches have been developed and used to achieve Eq. (1.46). Between previous and relevant studies, there are Prandtl (1925), Von Kármán (1930), Millikan (1939), Rotta (1962) and Townsend (1980). It is possible to observe that sometimes the theoretical arguments could differ. However, the main concept is that logarithmic region is associated with two main scales: the velocity scale u_* and any characteristic length scale with z , which is the distance from the wall. In agreement with this description, Townsend (1980) proposed that *the scaling from the wall can be associated with corresponding attached eddies, whose geometric lengths scale with z , and with population densities per characteristic eddy height that scale inversely with z* . The previous author illustrates an important characteristic: the streamwise and spanwise turbulence intensities follow a logarithmic profile of the form:

$$\overline{u^2}^+ = B_1 - A_1 \ln \left(\frac{z}{\delta} \right) \quad (1.48)$$

where $\overline{u^2}^+ = \overline{u^2}/u_*^2$ and δ is the boundary layer thickness.

When the logarithmic region extend is estimated, a big obstacle is represented by the fact that the mean velocity profiles deviate very slowly from Eq. (1.46). In this case, it is difficult to determine the bounds of the logarithmic region, especially at low Re numbers. A valid remediation is to use both the mean velocity profile Eq. (1.46) and the streamwise turbulence profile Eq. (1.48), as suggested by Marusic *et al.* (2013). The main explanation is that logarithmic region can be easily determined by using the profile of Eq. (1.48). The studies of Townsend (1980) are not recent, but today his intuitions and hypothesis can be supported by the data from experiments with high Re numbers.

With the aim of testing the universality of Eq. (1.46) and Eq. (1.48) at sufficiently high Re number, Marusic *et al.* (2013) has used four wind tunnel experimental datasets (e.g. Hultmark *et al.* (2012) and Hutchins *et al.* (2012) are between them). This study estimates that the data

analysed in the range $3 \text{Re}_\tau^{1/2} < z^+ < 0.15 \text{Re}_\tau$ fall within the logarithmic region. The previous range will be considered as the “Marusic relation” in the current thesis. According to (Marusic *et al.*, 2013), at low Re numbers, no clear logarithmic region in the mean flow nor the turbulence intensities exists. Nevertheless, in this case, we could use a graphical method to estimate the extension of the log-region. This approach will be called “Marusic method” in the next chapters.

According to the previous approach, the extension of the logarithmic region could be different with respect to the classical approach. The Marusic *et al.* (2013) results and conclusions need to be confirmed through further studies, especially at low Re numbers. However, the fact of having an additional approach can only be beneficial for the analysis we will do in the present work, as we will see in chapter 3.

1.1.5 Atmospheric dispersion state of the art

The literature on this subject is quite large and many reviews are available, like Leelóssy *et al.* (2014, 2018). The aim of this section is to have a solid overview of the atmospheric dispersion topic in order to face our challenges.

In many industrial, ecological and environmental applications, the dispersion of substances from a punctual or area source in an atmospheric turbulent flow is a physical phenomena of fundamental importance. The atmospheric transport allows substances to reach a wide area and affect a large number of people relatively very fast. For this reason, the numerical prediction of atmospheric dispersion of any substance is of primary importance. In fact, among the various substances involved, we can find contaminants that are dangerous for health or result in a long-term negative effect on our environment. Such episodes could have a huge economic impact, as illustrated in introduction of the thesis (pag. 19).

Atmospheric transport is widely determined by the wind-driven advection of the plume. On the other hand, turbulent diffusion provides horizontal and transversal mixing, while other source or sink terms could play an important role. We could describe the atmospheric dispersion process thanks to passive-scalar transport equation shown in Eq. (1.17), and reported here again for clarity:

$$\frac{\partial c}{\partial t} + \nabla(c \cdot \mathbf{u}) = \nabla \cdot (D_c \nabla c) + S_c$$

In the previous equation, c is the instantaneous concentration, \mathbf{u} is the wind vector and D_c is the molecular diffusivity or the diffusion coefficient. The second term in the left-hand side represents the advection term, while the first term of the right-hand side point out the molecular diffusion. The term S_c specifies sources and sinks, like emission, chemical reactions, radioactive decay, dry or wet deposition. The latter term could be calculated through an independent methodology. The current equation might be treated in an analytic, deterministic or stochastic way. A direct consequence is the Gaussian (plume), Eulerian (grid) and Lagrangian (particle) dispersion models, respectively.

The way in which the finite volume of polluted air, or the plume emitted continuously from a source, are transported and dispersed by the wind vary with the atmospheric conditions. The relationship between the scales of the turbulent fluctuations and the scale or the polluted cloud, or of the space domain in which the cloud evolves, determines the characteristic of the process. It could be convenient, for reasons of clarity, to analyse two extreme situations (Cancelli *et al.*, 2006):

- The first is that in which the dispersion is due to turbulent motions of a smaller spatial scale than any other significant length. In fact, the latter could be the linear dimension of the pollutant cloud, or that of the plume section, or the height from the ground to the source.

- The second is that in which the motion of the polluted air is almost exclusively due to large-scale vortex structures, whose linear dimensions exceeds the other significant lengths.

In the first case, the turbulent dispersion can be treated as if it were a molecular diffusion of great intensity. The dispersion of the pollutant in the space derives from a succession of movements of the fluid particles, which are not correlated to each other. The same behaviour occurs in the diffusion of molecules.

In the second case, the large dimension of the vortex structures that drag the volume of polluted air (and therefore the considerable duration of the correlation time T_L , i.e. the Lagrangian time) makes appropriate a study of the dispersion limited to time intervals t much shorter than T_L . Under an hypothesis of this kind, the process could be considered as quasi-stationary, i.e. the dispersion of a set of particles that move in space conserving the initial velocity.

As was to be expected, the two extreme situations, described above, are never (or almost never) present in nature. The turbulent flows are characterised by the presence of a multiplicity of scales. Moreover, in the boundary layer, there are both larger and smaller scales than the linear dimension of the cloud of polluted air. However, if the turbulence is homogeneous, it is possible to demonstrate that the two extreme situations could be considered as borderline situations of the same dispersion process. In the situation characterised by $t/T_L \rightarrow 0$, the linear behaviour is evident. It means that the shape of the plume is conical and the concentration variability in the plume section depends on the distribution of the velocity fluctuations. On the other hand, for $t/T_L \rightarrow \infty$, the dispersion process would acquire diffusive characteristics. In this case, the plume develops following a parabolic law and the concentration inside it presents a Gaussian distribution (Taylor, 1921). The Gaussian solution represents the asymptotic model towards which the plume configuration tends over time. In fact, the sequence of uncorrelated movements of the fluid particles cancels progressively the velocity field information and the particles tends to a distribution of the most unstructured form possible.

In the most of the real situation, the two limit condition are not commonly used. In the case of $t < T_L$, the limit condition is applicable only in the region very close to the source of emissions, where the phenomena of jet raising, bifurcation and mixing with surrounding air, make unrealistic both the pattern of the point source and the hypothesis that the vertical velocity distribution is identical to that of the atmosphere. The opposite limit involves moving too far downstream from the source. For instance, assuming that a convective boundary layer is characterised by a T_L of the order of tens of minutes and that the mean velocity of the wind is of the order of 10 m/s, the asymptotic behaviour of the plume could be observed only in a region located several kilometres away from the sources. The pollution problem becomes less critical at such a distance. In addition of these difficulties, some others derives from the lack of homogeneity of the turbulent motion of the boundary layer and from the variability of the module and direction of the mean velocity.

As we did for weather stability conditions, it is important to classify some typical forms of the plume. In the situations of low relevance of thermal flows, i.e. in a neutral condition, the common shape of the plume is shown in Figure 1.7 and is called *coning*. According to measurements data, this is the case that better match the previsions of the Gaussian model. This is the main form that interest our research. For the others, please consult Cancelli *et al.* (2006).

In order to explain the phenomenology presented here, we need to introduce the mean scalar field and the approaches to treat the turbulent dispersion. Moreover, the Gaussian solution could be taken as a solid conclusion for the state of art. Theses aspects will be covered in the following part of this subsection. However, some approximations will be better explained in the next chapters.

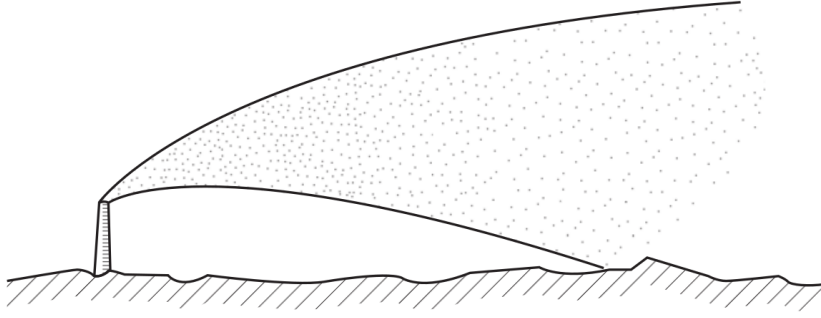


Figure 1.7: Typical form of the plume in the neutral condition of the atmosphere. The shape is almost coning. From: (Cancelli *et al.*, 2006)

Eulerian approach

One approach to determining the mean scalar field $\bar{c}(\mathbf{x}, t)$ is to solve its transport equation:

$$\frac{\partial \bar{c}}{\partial t} + \nabla \cdot (\bar{\mathbf{u}} \bar{c} + \overline{\mathbf{u}'c'}) = D_c \nabla^2 \bar{c} \quad (1.49)$$

Considering a model for the scalar flux $\overline{\mathbf{u}'c'}$, e.g. the turbulent diffusion hypothesis, the equation results:

$$\frac{\partial \bar{c}}{\partial t} + \nabla \cdot (\bar{\mathbf{u}} \bar{c}) = \nabla \cdot [(D_c + D_t) \nabla \bar{c}] \quad (1.50)$$

where D_c and D_t are respectively the molecular and turbulent diffusivities. It is important to highlight that D_t could be also expressed as a diffusivity symmetric tensor, denoted as \mathbb{K} .

Lagrangian approach

The alternative to the previous approach is the Lagrangian approach, which is an approach to deal with the turbulent dispersion originated with Taylor (1921) paper. The author argued that at high Re number the spatial transport of c due to molecular diffusion is negligible compared to the convection transport by the mean flow and turbulent motions. Therefore, c is conserved following a fluid particle ($Dc/Dt = 0$), and consequently the evolution of the mean field \bar{c} can be determined from the statistics of the motion of the particles. The relevant statistics will be considered below.

Dispersion from a point source

In this section, we consider the development presented by Pope (2000b). It is analysed the dispersion from a point source in statistically stationary isotropic turbulence. The unit source is:

$$c_0(\mathbf{x}) = \delta(\mathbf{x} - \mathbf{Y}_0) \quad (1.51)$$

where δ is the Dirac delta function. The origin of the source is located in $\mathbf{Y}_0 = 0$, and the release take place at time $t_0 = 0$. The isotropic turbulent velocity field is characterised by zero mean ($\bar{\mathbf{u}}(\mathbf{x}, t) = 0$). Further, it is maintained statistically stationary thanks to an artificial forcing. The root mean square (rms) velocity is u' so that the Reynolds stresses are $\overline{u_i u_j} = u'^2 \delta_{ij}$.

Under this conditions, the PDF $f_X(\mathbf{x}; t|0)$ of the position $\mathbf{X}^+(t, 0)$ of fluid particles emitted from the source can determine the mean scalar field $\bar{c}(\mathbf{x}, t)$:

$$\bar{c}(\mathbf{x}, t) = f_X(\mathbf{x}; t|\mathbf{Y}_0) \quad (1.52)$$

Consequently, the dispersion can be characterised by the first and second moments of this PDF, i.e. the mean and the variance of $\mathbf{X}^+(t, 0)$. The equation for fluid-motion $\partial \mathbf{X}^+ / \partial t = \mathbf{U}^+$ can be integrated:

$$\mathbf{X}^+(t, 0) = \int_0^t \mathbf{U}^+(t', 0) dt' \quad (1.53)$$

The Lagrangian velocity statistics can be used to express the statistics of \mathbf{X}^+ . Thus, the covariance of the fluid-particle position results:

$$\overline{X_i^+(t, 0) X_j^+(t, 0)} = \int_0^t \int_0^t \overline{U_i^+(t', 0) U_j^+(t'', 0)} dt' dt'' \quad (1.54)$$

Thanks to the characteristics of the turbulence, i.e. stationary and isotropic, the two-time Lagrangian velocity correlation is:

$$\overline{U_i^+(t', 0) U_j^+(t'', 0)} = u'^2 R(t' - t'') \delta_{ij} \quad (1.55)$$

where $R(\tau)$ is the Lagrangian velocity autocorrelation function. Further, the covariance of the position is written as:

$$\overline{X_i^+(t, 0) X_j^+(t, 0)} = \sigma_X^2(t) \delta_{ij} \quad (1.56)$$

The latter is characterised by the standard deviation $\sigma_X(t)$. From the previous three equations and using a mathematical manipulation, the following expression is obtained:

$$\sigma_X^2(t) = 2u'^2 \int_0^t (t - \tau) R(\tau) d\tau \quad (1.57)$$

Two asymptotic behaviours can be identified:

$$\sigma_X(t) \approx u' t \quad \text{for } t \ll T_L \quad (1.58)$$

$$\sigma_X(t) \approx \sqrt{2u'^2 T_L t} \quad \text{for } t \gg T_L \quad (1.59)$$

where T_L is the Lagrangian time.

For short times ($t \ll T_L$), associated with a “perfect” autocorrelation of the velocity fluctuations, flow particles follows straight-line motion and the standard deviation σ_X increases linearly. On the other hand, for large times ($t \gg T_L$), σ_X rises following the square root of the time. Further, the expression resulting represents the spreading given by the diffusion equation with the constant turbulent diffusivity:

$$D_t = u'^2 T_L \quad (1.60)$$

For all times, it is possible to formulate the dispersion in terms of a diffusivity $\hat{D}_t(t)$ defined by:

$$\hat{D}_t(t) \equiv \frac{d}{dt} \left(\frac{1}{2} \sigma_X^2 \right) \quad (1.61)$$

and using Eq. (1.57), it is obtained:

$$\hat{D}_t(t) = u'^2 \int_0^t R(\tau) d\tau \quad (1.62)$$

Finally, it is possible to affirm that the fluid particles disperse from the origin isotropically, as shown by Eq. (1.56). The behaviour at large ($t \gg T_L$) and small ($t \ll T_L$) times was presented mathematically here, confirming the behaviour presented at the beginning of the current subsection.

Knowing the behaviour at extremes, the complete turbulence dispersion is estimated by the Langevin model for the fluid-particle velocity. The model states that the Lagrangian velocity autocorrelation function has exponential form and it is equal to:

$$R(\tau) = \exp \left(\frac{-|\tau|}{T_L} \right) \quad (1.63)$$

Thanks to this expression of $R(\tau)$, Eq. (1.57) can be integrated to obtain:

$$\sigma_X(t)^2 = 2u'^2 T_L [t - T_L(1 - e^{-t/T_L})] \quad (1.64)$$

Figure 1.8 illustrates $\sigma_X(t)$ achieved through this formulation. The linear and square-root behaviours at small and large times can be easily observed.

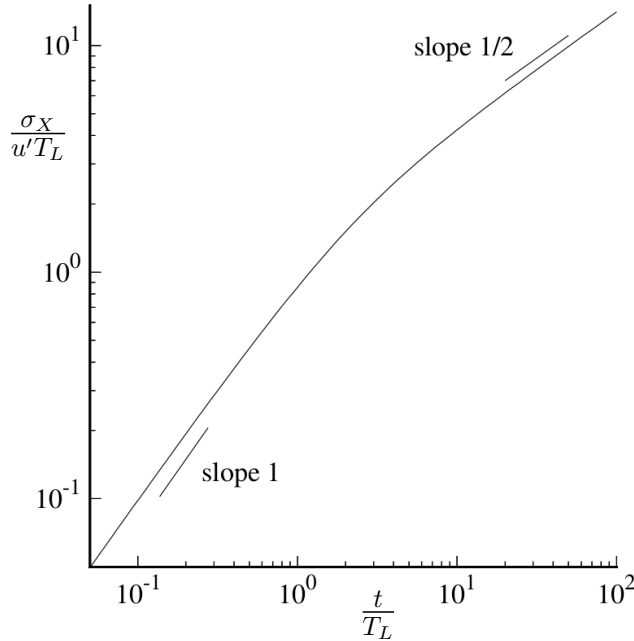


Figure 1.8: The standard deviation σ_X of dispersion from a point source thanks to the Langevin model, i.e. Eq. (1.64). From: (Pope, 2000c)

Gaussian solution

The conservation equation of the mean concentration Eq. (1.50) using a closure of the first order is well known. If the mean velocity $\bar{\mathbf{u}}$ is uniform in the integration domain, it is enough to choose a moving reference system with the same velocity in order to delete it. Furthermore, if the molecular diffusivity is neglected, the equation is reduced to the classical form of the heat equation, i.e. the Fourier equation:

$$\frac{\partial \bar{c}}{\partial t} = D_t \nabla^2 \bar{c} \quad (1.65)$$

The Eq. (1.65), as well as Eq. (1.50), is linear. Therefore, it is possible to build a complex configuration superimposing simple solutions. In order to compute the pollution due to several sources, the contribution of each source is computed and added together. There are a group of solutions of Eq. (1.50), employed to reproduce the pollution phenomena originating from sources of various forms, that can be considered as derived from a simple solution of Eq. (1.65), provided with spherical symmetry:

$$\bar{c}(r, t) = M_q (4\pi D_t t)^{-3/2} \exp\left(\frac{-r^2}{4D_t t}\right) \quad (1.66)$$

where r is the distance from the center. It is a spatial distribution of Gaussian form, with total mass M_q initially concentrated in the center of the cloud and diffused radially.

Note that the width of the cloud is literally unlimited at any instant, except in the initial one, due to the usual artefact of parabolic equations. Nevertheless, if the standard deviation of the form factor $\exp(-r^2/4D_t t)$, the usual law of the diffusive processes is found. With regard to size and speed of spreading:

$$\sigma_r \propto \sqrt{D_t t}$$

$$v_d \propto \sqrt{\frac{D_t}{t}}$$

with the only difference that now we have the turbulent diffusivity D_t instead of the molecular one D_c .

Numerous models for calculating the dispersion, which are called ‘‘Gaussian models’’, are based on a superimposition of this kind. Restoring the mean velocity of the wind, it is possible to represent the dispersion of a cloud. It is emitted from a punctual source at a certain time. So it is transported downwind and, in the meantime, it expands and dilutes. Otherwise, if considering a continuous succession of clouds generated by a fix point S , a Gaussian plume is obtained. It is useful to compute the concentration of a continuous emission from a punctual source, or that such can be considered. Finally, distributing the intensity of emissions along a line orthogonal to the wind, it is possible to have Gaussian models to linear sources.

Here is reported the mathematical expression of the Gaussian plume. If we have a punctual source S , which emits a pollutant with a mass flow rate Q [kg/s], and x is the downwind coordinate, with z the vertical coordinate and y the streamwise coordinate. Therefore, the equation of the Gaussian plume is:

$$\bar{c}(x, y, z) = \frac{Q}{2\pi\sigma_y\sigma_z\bar{u}_{adv}} \exp\left(-\frac{y^2}{2\sigma_y^2}\right) \exp\left(-\frac{z^2}{2\sigma_z^2}\right) \quad (1.67)$$

This equation is a stationary solution of Eq. (1.50), if it is imposed that:

$$\sigma_y^2 = \sigma_z^2 = 2D_t \frac{x}{\bar{u}_{adv}} \quad (1.68)$$

and the flow of turbulent nature in the x coordinate is negligible. So Eq. (1.67) thanks to Eq. (1.68) satisfies the equation:

$$\bar{u} \frac{\partial \bar{c}}{\partial x} = -D_t \left(\frac{\partial^2}{\partial y^2} + \frac{\partial^2}{\partial z^2} \right) \bar{c} \quad (1.69)$$

It is not difficult to manipulate Eq. (1.67) in order to take account of the surface reflection effect. The latter is due to the presence of the ground or of the external boundary of the ABL. For instance, to calculate the ground effect on concentrations, it is possible to use the virtual image technique. It adds to the real source a virtual source S' with the same intensity and positioned symmetrically with respect to the ground surface. Therefore, at the ground level, the pollutant flow that crosses the surface due to both the sources is zero for symmetry. Adding S' , it is simulated the concentration distribution that occurs if the ground completely reflects the pollutant particles (in this case the deposition is not taken into account). Conventionally, the presence of S' is introduced in Eq. (1.67) thanks to a simple superimposition of solutions. Moving the origin of the vertical axis to the ground and denoting h_s the source height, the plume equation becomes:

$$\bar{c}(x, y, z) = \frac{Q}{2\pi\sigma_y\sigma_z\bar{u}_{adv}} \exp\left(\frac{-y^2}{2\sigma_y^2}\right) \left[\exp\left(\frac{-(z-h_s)^2}{2\sigma_z^2}\right) + \exp\left(\frac{-(z+h_s)^2}{2\sigma_z^2}\right) \right] \quad (1.70)$$

Theoretically, it may be possible to compute the diffusivity coefficient D_t thanks to the fluctuation field \mathbf{u}' and use the Eq. (1.70) to determine the mean concentrations. Nevertheless, a more empirical way is preferable when the Gaussian model is used. In fact, the hypothesis that have allowed to present the Eq. (1.67) as deduced by the mean equation Eq. (1.49), the only surely correct, are not entirely reliable. For example: the turbulent flow field of the ABL is not homogeneous. Its characteristics vary rapidly with the height. The turbulent diffusion hypothesis is correct only asymptotically. The mean of a Lagrangian temporal scale in an homogeneous field is tricky. Therefore, it is preferable to conserve Eq. (1.67) and Eq. (1.70) in their form and consider the standard deviation σ_y and σ_z as characteristic dimensions of the straight section of the plume, whose variation with downwind distance must be empirically determined.

It is evident that the velocity, at which the polluted plume spreads, depends on the dynamical conditions of the ABL. So the empirical curves of σ_y and σ_z needs to be parameterized with something that allow to identify the condition of the boundary layer. The six stability classes of Pasquill-Gifford, already presented in subsection 1.1.2, are one of the approaches adapted to the current purpose. Based on some meteorological observation, the stability class for the analysed situation is identified. In this way, it is possible to compute the spread of the plume through the values of σ_y and σ_z obtained from the empirical curves of Figure 1.9 and Figure 1.10. Otherwise, they could be computed through numerical interpolation formulas, that are equivalent to the curves (Briggs, 1973). Finally, the computation of \bar{c} is conducted using Eq. (1.70), knowing σ_y and σ_z .

In the current subsection, the basic concepts and models for dealing with the atmospheric dispersion of a pollutant were presented. In the next section the numerical models will be better treated, while in the following chapters some hypotheses and approximations mentioned here will be deepened.

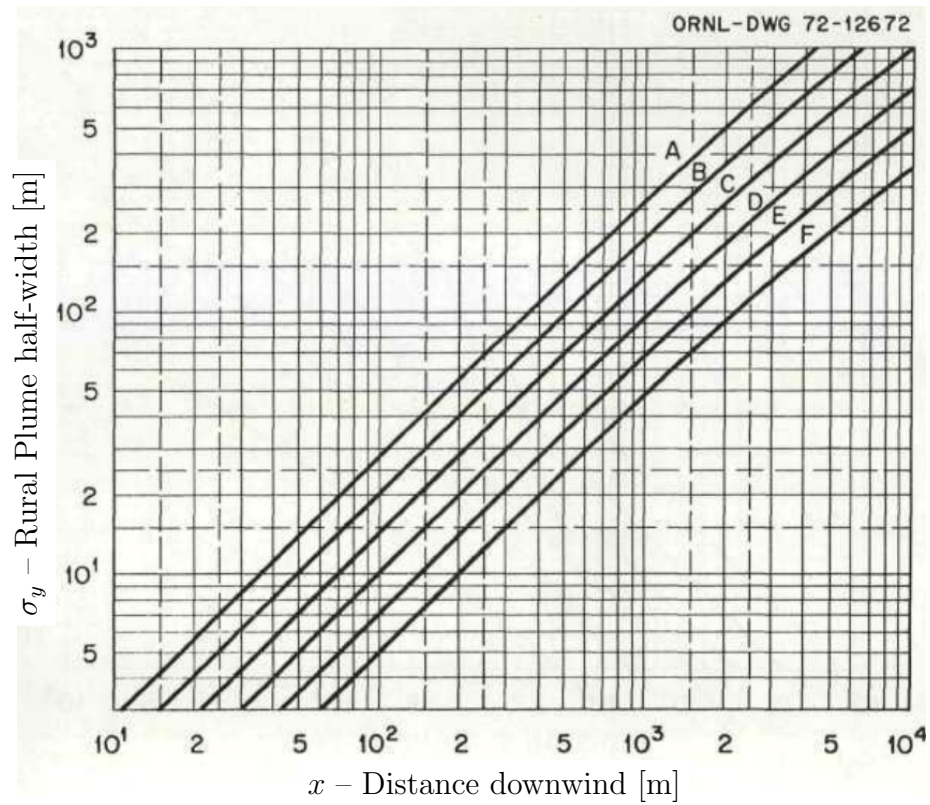


Figure 1.9: Evolution of the horizontal standard deviation σ_y as a function of the downwind distance from the source, (Briggs, 1973).

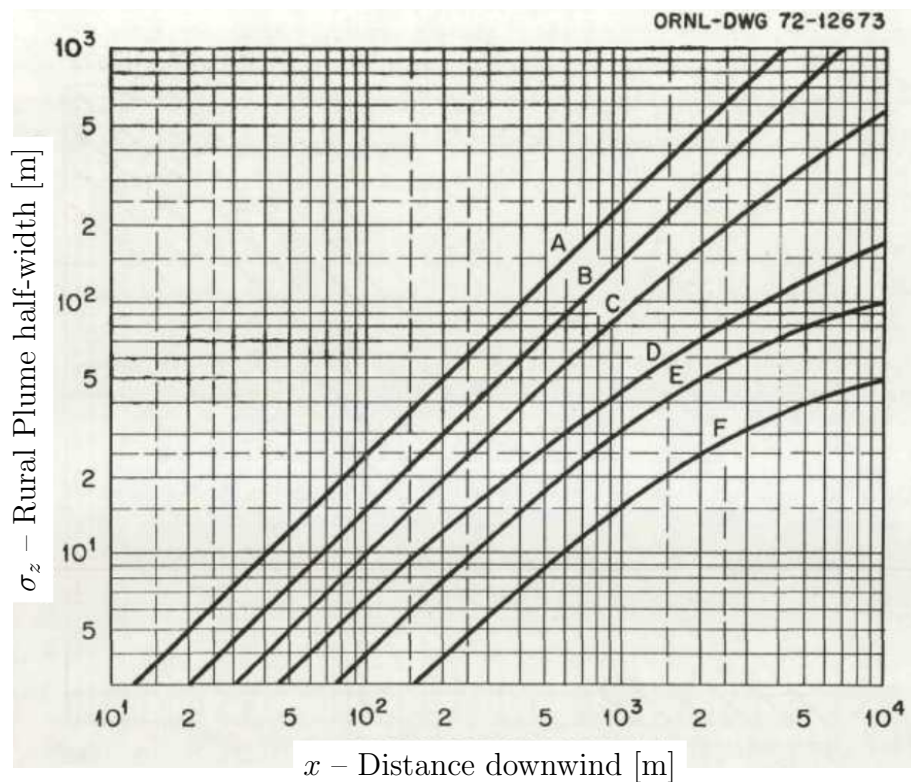


Figure 1.10: Evolution of the vertical standard deviation σ_z as a function of the downwind distance from the source, (Briggs, 1973).

1.2 Simulation tools

In order to understand the processes that govern the atmospheric flows and the turbulent dispersion of pollutants, it is fundamental to be capable to describe the characteristics of the observed phenomena. The first and direct approach that allows to collect data is the experimental observation in situ. It is based on direct measurements of the atmosphere and pollution. Many techniques have been developed to measure the wind field or more in general the meteorological variables as well as to measure the concentration of pollutants. This techniques are increasingly performing (a clear example are the new optical instruments presented and analysed in the current thesis) and contribute to build a useful database to study the atmosphere and the pollution. Nevertheless, the experimental observations in situ are difficult to carry out and are expensive. Moreover, the measurements allow to have only a discrete representation of the phenomena. In fact, the experimental data are usually constituted by some measurement points or profiles. In order to enhance the phenomena description, it could be convenient to have additional methods of representability or modeling of the physical phenomena of interest. The two main approaches are the experimentation in wind tunnel and the numerical modeling.

In the current section, we are focused on the latter approach because the understanding of it is crucial to our research. Consequently, we will present the numerical modeling techniques to study the atmospheric flow ([subsection 1.2.1](#)) and the atmospheric dispersion of pollutants ([subsection 1.2.2](#) and [subsection 1.2.3](#)).

1.2.1 Numerical modeling of the ABL

In the study of the fluid mechanics, the ultimate objective is to obtain a tractable quantitative theory or model that can be used to calculate the quantities of practical interest to describe the desired phenomena. Nevertheless, a century of experience has shown that the presence of turbulence makes the achievement of the objective very difficult due to the non-linearity of the Navier-Stokes equations. In fact, there are no prospects of a simple analytical theory. Conversely, the hope lies in the use of ever-increasing power of digital computers to achieve the objective of calculating the relevant properties of of the fluid mechanics and in particular of the turbulence.

In this context, the Computational Fluid Dynamics (CFD) has been developed. It is a science that, with the help of digital computers, generates quantitative predictions of the fluid flow phenomena based on those conservation laws governing fluid motion. These predictions normally take place under those conditions defined in terms of the flow geometry, the physical properties of a fluid, and the boundary and initial conditions of a flow field. However, the most challenging part is the turbulent flow modeling. So in order to treat this problem, many models have been developed in the last century and it is possible to distinguish many categories, briefly summarised below.

The Direct Numerical Simulation (DNS) consists in solving the Navier-Stokes equations, resolving all the scales of motion, with initial and boundary conditions appropriate to the flow considered. Each simulation produces a single realisation of the flow. This approach is the closest to an exact resolution of the flow but it needs a very fine spatial resolution. A direct consequence is that the computational time could be excessively long and it limits its application to the flows characterised of a low Reynolds number.

The second model presented is the Large-Eddy simulation (LES). In the LES, the larger three-dimensional unsteady turbulent motions are directly resolved while the effects of the smaller scale motions are modelled. The LES models are particularly adapted to the study of atmospheric flows, for which they were initially developed ([Deardorff *et al.*, 1970](#)). In computational expense, LES needs less computational time and resources than DNS.

The common and more diffused approach used to simulate turbulent flows is the Reynolds Average Navier-Stokes (RANS). In fact, for many application, it is not necessary to compute

the instantaneous evolution of the variables of interest but it is enough to determine the average values for a large number of realisations of the flow. For this scope, the equations of the average variables are used. They are obtained from the instantaneous equations thanks to the Reynolds decomposition. Nevertheless, the non-linear terms of the instantaneous equations implies the presence of fluctuations correlation terms in the RANS equations. Consequently, these terms needs to be modeled. The statistic modeling does not allow to get the details of the turbulence. However, it is a useful tool to study the mean fields, particularly in the case of flows around complex geometries. Many researches have used this type of modeling to study the atmospheric flow around obstacles (Zhang, 2009; Parente *et al.*, 2011b).

In the current thesis, the atmospheric boundary layer and in particular the surface boundary layer could be simulated and modeled thanks to CFD, and RANS and LES approaches in accordance with the time and space scales of interest. The CFD applied to atmospheric flows and the scales of interest will be explained below.

Spatial and temporal orders of magnitude of the ABL

In [subsection 1.1.1](#), it was presented the vertical structure of the atmosphere and of the different layers which compose it. For the current study, it is important to know the dimensions of the typical domain for our purposes. This limitation are going to contribute to focus on one part of the atmosphere, to better understand its mechanism and to identify the necessary hypothesis to model it. The aim is to develop the rest of this presentation in a targeted and concise way.

If it is desired to study the emissions of pollutants in an industrial site (e.g. TADI experiment or releases in refineries), most of the emissions are situated near the ground or at the height of chimneys in the site. In general, the height of the pollution sources could be placed approximately between the ground and a hundred meters above it.

The thickness of the ABL could be of the order of 1000 m, while the thickness of the SBL could reach the order of 100 m. It means that the most of the emissions are located in the SBL. The industrial site and the surroundings could have many square kilometres. Therefore, the dispersion need to be studied in this region, i.e. a distance of some kilometres. However, at the state of our research, the studies could be focused on smaller regions of the order of few hundreds of square meters. In fact, as we will see in [chapter 4](#), the experiment in situ considered has smaller dimensions than typical industrial site.

It is possible to find in literature some references, for instance [Briggs \(1973\)](#), to estimate the standard deviations of a passive scalar plume depending to many parameters, like the atmospheric stability or the type of ground surface (e.g. urban, rural, etc). It could help to limit our studies to some orders of magnitude for the dispersion to a certain height.

According to [Figure 1.10](#), the vertical dispersion of a plume is lower to 500 m for a downwind distance of 1 km regardless of the atmospheric stability. This information allow to fix the domain height for the numerical studies developed. Generally, domains of few hundred of meters are adopted. This choice guarantees the characterisation of almost every plume in a complex terrain. Furthermore, when the atmosphere is unstable, the height which denote the dispersion and the SBL height increase simultaneously. So this fast study help to highlight and confirm that our studies could be focused on the analysis of the SBL. The Ekman layer and the free layer are ignored. So, as already mentioned, it allows not to consider the Coriolis force and the other layers of the atmosphere.

The time scales of interest are mainly conditioned by the experiment constrains. The new optical instruments, used to measure the wind and concentration field, are characterised by a high sampling frequency. The frequencies, that are expected to be reproduced in a real scenario, range from a few Hz to a few hundreds of Hz. The maximum duration of the experiments can vary from a few tens of minutes to a maximum of about an hour. However, we are interested in phenomena lasting a few minutes because it is a fairly large window of time useful to develop and validate our methodology. The validation cannot be conducted through the comparison of

instantaneous fields but of the time average fields.

In accordance with the spatial and temporal scales, it is possible to affirm that our atmospheric conditions could be determined by the microscale meteorology and that we are interested in all phenomena smaller than synoptic scale. Moreover, the obstacles presented in the domain should be modeled as accurately as possible. Based on the previous considerations, the CFD simulation represents a valid option to study the atmospheric flow.

CFD applied to the ABL

Nowadays Computational Fluid Dynamics (CFD) is widely used to study a variety of processes in the lower part of the atmospheric boundary layer (ABL), i.e. the surface boundary layer (SBL), including pollutant dispersion and deposition, wind-driven rain, building ventilation, wind turbine wakes effects and others. CFD is important in commercial, operational and research wind engineering (Blocken *et al.*, 2007; Tian *et al.*, 2018; Baklanov, 2000).

According to Hargreaves and Wright (2007), two aspects of ABL are not reproduced by direct representation in CFD. The first is related to the extension of ABL. It covers a considerable distance above earth's surface and relative to building height. CFD could only represent a smaller finite distance because of hardware limitations and the complexity of including a meteorological model. Secondly, small scale features such as vegetation and buildings could not be included in the computational grid or they are included by making many approximations. In the case of $k-\epsilon$ turbulence model, the surface roughness (e.g. the effect of small scale features) is modelled through a wall function approach which is based on boundary layer theory for the computational cell immediately adjacent to the wall. Similarly, the Large-Eddy Simulation (LES) model needs a near-wall modeling. A near-wall resolution of the small features implies a very high computational cost, unsustainable for many of the present purposes, e.g. simulation of ABL over complex terrain.

The strategy of the current methodology is based on a gradual increment of complexity. The study is focused on obtaining a model which match as close as possible experimental data and catch the physical meaning of the phenomena. For this reason, the Monin-Obukhov similarity theory is taken into account as well as experimental studies. Moreover the numerical approaches considered are the RANS and LES models. Both of them need a proper formulation of the near wall model and a convenient definition of the boundary conditions. Above of all, the inlet profiles are of fundamental importance because they determine the development of the SBL, as we will see in chapter 2 and chapter 3.

Related to RANS model, the works of Richards and Hoxey (1993) and Hargreaves and Wright (2007) represent a depart point of this strategy. The research of Parente *et al.* (2011b), Vendel (2011) and Gryning *et al.* (2007) contributes to increase the complexity step by step. On the other hand, Tian *et al.* (2018) presents a comparison of the principal methods actually available to simulate the ABL through RANS model. Finally, some references for LES could be constituted by the researches of Xie *et al.* (2004b), Nakayama and Nagai (2009) and Ardeshiri *et al.* (2020), which compare the simulated turbulent flow against the wind-tunnel measurements.

1.2.2 Numerical approach for atmospheric dispersion

For the atmospheric dispersion, the most adequate modeling tool for a specific application mainly depends on the spatial scale of the dispersion. On the local scale, i.e. in the order of 1 – 10 km, the assumption of a horizontally homogeneous and stationary wind field is often used and it largely simplifies the numerical model. Nevertheless, this assumption neglects the mesoscale atmospheric phenomena that might become an important source of error. On the regional scale, i.e. in the order of 100 – 1000 km, the spatial and temporal changes in the meteorological condition have to be considered. As the scale increases, that is if a bigger portion of the planet is considered and no further assumption is taken into account, the limited computational power

could represent a big issue. In global simulations, the amount of meteorological data and the large number of particles, grid points or cells often demand a compromise between a sophisticated physical model and a feasible computational request. On the other hand, microscale simulations, i.e. in the order of 10 – 1000 m, are focused on the detailed solution of the flow and concentration field around buildings and other obstacles. Although the spatial scale is smaller, these simulations could have extraordinary hardware requirements comparable to or even larger than global scale problems. In fact, the computational power required does not simply depend on the spatial scale but rather on the portion of the energy spectrum (Figure 1.2) to be solved. Nowadays, computing the entire energy spectrum of the atmospheric flow is impossible. So, it is always needed to choose a portion of the spectrum to solve, while usually the smaller scales could be modelled and the bigger scales could be introduced as system forces. In any case, the microscale simulations are of fundamental importance on our research.

The atmospheric energy spectrum scales are not the only aspect that fix the complexity of the atmospheric transport process and consequently the accuracy of a modeling approach. More sophisticated models with large computational cost are required if:

- the dispersion takes place over complex terrain, (Raskob *et al.*, 2010).
- the weather is rapidly changing or is strongly affected by local effects, i.e. urban or coastal circulation, convective clouds and frontal systems, (Venkatesan *et al.*, 2002).
- the emitted material or source has significant feed-backs on the flow field, i.e. in case of large fires or dense gases, (Venetsanos *et al.*, 2003).

In order to reach this wide range of complexities and possible assumptions as well as to satisfy different user needs ranging from basic research to civil defence or risk events, a rich variety of atmospheric dispersion models have been developed and applied, (Perry, 1992; Mikkelsen *et al.*, 2003; Soulhac *et al.*, 2011; Marro *et al.*, 2018; Cheng and Liu, 2011).

Research and operational decision support are the two main fields of application for the atmospheric dispersion models. Research applications frequently concern retrospective events. Large amount of data is available and coupled to high-performance computing. These kind of simulations can be repeated and tuned to provide the best possible results. The use of the model is made as standalone code with specified input and output formats, or through a web interface. Differently the operational decision support is addressed to emergencies and practices, where a well-defined operational protocol needs to be performed based on the real-time accessible data, human resources and infrastructures. Thus, reliability, robustness and fast response are the key features of an operational model. The software is usually integrated into geographic information systems (GIS) or into a complex decision support toolboxes, (Bozon and Mohammadi, 2009).

Especially in case of accidental release but not only, a competent multidisciplinary cooperation is needed to achieve accurate results and a high quality decision support (Managi and Guan, 2017). Different levels of model results are available:

- The meteorological situation and forecast.
- The atmospheric concentration and ground deposition maps from several dispersion models.
- The expected dose rates and health effects at certain receptors.
- The combined effect of atmospheric pollution with other environmental risks and exposures.
- Quantitative information on uncertainties and sensitivities.

Finally, before to treat the different models available, it is important to focus briefly on the concepts of meteorological data, emissions and validation. The latter are part of the atmospheric dispersion modeling principles and inputs, and will be presented below.

Meteorological data

As already seen in [subsection 1.1.5](#), atmospheric transport processes of pollutants are affected by weather conditions. Consequently, meteorological data are a fundamental input for dispersion models. The atmospheric transport equation is directly influenced by the weather, i.e. the wind field, through its convective term. Furthermore, the treatment of the turbulent dispersion involves again the wind field.

In a simple local scale simulation, meteorological observations from a fixed monitoring station are used. Nevertheless, the spatial representativity of a single measurement is limited, and the three-dimensional structure of meteorological parameters can only be described by simple or sophisticated numerical weather prediction (NWP) models. Atmospheric dispersion models can be coupled with NWPs. However, the coupling approach could vary between different software and codes.

On the other hand, in a microscale simulation, NWPs do not have sufficient resolution to solve the atmospheric flow. In fact, the wind field is strongly influenced by the presence of obstacles (e.g. buildings, vegetation, etc) and turbulence plays a fundamental role. Therefore, it is rare to use NWP models. Whereas CFD simulations could be more adapted to simulate the local weather conditions. In this case, the similarity theory of Monin-Obukhov contributes to determine the meteorological parameters from experimental observations.

Emissions

After meteorology, another important input for a dispersion model is the emissions data. Dispersion models deal with the emission as boundary or initial condition of the simulation. Therefore, information on the release rates is necessary at each grid point and each time step for each component.

In a very simple approach, the assumption that the emission rate is known is adopted. It is possible to have a direct measurement of the release in the case of a single point source equipped with local detectors (e.g. it is very common in wind tunnel experiments). Conversely, if the release rate is unknown, two techniques can be employed to estimate the emission rate: the bottom-up or top-down. A typical bottom-up emission model constructs an inventory of the potentially released pollutant. The inventory is the result of a series of physical and chemical simulations aimed at studying the release process and estimating the amount of the release.

Concentration and deposition observations from monitoring sites are used in the top-down emission estimation. It is also common by the use of the inversion of atmospheric dispersion modelling to give an optimal estimation of the source term that might have caused the measured values ([Saunier *et al.*, 2013](#); [Ben Salem *et al.*, 2014](#); [Chai *et al.*, 2015](#)). Inversion modeling has high uncertainties, especially on the large scale or if location of the source is unknown, because some chemical and physical processes involved are irreversible in the atmosphere ([Haszpra, 2016](#)). However, if the position of the source is known and the number of accessible observation from monitoring sites is sufficiently high, an inversion modeling could reconstruct a complex emission time-line with good accuracy ([Katata *et al.*, 2015](#)). It is important to highlight that a top-down approach and an inversion modeling could give similar results but they are completely different methods.

In real-life cases, environmental observations have different sampling periods and errors, there is usually generous information on the emission inventory, and even remote sensing or mobile measurements may be available in an irregular basis. The integration of this variety of data can be made thanks to the data assimilation ([Jeong *et al.*, 2008](#)). In this scenario, the simulation starts with a bottom-up (first guess) estimate, and observations are included sequentially to calculate a result that optimally integrates all available information. Data assimilation is intimately related to inverse modeling, and although it is often used in NWPs, chemical data assimilation in atmospheric transport models is a subject of active research ([Bocquet *et al.*,](#)

2015). The data assimilation is a subject of interest in the development of the current thesis, as we will see in [chapter 4](#).

Validation

The validation of atmospheric dispersion model remains a challenge even today. The validation procedure requires a comparison between model and measurements. In the best of cases, it needs a known emission rate and observations from several monitoring points, as well as a direct source-receptor relationship. It is important that no other sources are present and that there is no variability on the background concentration. A precise numerical model is essential in the same way. If the previous conditions are respected, validation would be possible. Nevertheless, the uncertainties present in the validation process are numerous, making validation a real challenge.

Several aspects can be used to investigate the model performance, for example: the spatial extent of the plume, arrival time at specific locations, peak concentration values, the amount of deposited activity, concentration statistics, the integrated concentration (dose) throughout the pollution period ([Mosca et al., 1998](#)), column-integrated concentration (CIC) of an instantaneous release or similarly the integrated column amount of the trace gas along the line of sight of the virtual camera ([Dinger et al., 2018](#); [Kylling et al., 2020](#)). The performance parameters of statistical origin allow to compare better and easily numerical and experimental results. On the other hand, instantaneous parameters need to be interpreted adequately. Furthermore, in most cases they do not allow to carry out a quantitative but only qualitative validation.

A simple method to validate the atmospheric dispersion models is constituted by the wind tunnel experimentation. In this way, the emission and the boundary conditions of the test domain are well defined and the uncertainties are reduced as much as possible. Moreover, the measurements could be conducted for a long time, controlling that the simulation conditions remain stationary. Thanks to this approach, high order statistics of the quantities of interest are computed and compared with the numerical statistics. For the simulation of the dispersion in neutral atmospheric conditions, there were conducted some wind tunnel experiments of this kind (e.g. [Nironi et al. \(2015\)](#); [Fackrell and Robins \(1982\)](#)) as well as some validations (e.g. [Xie et al. \(2004b\)](#); [Ardeshiri et al. \(2020\)](#)).

The validation on a real scenario is more complicate. In fact, it should be borne in mind that the boundary conditions due to the meteorology of the site in question are not stationary and indeed vary continuously. This aspect alone is sufficient to greatly complicate the validation process and limit the use of statistic performance parameters. For this reason in the current thesis, the validation of the developed methodology is done thanks to the wind tunnel experiment of [Nironi \(2013\)](#). Whereas, an assimilation approach is used to study the real scenario case. We expect to be able to extract useful information for the interpretation of physical phenomena and enhance numerical and experimental approaches.

1.2.3 Numerical models for atmospheric dispersion

In the current subsection, the main numerical models to deal with atmospheric dispersion are presented.

Gaussian models

The core of the Gaussian models was derived in [subsection 1.1.5](#). In order to remember the assumptions made to derive these models, they are reported here:

- Stationary phenomena (e.g. wind field, release rate).
- Constant turbulent diffusivity coefficients.

- Wind uniform and constant, aligned with the x coordinate.
- Perfectly homogeneous and flat terrain.
- Streamwise turbulent diffusivity coefficient negligible compared to the simple transport contribution due to the wind in the same direction (only for the plume model).

The final mathematical formulation of [subsection 1.1.5](#) for the Gaussian plume model is expressed by Eq. (1.71).

$$\bar{c}(x, y, z) = \frac{Q}{2\pi\sigma_y\sigma_z\bar{u}_{adv}} \exp\left(\frac{-y^2}{2\sigma_y^2}\right) \left[\exp\left(\frac{-(z-h_s)^2}{2\sigma_z^2}\right) + \exp\left(\frac{-(z+h_s)^2}{2\sigma_z^2}\right) \right] \quad (1.71)$$

Here \bar{c} is the time-averaged concentration at a given position, Q is the source term, x is the downwind, y is the crosswind and z is the vertical direction and \bar{u}_{adv} is the advective velocity, i.e. the time-averaged wind speed at the height of the release h_s . σ_y and σ_z are the standard deviations and describe respectively the crosswind and vertical mixing of the pollutant. Therefore, Eq. (1.71) represents a mixing process that results in a Gauss concentration distribution both in crosswind and vertical directions, centred at the line downwind from the source. The last term of the equation point out a total reflection from the ground.

Gaussian (plume) models are based on this analytic result that yield good and extremely fast results on the micro and local scale ($\approx 0.01 - 10$ km). It has also become the standard of regulatory modeling for industrial stack releases and several environmental applications ([Holmes and Morawska, 2006](#); [Soulhac et al., 2011](#)). The Gaussian model requires the meteorological input for a single point and assumes that the meteorology is homogeneous in time and space. A representative advection velocity need to be estimated in order to apply the Gauss model. Consequently, observation data from monitoring stations or towers could be employed for retrospective and real-time simulations, while NWP results are used for dispersion forecast. The computational cost is very low, but meteorological data pre-processing and sophisticated turbulence parameterization could increment the computational cost.

The main potential of Gaussian models is their small input requirements and fast run-time. The access to gridded meteorological data (NWP or remote sensing) is not required to run this kind of model. However, their accuracy is limited over the spatial distance of a few tens of kilometres (maximum between 20 and 30 km). It also loses accuracy in complex conditions (e.g. orography, wind shear). With only a few parameters, a single plume can be calculated instantly even on a portable device, making Gaussian models a powerful tool for emergency decisions. On the other hand, these models are often applied to epidemiology studies, i.e. the local scale effects of long-term continuous pollution, calculating the sum of single plumes from each hour through several years ([Coudon et al., 2021](#)).

Eulerian models

The Eulerian models aims to resolve mathematically the atmospheric transport equation (Eq. (1.17)) using adequate boundary and initial conditions in a fixed coordinate frame. From a mathematical point of view, this model resolves a set of second-order differential equations (PDEs) with independent variables in space (x, y, z) and time (t). The spatio-temporal evolution of the concentration of pollutants is obtained by solving the previous equations. Due to the wind field characteristics and the presence of non-linear terms in the equations, it is not possible to adopt an analytic resolution of Eq. (1.17). Instead, it is convenient to use numerical methods, which are principally based on two steps. Firstly, the spatial discretisation transforms the PDEs into a system of ordinary differential equations (ODEs) depending on a single variable t . Mainly two discretisation techniques are available: the finite difference method (FDM) and

the finite volume method (FVM). In particular, the latter converts the volume integrals for both advection and diffusion terms into surface integrals using the divergence theorem. After the spatial discretisation, the second step aims to solve the discretised equations as an initial value problem through powerful integration methods, e.g. explicit or implicit methods. These methods have pros and cons in terms of stability, convergence and computational time.

The computational resources needed to solve a 3D Eulerian model are often significant, depending on the spatial and temporal scales to be solved and the models used. In order to reduce execution time, parallelisation and adaptive gridding are the two most efficient methods.

Parallelisation of dispersion model can be conducted thanks to distributed and parallel systems, e.g. supercomputer, clusters, grid systems or graphical processing units (GPU) (Molnar Jr *et al.*, 2010). The parallelisation of a sequential code for the solution of Eq. (1.17) requires the decomposition of the 3D domain into several smaller sub-domains. It allows to reduce the computational time by boosting the computational capabilities to numerically solve the problem. Nevertheless, each sub-domain needs to communicate with their neighbours across the borders. This characteristic limits the benefits of parallelisation. In fact, bigger is the number of sub-domains, more difficult is the exchange of information. This is the reason why it is worthwhile to carry out a speed-up test in order to identify the optimal number of subdivisions of the domain. Going beyond this number of sub-domains should only degrade the computational efficiency (Axtmann and Rist, 2016).

The second approach to increase computational efficiency is adaptive gridding or adaptive mesh refinement. In static mesh, the mesh does not change during the simulation. If there are refinement regions or nested grids, they remains circumscribed and do not vary. Conversely, an adaptive grid is conceived to adapt this mesh in space and time acting on regions where the model accuracy is sensible to mesh resolution. For example, it is the case of source and boundaries of the plume that can vary a lot during the simulation. There exists two main categories of adaptive gridding techniques: h-refinement and r-refinement. It is not of out interest to go further into details, for more information please consult: Garcia-Menendez and Odman (2011).

A large number of scientific communities develop and use different types of Eulerian models. These models differ only in the spatial and temporal scales of interest and respond to the specific needs of each scientific community. However, at the base they are all similar. Here some examples:

- The GEOS-Chem model, which is a global 3D dispersion model. It uses assimilated meteorological observations from the Goddard Earth Observing System of the NASA Global Modeling and Assimilation Office. This model is used to simulate various atmospheric composition problems in a global scale (Bey *et al.*, 2001).
- WRF-Chem, the Weather Research and Forecasting (WRF) model coupled with chemical transformations occurring in the atmosphere. This model is employed to investigate the regional-scale air quality problems and could-scale interactions between cloud and chemistry (Grell *et al.*, 2005).
- The Computational Multi-scale Air Quality (CMAQ). The model was developed to solve multiple air quality issues, such as tropospheric ozone, aerosols and acid deposition. CMAQ is multi-platform model that can be used for either urban or regional scale air quality modeling (Wang *et al.*, 2009).

Finally, it is important to specify that the computational fluid dynamics (CFD) belongs to the family of Eulerian models. In the field of atmospheric dispersion, it is focused on microscale problems, as explained below.

Computational fluid dynamics (CFD) for atmospheric dispersion

In microscale (less than 1 km) dispersion problems, the flow velocity field is significantly affected by the interaction between the atmospheric flow and the surface obstacles. A direct consequence is that concentration field also changes due to this interaction. In this case, the NWP models do not have sufficient resolution to resolve the phenomena derived from this interaction. On the other hand, CFD results are more adapted to simulate the flow and the concentration field among the buildings of an urban or industrial site.

The CFD approach is based on the Eulerian model. The CFD main parts are the mesh, the solver and the turbulence model. The first is related to the spatial discretisation of the PDEs and the construction of the system of ODEs. Whereas, the numerical methods to solve the system of ODEs are implemented in the solver. Finally, the turbulence model is used as a closure for the wind and concentration equations, depending on the CFD approach adopted.

Therefore, the wind and turbulence field as well as the concentration field are numerically resolved thanks to the Navier-Stokes equations and the atmospheric transport equation (Eq. (1.17)) on a fine mesh or grids, capable to calculate or model the turbulence up to a defined scale. In CFD, the simplest approach is obtained using the RANS model, which decomposes the instantaneous field into its time-averaged and fluctuating parts. So it solves time-averaged equations of motion and considers turbulent fluctuations as eddy viscosity and diffusivity terms. On the other hand, between the turbulence models used for the closure of RANS equations, one of the most popular in engineering and atmospheric applications is the $k-\varepsilon$ model (Tian *et al.*, 2018). Today a state-of-the-art solution for turbulence modelling is Large Eddy Simulation (LES), which filters the large scale (anisotropic) and small scale (isotropic) eddies, and solves the former (Cheng and Liu, 2011). Its high computational cost has not stopped it from becoming a widely used tool in the field of atmospheric boundary layer simulations. Moreover, the LES method allows to simulate explicitly the concentration probability density function (PDF) and its higher moments in real conditions and at very high Reynolds numbers typical of atmospheric flows (Philips *et al.*, 2013; Ardeshiri *et al.*, 2020).

Nevertheless, it is important to highlight that the appropriate setup of mesh resolution, boundary conditions and turbulence model of an atmospheric CFD simulation represents a big challenge (even today) and requires high computational cost. Moreover, when the scale increases, CFD has shown some weaknesses and a lower reliability. In order to compensate the possible drawbacks, some research works have presented promising results using WRF and CFD codes (Tewari *et al.*, 2010).

Among the available CFD software codes, atmospheric simulations are often computed using ANSYS Fluent (Di Sabatino *et al.*, 2008; Goricsán *et al.*, 2011) and the open-source OpenFOAM model (Flores *et al.*, 2013).

Lagrangian models

A stochastic approach to solve the atmospheric transport equation (Eq. (1.17)) is used by the Lagrangian particle dispersion models (LPDMs), already introduced in subsection 1.1.5.

In this method, the molecular diffusion is negligible in the atmospheric transport equation. So, the concentration c is conserved following a fluid particle (Dc/Dt). From the mathematical point of view, this model solves a set of first order stochastic ODEs that describe the motion of many particles. Thus, the release of a polluted source can be simulated by a great number of particles. The displacement of the particles at each time step of the simulation is governed by a velocity, which is composed by two terms. The first one is a deterministic term and is related to the mean velocity of the wind field. Whereas, the second is a stochastic term which represents the turbulent diffusion. The first term is usually obtained by coupling the Lagrangian model with the NWP model or CFD model. On the other hand, assuming that the stochastic term follows

a Markov process, the Langevin equation is used to compute it.

As already mentioned, the main output of the Lagrangian model is a set of 3D particles for each time step. These particles can represent pollutants in liquid, solid or gas phase. They are fictitious entities to which a certain amount of mass of pollutant is associated. Consequently, the concentration field is operationally computed as the total sum of the mass of each particle present in a volume around a computational grid. A fine resolution of the concentration field is possible through a large number of particles. Further, any modification of the mass along the trajectory should be implemented numerically in the particles. In this way, it is possible to reproduce deposition, radioactive decay, chemical reactions and otherSS phenomena.

In addition, there are two particular ways of using the Lagrangian model. The first is to use a reduced number of particles. It does not allow to compute the concentration field. Nevertheless, this approach is extremely useful to determine trajectories of the plume very fast. The stochastic term is neglected in order to consider only the advective term ([Povinec *et al.*, 2013](#)). The second usage is in the inversion problem. It aims to identify and quantify the sources thanks to backward trajectories ([Haszpra, 2016](#)).

Chapter 2

Reynolds-Averaged Navier-Stokes Methodology for the Neutral Boundary Layer

2.1 Overview of a RANS simulation approach for the SBL

In the atmospheric dispersion field, the RANS simulation approach is the most diffused numerical technique. In the current section, the RANS approach will be presented together with the useful tools to simulate the SBL. Firstly, the RANS conservation equations are described. Then, the closure problem together with the turbulent model are presented. Whereas in the last part of the section, the boundary conditions and the difficulties associated with them are treated.

2.1.1 RANS conservation equations

The Reynolds-Average Navier-Stokes (RANS) equations are ensemble-averaged equations of motion for fluid flow. It is based on the Reynolds decomposition:

$$u_i(x_i, t) = \bar{u}_i(x_i, t) + u'_i(x_i, t) \quad (2.1)$$

where $\bar{u}_i(x_i, t)$ is the mean velocity and $u'_i(x_i, t)$ is the fluctuation.

For a flow of an incompressible Newtonian fluid, the general RANS equations are described below.

Mean continuity equation

From the incompressible continuity equation (Eq. (1.11)) and thanks to the Reynolds decomposition (Eq. (2.1)), it is possible to obtain:

$$\nabla \cdot \mathbf{u} = \nabla \cdot (\bar{\mathbf{u}} + \mathbf{u}') = 0 \quad (2.2)$$

The mean velocity and the fluctuations are solenoidal. Therefore, the mean continuity equation is:

$$\nabla \cdot \bar{\mathbf{u}} = 0 \quad (2.3)$$

and a direct consequence is that:

$$\nabla \cdot \mathbf{u}' = 0 \quad (2.4)$$

Mean-momentum equation or Reynolds equation

The mean of the momentum equation (Eq. (1.15)) is less simple to obtain due to the nonlinear convective term. Firstly, it is important to write the substantial derivative in conservative form:

$$\frac{Du_j}{Dt} = \frac{\partial u_j}{\partial t} + \frac{\partial}{\partial x_i}(u_i u_j) \quad (2.5)$$

and apply the average operator to it:

$$\overline{\frac{Du_j}{Dt}} = \frac{\partial \bar{u}_j}{\partial t} + \frac{\partial}{\partial x_i}(\overline{u_i u_j}) \quad (2.6)$$

Substituting the Reynolds decomposition for u_i and u_j , the nonlinear term becomes:

$$\begin{aligned} \overline{u_i u_j} &= \overline{(\bar{u}_i + u'_i)(\bar{u}_j + u'_j)} = \overline{\bar{u}_i \bar{u}_j + u'_i \bar{u}_j + u'_j \bar{u}_i + u'_i u'_j} \\ &= \bar{u}_i \bar{u}_j + \overline{u'_i u'_j} \end{aligned} \quad (2.7)$$

The second term, i.e. the velocity covariance $\overline{u'_i u'_j}$, is called the Reynolds stress. Therefore, from the previous equation and Eq. (2.3), we could obtain:

$$\overline{\frac{Du_j}{Dt}} = \frac{\partial \bar{u}_j}{\partial t} + \frac{\partial}{\partial x_i}(\bar{u}_i \bar{u}_j + \overline{u'_i u'_j}) = \frac{\partial \bar{u}_j}{\partial t} + \bar{u}_i \frac{\partial \bar{u}_j}{\partial x_i} + \frac{\partial}{\partial x_i}(\overline{u'_i u'_j}) \quad (2.8)$$

The final result is written thanks to the definition of the mean substantial derivative:

$$\frac{\bar{D}}{\bar{D}t} = \frac{\partial}{\partial t} + \bar{\mathbf{u}} \cdot \nabla \quad (2.9)$$

In terms of this derivative, the Eq. (2.8) becomes:

$$\frac{\overline{Du_j}}{\bar{D}t} = \frac{\bar{D}}{\bar{D}t} \bar{u}_j + \frac{\partial}{\partial x_i} \overline{u'_i u'_j} \quad (2.10)$$

After this procedure, it results simpler to take the mean of the momentum equation (Eq. (1.15)) because the other terms are linear in \mathbf{u} and p . The result is the mean-momentum or Reynolds equations reported in Eq. (2.11), where a forcing term F_j has been added in accordance with section 1.1.3.

$$\frac{\bar{D}}{\bar{D}t} \bar{u}_j = \nu \nabla^2 \bar{u}_j - \frac{\partial \overline{u'_i u'_j}}{\partial x_i} - \frac{1}{\rho} \frac{\partial \bar{p}}{\partial x_j} + F_j \quad (2.11)$$

The Reynolds equations and the Navier-Stokes equations (Eq. (1.15)) are apparently the same, except for the Reynolds stresses.

In the same way as pressure $p(\mathbf{x}, t)$, the mean pressure field $\bar{p}(\mathbf{x}, t)$ satisfies the Poisson equation. This might be obtained by taking the divergence of the Reynolds equations:

$$-\frac{1}{\rho} \nabla^2 \bar{p} = \frac{\partial \bar{u}_i}{\partial x_j} \frac{\partial \bar{u}_j}{\partial x_i} = \frac{\partial \bar{u}_i}{\partial x_j} \frac{\partial \bar{u}_j}{\partial x_i} + \frac{\partial^2 \overline{u'_i u'_j}}{\partial x_i \partial x_j} \quad (2.12)$$

For a stationary flow, Eq. (2.11) becomes:

$$\frac{\partial}{\partial x_i}(\bar{u}_i \bar{u}_j) = \nu \nabla^2 \bar{u}_j + \frac{\partial \overline{u'_i u'_j}}{\partial x_i} - \frac{1}{\rho} \frac{\partial \bar{p}}{\partial x_j} + F_j \quad (2.13)$$

A closure for Reynolds stresses $\overline{\mathbf{u}'\mathbf{u}'}$ is required.

2.1.2 Reynolds stresses

The Reynolds stresses $\overline{u'_i u'_j}$ play a fundamental role in the equation for the mean velocity field \bar{u}_j . The main difference between the fields u_j and \bar{u}_j is due to the effect of the Reynolds stresses. The properties of the Reynolds stresses are investigated in more detail below.

Interpretation as stresses

The RANS momentum equation can be rewritten as:

$$\rho \frac{\bar{D}}{\bar{D}t} \bar{u}_j = \frac{\partial}{\partial x_i} \left[\mu \left(\frac{\bar{u}_i}{\partial x_j} + \frac{\bar{u}_j}{\partial x_i} \right) - \rho \overline{u'_i u'_j} - \bar{p} \delta_{ij} \right] + F_j \quad (2.14)$$

This is the general form of a momentum conservation equation in which the term in square brackets represents the sum of three stresses: the viscous stress, the apparent stress derived from the fluctuating velocity field, $\rho \overline{u'_i u'_j}$, and the isotropic pressure stress $\bar{p} \delta_{ij}$. The viscous stress derives from momentum transfer at the molecular level. The Reynolds stress derives from momentum transfer by the fluctuating velocity.

Tensor properties

The Reynolds stresses are the components of a second-order tensor, which is symmetric: $\overline{u'_i u'_j} = \overline{u'_j u'_i}$. The normal stresses are the diagonal components, i.e. $\overline{u'^2_1} = \overline{u'_1 u'_1}$, $\overline{u'^2_2}$ and $\overline{u'^2_3}$. Whereas, the off-diagonal components are the shear stresses, i.e. $\overline{u'_1 u'_2}$.

Related to the Reynolds stresses, the turbulent kinetic energy $k(\mathbf{x}, t)$ is the mean kinetic energy per unit mass associated with eddies in turbulent flow. It is typically defined to be half of the trace of the Reynolds stress tensor, as shown in Eq. (2.15).

$$k \equiv \frac{1}{2} \overline{u'_i u'_i} = \frac{1}{2} \overline{\mathbf{u}' \cdot \mathbf{u}'} \quad (2.15)$$

In the principal axis of the Reynolds stress tensor, the off-diagonal components are zero, while the normal stresses are the eigenvalues. Consequently, the Reynolds stress tensor is symmetric positive semi-definite. In general, the eigenvalues are strictly positive, but in rare cases one or more of them could be zero.

Anisotropy

The choice of coordinate system could determine the distinction between shear stresses and normal stresses. An intrinsic distinction can be made between isotropic and anisotropic stresses. The isotropic stress is $2/3 k \delta_{ij}$, and then the deviatoric anisotropic part is:

$$a_{ij} \equiv \overline{u'_i u'_j} - \frac{2}{3} k \delta_{ij} \quad (2.16)$$

In terms of anisotropy tensors, the Reynolds stress tensor is:

$$\overline{u'_i u'_j} = \frac{2}{3} k \delta_{ij} + a_{ij} \quad (2.17)$$

It is only the anisotropic component a_{ij} that is effective in transporting momentum:

$$\rho \frac{\partial \overline{u'_i u'_j}}{\partial x_i} + \frac{\partial \bar{p}}{\partial x_j} = \rho \frac{\partial a_{ij}}{\partial x_i} + \frac{\partial}{\partial x_j} \left(\bar{p} + \frac{2}{3} \rho k \right) \quad (2.18)$$

It shows that the isotropic component can be absorbed in a modified mean pressure.

Other properties

Other properties are the irrotational motion and the symmetries. The first states that the Reynolds stresses arising from an irrotational field $\mathbf{u}(\mathbf{x}, t)$ have absolutely no effect on the mean velocity field. On the other hand, for some flows, symmetries in the flow geometry determine properties of the Reynolds stresses. For more details, see Pope (2000c).

Finally, the closure problem will be treated in subsection 2.1.3 to finalise the description of the properties of the Reynolds stresses.

2.1.3 The closure problem

As previously exposed, there are four independent equations governing the mean velocity flow: three components of the mean momentum equation Eq. (2.13) and the mean continuity equation Eq. (2.3) or alternatively the Poisson equation for \bar{p} . However, the number of unknowns is higher than the number of available equations. In addition to \bar{u} and \bar{p} , there are also the Reynolds stresses.

In such manner the closure problem is manifested. In general, the evolution equations for a set of statistics contain additional statistics to those in the set considered. Consequently, the absence of separate information to determine the additional statistics compromises the solution of the set of equations. This set of equations, characterised by more unknowns than equations, is known as unclosed. So the Reynolds equations are unclosed. They could be solved only if the Reynolds stresses are determined in some way.

One way to determine Reynolds stress is to write its transport equation. Nevertheless, this procedure would need to know higher moments to close the problem, as we will see in subsection 2.1.4 for the turbulent kinetic energy.

Therefore, the closure problem derived from the Reynolds-averaging of the equations of fluid motion has led to the development of approximately models to close systems of RANS equations. Because of the practical importance of such models for weather forecasting, atmospheric dispersion and performance prediction for engineering devices, RANS-closure modeling efforts have existed for more than a century and continue to this day. In the subsection 2.1.5, the turbulent model is generally treated and a popular model in the atmospheric field is presented.

2.1.4 Turbulent kinetic energy

The exact equation for the turbulent kinetic energy is written in Eq. (2.19).

$$\frac{\bar{D}}{\bar{D}t} k \equiv \frac{\partial k}{\partial t} + \bar{u} \cdot \nabla k = -\nabla \cdot \mathbf{T}' + G_k - \varepsilon \quad (2.19)$$

The flux \mathbf{T}' is:

$$T'_i = \frac{1}{2} \overline{u'_i u'_j u'_j} + \frac{\overline{u'_i p'}}{\rho} - 2\nu \overline{u'_j s_{ij}} \quad (2.20)$$

where p' is the fluctuating pressure field ($p' = p - \bar{p}$) and s_{ij} is the fluctuating rate of strain:

$$s_{ij} = S_{ij} - \bar{S}_{ij} = \frac{1}{2} \left(\frac{\partial u'_i}{\partial x_j} + \frac{\partial u'_j}{\partial x_i} \right) \quad (2.21)$$

In the previous equation S_{ij} and \bar{S}_{ij} are respectively the rate of strain and the mean rate of strain. The term G_k in Eq. (2.19) is the production of turbulent kinetic energy or simply production and is defined as:

$$G_k \equiv -\overline{u'_i u'_j} \frac{\partial \bar{u}_i}{\partial x_j} \quad (2.22)$$

Whereas, ε is the dissipation term and is:

$$\varepsilon \equiv 2\nu \overline{s_{ij}s_{ij}} \quad (2.23)$$

In Eq. (2.19), any term that is completely determined by the known variables is said to be “in closed form”. This is the case of $\bar{D}k/\bar{D}t$. Conversely, the remaining terms $\nabla \cdot \mathbf{T}'$, G_k and ε are unknown. So they need to be modelled in order to obtain a closed set of model equations. This is possible through a “closure approximation” that models the unknowns in terms of the known variables.

2.1.5 Turbulent closure models

The Reynolds stresses appears as the unknowns in the Reynolds equations. The turbulent model contributes to determine the Reynolds stresses. There exists mainly two families of turbulent models. The first is based on the turbulent-viscosity hypothesis, while the second directly models the Reynolds-stress transport equations. We are focused on the first family of models. In particular, the first order models (e.g. k- ε model) will be treated because they were commonly used to simulate the SBL flows (Richards and Hoxey, 1993).

The turbulent-viscosity models are based on the turbulent-viscosity hypothesis. The hypothesis can be viewed in two parts:

- The intrinsic assumption that Reynolds-stress anisotropy, $a_{ij} \equiv \overline{u'_i u'_j} - \frac{2}{3}k\delta_{ij}$, is determined by the mean velocity gradient $\partial\bar{u}_i/\partial x_j$.
- The specific assumption that the relationship between a_{ij} and $\partial\bar{u}_i/\partial x_j$ is:

$$\overline{u'_i u'_j} - \frac{2}{3}k\delta_{ij} = -\nu_t \left(\frac{\partial\bar{u}_i}{\partial x_j} + \frac{\partial\bar{u}_j}{\partial x_i} \right) \quad (2.24)$$

or, equivalently,

$$a_{ij} = -2\nu_t \bar{S}_{ij} \quad (2.25)$$

where \bar{S}_{ij} is the mean rate-of-strain tensor.

Therefore, from the specific hypothesis, it is obtained the expression for the Reynolds stresses:

$$\overline{u'_i u'_j} = \frac{2}{3}k\delta_{ij} - \nu_t \left(\frac{\partial\bar{u}_i}{\partial x_j} + \frac{\partial\bar{u}_j}{\partial x_i} \right) \quad (2.26)$$

or in simple shear flows, the shear stress is:

$$\overline{u'_1 u'_3} = -\nu_t \left(\frac{\partial\bar{u}_1}{\partial x_3} \right) \quad (2.27)$$

Given the turbulent viscosity field $\nu_t(\mathbf{x}, t)$, Eq. (2.26) provides a convenient closure to Reynolds equations. In fact, it reduces the number of unknowns from six to one, i.e. ν_t . Moreover, it has the same form as the Navier-Stokes equations. Nevertheless, the accuracy of the hypothesis is poor for many flows.

If the turbulent-viscosity hypothesis is considered as an adequate approximation, the remained work is to determine an approximate specification of the turbulent viscosity $\nu_t(\mathbf{x}, t)$. Commonly, it can be written as the product of a velocity $u^*(\mathbf{x}, t)$ and a length $l^*(\mathbf{x}, t)$:

$$\nu_t = u^* l^* \quad (2.28)$$

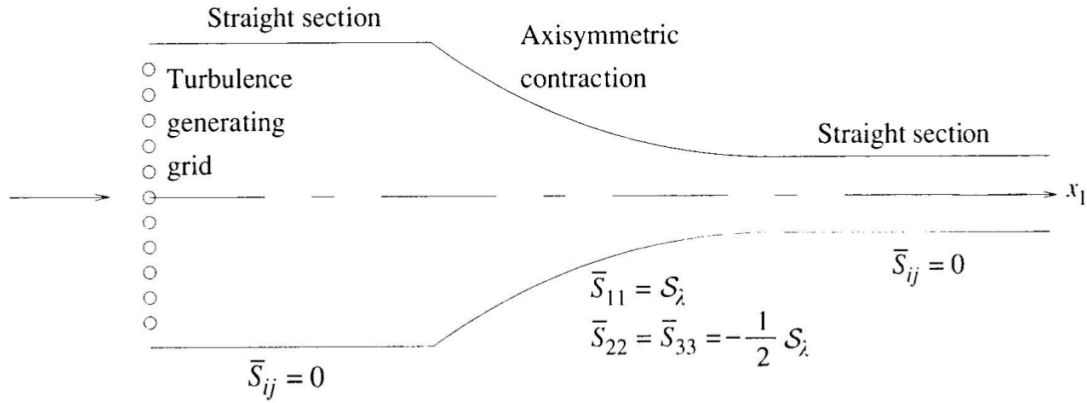


Figure 2.1: A sketch of an apparatus similar to that used by [Uberoi \(1956\)](#), to study the effect of axisymmetric mean straining on grid turbulence. From ([Pope, 2000c](#)).

In order to specify ν_t , u^* and l^* are required. In algebraic models, for example in the mixing-length model, the geometry of the flow helps to specify l^* . In two-equations models, like the $k-\varepsilon$ model, u^* and l^* are related to k and ε , for which modelled transport equations are solved.

Therefore, in addition to the previous mentioned models, there are also the one-equation models. For instance, the Spalart-Allmaras model is a one-equation model developed for aerodynamic applications ([Spalart and Allmaras, 1994](#)). Whereas, there exist many others two-equations models. In many of these, k is taken as one of the variables. Nevertheless there are different choices for the second one. Examples are quantities with dimensions of kL (where L is a lengthscale) ([Rotta, 1951](#)), turbulence frequency ω ([Kolmogorov, 1942](#)), ω^2 ([Saffman, 1970](#)) and timescale τ ([Speziale et al., 1992](#)).

In order to achieve our aims, it was chosen to treat the $k-\varepsilon$ model in more detail. In fact, it is commonly used to simulate the atmospheric flow, as we will see in [subsection 2.1.6](#) and [subsection 2.1.7](#).

Limits of the turbulent-viscosity model

It is possible to analyse some limits of the turbulent-viscosity models thanks to the wind tunnel experiment of [Uberoi \(1956\)](#), as highlighted by [Pope \(2000c\)](#). The latter experiment investigates the effects on turbulence of an axisymmetric contraction and the validity of the turbulent-viscosity hypothesis along the test section. The sketch of the experiment is shown in [Figure 2.1](#). Three parts constitute the test section, i.e. two straight sections separated by an axisymmetric contraction.

The limits of the turbulent-viscosity hypothesis are highlighted in the middle axisymmetric contraction and in the second straight section. In the first of these two sections, the evolution of the Reynolds stresses are better reproduced by the rapid-distortion theory (RDT). Whereas the turbulent-viscosity hypothesis is not appropriate to describe the effects of the contraction. Secondly, the straight section is expected to show Reynolds-stress anisotropies equal to zero. Nevertheless, it is not verified because the anisotropies produced in the contraction section decay slowly. The prior history of the flow explain this behaviour that again is not reproduced by the previous hypothesis. Therefore, in these cases, the local mean rate of strain does not govern the Reynolds-stresses anisotropies.

Finally, it is important to remember that there exist other flow for which the hypothesis is more reasonable. It is the case of simple turbulent shear flows, e.g.: the round jet, mixing layer, channel flow and boundary layer. The latter is of particular interest for our purposes.

2.1.6 The k - ε model

The k - ε model is the most widely used complete turbulence model and it is present in most commercial CFD codes. Moreover, it is very popular in atmospheric dispersion, as already mentioned in [section 1.2.3](#). As for all turbulence models, both the concept and details have evolved over the time. [Jones and Launder \(1972\)](#) are considered as the developers of the “standard k - ε model”, while [Launder and Sharma \(1974\)](#) had contributed to improve the model constants. Earlier contributions are cited by [Launder and Spalding \(1972\)](#).

This model is part of the class of two-equations models, in which model transport equations are solved for two turbulence quantities: the turbulent kinetic energy k and the turbulent dissipation rate ε . From these two quantities, it is possible to obtain a length-scale $L = k^{3/2}/\varepsilon$, a time-scale $\mathcal{T} = k/\varepsilon$, and a quantity of dimension ν_t (k^2/ε). Consequently, two-equation model can be complete. In fact, considering Eq. (2.28), we have $l_* \sim k^{3/2}/\varepsilon$ and $u_* \sim k^{1/2}$.

In addition to turbulence-viscosity hypothesis, the k - ε model considers:

- The model transport equation for k .

$$\frac{\bar{D}k}{\bar{D}t} = \nabla \cdot \left(\frac{\nu_t}{\sigma_k} \nabla k \right) + G_k - \varepsilon \quad (2.29)$$

where G_k is the turbulent kinetic energy production term and σ_k is the first coefficient of the model. In fact, the flux \mathbf{T}' of the exact k equation (Eq. (2.19)) is modelled through a gradient-diffusion hypothesis and the first term of the right-hand side of the Eq. (2.29) is obtained, with σ_k being constant and playing the role of a turbulent Prandtl or Schmidt number for k .

- The model transport equation for ε .

$$\frac{\bar{D}\varepsilon}{\bar{D}t} = \nabla \cdot \left(\frac{\nu_t}{\sigma_\varepsilon} \nabla \varepsilon \right) + C_{\varepsilon 1} \frac{G_k \varepsilon}{k} - C_{\varepsilon 2} \frac{\varepsilon}{k} \quad (2.30)$$

where σ_ε , $C_{\varepsilon 1}$ and $C_{\varepsilon 2}$ are the other coefficients. Similarly, σ_ε plays the role of turbulent dissipation Prandtl number.

- The specification of the turbulent viscosity.

$$\nu_t = C_\mu \frac{k^2}{\varepsilon} \quad (2.31)$$

where C_μ is the last of the five model coefficients.

While the exact equation for k is used (with the appropriate closure), the exact equation for ε can be derived but it is not a useful starting point for the ε model equation ([Pope, 2000c](#)). In fact, ε is viewed as the energy-flow rate in the energy cascade. In the model, it is determined by the large scale motions and independently of the viscosity at high Re number. On the other hand, the real equation of ε is related to the processes in the dissipative range. The direct consequence is that the standard model equation for ε is an empirical equation.

The five coefficients of the model are: σ_k , σ_ε , $C_{\varepsilon 1}$, $C_{\varepsilon 2}$ and C_μ . Some sets of model coefficient values are shown in [Table 2.1](#). Whereas, the values of [Launder and Sharma \(1974\)](#) represent a compromise chosen (with subjective judgement) to give the best performance for a range of flows. There are some other sets of values adapted for many particular flow, like for decaying turbulence, round jets or atmospheric flows. Such ad hoc flow-dependent adjustment of the coefficients represents a limit of the k - ε model. The appropriate coefficients for the atmospheric flow, studied in this chapter, will be presented in the following subsection.

2.1.7 The Richards and Hoxey (R&H) approach

After the generic overview of the RANS approach, the current subsection presents a well known and fundamental approach to model and simulate the turbulent ABL flow under neutral conditions. In fact, many ABL studies using CFD were carried out over the past 30 years, often assuming neutral equilibrium (Blocken *et al.*, 2007). In this case, the ABL could be considered as a horizontally homogeneous flow. Practical simulations of ABL flows are often performed using the RANS approach combining with two-equations turbulence model, being the k - ε model the most popular. However, difficulties were encountered in wide-ranging literature (Richards and Hoxey, 1993; Blocken *et al.*, 2007; Parente *et al.*, 2011a; O’Sullivan *et al.*, 2011; Richards and Norris, 2011).

The studies of Richards and Hoxey (1993) and Hargreaves and Wright (2007) could be considered as a fundamental reference for the ABL modelling. It represents a clear guideline to deal with this challenging problem and laid the foundations for more recent and complex models. For convenience, the modelling approach, resulting from this two studies, will be called “R&H approach” from here on. We are interested to study the bottom part of the ABL, also known as surface boundary layer (SBL) or atmospheric surface layer. According to the authors the flow in this region should normally be modelled as a homogeneous horizontal flow. Thus, velocity and turbulence profiles associated with the k - ε turbulence model needs to produce horizontally homogeneous conditions, which implies that the streamwise gradients of all variables should be zero and it is not trivial. Without considering its generation, a suitable model for the SBL is based on any flow that is fully aerodynamically rough, horizontally homogeneous and relatively free from any pressure gradients. For computational modelling, fully aerodynamically rough flow implies that the shear stress should be determined by Reynolds stresses. Moreover, the harder characteristic to achieve is the horizontal homogeneity. This condition can exist only in regions remote from any kind of obstructions and imposes that the streamwise gradient of all variables are zero. Many numerical works (Yang *et al.*, 2009; Tian *et al.*, 2018) have underlined that the use of empirical equations for inflow boundary conditions, e.g. power law for velocity or polynomial fit for experimental turbulence kinetic energy, changes rapidly in the inlet region of the domain. The flow near the surface tends to accelerate considerably before been retarded by the influence of obstacles. In order to avoid this problem, it is very important that the velocity and turbulence profiles at the inlet, the ground shear stress and the turbulence model should be in equilibrium. Nevertheless, Hargreaves and Wright (2007) have demonstrated that the latter conditions are not enough to produce a sustainable SBL. In order to reproduce a sustainable SBL, the computational approach needs further precautions regarding the wall function and the top boundary condition.

Before describing the R&H approach in more details, a brief presentation of the context in which it was developed is reported. In fact, it is highlighted that some aspects of the Richards and Hoxey (1993) work had become a standard among practitioners in computational wind engineering in the early part of the 21st century. Many users of commercial codes (e.g. Fluent 6.1 (2003) and CFX 5.7 (2004)) used versions of the R&H inlet boundary conditions in CFD simulations (Parker and Kinnersley, 2004). Other works (Zhang, 2009) have employed even more complex expressions for the streamwise component of the wind and turbulence quantities at the inlet. Nevertheless, these profiles decayed in the same way as the less complex models due to the inability of the chosen turbulence model, boundary conditions and wall functions to sustain them.

In a blind-test of CFD software in modelling wind loading on the full-scale Silsoe cube, as prerequisite, participants were asked to demonstrate that they could model a suitable ABL (Richards *et al.*, 2002). Between the participants, only Richards was able to maintain the inlet profiles along the domain. The other participants largely used unmodified versions of two commercial codes: Fluent and CFX. On the other hand, Richards used an open-source code, which was modified for the purpose. About 20 years have passed since then and several

changes have been made to all the codes used today for this type of simulation, as we will see in [section 2.2](#).

Now we can move on to the description of the considered approach. In the k - ε turbulence model and 2D case for simplicity, the Reynolds stresses are modelled by an effective turbulent viscosity:

$$\overline{u'w'} = -\mu_t \left(\frac{\partial \bar{u}}{\partial z} + \frac{\partial \bar{w}}{\partial x} \right) \quad (2.32)$$

where \bar{u} and \bar{w} are the mean streamwise and vertical velocity. Whereas u' and w' are the corresponding velocity fluctuations and μ_t is related to turbulent kinetic energy (Eq. (2.15)).

[Richards and Hoxey \(1993\)](#) made the following assumptions in order to model an homogeneous 2D ABL:

1. The mean vertical velocity is zero.
2. The pressure is constant in both the vertical and streamwise direction. Therefore, there is not pressure gradient.
3. The shear stress, τ_w , is constant throughout the boundary layer, i.e.

$$\tau_w = \mu_t \frac{\partial \bar{u}}{\partial z} = \rho u_*^2 \quad (2.33)$$

where μ_t is the turbulent viscosity, \bar{u} is the streamwise component of the wind speed, ρ is the air density and u_* is the friction velocity.

4. The turbulent kinetic energy k and the dissipation rate ε satisfy their respective conservation equations, which are reduced to:

$$\frac{\partial}{\partial z} \left(\frac{\mu_t}{\sigma_k} \frac{\partial k}{\partial z} \right) + G_k - \rho \varepsilon = 0 \quad (2.34)$$

$$\frac{\partial}{\partial z} \left(\frac{\mu_t}{\sigma_\varepsilon} \frac{\partial \varepsilon}{\partial z} \right) + C_{\varepsilon 1} G_k \frac{\varepsilon}{k} - C_{\varepsilon 2} \rho \frac{\varepsilon^2}{k} = 0 \quad (2.35)$$

where the production of turbulent kinetic energy (Eq. (2.22)) is given by:

$$G_k = \overline{u'w'} \left(\frac{\partial \bar{u}}{\partial z} \right) = \mu_t \left(\frac{\partial \bar{u}}{\partial z} \right)^2 \quad (2.36)$$

and the turbulent viscosity μ_t is :

$$\mu_t = \rho C_\mu \frac{k^2}{\varepsilon} \quad (2.37)$$

In order to guarantee the equilibrium of the turbulence model, Richards and Hoxey then suggest that the above equations can be satisfy by the inlet profiles of Eqs. (2.38)-(2.40). These profiles are mainly employed in [section 2.2](#) and they are called ‘‘R&H profiles’’.

$$\bar{u}(z) = \frac{u_*}{\kappa} \ln \left(\frac{z + z_0}{z_0} \right) \quad (2.38)$$

$$k = \frac{u_*^2}{\sqrt{C_\mu}} \quad (2.39)$$

$$\varepsilon(z) = \frac{u_*^3}{\kappa(z + z_0)} \quad (2.40)$$

The authors of the articles found that from Eq. (2.38) to Eq. (2.40) satisfy Eq. (2.34) automatically, but Eq. (2.35) only when:

$$\sigma_\varepsilon = \frac{\kappa^2}{(C_{\varepsilon 2} - C_{\varepsilon 1})\sqrt{C_\mu}} \quad (2.41)$$

So considering $\kappa = 0.4$, it is important to choose properly the five k- ε coefficients. The Table 2.1 illustrates three different set of coefficients. The first one was proposed by [Launder and Sharma \(1974\)](#) who participated to the formulation and the improvement of this model in the seventies. These coefficients are considered as standard coefficients, setting as default values by different CFD codes, like Fluent and OpenFOAM. However, the latter set is not in agreement with the characteristics of our flow and does not satisfy the condition of Eq. (2.41). Therefore, [Hargreaves and Wright \(2007\)](#) revisited the study of R&H and introduced a new set which differs only with regard to the σ_ε value. This procedure aims to balance the current case through the modification of the coefficients based on standard ones. Nevertheless, [Duynderke \(1988\)](#) has still suggested a different set of coefficients in order to reproduce the characteristics of the atmospheric SBL in neutral conditions. The atmosphere is characterised by a ratio B between the turbulent kinetic energy and the square of the friction velocity higher than a typical near wall turbulence, as taken into account by Launder and Sharma. According to [Hargreaves and Wright \(2007\)](#), the ratio B is 4.17, while it is almost 5.20 for [Duynderke \(1988\)](#). This determines different sets of coefficients.

	σ_k	σ_ε	$C_{\varepsilon 1}$	$C_{\varepsilon 2}$	C_μ
Launder and Sharma (1974)	1.0	1.3	1.44	1.92	0.09
Hargreaves and Wright (2007)	1.0	1.11	1.44	1.92	0.09
Duynderke (1988)	1.0	2.38	1.46	1.83	0.033

Table 2.1: Set of different k- ε coefficients.

The current SBL modelling approach is full of tips that we have tested in [section 2.2](#). So three different case studies, performed using two CFD codes (i.e. OpenFOAM and Fluent), complement the current section in order to show operationally the impact of issues mentioned and of improvements suggested. On the other hand, the next subsection presents the precautions necessary to treat the boundary conditions. In order to have all the tools to complete this academic test.

2.1.8 Boundary conditions

In this section, the principal boundary conditions are presented. In fact, it is important to pay particular attention to the inlet, top and ground boundary conditions for correctly performing a RANS simulation of the neutral SBL. Moreover, it is also presented the equilibrium between the turbulence model and the boundary conditions.

Inlet boundary condition

The typical R&H inlet numerical profiles, already presented in the previous [subsection 2.1.7](#), are shown in the [Figure 2.2](#) for a SBL of 300 m. They follow the Eqs. (2.38)-(2.40). In the current thesis, these profiles will be adopted because they are enough for our tests of [section 2.2](#).

Nevertheless, it is important to highlight that some other profiles exist because the R&H profiles present some drawbacks. For instance, a weakness of R&H profiles are the constant

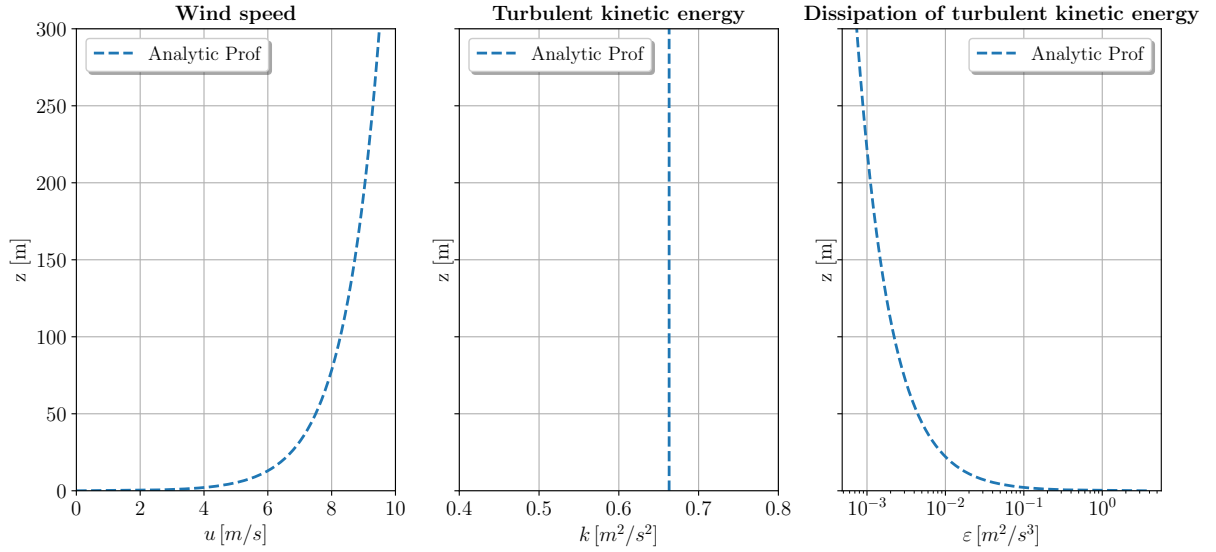


Figure 2.2: Inlet profiles

value of the shear stress in all SBL height. In fact, experiments demonstrate that shear stress is a variant along height and decreases vertically (Xie *et al.*, 2004b; Yang *et al.*, 2009). According to the work of Zhang (2009), an alternative semi-empirical shear stress model is presented:

$$\overline{u'w'}(z) = -u_*^2 \left(1 - \frac{z}{h_g}\right)^2 \quad (2.42)$$

where h_g is the height of the SBL and defined as (Tennekes, 1984):

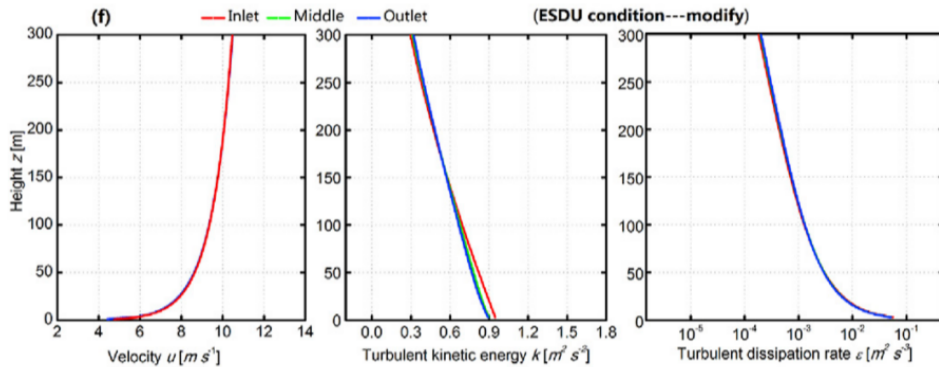
$$h_g = \frac{u_*}{6f} \quad (2.43)$$

Here, f is the Coriolis parameter (for a typical mid-latitude location: $f = 10^{-4} \text{ rad} \cdot \text{s}^{-1}$). Consequently, the k expressions becomes:

$$k(z) = \frac{u_*^2}{\sqrt{C_\mu}} \left(1 - \frac{z}{h_g}\right)^2 \quad (2.44)$$

while $\bar{u}(z)$ and $\varepsilon(z)$ remain the same (Eq. (2.38) and Eq. (2.40)).

The previous k profiles were also employed by the Engineering Science Data Unit (ESDU, 1982) for Computed Wind Engineering studies, as observed in Figure 2.3. In this case the set of profiles includes Eq. (2.38) and a modified version of the ε profile:

Figure 2.3: ESDU profiles. From: (Tian *et al.*, 2018)

$$\varepsilon(z) = \frac{u_*^3}{\kappa(z + z_0)} \left(1 - \frac{z}{h_g}\right)^2 \quad (2.45)$$

Another alternative inlet condition for k is (Yang *et al.*, 2009; Parente *et al.*, 2011a):

$$k = \sqrt{D_1 \ln\left(\frac{z + z_0}{z_0}\right) + D_2} \quad (2.46)$$

where D_1 and D_2 are two constants that describe the inflow turbulence level, determined via experimental data fitting. The latter profile for k is obtained as a solution of the turbulent kinetic energy transport equation, assuming that C_μ is constant and the local equilibrium between production and dissipation:

$$\varepsilon(z) = \sqrt{C_\mu} k \frac{\partial u}{\partial z} \quad (2.47)$$

Here C_μ needs to be properly specified in order to ensure the correct level of turbulent kinetic energy throughout the domain.

In the next section, the case studies will use the R&H and Zhang profiles.

Top boundary condition

Richards and Hoxey (1993) and Hargreaves and Wright (2007) point out the problem of top boundary condition. At the beginning of the research in this area, the less accurate simulations had used a symmetry boundary condition that imposes a zero gradient normal to the top patch. This condition does not guarantee the conservation of \bar{u} , k and ε profiles along the domain, except if the inlet profiles results perpendicular to the top patch. The latter exception could be physical but it is not found very often. For this reason, the earlier authors have proposed the use of an imposed shear stress which allows the equilibrium at the top. This condition could be interpreted also as a fixed gradient obtained from the inlet profiles. Moreover, a fixed velocity brings to a similar result, as shown by Tian *et al.* (2018). An alternative solution is related to the third hypothesis of Richards and Hoxey. Consequently, it is possible to introduce a constant momentum source in the x and y direction (Vendel *et al.*, 2010). All the previous approaches are equivalent but could present some limitations. Fixing the top shear stress, gradient or velocity could modify the flow field, above all, when there are obstacles in the domain. This last limitation can be alleviated if a suitable height of the domain is considered. The top boundary needs to be at a suitable distance from the obstacles. In the same way, the third hypothesis of Richards and Hoxey is not a physical condition because many experiments prove its inaccuracy (Xie *et al.*, 2004b).

Being aware of the limitations, one of the above approaches can be taken to define the top boundary condition. We have decided to mainly adopt a fixed gradient for \bar{u} and ε because this approach is already implemented in OpenFOAM.

Wall function

In previous studies, a standard treatment of a rough wall could not be appropriate when we simulate an SBL because it is quite common to have the value of the first bottom cell outside the log-law region (subsection 1.1.4) that is recommended to apply the logarithmic law of the wall. If we use a commercial CFD code, it is important to take into account the possible error due to the use of a wall function with a standard roughness model and the need of a manual correction, e.g. through a User Defined Function. Open-source codes, like OpenFOAM, allow to correct directly the source code of the wall functions, as Richards and Hoxey made. However, with respect to the standard wall functions used by Hargreaves and Wright (2007), OpenFOAM provides wall functions based on standard roughness model with good performances also outside of the

logarithmic regions, as we will see in [subsection 2.2.3](#). Open-source codes could also present the wall function correction suggested by [Hargreaves and Wright \(2007\)](#).

The latter approaches will be presented in [section 2.2](#), where it will also be highlighted the evolution of wall function codes with respect to previous versions, presented in the papers cited so far. Moreover, the treatment of rough surfaces implies the use of wall function adapted to simulate roughness effects. These kind of wall function are described in [section A.1](#) for OpenFOAM code.

Equilibrium of k - ε equations

The equilibrium of k - ε equations is fundamental to conserve the inlet profile along the simulation domain.

Two approaches to obtain the equilibrium of the k - ε equations are presented here. The first one is based on the Eq. (2.41) and aims to conserve the R&H profiles, as illustrated in [subsection 2.1.7](#). The second and third set of coefficients of [Table 2.1](#) derived from this approach and from experiments, which point out that the rate between the turbulent kinetic energy and the square of the friction velocity is higher for the atmosphere.

The second approach is constituted by the addition of a source term in the ε equation. It is also used when R&H profiles are employed and yield to the following source term:

$$R_\varepsilon = \frac{u_*}{z + z_0} \left[\frac{(C_{\varepsilon 2} - C_{\varepsilon 1}) \sqrt{C_\mu}}{\kappa^2} - \frac{1}{\sigma_\varepsilon} \right] \quad (2.48)$$

On the other hand, the use of ESDU profiles implies the addition of a second source term in the k equation:

$$R_k = \frac{2u_*^3 \kappa}{\sqrt{C_\mu} h_g \sigma_k} \left(1 - \frac{z}{h_g} \right)^2 \left[\frac{4z + 3z_0}{h_g} - 1 \right] \quad (2.49)$$

The R_k and R_ε of the ESDU model ought to be added as source terms into the k and ε transport equations, respectively to ascertain the full consistency ([Figure 2.3](#)).

In this phase of the research, our goal is to thoroughly understand and easily manipulate the simplest of academic cases. For this reason, we have focused on the R&H approach and its profiles.

2.1.9 Mean scalar equation

Up to now, it is possible to affirm that the simple description of the velocity field $\mathbf{u}(\mathbf{x}, t)$ is given by its mean field $\bar{\mathbf{u}}(\mathbf{x}, t)$. Similarly, the mean passive scalar field $c(\mathbf{x}, t)$ is used for a basic description of the passive scalar field $c(\mathbf{x}, t)$. The mean passive scalar field was briefly introduced in [subsection 1.1.5](#) in order to present the state-of-the-art of the atmospheric dispersion. More details will be presented here.

In order to obtain the equation for $\bar{c}(\mathbf{x}, t)$, the Reynolds decomposition is still used:

$$c(\mathbf{x}, t) = \bar{c}(\mathbf{x}, t) + c'(\mathbf{x}, t) \quad (2.50)$$

Therefore, the conservation equation for $c(\mathbf{x}, t)$ (Eq. (1.17)), without considering the source term S_c , is written as:

$$\frac{\partial c}{\partial t} + \nabla(\mathbf{u} c) = \nabla \cdot (D_c \nabla c) \quad (2.51)$$

The convective flux $\mathbf{u} c$ is the only nonlinear term and its mean is:

$$\overline{\mathbf{u} c} = \overline{(\bar{\mathbf{u}} + \mathbf{u}')(\bar{c} + c')} = \bar{\mathbf{u}} \bar{c} + \overline{\mathbf{u}' c'} \quad (2.52)$$

The velocity-scalar covariance $\overline{\mathbf{u}'c'}$ is the turbulent scalar flux. It represents the flux of the scalar due to the fluctuating velocity field. Consequently, taking the mean of Eq. (2.51), we obtain (Eq. (1.49)):

$$\frac{\partial \bar{c}}{\partial t} + \nabla \cdot (\bar{\mathbf{u}} \bar{c} + \overline{\mathbf{u}'c'}) = D_c \nabla^2 \bar{c} \quad (2.53)$$

or equivalently in terms of the mean substantial derivative:

$$\frac{\bar{D}\bar{c}}{\bar{D}t} = \nabla \cdot (D_c \nabla \bar{c} - \overline{\mathbf{u}'c'}) \quad (2.54)$$

The scalar fluxes and the Reynolds stresses play an analogous role respectively in the mean-scalar equation and in the mean-momentum equations. Similarly, they lead to the closure problem. In fact, knowing $\bar{\mathbf{u}}$ is not enough, the modeling of $\overline{\mathbf{u}'c'}$ is needed to solve the Eq. (2.54) for \bar{c} . The direction and the magnitude of the turbulent transport of the conserved scalar c are determined by the scalar flux vector. According to the gradient-diffusion hypothesis, this transport is carried out along the mean scalar gradient and in the direction of $-\nabla \bar{c}$. In this way, according to the hypothesis, there exist a positive scalar $D_t(\mathbf{x}, t)$, i.e. the turbulent diffusivity, that yields to:

$$\overline{\mathbf{u}'c'} = -D_t \nabla \bar{c} \quad (2.55)$$

Consequently, Eq. (2.54) becomes:

$$\frac{\partial \bar{c}}{\partial t} + \bar{\mathbf{u}} \cdot \nabla \bar{c} = \nabla \cdot [(D_c + D_t) \nabla \bar{c}] \quad (2.56)$$

The effective diffusivity D_{eff} is defined as the sum of the molecular and turbulent diffusivities:

$$D_{\text{eff}} = D_c + D_t(\mathbf{x}, t) \quad (2.57)$$

Finally, the mean passive scalar field could be expressed as:

$$\frac{\bar{D}\bar{c}}{\bar{D}t} = \nabla \cdot (D_{\text{eff}} \nabla \bar{c}) \quad (2.58)$$

The latter equation is the same as the conservation equation for c (Eq. (1.17)) but with $\bar{\mathbf{u}}$, \bar{c} and D_{eff} in place of \mathbf{u} , c and D_c .

From the operational point of view, the turbulent diffusivity is modeled by:

$$D_t = \frac{\nu_t}{\text{Sc}_t} \quad (2.59)$$

where ν_t is the turbulent viscosity, derived from the mean velocity field, and Sc_t is the turbulent Schmidt number. In fact, the Fickian diffusion approximation based on turbulent diffusivity remains the most popular and diffused approach so far (Gualtieri *et al.*, 2017).

2.2 Issues, improvements and comparison of RANS literature cases

As discussed in the previous chapter, several commercial CFD codes (e.g. CFX, Ansys Fluent, etc) have been shown unable to maintain standard atmospheric wind speed and turbulence profiles over a flat terrain with homogeneous roughness using the standard k - ε model and wall functions (Hargreaves and Wright, 2007). The main cause is the inconsistent formulations of the boundary conditions with respect to the k - ε model.

In the current section, we test our modeling approach based on the R&H approach to simulate a 2D neutral SBL using two CFD codes: OpenFOAM and Ansys Fluent. The 2D simulation does not truly represent 3D turbulence but it serves the purpose of illustrating the problems mentioned above and economically evaluating possible remedial measures or proving that current codes have already overcome the difficulties of the past. The approach is compared to 3 study cases from literature: Segersson (2017) in subsection 2.2.1, Blocken *et al.* (2007) in subsection 2.2.2 and Hargreaves and Wright (2007) in subsection 2.2.3. The aim is to show the influence of the boundary conditions on the development of a horizontal homogeneous atmospheric flow and the equilibrium due to k - ε coefficients. In particular, the work is focused on the study of:

- the inlet boundary conditions,
- the top boundary conditions,
- the wall function, and
- the interaction of the k - ε coefficients with the boundary conditions.

From this point of view, the whole effort is addressed to understand the state of the art and the capabilities of the RANS CFD tools today, and become familiar with them. Moreover, the study of the RANS boundary conditions is also useful to approaching LES simulations and begin to understand the difficulties to be faced in chapter 3.

For all the following simulations, the CFD codes used are OpenFOAM 5.0 or/and v1812 and Ansys Fluent 18.2. The 2D RANS equations and the continuity equations are solved using the control volume method and the closure is obtained thanks to the k - ε model. Pressure-velocity coupling is treated by the SIMPLE algorithm. Second-order discretisation schemes are used for the momentum and turbulence transport equations, including the convection and viscous terms. The kinematic viscosity considered is $\nu = 1.460 \times 10^{-5} \text{ m}^2/\text{s}$.

2.2.1 Irvine case

The current study case is called “Irvine case”. It takes inspiration from the measurement campaign of Irvine *et al.* (1997), where the measurements are made at a forest edge, with four meteorological masts, carrying three anemometers each. However the numerical analysis is provided by the tutorial of Segersson (2017), which describes step by step how to simulate a neutral ABL in an urban environment using a steady state incompressible solver. Although it is not the simplest numerical case, it remains the most detailed tutorial we faced at the beginning of the current research. Moreover, this has proved helpful in achieving the objectives of this section.

In this case study, two CFD codes are employed: OpenFOAM v5 and Ansys Fluent 18.2. The aim is to analyse the influence of the top boundary condition on maintaining the inlet profiles along the length of the domain with respect to two families of inlet profiles (i.e. the R&H profiles and Zhang profiles).

Following the work of Segersson (2017) and Vendel (2011), a 2D domain is taken into account. The length and height of the domain are respectively 20 km and 300 m. The domain

is schematically resumed by [Figure 2.4](#). It is sufficiently long to test the profile conservation capability of all the approaches adopted. Whereas the height is appropriate to describe the SBL and the presence of obstacles (e.g. industrial buildings), as illustrated in [subsection 1.2.1](#). [Figure 2.4](#) also illustrate the characteristics of the adopted hexahedral structured mesh. The total number of cells in the mesh is 400 000. While no expansion ratio was employed along x coordinate (i.e. $R_x = 1$), a ratio of $R_z = 2$ was employed along z . Hence, in the x coordinate, the mesh present uniform cell of size $\Delta x = 4.00$ m. On the other hand, in the z coordinate, the cell adjacent to the wall has a size of 2.59 m and the cell close to the top patch has a size of 5.18 m. As already mentioned, we are doing a 2D simulation so we have a single cell in the y direction with an arbitrary size of $\Delta y = 2.00$ m.

z_0	0.06 m	Aerodynamic roughness or roughness length
\bar{u}_{ref}	6.17 m/s	Wind reference velocity
z_{ref}	15.00 m	Reference height
P_0	1.00×10^5 Pa	Reference pressure

Table 2.2: Neutral SBL characteristics of the Irvine case.

The SBL characteristics are summarised in [Table 2.2](#). The values of the reference velocity \bar{u}_{ref} and the roughness length z_0 is estimated from statistical wind profiles of the measurement campaign ([Irvine et al., 1997](#)). The statistical profiles are obtained from 3 experiment runs, all close to neutral conditions. In the same way, the roughness length is estimated to 0.06 m.

The three study cases are summarised together with a schematic list of the boundary conditions on [Table 2.3](#). The inlet boundary conditions are constituted by the R&H profiles for the case CS1 and CS3, and the Zhang profiles for the case CS2. The top boundary condition varies between the cases. In fact, CS1 uses a symmetric boundary condition. On the other hand, case CS2 employs momentum sources, which is a method already implemented by our research team for Fluent. In addition to momentum sources, the case CS3 uses a fixed gradient for \bar{u} and ε in the top boundary condition. The latter is an approach more adapted for OpenFOAM, because (as before) it was already implemented in the code. All the cases use the same standard wall-function for rough surfaces available in OpenFOAM and Fluent, which are respectively “nutkRoughWallFunction” and “log-of-the wall modified for roughness”. Finally, the k - ε coefficients are those suggested by [Hargreaves and Wright \(2007\)](#) and reported in [Table 2.1](#).

All figures below show vertical profiles of the mean streamwise velocity, the mean turbulent kinetic energy (TKE) and the mean dissipation rate of TKE at different distances from the inlet

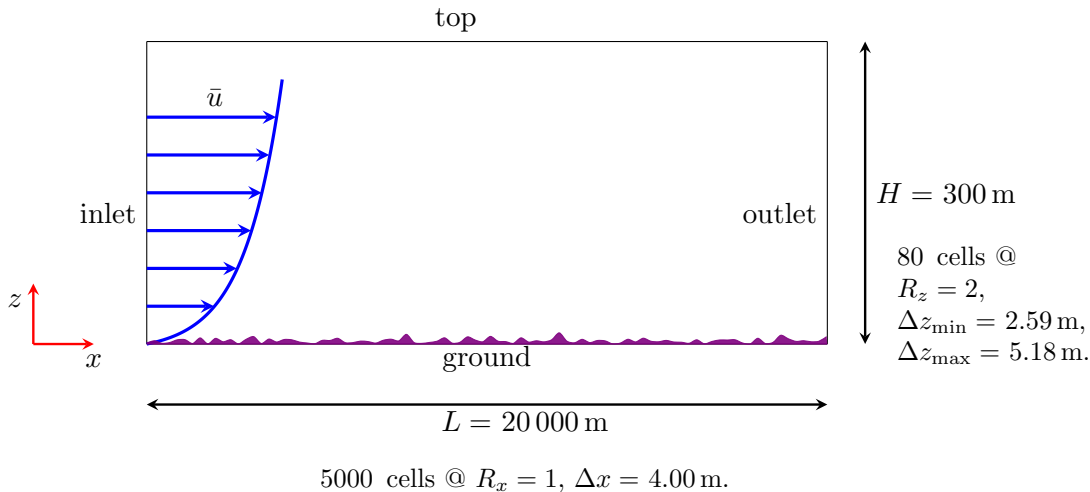


Figure 2.4: 2D domain for the Irvine case.

patch: 1 km, 2 km, 5 km, 10 km and 20 km or outlet profile. Moreover, the analytical profile is plotted for every involved variable. The case CS1, characterised by a symmetry boundary condition for the top patch and R&H inlet profiles, allows to find the same inconsistency of some previous studies (e.g. Mathews (1987)). Both OpenFOAM and Fluent does not conserve the inlet profiles along the domain. Above of all, the turbulent kinetic energy and the dissipation of turbulent kinetic energy decrease gradually along the streamwise, see Figure 2.5 and Figure 2.6.

The second comparison, i.e. case CS2, applies a correction to the top boundary condition using the Fluent code. So the correction is based on a band adjacent to the top patch, which introduces a momentum source in the x and y direction. This correction approach is not implemented by default in OpenFOAM. Consequently, only the Fluent results are analysed here. In this case, the Zhang profiles are employed as inlet boundary conditions instead of the R&H profiles. This profiles were presented in section 2.1.8. The main problem, as shown by Figure 2.7, is the no-equilibrium of k - ε equations with respect to the considered inlet profiles. This is the reason why the turbulent kinetic energy and the dissipation of turbulent kinetic energy profiles tend to a constant profile as they develop along the domain. In fact, they try to return to an equilibrium condition which is close to the R&H profiles.

The last case also applies a correction to the top boundary condition. In addition to the momentum source method used for Fluent, a fixed gradient are used in OpenFOAM simulation. The gradients are computed from the inlet profiles, which are the R&H profiles. For OpenFOAM, Figure 2.8 shows a good equilibrium between the k - ε equations and the boundary conditions, which allows to conserve our profiles along the domain. The OpenFOAM and Fluent results have similar performance.

The Irvine case study allows to confirm that the symmetric boundary condition at the top of the domain causes the input profiles not to be conserved along the domain. In fact, it generates the deceleration of the velocity input profiles and a reduction in turbulence along the domain. Only a suitable top boundary condition could solve the problem (as explained in section 2.1.8). Moreover, another consequence of the current study is that the inlet profiles needs to be in equilibrium with the k - ε equations. Otherwise, the inlet profiles are going to tend towards an undesirable equilibrium condition.

CS1		CS2	
Boundary ID	Boundary Conditions	Boundary ID	Boundary Conditions
inlet	R&H profiles	inlet	Zhang profiles
outlet	inletOutlet	outlet	inletOutlet
side1	empty (2D)	side1	empty (2D)
side2	empty (2D)	side2	empty (2D)
ground	wall-function	ground	wall-function
top	symmetry	top	momentum sources

CS3	
Boundary ID	Boundary Conditions
inlet	R&H profiles
outlet	inletOutlet
side1	empty (2D)
side2	empty (2D)
ground	wall-function
top	fixedGradient or momentum sources

Table 2.3: Irvine study cases and the scheme of the related boundary conditions

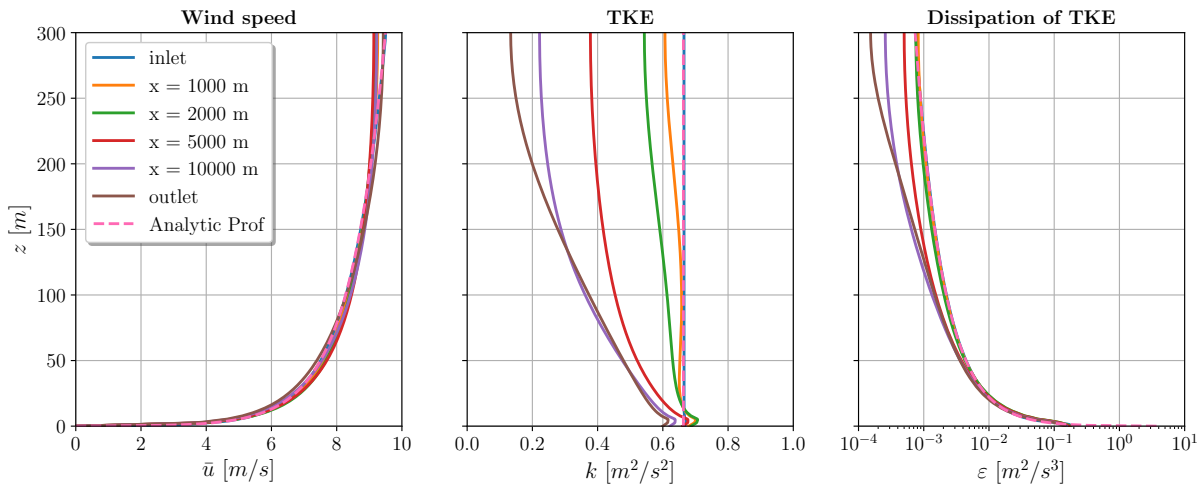


Figure 2.5: CS1 case profiles computed using OpenFOAM.

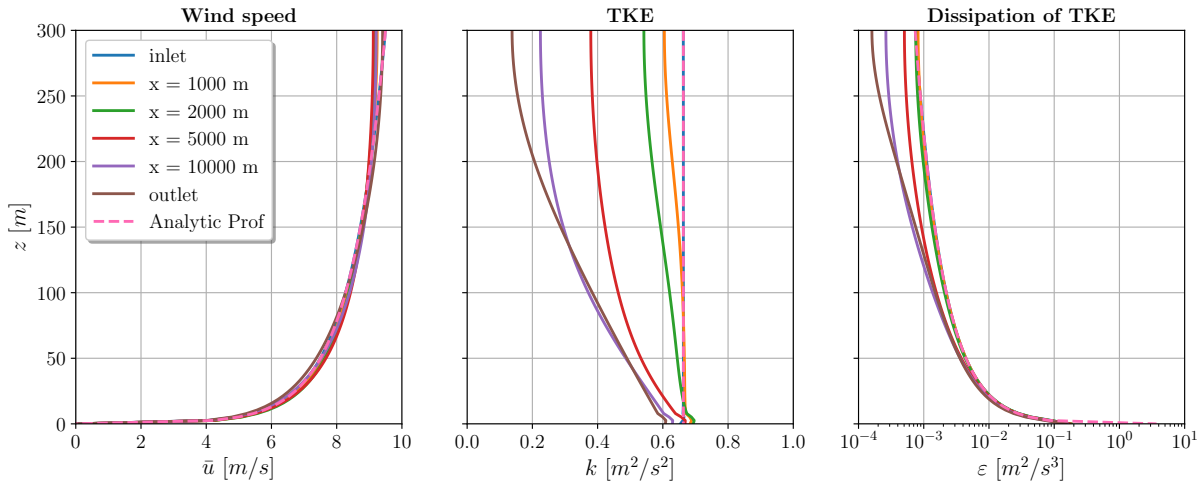


Figure 2.6: CS1 case profiles computed using Fluent.

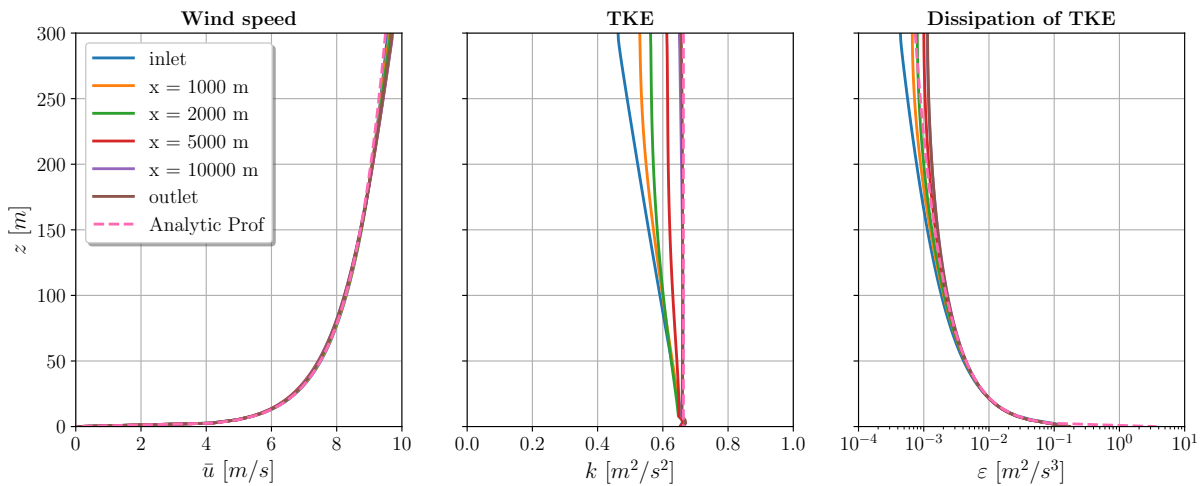


Figure 2.7: CS2 case profiles computed using Fluent.

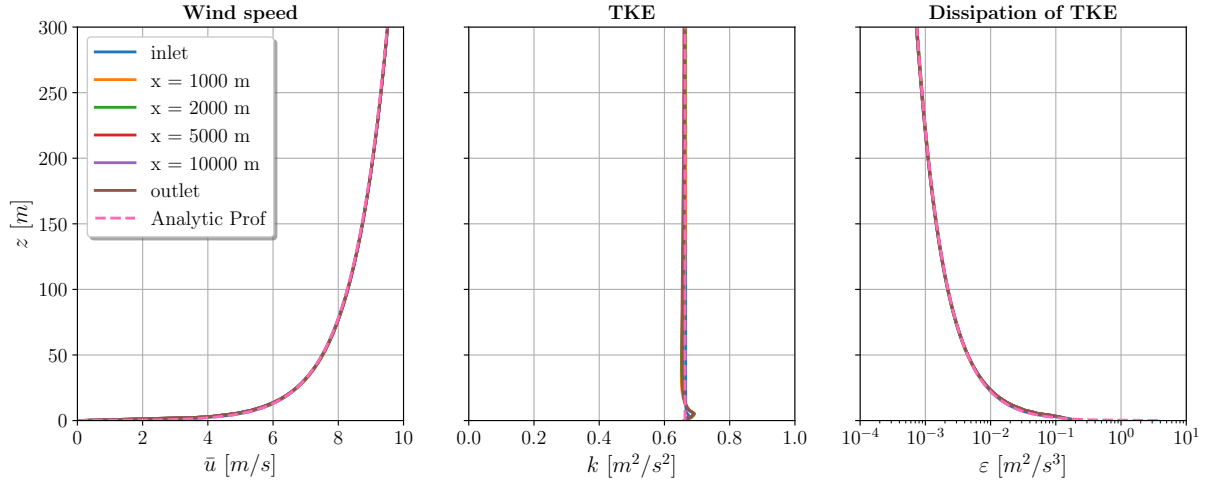


Figure 2.8: CS3 case profiles computed using OpenFOAM.

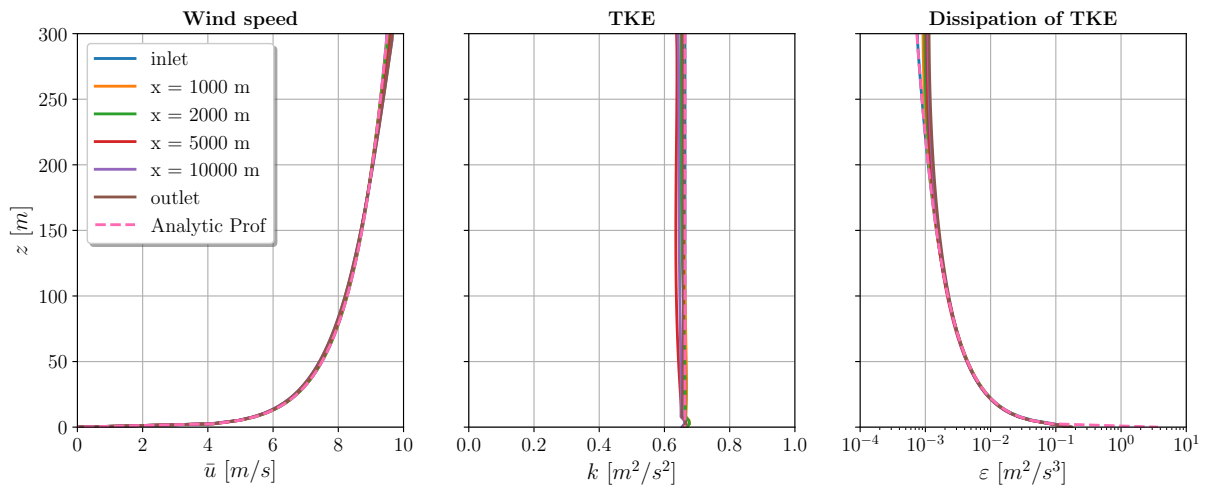


Figure 2.9: CS3 case profiles computed using Fluent.

2.2.2 Blocken case

After the study of the top boundary condition and the comparison between the two CFD codes, the current study case wants to analyse the influence of the wall-function type on the equilibrium with the turbulence model using OpenFOAM. For this reason, two important cases of the literature are taken into consideration. In the current subsection, the [Blocken *et al.* \(2007\)](#) research is investigated, while in the following subsection the [Hargreaves and Wright \(2007\)](#) research is considered.

Here the aim is to simulate the same SBL of the reference case, focusing on the wall-function performance. In particular, the [Figure 2.11](#) illustrates the expected results if any specific modification of the wall-function is considered and respecting the set of 4 requirements distilled from various sources, e.g. CFD literature and CFD software manuals at the time of the [Blocken *et al.* \(2007\)](#) article. Therefore we want to demonstrate that our boundary conditions, in particular the wall-function, allow to generate a horizontally homogeneous atmospheric flow without any modification to the source codes (already implemented).

The set of requirements, previously cited, are:

1. A sufficiently high mesh resolution in the vertical direction close to the bottom of the computational domain.
2. A horizontally homogeneous ABL in the downstream and upstream region of the domain.
3. A distance z_p from the centre point P of the wall-adjacent cell to the wall (bottom of domain) that is larger than the physical roughness height K_s of the terrain ($z_p > K_s$).

As already seen, it seems that, although the 4 requirements are respected, the [Blocken *et al.* \(2007\)](#) results are not satisfactory. The authors suggest that the main reason is due to the use of a wall model of the K_s -type family. Today, this family seems to be no more present in the CFD codes or be capable to perform as well as z_0 -type family. Conversely, as we will show here, the z_0 -type family is diffused and its results have better performance because more adapted to atmospheric flows. It is not in our interest to delve into the details of the distinction between z_0 -type and K_s -type families but, for more details about this family, please consult [Blocken *et al.* \(2007\)](#).

The CFD simulation of the SBL flow was performed in a 2D empty computational domain. The original simulation was conducted with Fluent 6.1.22, while the current study uses OpenFOAM v1812. The dimensions of the 2D domain are shown in [Figure 2.10](#) and are the same of the reference case. A structured mesh was used and its characterised are illustrated in the same figure. In this case, the total number of cell is 46 000. An aspect ratio of $R_z = 15$ is present in the z direction. Therefore, the size of the fist cell adjacent to the wall is $\Delta z_{\min} = 2.08$ m.

The neutral SBL characteristics are pointed out by the [Table 2.4](#). The inlet profiles (i.e. the R&H profiles) are characterised thanks to $z_0 = 0.1$ m and $u_* = 0.869$ m/s. Whereas, the boundary conditions are resumed schematically in [Table 2.5](#). So, at the bottom of the domain, a standard OpenFOAM rough wall-function (i.e. `nutkRoughWallFunction`) is used, with $K_s = 1.959$ m and with the default roughness constant $C_s = 0.50$. Here, Eq. [\(A.2\)](#) is the empirical equation that governs the relation between z_0 and K_s . This wall function is a z_0 -type wall function. On the other hand, the original case applies a K_s -type wall function. The latter is

z_0	0.1 m	Aerodynamic roughness
\bar{u}_{ref}	18.5 m/s	Wind reference velocity
z_{ref}	500 m	Reference height
u_*	0.869 m/s	Friction velocity

Table 2.4: SBL characteristics.

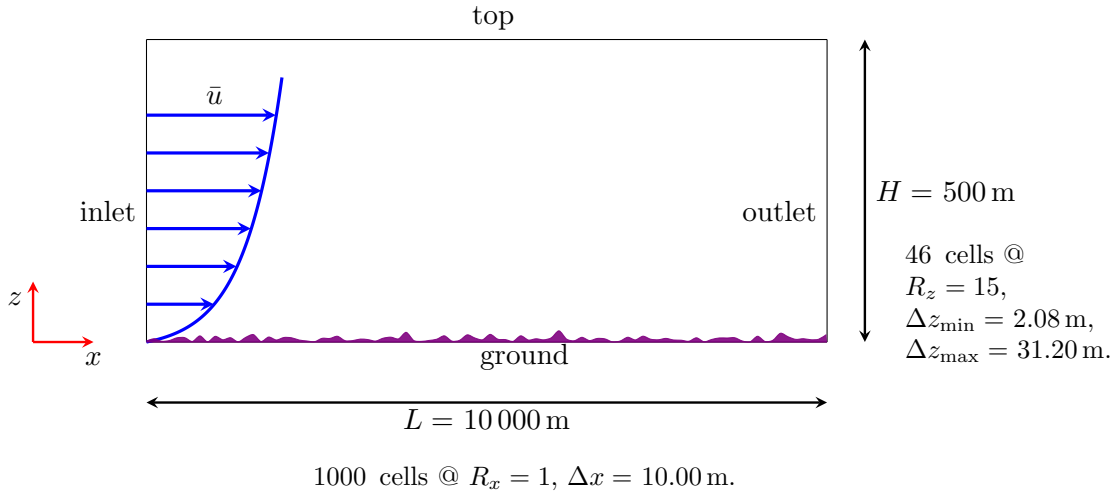


Figure 2.10: 2D domain for the Blocken case.

the only wall function available on Ansys Fluent 6.2 and it is more commonly used for flows over sand-grain roughened surfaces. Following the [Richards and Hoxey \(1993\)](#) indications, the current article takes particular attention to the top boundary conditions. Therefore, the values of \bar{u} , k and ε are imposed along the top boundary and they are: $\bar{u} = 18.5$ m/s, $k = 2.77$ m²/s² and $\varepsilon = 0.0036$ m²/s³. This is done by fixing these constant values in the top layer of cells in the domain. Differently from this approach of the article, we have chosen to use a fixed gradient in the top patch of the domain:

$$\left. \frac{\partial \bar{u}}{\partial z} \right|_{z=500 \text{ m}} = \frac{u_*}{\kappa} \frac{1}{z + z_0} \Big|_{z=500 \text{ m}} = 4.34 \times 10^{-3} \text{ m/s}^2 \quad (2.60)$$

$$\left. \frac{\partial \varepsilon}{\partial z} \right|_{z=500 \text{ m}} = - \frac{u_*^3}{\kappa} \frac{1}{(z + z_0)^2} \Big|_{z=500 \text{ m}} = -6.55 \times 10^{-6} \text{ m/s}^3 \quad (2.61)$$

where these expressions were derived from Eq. (2.38) and Eq. (2.40).

These kind of approaches have demonstrated better performance than symmetry or slip wall boundary condition, as already shown in [subsection 2.2.1](#). It is important to highlight that the u_* is slightly different with respect to [Blocken *et al.* \(2007\)](#) because the value proposed by the articles was not consistent with the values of the profiles at the top boundary. Nevertheless, the u_* proposed here respects the consistency with the profiles analysed.

The results of [Blocken *et al.* \(2007\)](#) are illustrated in [Figure 2.11](#). The profiles are not conserved along the domain, though the set of 4 requirements are respected. The main problem is identified on the type of wall-function implemented on the CFD code. The z_0 -type is suggested as the most appropriated, following the study of [Richards and Hoxey \(1993\)](#). Nevertheless, at the

Boundary ID	Boundary Conditions
inlet	R&H profiles
outlet	inletOutlet
side1	empty (2D)
side2	empty (2D)
ground	wall-function
top	fixedGradient

Table 2.5: Scheme of the boundary conditions for the Blocken case.

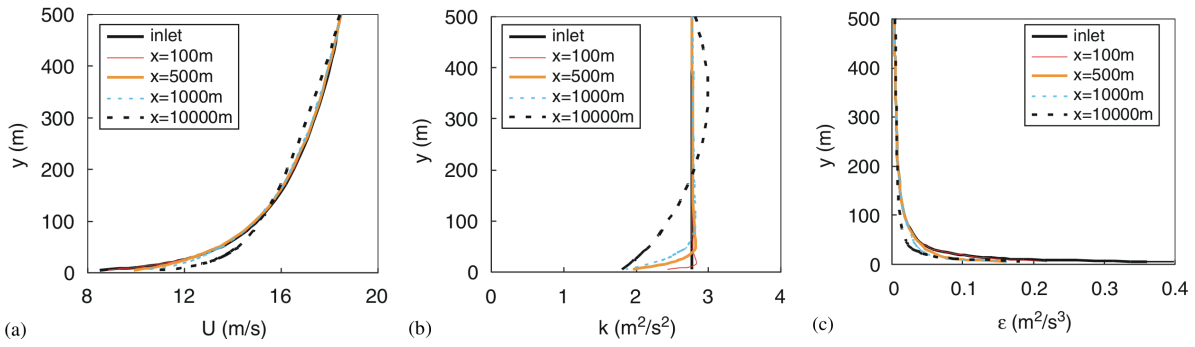


Figure 2.11: Blocken *et al.* (2007) results

time of the article, many existing CFD codes such type of wall-function are neither implemented nor the user always implement them easily.

Figure 2.12 shows the results of our approach. The vertical profiles of \bar{u} , k and ε are conserved along the domain. All the cited requirements are respected except the last one. Nevertheless, the condition $z_p > K_s$ only avoids having numerical results, which lack of physical meaning, but does not affect the performance of the methodology, as observed from the results.

In this way, it is possible to affirm that the z_0 -type wall-functions are more appropriated to reproduce horizontal homogeneity of the atmospheric flow. Furthermore, the Ansys Fluent results of the Irvine case are similar to the OpenFOAM results. It proves that today this kind of wall-function is more diffused or that today there is not distinction between the two families.

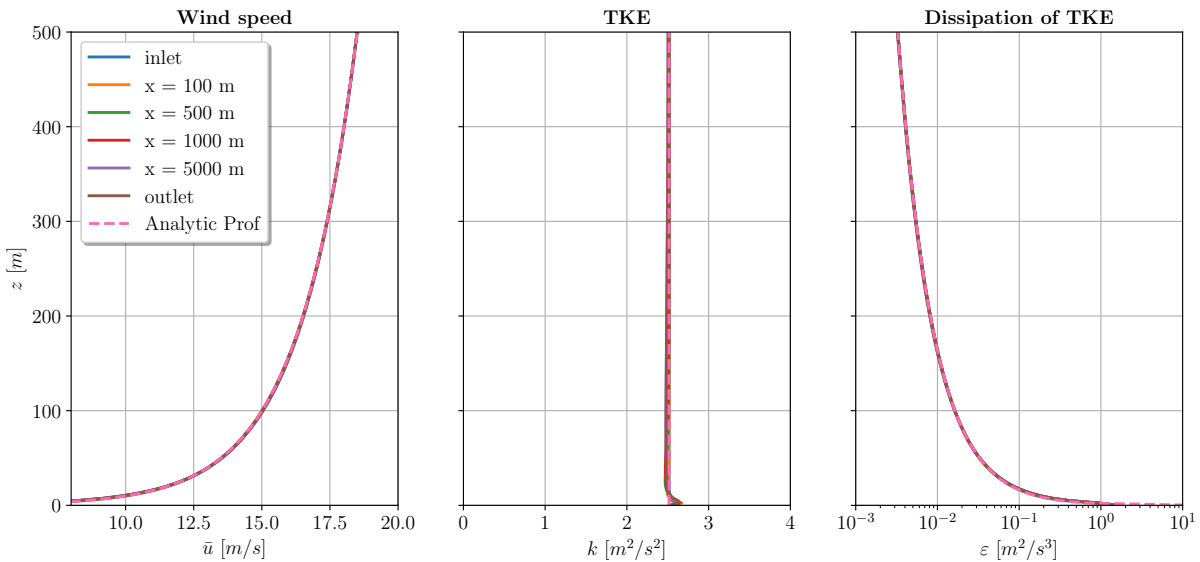


Figure 2.12: Blocken case simulation computed using OpenFOAM.

2.2.3 Hargreaves and Wright case

Roughly contemporary with the [Blocken *et al.* \(2007\)](#) case, the current study case is based on the research work of [Hargreaves and Wright \(2007\)](#). The latter pointed out that the neutral ABL can be maintained along an atmospheric domain only with a modified law of the wall and with a shear stress applied to the top boundary of the domain.

In this case, our work is focused on reproducing the [Hargreaves and Wright \(2007\)](#) results with OpenFOAM v1812 and evaluates the current validity of the authors' suggestions. It was also used the oldest version of OpenFOAM that we managed to get, i.e. OpenFOAM v2.3.1. The use of the previous version is addressed to compare the results of two different versions of OpenFOAM. Then, the results of the article of reference is reproduced using the Ansys Fluent approach of Irvine case ([subsection 2.2.1](#)). Finally, the development of a SBL over a surface, which presents a central smooth region, is shown in order to test our approach with OpenFOAM v1812.

The first domain used is illustrated in [Figure 2.13](#), as well as the characteristics of the hexahedral mesh. The length of the domain is sufficiently long to allow any inlet effects to dissipate and to ensure a developed atmospheric flow. An expansion ratio $R_z = 36$ was chosen for the vertical grid. It means that the height of the cell adjacent to the wall is $\Delta z_{min} = 1.00$ m, while the height of the the cell adjacent to the top patch is $\Delta z_{max} = 36.00$ m.

The second domain employed is presented in [Figure 2.14](#). It is possible to identify 3 zones: an inlet rough zone of 1.5 km, a smooth intermediate zone of 1.0 km and an again a rough outlet zone of 2.5 km. The mesh characteristics are the same of the first domain. The only difference is related to the type of wall surfaces at the ground patch.

For both domains, the wind profiles used are taken from the blind-test exercise mentioned by [Richards *et al.* \(2002\)](#) and its characteristics are summarised in [Table 2.6](#). Therefore, the inlet profiles (i.e. the R&H profiles) are characterised thanks to $z_0 = 0.01$ m and $u_* = 0.65$ m/s. The boundary conditions are schematically presented in [Table 2.7](#). In the original article, the surface roughness is incorporated through a wall-function approach that is based on boundary layer theory for the computational cell immediately adjacent to the wall. On the other hand, the wall-function used here is the `nutkRoughWallFunction` available in OpenFOAM v1812. The reference article uses a symmetric boundary condition at the top patch, while the current study employs a fixed gradient in agreement with our approach. The gradients applied are: $\partial\bar{u}/\partial z = 3.18 \times 10^{-3}$ m/s² and $\partial\varepsilon/\partial z = -2.53 \times 10^{-6}$ m/s³. They are computed thanks to [Eq. \(2.60\)](#) and [Eq. \(2.61\)](#). The effect of the choice made by the authors of the article is less evident in the results because it was chosen to show only profiles between 0 and 50 times z_{ref} , i.e. 300 m.

z_0	0.01 m	Aerodynamic roughness
\bar{u}_{ref}	10.00 m/s	Wind reference velocity
z_{ref}	6.00 m	Reference height
u_*	0.65 m/s	Friction velocity

Table 2.6: Neutral SBL characteristics.

[Hargreaves and Wright \(2007\)](#) affirm that [Figure 2.15](#) represent the typical plot produced by computational wind engineers when showing that their simulation of the ABL is satisfactory. The three profiles are simulated by Ansys Fluent 6.1 and are plotted up to a height of 50 z_{ref} and at distances of 2500 m and 4000 m along the streamwise direction. At first sight, the development of the velocity and dissipation rate profiles seems encouraging. However, the abrupt loss of the turbulent kinetic energy profile points out the problem. Moreover, a zoom close to the ground highlight better the inaccuracies in maintaining \bar{u} and ε profiles, e.g. the velocity in the cell next to the ground decreased from 6 m/s to 5 m/s. The article illustrates similar results also employing CFX 5.7.

Boundary ID	Boundary Conditions
inlet	R&H profiles
outlet	inletOutlet
side1	empty (2D)
side2	empty (2D)
ground	wall-function
top	fixedGradient or momentum sources

Table 2.7: Scheme of the boundary conditions for the Blocken case.

Figure 2.16 and Figure 2.17 show the results of our approach. The only difference between them is the boundary condition used in the ground patch. The first uses the standard rough wall-function implemented in OpenFOAM : *nutkRoughWallFunction*. Here the relation between z_0 and K_s is governed by the empirical equation: Eq. (A.2). Whereas the second adopts a wall-function inspired to the work of Richards and Hoxey (1993) and Hargreaves and Wright (2007): *nutkAtmRoughWallFunction*. For this wall-function, z_0 is used directly. In both cases, the profiles are conserved along the domain. This is a sign that a horizontal homogeneous atmospheric flow has finally developed. Some slight difference is found near the wall due to the peak of the turbulent kinetic energy. The OpenFOAM v2.3.1, published on December 2014, present the same results of previous simulations, see Figure 2.18. It demonstrates that the standard rough wall-function was correctly implemented since 2014. Then, the Figure 2.19 illustrate the same results but testing the Ansys Fluent 18.2. It further proves that today commercial codes also exhibit good behaviour in generating horizontally homogeneous SBL flows.

Finally, the evolution of the SBL profiles over a simple complex terrain is presented. The central surface is smooth. Therefore, in this region, the profiles diverge from the R&H profiles. Nevertheless, when the flow comes back to the rough region, it return to the desired equilibrium condition for the rough region. It proves the consistency of our approach.

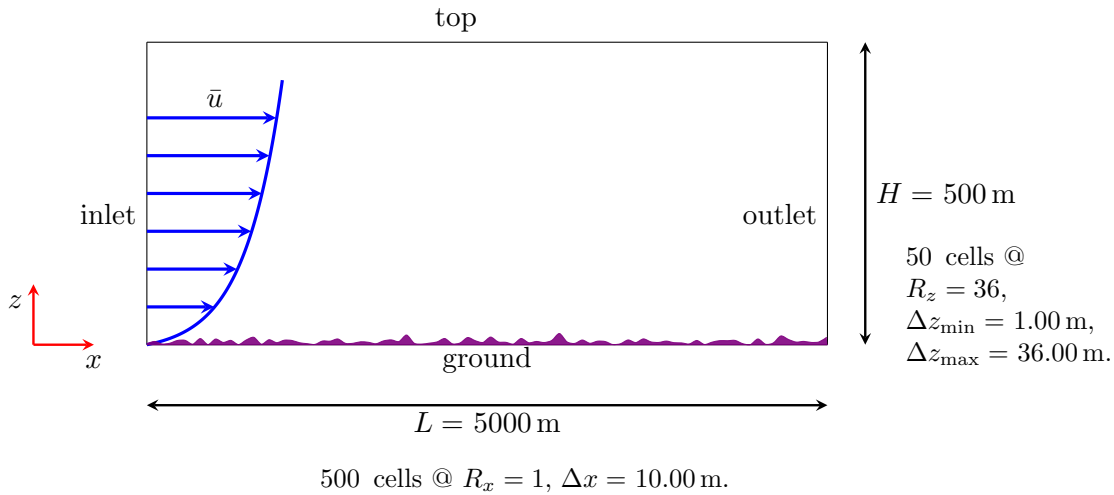


Figure 2.13: First 2D domain for the Hargreaves case.

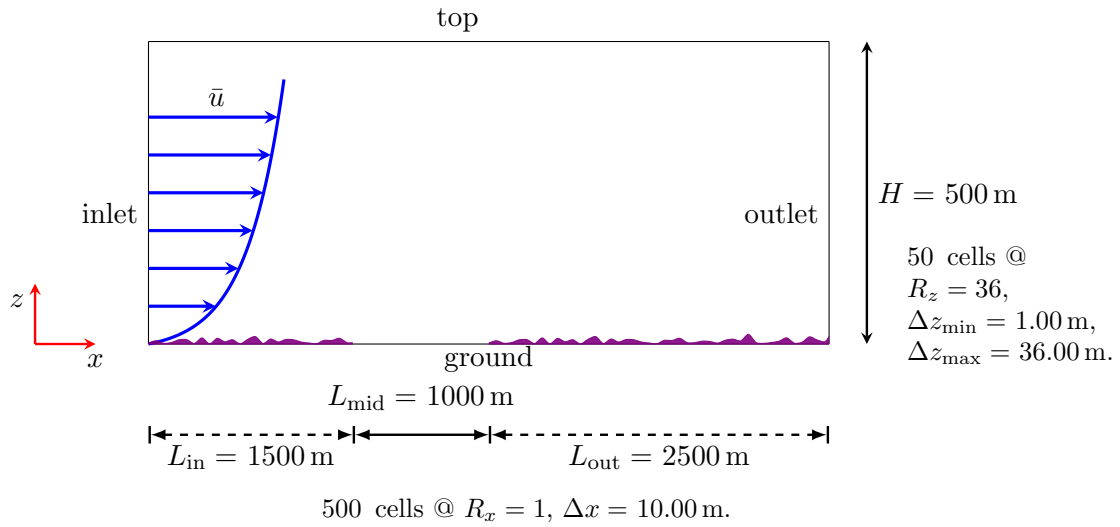


Figure 2.14: Second 2D domain for the Hargreaves case.

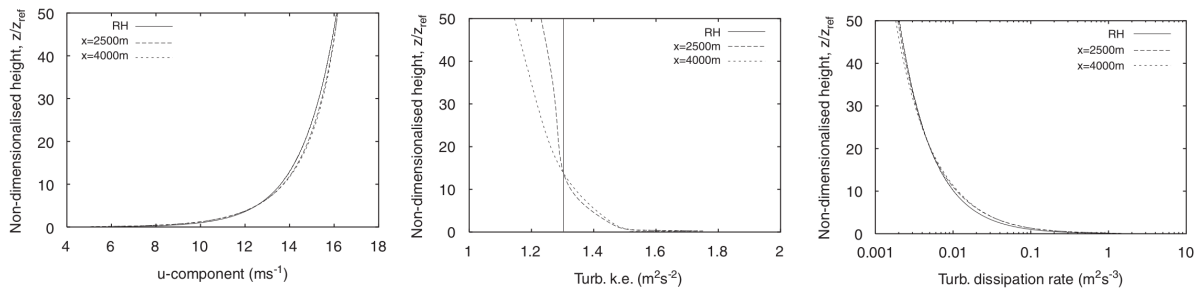


Figure 2.15: From right to left, plots of \bar{u} , turbulent kinetic energy k and turbulent dissipation rate ϵ for the Fluent simulation. From: (Hargreaves and Wright, 2007).

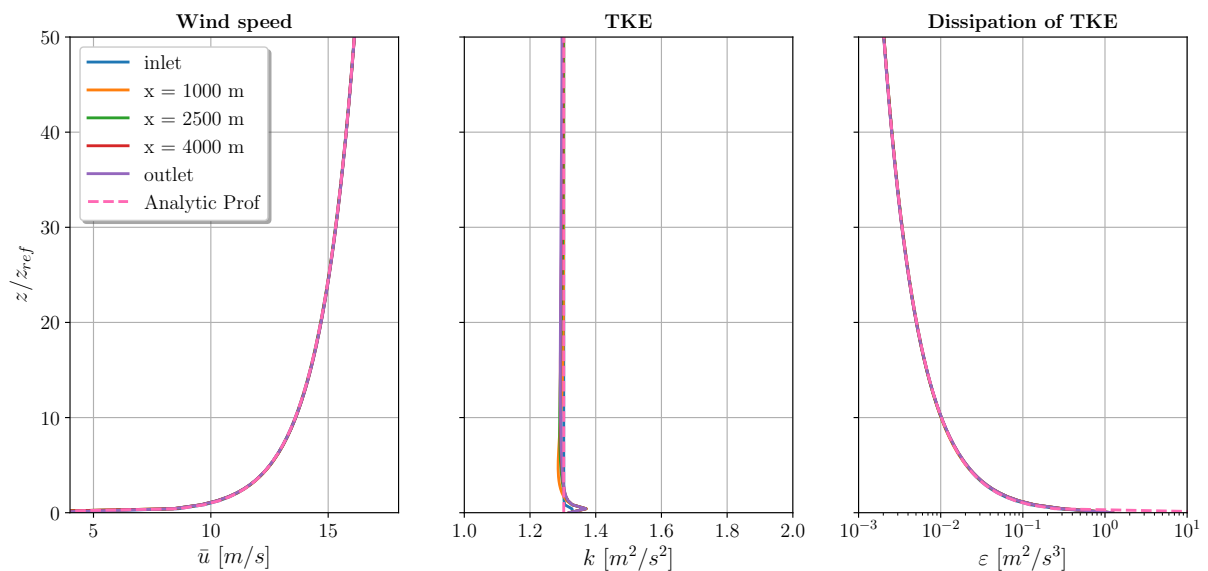


Figure 2.16: Evolution of velocity, turbulent kinetic energy and dissipation of turbulent kinetic energy profiles along 2D domain of 5 km and with z_{ref} of 6 m. Overall setting: Hargreaves and Wright (2007). The intermediate profiles are at 1 km, 2.5 km and 4 km. The ground wall-function uses a standard roughness model (*nutkRoughWallFunction*), available in OpenFOAM v1812.

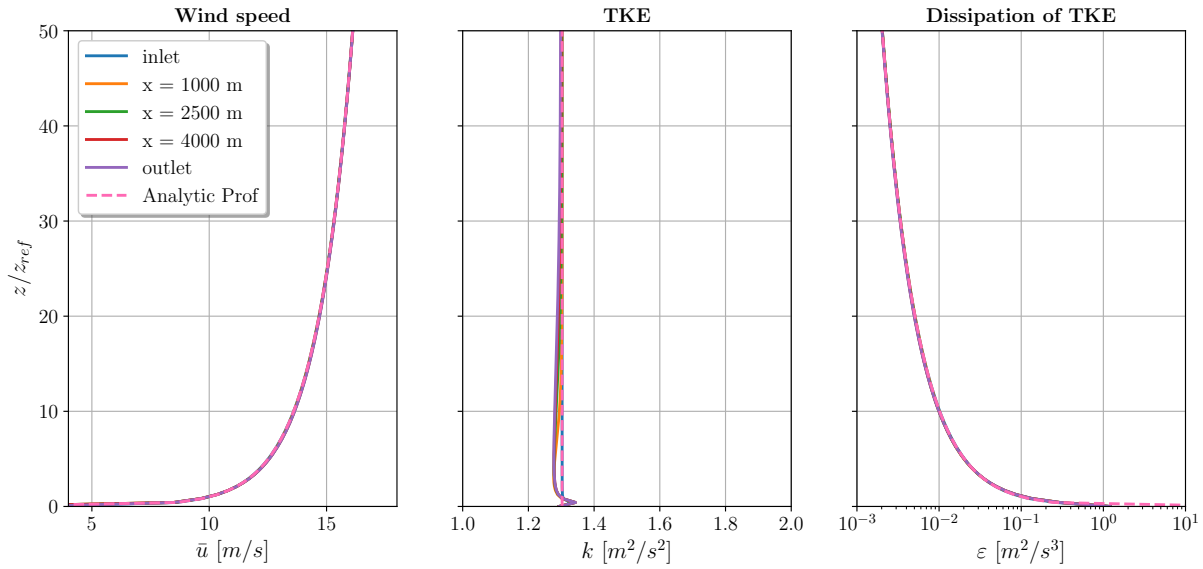


Figure 2.17: Evolution of velocity, turbulent kinetic energy and dissipation of turbulent kinetic energy profiles along 2D domain of 5 km and with z_{ref} of 6 m. The ground wall-function uses the correction suggested by [Hargreaves and Wright \(2007\)](#). In OpenFOAM v1812: *nutkAtm-RoughWallFunction*.

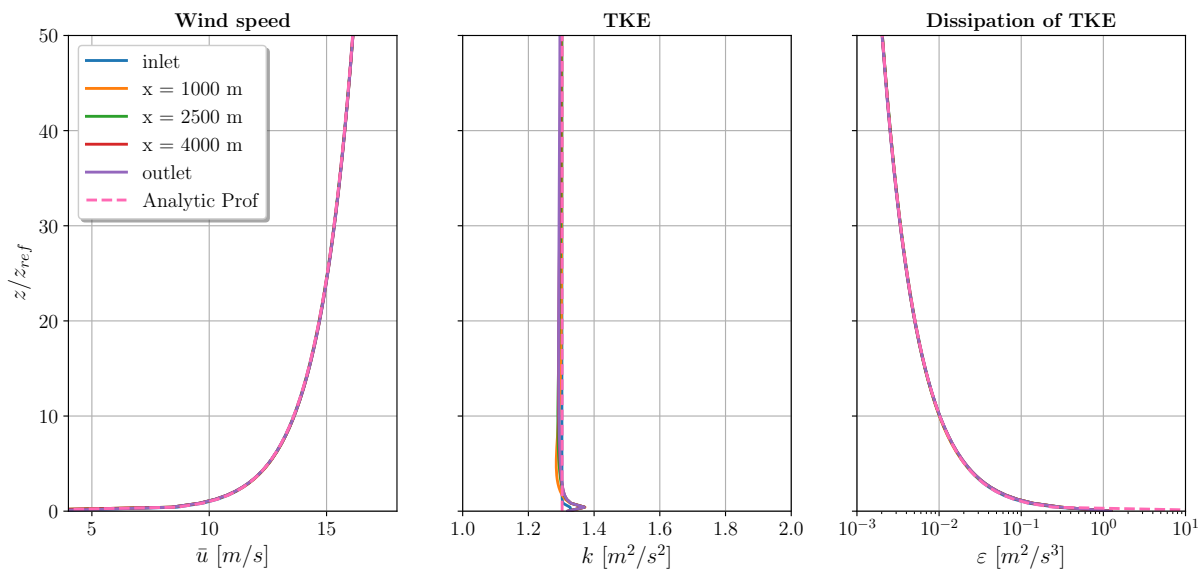


Figure 2.18: Evolution of velocity, turbulent kinetic energy and dissipation of turbulent kinetic energy profiles along 2D domain of 5 km and with z_{ref} of 6 m. Overall setting: [Hargreaves and Wright \(2007\)](#). The intermediate profiles are at 1 km, 2.5 km and 4 km. The ground wall-function uses a standard roughness model (*nutkRoughWallFunction*), available also in OpenFOAM v2.3.1.

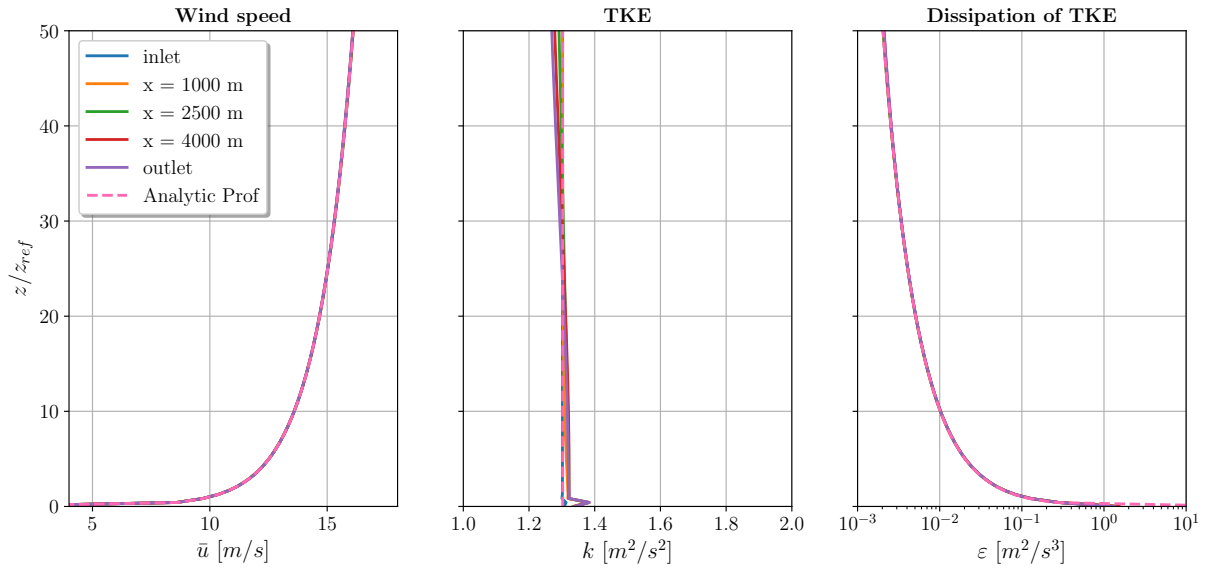


Figure 2.19: Evolution of velocity, turbulent kinetic energy and dissipation of turbulent kinetic energy profiles along 2D domain of 5 km and with z_{ref} of 6 m. The ground wall-function uses the standard rough wall-function in Ansys Fluent 18.2.

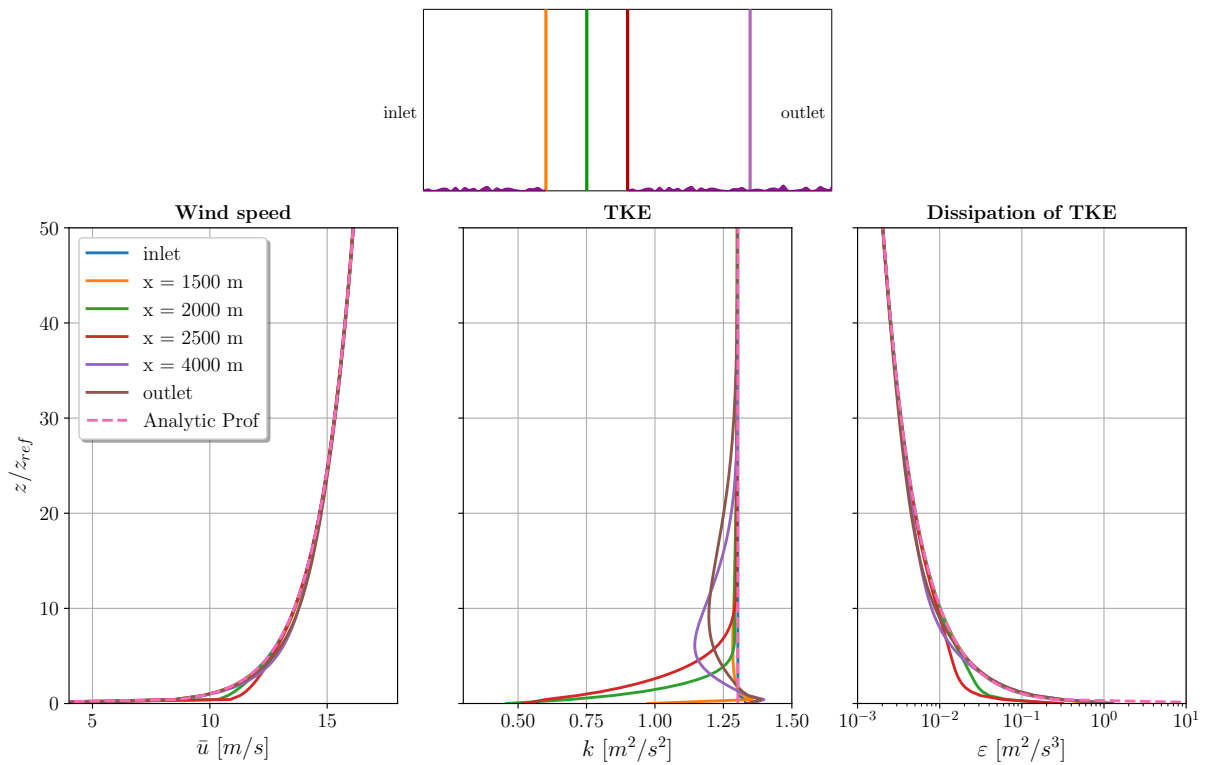


Figure 2.20: Evolution of velocity, turbulent kinetic energy and dissipation of turbulent kinetic energy profiles along 2D domain of 5 km with a central smooth region and two rough regions. OpenFOAM v1812 simulation.

2.3 Conclusions

The current CFD codes, commercial or open-source, are able to conserve the horizontal homogeneity of the SBL along the whole domain. At least since 2014 this capacity is valid and no ad-hoc modification to the wall-function is needed. It is only required to respect the equilibrium between the turbulence model and the boundary conditions employed. Whereas, the inlet profiles needs to be in equilibrium with the turbulence model. The top boundary condition needs to help the flow not to decay. Therefore, a top band which imposes the values at the cell adjacent to the top or a fixed gradient applied to the top patch are two valid alternatives.

Moreover, it seems that nowadays there is not really a distinction between K_s -type and z_0 -type wall models. Both of them shows similar performances. It is also important to remember that the cell-center adjacent to the wall z_p could be inferior than K_s . Numerically, this is not a problem as long as z_p is not positioned in the viscous sublayer. The result will not change but computational resources are wasted by refining unnecessarily. So it is recommended to have z_p in the logarithmic region ([subsection 1.1.4](#)).

Finally, the different case studies have allowed to test the OpenFOAM performance and to accumulate enough knowledge to continue the research using only this open-source code. Most of the results of this section were brought to the HARMO19 conference, ([Mejia Estrada *et al.*, 2019](#)).

Chapter 3

Development of a Large-Eddy Simulation Methodology for the Dispersion in the Neutral Surface Boundary Layer

3.1 Overview of a LES simulation approach for the dispersion in the neutral SBL

The simulation of turbulent flows by numerical resolution of Navier-Stokes equations requires the solution of a wide range of time and length scales, all of which affect the flow field. This is done precisely with DNS but it is extremely expensive. From the point of view of the computational cost, LES models are placed between RANS and DNS. Nowadays, LES could be viewed as a reference method to simulate the atmospheric flow and dispersion, especially when it is desired to have high-order moments or compare numerical results with optical measurements (e.g. from multispectral cameras, LIDAR, etc). The latter is the case of our research.

The LES model is based on the separation of turbulent scales in a flow. It introduces an arbitrary scale and models the smaller scales, while the bigger scales are computed. This consideration is supported by Kolmogorov who establishes that, at sufficiently high Reynolds number, the statistics of the small scale motions have a universal form for different flows ([Kolmogorov, 1941](#)). On the other hand, the large scales are not universal and are flow dependent.

The choice of the arbitrary scale has to primarily satisfy some physical criteria, as we will see in the next sections. Therefore, LES could benefit from finer meshes as long as it meets the appropriate criteria dictated by the physics and modelling of the specific flow. In the contrary, a consistent refinement of RANS mesh may bring no further improvements.

There exist 4 conceptual steps in LES:

1. **Decomposition.** It is done thanks to filter, which decompose the velocity $\mathbf{u}(\mathbf{x}, t)$ into the sum of a filtered component and a residual component. The filtered velocity field represents the motion of the large eddies.
2. **Write the equations to solve.** The equation for the evolution of the filtered velocity field derives from the Navier-Stokes equations.
3. **SGS tensor.** Modelling of the residual stress tensor or subgrid stress (SGS) tensor, which arises from the residual motions and make the problem unclosed.
4. **Numerical resolution.** The model filtered equations are solved numerically for the filtered velocity field, given an approximation of the large scale motions.

We consider that two ways of approaching are available. The first consists to deal with modelling issues (steps 1, 2 and 3) and numerical solution (step 4) through an iterative approach, following some similar researches on literature and a trial and error method. Differently, the second approach is based on the development of some physical and modelling criteria that allow to correctly settle the modelling issues and get a desired numerical solution. Our methodology embraces the second approach, but some iterations following the first approach were useful to define the criteria.

Similarly to the RANS overview presented in [section 2.1](#), at first the LES is presented in a general way and little by little we focus on the useful concepts to simulate a neutral SBL and the dispersion of a passive scalar. After the concise presentation of the filtering operation ([subsection 3.1.1](#)), the LES conservation equations are illustrated and discussed in [subsection 3.1.2](#). Then the closure problem together with the SGS models are treated in [section 3.1.2](#). Subsequently, the boundary conditions that require special attention are analysed in [subsection 3.1.6](#) and the rough wall modelling is deepened in [subsection 3.1.8](#). Finally, the filtered transport equation of the passive scalar is presented together with modelling closure in [subsection 3.1.13](#).

All these concepts are fundamental to develop the LES methodology of the current research.

3.1.1 LES filtering

The concept of scale separation is mathematically accomplished through a scale high-pass filter, i.e. low-pass filter in frequency, applied to the exact solution ([Sagaut, 2006](#)). In this way, the LES could resolve the filtered velocity field $\tilde{\mathbf{u}}(\mathbf{x}, t)$ with a relative coarse computational mesh with respect to a DNS resolution. It is convenient to set the filter width as somewhat smaller than the length l_{EI} , which represents the size of the smallest energy-containing motions. Moreover, l_{EI} could be considered as the demarcation between the anisotropic large eddies ($l > l_{EI}$) and the isotropic small eddies ($l < l_{EI}$). Thus, it represents the confine between the energy-containing range ($l > l_{EI}$) and the inertial subrange, which together with the dissipation range are part of the universal equilibrium range ($l < l_{EI}$) ([Pope, 2000c](#)).

Consequently, the grid/cell size is conditioned by the constraint according to which the energy-containing motions need to be resolved. The LES purpose is to reduce the computational cost by neglecting the smallest scales, which have a universal form ([Kolmogorov, 1941](#)) and are more appropriated to be modelled. In this way, the velocity field is decomposed into a filtered field $\tilde{\mathbf{u}}$ and a residual field \mathbf{u}' :

$$u_i = \tilde{u}_i + u'_i \quad (3.1)$$

The similarity between the current decomposition and the Reynolds one is evident. Nevertheless, it is important to highlight that \tilde{u}_i is a random field and that in general the Reynolds average of the filtered residuals are not zero:

$$\overline{\mathbf{u}'}(\mathbf{x}, t) \neq 0$$

Returning to filtering, the general filtering operation, introduced by [Leonard \(1975\)](#), is mathematically represented in physical space as a convolution product. It is illustrated in Eq. [\(3.2\)](#).

$$\tilde{\mathbf{u}}(\mathbf{x}, t) = \iiint G(\mathbf{r}, \mathbf{x}) \mathbf{u}(\mathbf{x} - \mathbf{r}, t) d\mathbf{r} \quad (3.2)$$

Here G is the filter function and the integration is over the entire flow domain. There exists different kinds of filters. In [Table 3.1](#) are listed some of them.

Name	Filter function	Transfer function
General	$G(r)$	$\hat{G} = \int_{-\infty}^{\infty} e^{i\kappa r} G(r) dr$
Box	$\frac{1}{\Delta} H(\frac{1}{2}\Delta - r)$	$\frac{\sin(\frac{1}{2}\kappa\Delta)}{\frac{1}{2}\kappa\Delta}$
Gaussian	$(\frac{6}{\pi\Delta^2})^{\frac{1}{2}} \exp\left(-\frac{6r^2}{\Delta^2}\right)$	$\exp\left(-\frac{\kappa^2\Delta^2}{24}\right)$
Sharp spectral	$\frac{\sin(\frac{\pi r}{\Delta})}{\pi r}$	$H(\kappa_c - \kappa),$ $\kappa_c \equiv \pi/\Delta$
Cauchy	$\frac{a}{\pi\Delta[(r/\Delta)^2+a^2]}, a = \frac{\pi}{24}$	$\exp(-a\Delta \kappa)$
Pao		$\exp\left(-\frac{\pi^{2/3}}{24}(\Delta \kappa)^{4/3}\right)$

Table 3.1: Filter functions and transfer functions, (Pope, 2000c)

OpenFOAM filtering

In order to understand the practical filtering operation in OpenFOAM, the main aspects are presented below. The work of Mukha *et al.* (2018) is taken as reference.

Firstly, it is important to highlight that the method used to solve the governing equations is the finite volume method. The latter represents the unknowns at the cell centres. Whereas the average value of the respective quantities across the volume of the cells are approximated with second-order accuracy. Therefore, for a cell with volume V_c and center point \mathbf{x}_p , the cell-centred velocity value $\tilde{\mathbf{u}}(\mathbf{x}_p, t)$ is approximated by:

$$\frac{1}{V_c} \iiint_{V_c} \mathbf{u}(\mathbf{r}, t) d\mathbf{r} \quad (3.3)$$

It is important to highlight that the latter equation is exactly the right-hand-side of Eq. (3.2) for the filter kernel $G(\mathbf{r}, \mathbf{x}_p) = H_c(\mathbf{r})/V_c$, where H_c is the Heaviside function corresponding to the cell. This reflects the natural relation between the LES filtering and the finite volume framework. It means that each cell filters directly the unknowns. In this case, it is not possible to dissociate the filter size from the mesh size.

3.1.2 LES conservation equations

The conservation equations governing the filtered velocity field $\tilde{\mathbf{u}}(x, t)$ are obtained by applying the filtering operation to the Navier-Stokes equations. We consider spatially uniform filters, so that filtering and differentiation commute. For an unsteady flow of incompressible Newtonian fluid, the general LES equations are described below.

Mass conservation

The filtered continuity equation is:

$$\left(\widetilde{\frac{\partial u_i}{\partial x_i}}\right) = \frac{\partial \tilde{u}_i}{\partial x_i} = 0 \quad (3.4)$$

From which we obtain the residual part:

$$\frac{\partial u'_i}{\partial x_i} = \frac{\partial}{\partial x_i}(u_i - \tilde{u}_i) = 0 \quad (3.5)$$

Both the filtered field $\tilde{\mathbf{u}}$ and the residual field \mathbf{u}' are solenoidal.

Conservation of momentum

The filtered momentum equation is reported in Eq. (3.6).

$$\frac{\partial \tilde{u}_j}{\partial t} + \frac{\partial \tilde{u}_i \tilde{u}_j}{\partial x_i} = \nu \frac{\partial^2 \tilde{u}_j}{\partial x_i \partial x_i} - \frac{1}{\rho} \frac{\partial \tilde{p}}{\partial x_j} \quad (3.6)$$

Here $\tilde{p}(x, t)$ is the filtered pressure field. This equation differs from the Navier-Stokes equations because the filtered product $\tilde{u}_i \tilde{u}_j$ is different than the product of the filtered velocities $\tilde{u}_i \tilde{u}_j$. The main difference is the residual-stress tensor defined in Eq. (3.7).

$$\tau_{ij}^R \equiv \overline{\tilde{u}_i \tilde{u}_j} - \tilde{u}_i \tilde{u}_j \quad (3.7)$$

The latter is analogous to the Reynolds-stress tensor:

$$\overline{u'_i u'_j} = \overline{u_i u_j} - \bar{u}_i \bar{u}_j \quad (3.8)$$

It is important to remark that respectively the stress tensor are $-\rho \tau_{ij}^R$ and $-\rho \overline{u'_i u'_j}$. The residual kinetic energy is:

$$k_r \equiv \frac{1}{2} \tau_{ii}^R \quad (3.9)$$

where “ \equiv ” is the symbol used to define a value. Whereas, the anisotropic residual-stress tensor is defined by:

$$\tau_{ij}^r \equiv \tau_{ij}^R - \frac{2}{3} k_r \delta_{ij} \quad (3.10)$$

The isotropic residual stress is included in the modified filtered pressure:

$$\tilde{P} \equiv \tilde{p} + \frac{2}{3} \rho k_r \quad (3.11)$$

With these definitions, it is possible to rewrite the filtered momentum equation and add a forcing term F_j (e.g. gravity or other atmospheric force) in accordance with section 1.1.3:

$$\frac{\partial \tilde{u}_j}{\partial t} + \tilde{u}_i \frac{\partial \tilde{u}_j}{\partial x_i} = \nu \frac{\partial^2 \tilde{u}_j}{\partial x_i \partial x_i} - \frac{\partial \tau_{ij}^r}{\partial x_i} - \frac{1}{\rho} \frac{\partial \tilde{P}}{\partial x_j} + F_j \quad (3.12)$$

or:

$$\frac{\tilde{D} \tilde{\mathbf{u}}}{\tilde{D} t} = \nabla \cdot (\nu \nabla \tilde{\mathbf{u}} - \tau^r) - \frac{1}{\rho} \nabla \tilde{P} + \mathbf{F} \quad (3.13)$$

As for the RANS case, the divergence of the momentum equation yields a Poisson equation for the modified pressure \tilde{P} .

In the same way as for Reynolds equations, the filtered equations for $\tilde{\mathbf{u}}$ (Eq. (3.4) and Eq. (3.12)) are unclosed. Closure is achieved by modelling the residual (or SGS) stress tensor τ_{ij}^r .

It is important to highlight that the filtered equations are quite different than the Reynolds equations. The fields which play an important role, i.e. $\tilde{u}_i(x_i, t)$, $\tilde{P}(x_i, t)$ and $\tau_{ij}^r(x_i, t)$, are three-dimensional and unsteady, even if the flow is statistically stationary or homogeneous. Also the stress tensor to be modelled depends on the specification of the type and width of the filter.

With $\tau_{ij}^r(x, t)$ be given by a residual-stress model, Eq. (3.4) and Eq. (3.12) can be solved to determine $\tilde{u}_i(x_i, t)$ and $\tilde{P}(x_i, t)$. The filtered velocity field depends on the type of filter and the filter width Δ . Nevertheless these quantities do not appear directly in the equations, they appear only indirectly through the model for $\tau_{ij}^r(x, t)$.

Conservation of energy

Although not used directly in this study but for the sake of completeness, we also present energy conservation. An important issue is related to the transfer of kinetic energy between the filtered velocity field and the residual motions. The filtered kinetic energy $\tilde{E}(\mathbf{x}, t)$ is obtained by filtering the kinetic-energy field $E(\mathbf{x}, t) = \frac{1}{2} \mathbf{u} \cdot \mathbf{u}$. Consequently:

$$\tilde{E} = \frac{1}{2} \widetilde{\mathbf{u} \cdot \mathbf{u}} \quad (3.14)$$

The filtered kinetic energy could be decomposed:

$$\tilde{E} = E_f + k_r \quad (3.15)$$

where the kinetic energy of the filtered velocity field is:

$$E_f = \frac{1}{2} \tilde{\mathbf{u}} \cdot \tilde{\mathbf{u}} \quad (3.16)$$

and the residual kinetic energy is:

$$k_r = \frac{1}{2} \widetilde{\mathbf{u} \cdot \mathbf{u}} - \frac{1}{2} \tilde{\mathbf{u}} \cdot \tilde{\mathbf{u}} = \frac{1}{2} \tau_{ii}^R \quad (3.17)$$

The conservation equation of E_f is obtained by multiplying Eq. (3.12) by \tilde{u}_j . The result is shown in Eq. (3.18).

$$\frac{\tilde{D}E_f}{\tilde{D}t} - \frac{\partial}{\partial x_i} \left[\tilde{u}_j \left(2\nu \tilde{S}_{ij} - \tau_{ij}^r - \frac{\tilde{P}}{\rho} \delta_{ij} \right) \right] = -\varepsilon_f - \mathcal{P}_r \quad (3.18)$$

where ε_f and \mathcal{P}_r are respectively:

$$\varepsilon_f \equiv 2\nu \tilde{S}_{ij} \tilde{S}_{ij} \quad (3.19)$$

$$\mathcal{P}_r \equiv -\tau_{ij}^r \tilde{S}_{ij} \quad (3.20)$$

The terms of the left-hand side of Eq. (3.18) illustrate transport. Nevertheless, the sink and source terms of right-hand side are more interesting. The sink term ε_f represents viscous dissipation from filtered velocity field. For a high Reynolds number flow with a filter width much larger than the Kolmogorov scale, this term is small.

The final term is the production of residual kinetic energy \mathcal{P}_r . The term is a sink ($-\mathcal{P}_r$) in the equation for E_f and a source ($+\mathcal{P}_r$) in the equation for k_r . Therefore, it represents the rate of transfer of energy from the filtered motions to the residual motions. Sometimes \mathcal{P}_r is called the SGS dissipation and denoted by ε_s . Nevertheless, it is not correct because \mathcal{P}_r is due to inviscid, inertial processes, and it can be negative.

At a high Reynolds number and with the filter in the inertial subrange, the filtered velocity field accounts for nearly all of the kinetic energy. It means:

$$\widetilde{\tilde{E}} \approx \overline{E}$$

The dominant sink in the equation for $\widetilde{\tilde{E}}$ is $\overline{\mathcal{P}_r}$, while in the equation for \overline{E} is the rate of dissipation of kinetic energy ε . Consequently, under these circumstances, these two quantities are nearly equal:

$$\overline{\mathcal{P}_r} \approx \varepsilon$$

An equivalent view of this result is that, in the equation of mean kinetic energy $\overline{k_r}$, there is a close balance between production $\overline{\mathcal{P}_r}$ and dissipation ε , (Lilly, 1967).

While, in the mean, energy is transferred from the large scales $\overline{\mathcal{P}_r} > 0$, locally a back-scatter is possible, i.e. transfer of energy from the residual motions to the filtered velocity field, $\mathcal{P}_r < 0$.

Closure problem and SGS models

A model for the anisotropic residual stress tensor τ_{ij}^r is needed in order to overcome the closure problem.

The simplest model is the Smagorinsky subgrid-scale (SGS) model. This model was developed by Joseph Smagorinsky in the meteorological community in the 1960s, (Smagorinsky, 1963). It represents the basis for several of more advanced models. In this subsection, the latter model is firstly treated as well as its drawbacks, its behaviour in the inertial subrange and its implementation in OpenFOAM. Then, the subgrid kinetic energy model is presented. Finally, the Wall Adapting Local Eddy-Viscosity (WALE) model is illustrated.

3.1.3 Smagorinsky model

The Smagorinsky model can be analysed in two parts:

1. The current subgrid scale model is based on the eddy-viscosity assumption to model the residual stress tensor or SGS shear stress:

$$\tau_{ij}^r = -2\nu_{\text{sgs}} \tilde{S}_{ij}$$

where

$$\tilde{S}_{ij} = \frac{1}{2} \left(\frac{\partial \tilde{u}_i}{\partial x_j} + \frac{\partial \tilde{u}_j}{\partial x_i} \right)$$

is the deformation tensor of the resolved field or resolved-scale strain rate tensor. This model postulates a linear relationship between the SGS shear stress and the resolved-scale strain rate tensor. The coefficient of proportionality $\nu_{\text{sgs}}(\mathbf{x}, t)$ is the eddy-viscosity of the residual motions or the SGS eddy-viscosity.

2. By analogy to the mixing-length hypothesis the eddy-viscosity is modelled as:

$$\nu_{\text{sgs}} = l_s^2 \tilde{\mathcal{S}} = (C_s \Delta)^2 \tilde{\mathcal{S}} \quad (3.21)$$

where $\tilde{\mathcal{S}} = (2 \tilde{S}_{ij} \tilde{S}_{ij})^{1/2}$ is the characteristic filtered rate of strain and l_s is the Smagorinsky length scale, analogous to the mixing length scale. The latter, thanks to the Smagorinsky coefficient C_s , is proportional to the filter width Δ . So the eddy-viscosity is assumed to be proportional to the subgrid characteristic length scale Δ and to a characteristic turbulent velocity represented by the local strain rate $\tilde{\mathcal{S}}$.

According to the eddy-viscosity model, the rate of energy transfer of the residual motions is:

$$\mathcal{P}_r = -\tau_{ij}^r \tilde{S}_{ij} = 2\nu_{\text{sgs}} \tilde{S}_{ij} \tilde{S}_{ij} = \nu_{\text{sgs}} \tilde{\mathcal{S}}^2 \quad (3.22)$$

For the Smagorinsky model (or for any other eddy-viscosity model with $\nu_{\text{sgs}} > 0$), this energy transfer is everywhere from the filtered motions to the residual motions. There is no back-scatter.

Conforming to Lilly (1992), the constant C_s may be computed by assuming that the cut-off wave-number $k_c = \pi/\Delta$ lies within the $k^{-5/3}$ range and requiring that the ensemble-averaged subgrid dissipation is identical to ε . An approximated value of the constant is given by:

$$C_s = \frac{1}{\pi} \left(\frac{3C_K}{2} \right)^{-3/4} \quad (3.23)$$

For a Kolmogorov constant $C_K \simeq 1.55$, it results $C_s \simeq 0.17$.

Smagorinsky drawbacks

The Smagorinsky disadvantages presented here have been reported in the works of [Nicoud and Ducros \(1999\)](#) and [Pope \(2000c\)](#). It is in our interest to underline the drawbacks which could affect the purposes of the thesis. Thus, the current analysis is focused on:

- the transfer of energy between subgrid-scales and dissipation region,
- filter being in the dissipation range,
- near wall behaviour, and
- complex geometries.

Firstly, the transfer of energy from the resolved scales to the subgrid ones is governed by the SGS eddy-viscosity ν_{sgs} . The latter is mainly determined by the filtered rate of strain \tilde{S} (i.e. $\tilde{S} = (2\tilde{S}_{ij}\tilde{S}_{ij})^{1/2}$). Nevertheless, the numerical experiment of [Wray and Hunt \(1989\)](#) shows that the Smagorinsky model is not able to reproduce the dissipation activity when eddies are present in the flow. The reason is that these regions are dominated by vorticity and not by irrotational strain. Therefore, a better SGS model needs to consider both \tilde{S} and the rotational rate.

Secondly, if the filter is placed in the far dissipation range (i.e. the filter width is very small), the Smagorinsky coefficient C_s could adopt a lower or higher value with respect to the inertial subrange value of $C_s \approx 0.17$. The mean rate of transfer of energy to the residual scales need to be balanced by C_s with respect to the approximation used in the dissipation range. This aspect point out the poor description of the residual stresses at fine level. Therefore, it is important to pay attention to the correct setting of C_s when the filter is not situated in the inertial subrange. The Smagorinsky coefficient cannot be fixed independently from the filter width.

Then, the near wall behaviour of eddy-viscosity represents another limit of the current model. The SGS viscosity ν_{sgs} is not zero as soon as the velocity gradient exists. Whereas, as explained in [subsection 1.1.4](#), the Reynolds stresses should go to zero. A possible solution to this problem was proposed by [Driest \(1956\)](#) through an exponential damping function. However, the use of this function is limited to simple geometries and sometimes requires smaller value for Smagorinsky constant ([Moin and Kim, 1982](#)). Furthermore, another disadvantage of the damping function is that it produces $\nu_{\text{sgs}} = O(z^2)$ and not $\nu_{\text{sgs}} = O(z^3)$, as it should be expected.

Finally, it is discussed the necessity to deal with complex geometries without direction of flow homogeneity and/or unstructured numerical methods. In this case, it does not represent a limit for the Smagorinsky model. The computation of the eddy-viscosity only involves local gradients. Thus, models similar to the Smagorinsky one are preferable to our purposes. It is important to highlight that all models do not present this characteristic. A clear example is represented by the models in Fourier space which have good filtering performances for simple geometries but not for complex ones.

Behaviour in the inertial subrange

The Smagorinsky model applied to high-Re turbulence is commonly used setting the filter width Δ in the inertial subrange (i.e. $l_{DI} < \Delta < l_{EI}$), as illustrated in [subsection 3.1.1](#). It contributes to a precise definition of the Smagorinsky coefficient C_s and confirm that length scale l_s scales with Δ . In this case, there exist a balance between the mean transfer of energy to residual motions $\overline{\mathcal{P}_r}$ and the dissipation ε . It is shown by the relation:

$$\varepsilon = \overline{\mathcal{P}_r} = \overline{\nu_{\text{sgs}} \tilde{\mathcal{S}}^2} = l_s^2 \overline{\tilde{\mathcal{S}}^3}$$

The development of this expression led Lilly (1967) to formulate the expression of C_s (Eq. (3.23)) and to suggest $C_s \simeq 0.17$. Moreover, ν_{sgs} and τ_{ij}^r can be scaled thanks to Δ . For more details, consult Pope (2000a).

Implementation in OpenFOAM

The Smagorinsky SGS model is one of the best known models. The following implementation was deduced through the information from the OpenFOAM v1812 code source and the help of the OpenFOAM community.

Beginning from the definition of the subgrid scale stress tensor or residual-stress tensor, τ_{ij}^R or here simply τ_{ij} .

$$\begin{aligned} \tau_{ij} &= \widetilde{u_i u_j} - \widetilde{u_i} \widetilde{u_j} \\ &= \frac{1}{3} \tau_{kk} \delta_{ij} + \left(\tau_{ij} - \frac{1}{3} \tau_{kk} \delta_{ij} \right) \\ &= \frac{1}{3} \tau_{kk} \delta_{ij} + \tau_{ij}^r \\ &\approx \frac{1}{3} \tau_{kk} \delta_{ij} - 2 \nu_{\text{sgs}} \widetilde{D}_{ij} \\ &= \frac{2}{3} k_{\text{sgs}} \delta_{ij} - 2 \nu_{\text{sgs}} \widetilde{D}_{ij} \end{aligned} \tag{3.24}$$

where ν_{sgs} is the SGS eddy viscosity and the deviatoric stress \widetilde{D}_{ij} is defined as:

$$\widetilde{D}_{ij} = \widetilde{S}_{ij} - \frac{1}{3} \delta_{ij} \widetilde{S}_{kk}$$

To remind, the resolved-scale strain rate tensor \widetilde{S}_{ij} is:

$$\widetilde{S}_{ij} = \frac{1}{2} \left(\frac{\partial \widetilde{u}_i}{\partial x_j} + \frac{\partial \widetilde{u}_j}{\partial x_i} \right)$$

and the SGS kinetic energy k_{sgs} (or k_r) is:

$$k_{\text{sgs}} = \frac{1}{2} \tau_{kk} = \frac{1}{2} (\widetilde{u_k u_k} - \widetilde{u_k} \widetilde{u_k})$$

The subgrid scale stress tensor τ_{ij} is divided into an isotropic part $\frac{1}{3} \tau_{kk} \delta_{ij}$ and an anisotropic part $\tau_{ij} - \frac{1}{3} \tau_{kk} \delta_{ij}$ in Eq. (3.24). The term \widetilde{D}_{ij} is used because the anisotropic part is a trace-less tensor.

Therefore, in OpenFOAM the subgrid scale viscosity is computed as:

$$\nu_{\text{sgs}} = C_k \Delta \sqrt{k_{\text{sgs}}} \tag{3.25}$$

where C_k is a model constant whose default value is 0.094 and Δ is the cell size that defines the subgrid length scale.

It remains to evaluate the subgrid scale kinematic energy k_{sgs} . It is computed thanks to the assumption of the balance between the subgrid scale energy production and dissipation:

$$\widetilde{S}_{ij} \tau_{ij} + C_\varepsilon \frac{k_{\text{sgs}}^{1.5}}{\Delta} = 0$$

It could be solved as shown below:

$$\begin{aligned}
\tilde{S}_{ij} \left(\frac{2}{3} k_{\text{sgs}} \delta_{ij} - 2 \nu_{\text{sgs}} \tilde{D}_{ij} \right) + C_\varepsilon \frac{k_{\text{sgs}}^{1.5}}{\Delta} &= 0 \\
\tilde{S}_{ij} \left(\frac{2}{3} k_{\text{sgs}} \delta_{ij} - 2 C_k \Delta \sqrt{k_{\text{sgs}}} \tilde{D}_{ij} \right) + C_\varepsilon \frac{k_{\text{sgs}}^{1.5}}{\Delta} &= 0 \\
\sqrt{k_{\text{sgs}}} \left(\frac{C_\varepsilon}{\Delta} k_{\text{sgs}} + \frac{2}{3} \tilde{S}_{ii} \sqrt{k_{\text{sgs}}} - 2 C_k \Delta \tilde{S}_{ij} \tilde{D}_{ij} \right) &= 0 \\
a k_{\text{sgs}} + b \sqrt{k_{\text{sgs}}} - c &= 0
\end{aligned} \tag{3.26}$$

It results:

$$k_{\text{sgs}} = \left(\frac{-b + \sqrt{b^2 + 4ac}}{2a} \right)^2 \tag{3.27}$$

where:

$$\begin{cases} a = \frac{C_\varepsilon}{\Delta} \\ b = \frac{2}{3} \tilde{S}_{ii} \\ c = 2 C_k \Delta \tilde{S}_{ij} \tilde{D}_{ij} \end{cases} \tag{3.28}$$

In the case of incompressible flow, Eq. (3.28) reduces to:

$$\begin{cases} b = \frac{2}{3} \tilde{S}_{ii} = 0 \\ c = 2 C_k \Delta \tilde{S}_{ij} \tilde{D}_{ij} = C_k \Delta |\tilde{\mathcal{S}}|^2 \end{cases} \tag{3.29}$$

where:

$$|\tilde{\mathcal{S}}| = \sqrt{2 \tilde{S}_{ij} \tilde{S}_{ij}}$$

Substituting in Eq. (3.27), it yields to:

$$k_{\text{sgs}} = \frac{c}{a} = \frac{C_k \Delta^2 |\tilde{\mathcal{S}}|^2}{C_\varepsilon} \tag{3.30}$$

Finally, it is possible to obtain the final expression of the SGS eddy viscosity in the case of incompressible flow:

$$\nu_{\text{sgs}} = C_k \sqrt{\frac{C_k}{C_\varepsilon}} \Delta^2 |\tilde{\mathcal{S}}| \tag{3.31}$$

Comparing it with Eq. (3.21), the following relation for the Smagorinsky constant C_s is obtained:

$$C_s^2 = C_k \sqrt{\frac{C_k}{C_\varepsilon}} \tag{3.32}$$

The default values of C_k and C_ε in OpenFOAM are respectively 0.094 and 1.048, which yields to $C_s \simeq 0.17$ in agreement with Lilly (1967).

3.1.4 Subgrid Kinetic Energy model

This one equation model was developed independently by many authors: [Horiuti \(1985\)](#), [Schumann \(1975\)](#), [Yoshizawa \(1982\)](#) and others. The subgrid viscosity is calculated from the kinetic energy of the subgrid scales ([Sagaut, 2006](#)), as shown in Eq. (3.33).

$$\nu_{\text{sgs}}(x, t) = C_m \Delta \sqrt{k_{\text{sgs}}^2(\mathbf{x}, t)} \quad (3.33)$$

Here k_{sgs}^2 (or k_r^2) is:

$$k_{\text{sgs}}^2(\mathbf{x}, t) = \left(\frac{1}{2} \widetilde{\mathbf{u}} \cdot \widetilde{\mathbf{u}} - \frac{1}{2} \widetilde{\mathbf{u}} \cdot \widetilde{\mathbf{u}} \right)^2$$

and C_m is computed from the relation:

$$\nu_{\text{sgs}} = \sqrt{\frac{2}{3}} \frac{A}{\pi K_0^{3/2}} \Delta \sqrt{k_{\text{sgs}}^2}$$

The subgrid kinetic energy constitutes another variable in the problem. It is an unknown and its evolution equation is used to compute it. This equation is obtained from the exact evolution equation Eq. (2.19), whose unknown terms are modeled following Lilly's suggestions ([Lilly, 1967](#)), or by re-normalisation method. The various terms are modelled as explain below:

- A gradient hypothesis is used to model the diffusion term. It is stated that the non-linear term is proportional to the kinetic energy k_{sgs}^2 gradient (Kolmogorov-Prandtl relation):

$$\frac{\partial}{\partial x_j} \left(\frac{1}{2} \widetilde{u'_i u'_j u'_j} + \frac{\widetilde{u'_i p'}}{\rho} \right) = C_2 \frac{\partial}{\partial x_j} \left(\Delta \sqrt{k_{\text{sgs}}^2} \frac{\partial k_{\text{sgs}}^2}{\partial x_j} \right)$$

- The dissipation term is modeled using dimensional analysis, by:

$$\varepsilon = \frac{\nu}{2} \frac{\partial \widetilde{u'_i}}{\partial x_j} \frac{\partial \widetilde{u'_i}}{\partial x_j} = C_1 \frac{(k_{\text{sgs}}^2)^{3/2}}{\Delta}$$

The resulting evolution equation is presented in Eq. (3.34).

$$\frac{\partial k_{\text{sgs}}^2}{\partial t} + \frac{\partial \widetilde{u}_j k_{\text{sgs}}^2}{\partial x_j} = -\tau_{ij}^r \widetilde{S}_{ij} - C_1 \frac{(k_{\text{sgs}}^2)^{3/2}}{\Delta} + C_2 \frac{\partial}{\partial x_j} \left(\Delta \sqrt{k_{\text{sgs}}^2} \frac{\partial k_{\text{sgs}}^2}{\partial x_j} \right) + \nu_{\text{sgs}} \frac{\partial^2 k_{\text{sgs}}^2}{\partial x_j \partial x_j} \quad (3.34)$$

The second left term is the advective one, while in the right side the terms are respectively the production of turbulent kinetic energy by resolved modes \mathcal{P}_r (Eq. (3.22)), turbulent dissipation, turbulent diffusion and viscous dissipation. Thanks to an analytical theory of turbulence, [Yoshizawa \(1982\)](#) and [Horiuti \(1985\)](#) proposed $C_1 = 1$ and $C_2 = 0.1$.

3.1.5 WALE model

The Wall Adapting Local Eddy-Viscosity (WALE) model was developed by [Nicoud and Ducros \(1999\)](#) in order to compensate for the drawbacks of the Smagorinsky model and obtain a model adapted to treat wall bounded flows and complex geometries.

The generic form of the SGS eddy-viscosity, expressed in Eq. (3.35), can summarise the previous models presented so far.

$$\nu_{\text{sgs}} = C_m \Delta^2 \overline{OP}(x_i, t) \quad (3.35)$$

Here C_m is the constant of the model, Δ is the subgrid characteristic length scale (i.e. for us the size of the mesh) and \overline{OP} is an operator of space and time, homogeneous to a frequency, and defined from the resolved fields.

The operator \overline{OP} is defined as the ratio of two operators, i.e. \overline{OP}_1 and \overline{OP}_2 . This operator assures two constraints. Firstly, \overline{OP} is a function of the strain and rotation rates. Secondly, its value should go to zero at the wall behaving like $O(z^3)$ (more details in [section A.2](#)). Consequently, the final SGS eddy-viscosity expression proposed by [Nicoud and Ducros \(1999\)](#) is:

$$\nu_{\text{sgs}} = (C_w \Delta)^2 \frac{\overline{OP}_1}{\overline{OP}_2} = (C_w \Delta)^2 \frac{(\mathcal{S}_{ij}^d \mathcal{S}_{ij}^d)^{3/2}}{(\tilde{S}_{ij} \tilde{S}_{ij})^{5/2} + (\mathcal{S}_{ij}^d \mathcal{S}_{ij}^d)^{5/4}} \quad (3.36)$$

where C_w is a constant. From a practical point of view, the determination of this constant is important to correctly set up the model. The authors suggest to assume that the WALE model gives the same ensemble-average ($\langle \rangle$) subgrid kinetic energy dissipation as the classical Smagorinsky model. Therefore, C_w can be expressed as:

$$C_w^2 = C_s^2 \frac{\langle \sqrt{2} (\tilde{S}_{ij} \tilde{S}_{ij})^{\frac{3}{2}} \rangle}{\langle \tilde{S}_{ij} \tilde{S}_{ij} \frac{\overline{OP}_1}{\overline{OP}_2} \rangle} \quad (3.37)$$

The value of C_w could be estimated numerically employing several fields of homogeneous isotropic turbulence or other experiments. [Nicoud and Ducros \(1999\)](#) states that a value of C_w in the range $0.550 \leq C_w \leq 0.600$ is appropriate for $C_s = 0.180$ according to six different turbulent fields obtained from LES simulations. Nevertheless, the authors highlight that more accurate estimations are possible. In fact, OpenFOAM developers have estimated this value equal to $C_w = 0.325$. Moreover, thanks to a trial-and-error approach, it was estimated that a value of $C_w = 0.495$ is more appropriated for our simulations.

3.1.6 Overview of the boundary conditions

As already mentioned, the boundary conditions (BCs) represent a challenge in simulating atmospheric flows. In fact, the performance of the simulation depends in a consistent way on the choice of the boundary conditions that best represent the reality at the boundaries of the computational domain.

We have treated the BCs for the RANS approach in the [subsection 2.1.8](#), while the case studies of [section 2.2](#) showed us how to deal with them in practice. In the latter approach, the critical BCs are the inlet, ground and top BCs. Conversely, for the LES, only the inlet and ground BCs require particular attention. In fact, top BC could be fixed as a slip condition because the forcing of the flow is commonly imposed through a pressure gradient. This approach is widely accepted and widespread among the scientific community as the literature can confirm ([Xie et al., 2004b](#)). Following the works of the literature (e.g. [Vasaturo et al. \(2018\)](#)), the lateral boundary conditions of the domain are usually periodic and this approach is adopted. Instead, the outlet boundary condition depends on the inlet. If the inlet is periodic, the outlet needs to be periodic. Nevertheless, when the inlet boundary condition fixes a velocity profile, the outlet

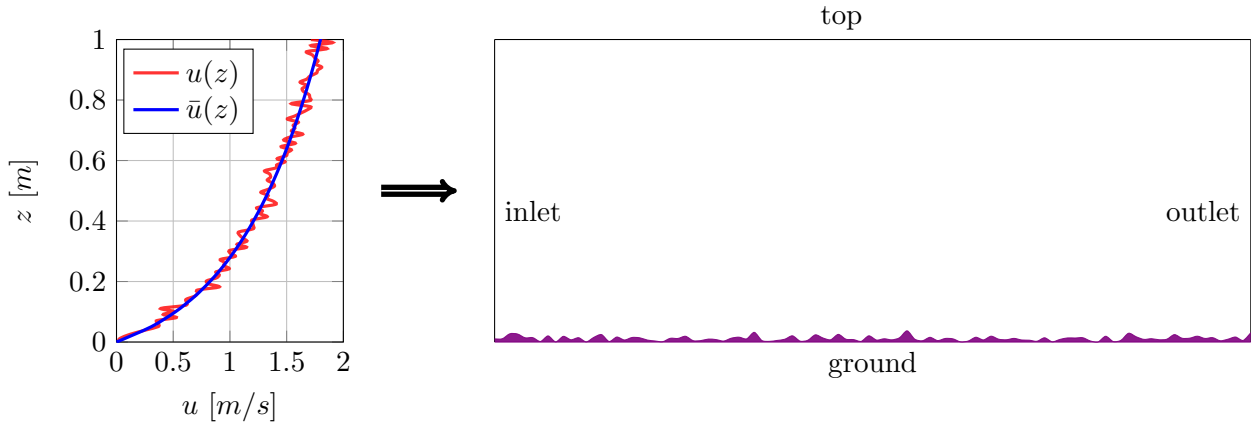


Figure 3.1: Inlet boundary condition sketch.

boundary condition needs to fix the pressure (usually equal to zero) and guarantees the flow exit from the domain, avoiding backward flow.

In [subsection 3.1.7](#), the inlet BC will be treated. Whereas the requested inlet BC for the RANS case is a profile of the mean computed variables (e.g. \bar{u}_i , k and ε), the LES simulation needs an instantaneous field profile of the main variables. We can try to understand this concept thanks to [Figure 3.1](#), which shows the mean and the instantaneous velocity profile respectively $\bar{u}(z)$ and $u(z)$. As a first approximation, one could think of decomposing the instantaneous velocity at the inlet boundary as the sum of a mean velocity and a kind of fluctuation to be characterised. As we shall see, this principle will be used by some profile generator methods. On the other hand, another option is to develop the instantaneous fields from a stationary initial condition. These two methods present advantages and disadvantages.

Similarly, the wall modelling technique is not the same as for the RANS approach. Although the logarithmic-law for the mean velocity field remains valid, the LES wall model has to take into account also the unsteady behaviour of the flow and its effects. In fact, there are not experimental evidences supporting the application of the logarithmic-law on the instantaneous velocity field. However, it is possible to empirically adopt this solution. Some models of the scientific literature apply the logarithmic-law to both the mean and instantaneous velocity fields, while others only to the latter. The final purpose and the challenge of the wall model is to introduce the roughness effect directly to the momentum equation through a forcing applied on the mesh cell adjacent to the wall. The techniques available to treat LES wall modelling are covered exhaustively in [subsection 3.1.8](#).

Here, the boundary conditions are generically resumed:

- **Inlet:** Periodic BC or an appropriate wind velocity profile (and its turbulence if necessary), using a method to generate an instantaneous field.
- **Outlet:** Periodic BC or fixed pressure, avoiding backward flow.
- **Top:** Slip BC.
- **Lateral:** Periodic BC.
- **Wall:** Wall model imposes a term in the momentum equation to reproduce the effect of a rough wall.

As already mentioned, the inlet and wall boundary conditions are treated in depth in the following two sections. Whereas the operational boundary conditions adopted for our LES simulation are examined in [subsection 3.3.4](#).

3.1.7 Inlet boundary condition

Hence, in LES case, a time-varying field must be specified at the inlet boundary using an appropriate inflow generator. The generated unsteady flow should faithfully represent the mean wind velocity and turbulence characteristics of the flow field target (Tabor and Baba-Ahmadi, 2010; Tamura, 2008; Wu, 2017). According to the work of Tamura (2008), it is possible to identify two families of inflow methods:

- Precursor-successor methods or called simply precursor methods.
- Synthetic methods.

In order to understand the performance of these methods and make the convenient choice for our research, the work of Vasaturo *et al.* (2018) has proved to be relevant. The study compares the performance of a precursor method to that of two basic but valid synthetic methods, i.e. the Vortex Method (VM) (Mathey *et al.*, 2006) and the random flow generation (RFG) method (Smirnov *et al.*, 2001), for the LES simulation of the neutral atmospheric boundary layer in an empty domain with three different types of rough terrains: rural, suburban and urban.

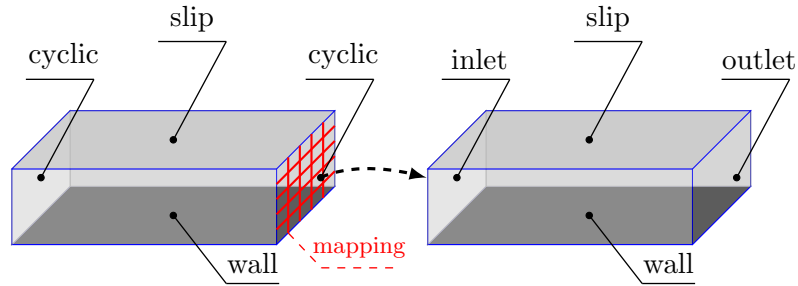


Figure 3.2: Precursor-successor method.

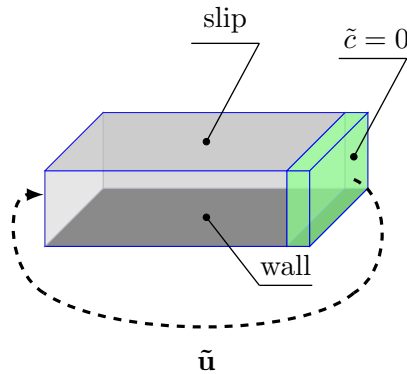


Figure 3.3: Cyclic-Dispersion Domain (CDD).

A simple and powerful method to obtain inflow data is to simulate a precursor domain (PD) with periodic or cyclic boundary conditions driven by a forcing term (e.g. a pressure gradient). When the flow is fully developed, a sampling operation of the velocity field and any other useful field is realised in a cross-sectional plane. After, the sampling data is stored in a database. The latter could be employed to provide the inflow BCs for the main simulation domain, i.e. the successor domain (SD). The method is summarised schematically by Figure 3.2. There are many variants of this method as highlighted by the works of Lund *et al.* (1998), Tabor and Baba-Ahmadi (2010), Yang and Meneveau (2016) and others. A variant used in our research aims to combine the precursor and successor domain into a single computational domain. For

convenience, the domain that derives from this method is called “cyclic-dispersion domain” (CDD) in the current research. As we will observe in more details in [section 3.3.1](#), the flow field is decoupled by the concentration field in the latter method, as illustrated in [Figure 3.3](#). The first field is periodic, while the second one is non-periodic. Thanks to a sink term, the concentration field is reset to zero before it returns to the inlet patch.

According to [Vasaturo *et al.* \(2018\)](#), synthetic methods can be classified in several groups:

- The group of Fourier methods. This group generates turbulence through a summation of harmonic functions. Some methods that fall into this group are: the random flow generation (RFG) method, developed by [Smirnov *et al.* \(2001\)](#), the discretizing and synthesising random flow generation (DSRFG) method ([Huang *et al.*, 2010](#)) and the consistent discrete random flow generation (CDRFG) method ([Aboshosha *et al.*, 2015](#)). It is not in our interest to further investigate them.
- The digital filter methods represents another group. They are focused on generating velocity fluctuations from a set of random data employing a digital filter based on a correlation function. Some examples of this method are present in: [Di Mare *et al.* \(2006\)](#), [Veloudis *et al.* \(2007\)](#), [Xie and Castro \(2008\)](#), [Kim *et al.* \(2013\)](#) and [Okaze and Mochida \(2017\)](#).
- Between the remained synthetic methods, there are: the proper orthogonal decomposition (POD) methods ([Tabor and Baba-Ahmadi, 2010](#)) the vortex method (VM) [Sergent \(2002\)](#); [Mathey *et al.* \(2006\)](#) and the synthetic eddy method (SEM) ([Jarrin *et al.*, 2006](#)). In the preliminary stage of the thesis, particular attention was dedicated to the latter method because its divergence-free version ([Poletto *et al.*, 2013](#)), i.e. DFSEM, is available in OpenFOAM v1812 and in the most recent versions. This method is capable to reproduce inflow turbulence with fixed mean velocity, turbulence length scale and Reynolds stresses. The inflow turbulence is a result of a sum of synthetic eddies that are convected through a virtual box that encloses the inlet patch.

The results of the [Vasaturo *et al.* \(2018\)](#) study shows that the precursor method allows to preserve better the wind field profiles along the domain as expected from this type of method. [Figure 3.4](#) and [Figure 3.5](#) illustrate the previous behaviour and in general show the development of the mean velocity and the turbulent kinetic energy along the domain. The conservation of the profiles is less evident in the other two synthetic methods, especially as regards the evolution of the turbulence kinetic energy. It was of our interest to reproduce the results of this work. However, this intent turned out to be complicated. An exhaustive list of case settings (and a clear

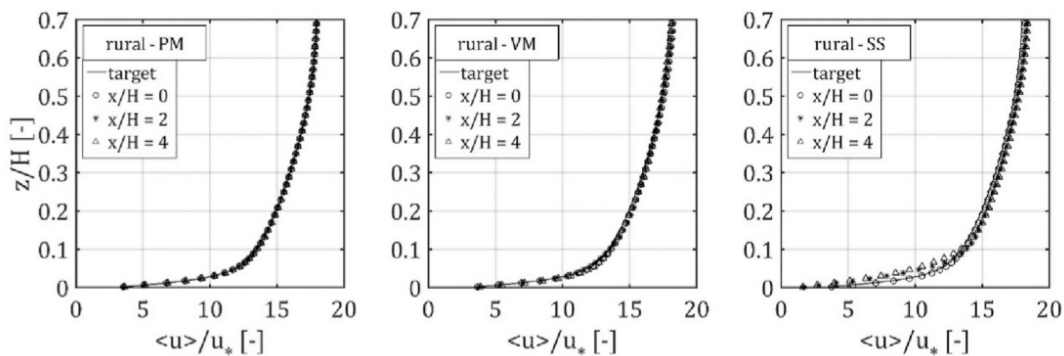


Figure 3.4: Evolution of the mean velocity for rural case ($z_0 = 0.23$ m). From right to left: Precursor Method (PM), Vortex Method (VM) and Spectral Synthesizer (SS). From: [Vasaturo *et al.* \(2018\)](#)

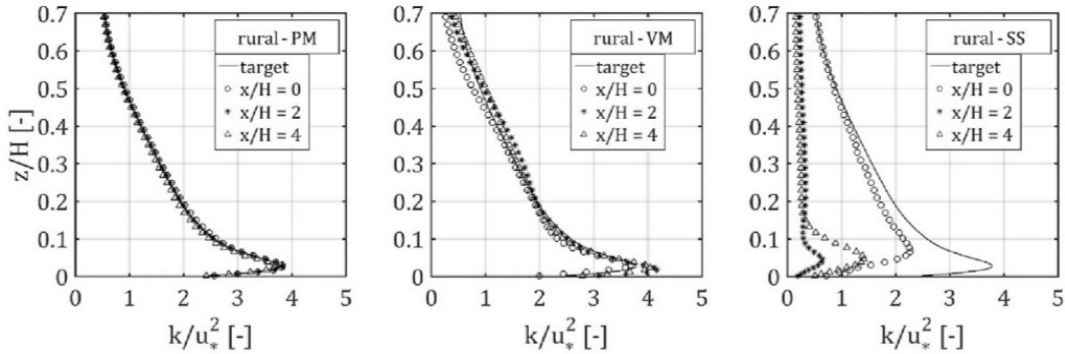


Figure 3.5: Evolution of the turbulent kinetic energy for rural case ($z_0 = 0.23$ m). From right to left: Precursor Method (PM), Vortex Method (VM) and Spectral Synthesizer (SS). From: [Vasaturo *et al.* \(2018\)](#)

description of the methodology) is not available in the article, not allowing the reproducibility of the simulation. One of the difficulties is the determination of the constant streamwise driven force (equivalent to a constant streamwise pressure gradient), which is implemented as a source term in the x -momentum equation and whose value is not known a priori. In fact, as highlighted by the authors, in the simulation the source term is determined using a trial-and-error approach in order to reproduce the theoretical logarithmic mean velocity profile and the friction velocity for a corresponding roughness length as closely as possible. Moreover, from the previous figures it is not possible to have information about the upper part of the profiles, which remains unknown.

Although precursor-successor methods accurately preserve the inlet profiles, it is important to remark that they need more computational resources than the synthetic methods. In fact, the procedure to arrive until the final simulation is longer and usually implies two domains. Moreover, it is not possible to specify directly the profiles at the inlet patch. The profiles are developed respecting the BCs and the applied forcing. Nevertheless, the profiles obtained are in equilibrium with the governing equations and with the models. This guarantee the accuracy previously cited. On the other hand, the synthetic methods need less computational resources. They allow to define specific profiles at the inlet patch, but the profiles could not be in equilibrium with the governing equations and the different models used. In this case, ensure the equilibrium is possible but not easy (especially for beginners in this field).

For our research, the [Vasaturo *et al.* \(2018\)](#) work has led us towards the use of the precursor method and the synthetic methods similar to the vortex method (in particular DFSEM which was available in OpenFOAM). Nevertheless, the first was preferred because it was easier to employ at an intermediate stage of the LES methodology development in our research.

3.1.8 Rough wall model for LES simulations

Together with the generation of the inlet flow, the modelling of the rough wall represents one of the most important obstacles to correctly simulate the SBL. In the current section, it is treated the effects of roughness on the SGS model, the experimental observations and the fundamentals of rough wall modelling. Moreover, the wall models taken into consideration by our methodology are listed here, while they will be examined in more detail in the following subsections.

There are different ways to approach the terrain roughness typical of the ABL. However, in LES, three main categories of methods exists to treat the roughness modelling ([Rodi *et al.*, 2013](#)). They are:

- Explicitly model the roughness elements whose walls are treated as no-slip walls in the CFD code.
- Another approach consists of applying momentum forcing terms, which is commonly used to model the effect of vegetation on the flow field.
- The third approach takes into account the ground roughness thanks to the prescription of shear stresses at the wall.

The first approach might be the best. However it has a computational cost that is often prohibitive because the roughness elements are small and needs really fine meshes (Piomelli and Balaras, 2002). The remained approaches are more convenient. Based on the bibliographic research and on the numerical implementation, we have decided to analyse the third approach in more details as we will see below.

The bibliographic research over wall models and our current experience in wall modelling have led to remark that one of the greatest challenges in applying LES to low- and high-Reynolds number flow over rigid walls is the wall model. Piomelli (1999) identified three main reasons:

1. The growth of the small scales is inhibited by the presence of the wall.
2. The exchange mechanisms between the resolved and subgrid-scale (SGS) are modified.
3. The length scale of the energy-carrying large structures is Reynolds-number dependent near the wall.

As highlighted by Xie *et al.* (2004b), the previous physical effects interact with the SGS modelling. For instance, in the neutral atmospheric boundary layer, the work of Mason and Thomson (1992) remarks that the departure of the mean velocity profile from the logarithmic law is caused by the Smagorinsky SGS model. In fact, the latter does not take into account the fluctuation of the SGS stresses. Stochastic fluctuations characterise the SGS stresses and it leads to a backscatter of energy from subgrid-scale.

The experimental observations, conducted by (Krogstad *et al.*, 1992; Krogstad and Antonia, 1994), point out two important characteristics concerning the roughness. Firstly, the fact that roughness elements increases the wall-normal velocity. Secondly, a moderately higher roughness dependence of the principal Reynolds shear stress (e.g. τ_{xz}) is noted. Moreover, the behaviour of the longitudinal turbulence intensity is the same as that of the smooth wall. Nevertheless, standard LES models are not able to reproduce these peculiarities identified experimentally.

Moreover, it is well-known that shear flows near solid boundaries contain alternating streak of high- and low-speed fluid. The streaks are thin and if they are not adequately resolved, the turbulence energy production at the vicinity of the wall (which is a large fraction of the total energy production) is under-predicted (Kim and Moin, 1989). Generally, under-prediction of the turbulence production results in reduction of the Reynolds stress and, thus, the skin friction. Consequently, some of the overall parameters of the flow will not be predicted correctly.

Nevertheless, the previous difficulties could be overcome, for example through a wall model. Simulations and experiments suggest that wall-region turbulence and turbulence far from the wall are relatively loosely coupled. In fact, in the context of rough-wall boundary layer, there exists the hypothesis labelled “wall similarity hypothesis” or “Reynolds number similarity hypothesis of Townsend” (Townsend, 1980; Flack *et al.*, 2005). It states that, outside the roughness sublayer (a region influenced by length scales associated with the roughness elements and extending to about five times the roughness height K_s), turbulence motions are independent of the wall roughness at sufficient large Reynolds numbers. Chapman and Kuhn (1986) illustrated that a simulation with an artificial boundary condition imposed at the top of the buffer layer (almost at $z^+ = 100$) displayed most of the characteristics of the wall layer found in a simulation in which the entire flow is computed. Thus, accurate prediction of the flow near the wall does

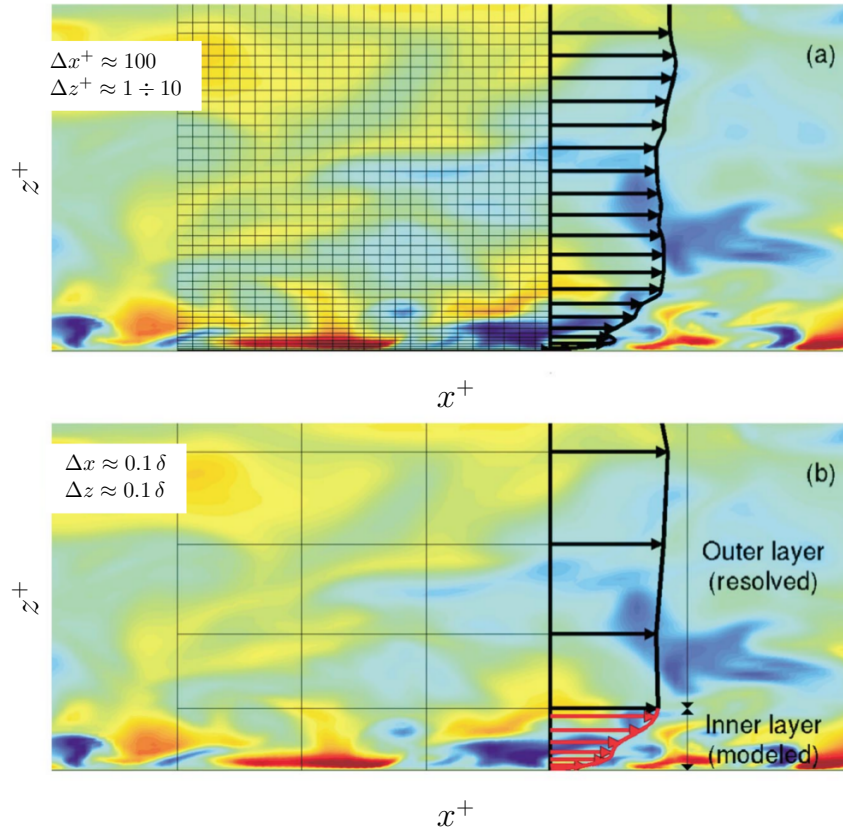


Figure 3.6: Sketch to illustrate the wall modelling philosophy. (a) Inner layer resolved and (b) inner layer modeled. Image modified from [Piomelli and Balaras \(2002\)](#).

not require accurate simulation of the outer flow. On the other hand, [Piomelli *et al.* \(1987\)](#) and others have shown that, by using relatively crude lower boundary conditions to represent the effect of the wall region, one can accurately simulate the central part of the flow in a channel. Consequently, the details of the flow in the wall region need not to be known in order to simulate the outer region. According to [Ferziger \(1993\)](#), it is possible to conclude that both regions can be well-simulated if it is given the correct shear stress and a reasonable approximation of the fluctuations at the interface between the two regions. So these results suggest that useful simulations can be done without resolving the entire flow. This is important because (as it was highlighted at the beginning of the current section) a very fine computational mesh in all directions is required to resolve the wall region. Therefore, if it can be represented by a model, a huge computational saving can result.

Deepening the concept expressed in [Piomelli *et al.* \(1987\)](#), most wall-layer models or simply wall models consider (explicitly or implicitly) the inner layer in a Reynolds-average sense ([Piomelli and Balaras, 2002](#)). According to the previous authors, when a grid or cell is so coarse that it is capable to enclose a large number of eddies, as illustrated in [Figure 3.6](#), the wall model could represent only the average effect of the eddies. In this situation, the time scale of the numerical outer-flow is quite large with respect to the time scale of the near-wall eddies. It means that, for each time step, many eddies pass through the cells in the wall region. So the inner layer is assumed to be governed by the RANS equations.

In order to respect the validity of the previous assumption, the grid or cell size must be very large. The work of ([Piomelli and Balaras, 2002](#)) allows to have an estimation of the grid size in the case of plane channel flow. Moreover, it suggests not using cells that are too fine. For the channel flow, the estimation proposes to use a grid of the order of 1500 wall units in the

streamwise direction and 700 in the spanwise direction. On the other hand, two cases with too small grids are highlighted. The first regards grids that do not respect the previous dimensions in the streamwise and spanwise direction. Whereas, it is important to include also the case in which only the grid in the direction perpendicular to the wall is not conform (e.g. $z_p^+ < 50$). It does not allow to resolve the turbulent eddies in this region, resulting in aliasing errors that degrade the velocity field. These issues contribute to explain why wall models tend to be more accurate at very high Reynolds numbers (e.g. atmospheric flows) than at low or moderate ones (e.g. wind tunnel experiments).

Therefore, as a general rule, the first grid or cell adjacent to the wall need to be placed in the outer layer ($z^+ > 50$) and more precisely in the part of the logarithmic region inside the outer layer (see Table 1.3 in subsection 1.1.4). The logarithmic region could be estimated following the classical theory, so between $z^+ > 30$ and $z/\delta < 0.3$ (Pope, 2000c). Otherwise, if the experimental data are available, both mean velocity profile (Eq. (1.46)) and streamwise turbulent intensities' profile (Eq. (1.48)) could be used to better determine the logarithmic region, following the methodology proposed by Marusic *et al.* (2013) (as explained in section 1.1.4).

For rough walls, one has little choice but to use a model to represent the wall region. A possible classification of the wall models is based on the type of contribution for modelling the vicinity of a rough wall. So the two groups are those that (Xie *et al.*, 2004b):

1. Enhance the fluctuating component of the SGS vertical fluxes at the wall surface.
2. Inject backscatter energy into the resolved velocity field.

The first group is simpler and easier to implement and does not increase the computational cost significantly. Whereas the second is more complex, since some parameters need to be determined by numerical experiment or otherwise. They are more computationally expensive and sometimes may give rise to numerical instabilities.

The models investigated in the current research belong to the first group and are briefly presented here. One of the first models developed is the Deardorff *et al.* (1970) wall model. It contained weaknesses that were soon remediated by Schumann (1975). The latter model, with some modifications, is still widely used. It assumes that the instantaneous velocity at the grid point nearest a wall is exactly correlated with the shear stress at the wall point directly below it. Thomas and Williams (1999) developed a synthetic rough wall boundary condition based on the well-known Schumann (1975) wall model. They consider the instantaneous stress as a linear combination of the mean and fluctuating components, where the fluctuating part responds less to the roughness and consequently contributes less to the local shear stress than in the standard Schumann (1975) wall model. This behaviour is made possible thanks to a damping coefficient or weighting coefficient β applied to the mean and fluctuating components. Conversely, the Mason and Callen (1986) rough wall model takes into account only fluctuating components. In this case, the similarity between the latter model and the model proposed by Thomas and Williams (1999) is particularly noted. Finally, based on the Thomas and Williams (1999) wall model, Xie *et al.* (2004b) develop a family of wall models in which the weighting coefficient β can be estimated theoretically rather than determined by numerical experiments.

In the next sub-sections, the previous models will be treated in more detail because they will be used in the current research. Firstly the Schumann one (subsection 3.1.9), then the Mason and Callen wall model (subsection 3.1.10) and the Thomas and Williams' rough wall model (subsection 3.1.11) and finally the family of wall models developed by Xie *et al.* (2004b) (subsection 3.1.12).

3.1.9 Schumann wall model

This wall model relies on a linear relation between the wall stress and the velocity component at the first off-wall grid point or cell. The skin friction is an entry parameter for the model.

The author has developed a wall model for performing a plane channel flow simulation at a finite Reynolds number. It is based on the extended turbulent relation (with the density ρ appropriately simplified):

$$\langle \tau_{p,xz} \rangle = - \left(\frac{1}{z} \int_0^z \frac{1}{\nu_{tot}(z)} dz \right)^{-1} \frac{\langle \tilde{u}_x(z) \rangle}{z}$$

where $\langle \rangle$ is a statistical average (associated with a time average) and:

$$\nu_{\text{eff}} = \left(\frac{1}{z} \int_0^z \frac{1}{\nu_{tot}(z)} dz \right)^{-1}$$

Using dimensional analysis, the effective viscosity can be evaluated using:

$$\nu_{\text{eff}} = \frac{z_p}{2} \frac{\langle \tau_p \rangle}{\langle \tilde{u}_x(x, y, z_p) \rangle}$$

The resulting boundary conditions are:

$$\begin{aligned} \tau_{p,xz}(x, y) &= \left(\frac{\tilde{u}_x(x, y, z_p)}{\langle \tilde{u}_x(x, y, z_p) \rangle} \right) \langle \tau_p \rangle \\ \tilde{u}_z &= 0 \\ \tau_{p,yz}(x, y) &= \frac{2}{Re_\tau} \left(\frac{\tilde{u}_z(x, y, z_p)}{z_p} \right) \end{aligned} \quad (3.38)$$

where z_p is the distance of the first point/center-cell to the wall and $Re_\tau = u_* \delta / \nu$. The first equation is equivalent to assume that the longitudinal velocity component at position z_p is in phase with the instantaneous wall shear stress. The mean velocity profile can be obtained by the logarithmic law, and the mean wall shear stress $\langle \tau_p \rangle$ is, for a plane channel flow, related to the driving pressure gradient. This wall model therefore implies that the mean velocity field verifies the logarithmic law and can be applied almost exclusively to plane channel flows for which the value of the driving pressure gradient is known a priori. The second condition is related to the impermeability condition, and the third corresponds to a no-slip condition for the transverse velocity component \tilde{u}_y . Finally, it is important to highlight that, for the current model and for the following ones, the shear stress is numerically imposed as an external forcing which interacts in the momentum equation.

3.1.10 Mason and Callen model

The wall model proposed by [Mason and Callen \(1986\)](#) aims to include the roughness effects. This model is based on the hypothesis that the logarithmic distribution is verified locally and instantaneously by the velocity field, ([Sagaut, 2006](#)). This is a very strong hypothesis but its results are suitable as we shall see in [section 3.4](#). Moreover, the model is very simple to implement due to the fact that it uses directly the filtered velocity field.

The three velocity components are specified at the first computational point or cell adjacent to the wall by the relations of Eqs. (3.39)-(3.41).

$$\tilde{u}_x(x, y, z_p) = \cos \theta \left(\frac{u_*(x, y)}{\kappa} \right) \ln \left(1 + \frac{z_p}{z_0} \right) \quad (3.39)$$

$$\tilde{u}_y(x, y, z_p) = \sin \theta \left(\frac{u_*(x, y)}{\kappa} \right) \ln \left(1 + \frac{z_p}{z_0} \right) \quad (3.40)$$

$$\tilde{u}_z(x, y, z_p) = 0 \quad (3.41)$$

where z_0 is the roughness thickness of the wall and the angle θ is given by the relation $\theta = \arctan(\tilde{u}_y(z_p)/\tilde{u}_x(z_p))$. The friction velocity u_* is computed as a function of the instantaneous velocity components \tilde{u}_x and \tilde{u}_y thanks to the previous equations. The instantaneous surface friction vector \mathbf{u}_* is given by:

$$\mathbf{u}_*^2 = \left(\frac{\kappa^2}{\ln^2(1 + z_p/z_0)} \right) |\mathbf{u}_{||}| \mathbf{u}_{||} \quad (3.42)$$

where $\mathbf{u}_{||}$ is $(\tilde{u}_x(x, y, z_p), \tilde{u}_y(x, y, z_p), 0)$.

Consequently, the instantaneous wall shear stresses in the x and y direction are deduced by the relation Eq. (1.29). The latter could be approximated to $\tau_w \approx u_*^2$ and contributes to obtain the final expression of the wall shear stresses for the current model, as shown by Eq. (3.43) and Eq. (3.44).

$$\tau_{xz} = \left(\frac{\kappa^2}{\ln^2(1 + z_p/z_0)} \right) (\tilde{u}_x^2 + \tilde{u}_y^2)^{1/2} \tilde{u}_x \quad (3.43)$$

$$\tau_{yz} = \left(\frac{\kappa^2}{\ln^2(1 + z_p/z_0)} \right) (\tilde{u}_x^2 + \tilde{u}_y^2)^{1/2} \tilde{u}_y \quad (3.44)$$

3.1.11 Thomas and Williams model

The current wall model is inspired by the one proposed by Schumann (1975). A linear combination between the mean and fluctuating components of the filtered velocity field are used by the current model to estimate the instantaneous stress. As we will see below, the reaction to the roughness of the fluctuating part is less important. In other words, it can be interpreted as if the steady flow sees a rough wall, while the unsteady flow sees a less rough wall (Thomas and Williams, 1999). The wall model is expressed by Eq. (3.45) and Eq. (3.46).

$$\frac{\tau_{xz}}{u_*^2} = \frac{1}{U_p} [\langle \tilde{u}_x \rangle + \beta(\tilde{u}_x - \langle \tilde{u}_x \rangle)], \quad 0 < \beta \leq 1 \quad (3.45)$$

$$\frac{\tau_{yz}}{u_*^2} = \frac{1}{U_p} [\langle \tilde{u}_y \rangle + \beta(\tilde{u}_y - \langle \tilde{u}_y \rangle)], \quad 0 < \beta \leq 1 \quad (3.46)$$

where $\langle \rangle$ represents averaging over the horizontal plane in the flow field, assumed to be approximately equivalent to ensemble averaging. U_p is the mean streamwise velocity \bar{u}_x at the first grid location from the wall as derived from:

$$\bar{u}_x = \frac{u_*}{\kappa} \ln \left(\frac{z + z_0}{z_0} \right)$$

Whereas τ_{xz} is the instantaneous principal shear stress at the same location. Finally β is a damping factor ranging from 0 to 1.

The work of Xie *et al.* (2004b) helps to understand the idea behind the current model. Considering only τ_{xz} for simplicity, the authors affirms that the local shear stress τ_{xz} is less influenced by the fluctuating part $(\tilde{u}_x - \langle \tilde{u}_x \rangle)$ than by the mean part $\langle \tilde{u}_x \rangle$. It could be interpreted by highlighting that the local shear stress is the result of the impact force of the fluid's movement to the roughness elements. Thus, a direct consequence is that the mean flow will always make its contribution felt. However, the contribution of fluctuations is not always completely present because it may decay before to reach the rough surface. The eddies, which constitute the fluctuations, would last for a short time. It is shown by the schematic eddies in Figure 3.7. These behaviours justify the introduction of the damping factor β in Eq. (3.45). Similar reasoning could be also made for Eq. (3.46).

Averaging Eq. (3.45) over the horizontal plane, we find this wall model obeys the constraint:

$$\frac{\langle \tau_{xz} \rangle}{u_*^2} = \frac{\langle \tilde{u}_x \rangle}{U_p} \quad (3.47)$$

According to [Xie *et al.* \(2004b\)](#), most wall models obey this constraint (i.e. Schumann, and Thomas and Williams), though some wall models might not (i.e. Mason and Callen model). Actually, for this wall model, the damping factor β is fixed to 0.3. The authors of the wall model found that this value was satisfactory to suit their applications (i.e. simulation of bluff body flows). Nevertheless, the magnitude of β remains an open problem and the next subsection will face up to this problem.

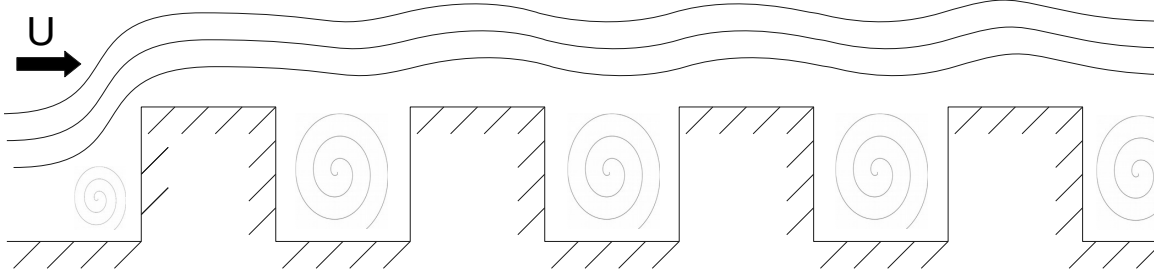


Figure 3.7: Explanation sketch: the eddies are almost dissipated before reaching the roughness elements while the mean velocity always exerts its influence.

3.1.12 Xie model

The model developed by [Xie *et al.* \(2004b\)](#) take inspiration from the previous models. The shear stress expressions are the same of Eq. (3.45) and Eq. (3.46). The current model is focused on determining more precisely the damping factor β .

According to the authors, the damping factor can be estimated through the following expression:

$$\beta^2 = \left(\frac{U_p^2}{u_*^2} \right) \left(\frac{\overline{w'^2}}{u_*^2} \right) [1 + \overline{u'w'^2} / \overline{u'^2} \overline{w'^2}] \quad (3.48)$$

The procedure to arrive until Eq. (3.48) and the explanation of its terms are exposed in the work of [Xie *et al.* \(2004b\)](#). Here, the main terms of the previous equation are briefly treated. Firstly, it is important to remark that $\overline{u'w'^2} / \overline{u'^2} \overline{w'^2}$ is almost 0.1 in a neutral SBL. Therefore, this term could be considered as negligible. Moreover, it is evident that β is a function of $\overline{w'^2} / u_*^2$ and U_p^2 / u_*^2 . It implies that U_p needs to be limited because β can only assume values between 0 and 1. In fact, z_p^+ must be located in the logarithmic layer, for instance in an intermediate position of the interval $z^+ > 30$ and $z/\delta < 0.3$, according to the classical theory, or in the interval $3 Re_\tau^{1/2} < z^+ < 0.15 Re_\tau$ for high-Re flows ([Marusic *et al.*, 2013](#)). It is possible to remark that the limitation of U_p is fundamental in Eq. (3.47). The ratio $\overline{w'^2} / u_*^2$ can be settled thanks to experimental measurements. If it is not possible, some similarity relations presented in literature (e.g. [Stull \(2012\)](#)) can be used for a neutral ABL flow.

Finally, it is highlighted that the friction velocity u_* does not need to be imposed but it represents an important result of the wall model, as we will see in [section 3.4](#).

3.1.13 Passive scalar equation

In order to complete the overview, the conservation equation governing the filtered passive scalar field $\tilde{c}(\mathbf{x}, t)$ is presented in the current subsection. Moreover, one of the most common modelling closure is also treated.

To obtain the equation of $\tilde{c}(\mathbf{x}, t)$, the filter operator is applied to the conservation equation of the passive scalar $c(\mathbf{x}, t)$ (i.e. Eq. (1.17)). Without considering the source term, it yields to:

$$\frac{\partial \tilde{c}}{\partial t} + \nabla \cdot (\tilde{\mathbf{u}} \tilde{c}) = \nabla \cdot (D_c \nabla \tilde{c}) \quad (3.49)$$

where D_c is the molecular diffusivity. Moreover, splitting the filtered nonlinear term $\tilde{\mathbf{u}} \tilde{c}$ into a resolved and subgrid part, the following equation is obtained:

$$\frac{\partial \tilde{c}}{\partial t} + \tilde{\mathbf{u}} \cdot \nabla \tilde{c} = \nabla \cdot (D_c \nabla \tilde{c}) - \nabla \cdot \tau_c^R \quad (3.50)$$

where the subgrid scalar flux τ_c^R is defined as:

$$\tau_c^R \equiv \tilde{\mathbf{u}} \tilde{c} - \tilde{\mathbf{u}} \tilde{c} \quad (3.51)$$

Closure is achieved by modelling the latter subgrid scalar flux. Similarly to RANS and to the subgrid momentum flux in LES, the gradient-diffusion hypothesis is used to obtain:

$$\tau_c^R = -D_{\text{sgs}} \nabla \tilde{c} \quad (3.52)$$

where D_{sgs} is the subgrid turbulent diffusivity. Most studies of heat transfer or concentration dispersion problems (Sykes and Henn, 1992; Meeder and Nieuwstadt, 2000; Xie *et al.*, 2004a) have applied a SGS eddy-viscosity combined with a subgrid eddy Prandtl number Pr_{sgs} or Schmidt number Sc_{sgs} , which are set as constant or calculated dynamically. So, it yields to:

$$D_{\text{sgs}} = \frac{\nu_{\text{sgs}}}{Sc_{\text{sgs}}} \quad (3.53)$$

or:

$$D_{\text{sgs}} = \frac{\nu_{\text{sgs}}}{Pr_{\text{sgs}}} \quad (3.54)$$

here ν_{sgs} is the SGS eddy-viscosity.

Although, this closure is not perfect from a purely theoretical point of view, this approach is very often used in simulations in the physical space, as previously cited. Further, there is no universal and well-justified methodology that allow to choose an appropriate value of the subgrid Prandtl or Schmidt number. The latter appears as an adjustable parameter which can be tuned in an ad-hoc way to obtain the best fit with the reference data. Values found in literature range from 0.1 and 1.2 (Xie *et al.*, 2004a; Sagaut, 2006). Nevertheless it is important to highlight that this approach is not valid in cases where the velocity field is fully resolved. In fact, it yields to $\nu_{\text{sgs}} = 0$, while some subgrid scalar fluctuations exist. It is important to place the filter within the inertial subrange. For further closure approaches please consult Sagaut (2006).

Finally, the current closure yields to:

$$\frac{\partial \tilde{c}}{\partial t} + \tilde{\mathbf{u}} \cdot \nabla \tilde{c} = \nabla \cdot [(D_c + D_{\text{sgs}}) \nabla \tilde{c}] \quad (3.55)$$

where, similarly to the RANS approach, the effective diffusivity D_{eff} could be used. Consequently:

$$D_{\text{eff}} = D_c + D_{\text{sgs}} \quad (3.56)$$

3.2 Nironi experiment and LES methodology inputs

In the previous overview, the knowledge necessary to deal with an LES simulation of an atmospheric boundary layer in neutral conditions has been presented. The current section illustrates the experimental wind tunnel selected to test and validate our LES methodology.

Many studies have been done to simulate the atmospheric boundary layer (ABL) flow through the wind tunnel experimental method (e.g. [Robins and AG \(1979\)](#); [Fackrell and Robins \(1982\)](#); [Deardorff and Willis \(1984\)](#); [Yee *et al.* \(1993a,b\)](#); [Mole and Jones \(1994\)](#); [Robins *et al.* \(2001\)](#)). However, not all of them are suitable for our purposes either because the phenomenon is complex to simulate or because we do not have a complete set of experimental data. The complexity of the simulation is due to several causes, among the most important:

- Extremely small sources, which require too high computational resources to be simulated.
- Emissions and measurements situated very close to the ground.
- Measurements conducted too far from the sources.

Therefore, for the current study and validation, the [Nironi \(2013\)](#) (or equivalently [Nironi *et al.* \(2015\)](#)) experiment has been chosen. It reproduces a neutrally-stratified boundary layer. Although it has some limitations, this wind tunnel experiment demonstrates its suitability to be reproduced numerically without major difficulties. The experimental limitations and the computational setting will be discussed in the current section and in [section 3.3](#). Furthermore, we have counted on the direct support of the research team, which was actively involved in the Nironi's experiment.

Here, after the presentation of the [Nironi \(2013\)](#) experiment ([subsection 3.2.1](#)), the boundary layer and the concentration field characteristics are analysed respectively in [subsection 3.2.2](#) and [subsection 3.2.3](#). The analysis focuses on how to numerically represent the physics of the phenomena studied. This will be essential to understand the approach with which the inputs of the LES methodology could be obtained thanks to experimental data. The latter approach is also introduced in the current section.

3.2.1 Nironi neutral boundary layer experiment

The [Nironi *et al.* \(2015\)](#) experiment was focused on the study of the Turbulent Boundary Layer (TBL) over a rough surface, which reproduces a neutral atmospheric boundary layer, and its role in the dispersion of pollutants. The experimental campaign was conducted by the Atmosphere Impact and Risk (AIR) research team in the atmospheric wind tunnel of the Laboratoire de Mécanique des Fluides et d'Acoustique (LMFA) of the École Centrale de Lyon, France. The wind tunnel measures 24 m long, 7.2 m wide and 7.4 m high, as highlighted in green in [Figure 3.8](#). Whereas, the test section (in red in [Figure 3.8](#)) is 14.0 m long, 3.8 m wide and 2.0 m high. In order to control the longitudinal pressure gradients, it is possible to regulate the ceiling slope. The temperature in the working section is controlled so that its variation is limited in the range $\pm 0.5^\circ\text{C}$ during 1-day test.

The generation of a neutrally-stratified boundary layer is obtained by combining the effects of a grid turbulence and a row of spires ([Irwin, 1981](#)), located at the beginning of the test section, and roughness elements on the ground. The upwind turbulence grid is not common on a boundary layer simulation system, but here it is needed to reduce the inhomogeneities of the flow in the transversal direction. The spires used are of the Irwin type and measure 0.50 m in height, laterally spaced by 0.25 m. The roughness is generated by cubes of side $h = 0.02$ m distributed throughout the test section. A staggered array was adopted to place the cubes, covering almost 1.8% of the tunnel floor surface. A boundary layer depth $\delta \approx 0.70$ m \div 0.80 m is reproduced with this experimental set-up. An adequate simulation of a fully turbulent flow is

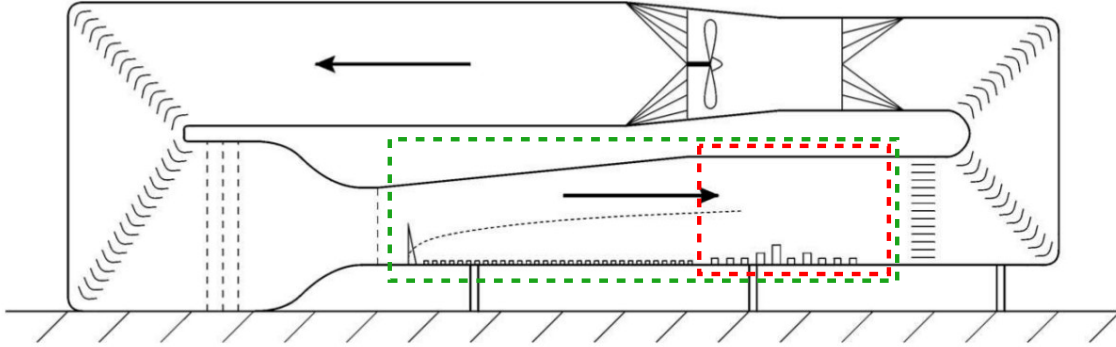


Figure 3.8: The atmospheric wind tunnel of LMFA, AIR.

guaranteed by a sufficiently high $Re = \delta U_\infty / \nu \approx 2.7 \times 10^5$ (Jiménez, 2004), with a free stream velocity $U_\infty = 5.0$ m/s and a kinematic viscosity of the air ν .

Regarding the dispersion of pollutants, the tracer used for the experiment is ethane (C_2H_6) because it has a density quite close to the air. The experiment studies different elevations and diameters of the source. For the current validation, it was selected the elevated source at $h_s = 152$ mm from the ground with a diameter of $\sigma_0 = 6$ mm. The source is made of a metallic L-shaped tube and it is placed at a distance of 6.0 m (i.e. $\approx 8.57 \delta$, if $\delta = 0.70$ m) from the beginning of the test section, where the boundary layer is estimated to be fully developed. In order to reduce the influence of the vertical tube on the tracer dispersion, the horizontal side of the tube was approximately 30 times the source diameter. For the experiment data employed, the spatial-average velocity of the ethane-air mixture $\langle u_s \rangle$ corresponded to that in the surrounding flow at the source height, a condition called “isokinetic”.

In the original study, the measurements of the experiment was compared to three experimental datasets. The validation of the wind field and above all of the concentration field was achieved thanks to the Fackrell and Robins (1982) dataset. On the other hand, Raupach *et al.* (1991) and Krogstad and Antonia (1994) have contribute to corroborate the meaning of the velocity higher order statistics and the integral length scales.

The experimental data used to validate our numerical simulations and the whole LES methodology were acquired thanks to the following instruments and their respective measurement techniques: the hot wire anemometer for the velocity field and the fast flame ionisation detector for the concentration field.

Hot wire anemometer

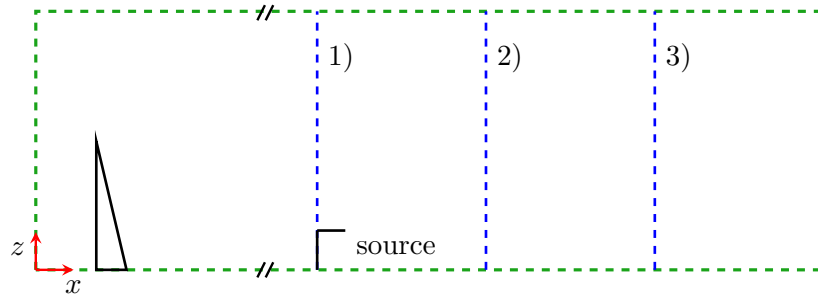


Figure 3.9: Position of available wind profiles: 1) 6 m, 2) 8 m and 3) 10 m

In the wind tunnel, the velocity field was measured thanks to a hot wire anemometer equipped with an X-wire probe with a velocity-vector acceptance angle of $\pm 45^\circ$. In this way, longitudinal and transversal velocity components could be measured simultaneously. The X-wire probe and the anemometer employed was produced by the Dantec Dynamics. This configuration allowed to measure many horizontal and vertical profiles. We have had access to vertical profiles at 3 distance from the beginning of the test section: 6 m, 8 m and 10 m (in x/δ coordinate respectively 8.57, 11.42 and 14.28 with $\delta = 0.70$ m), as shown in [Figure 3.9](#). For each measurement point, 120 s or 300 s time series were sampled with a sampling frequency of 5000 Hz.

Fast flame ionisation detector

The concentration field measurements were performed by a fast flame ionisation detector (FID), which detect a gas tracer continuously emitted from a point source. As mentioned, the tracer used was ethane (C_2H_6) and it was released mixed with air. This gas is not reactive and has a molar weight of almost $30.07 \text{ g} \cdot \text{mol}^{-1}$, against $28.97 \text{ g} \cdot \text{mol}^{-1}$ for the air. Thus the released obtained was neutrally buoyant and passive.

The instrument used in this experiment was an HFR400 Fast FID, produced by Cambustion LTD. The sampling tube was 0.3 m long, while the sampling frequency was 1000 Hz, so that concentration spectra were calculated with a frequency up to 300 Hz. The profiles available are horizontal and vertical profiles at 6 distances from the source: 0.25 m, 0.50 m, 1.00 m, 2.00 m, 3.00 m and 4.00 m (for x/δ respectively 0.35, 0.71, 1.42, 2.85, 4.28 and 5.71), see [Figure 3.10](#) and [Figure 3.11](#).

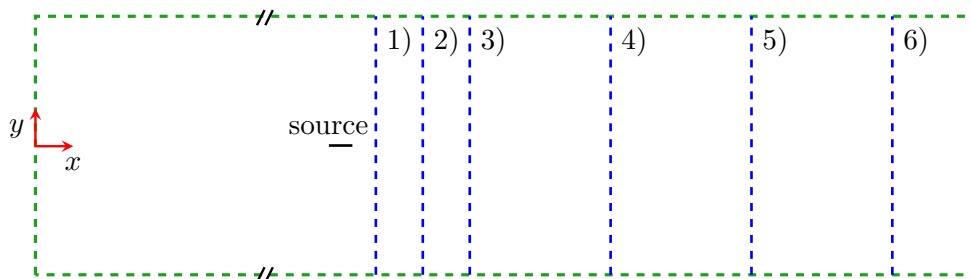


Figure 3.10: Horizontal profiles of concentration. Six profiles was measured at: 1) 0.25 m, 2) 0.50 m, 3) 1.00 m, 4) 2.00 m, 5) 3.00 m and 6) 4.00 m from the source.

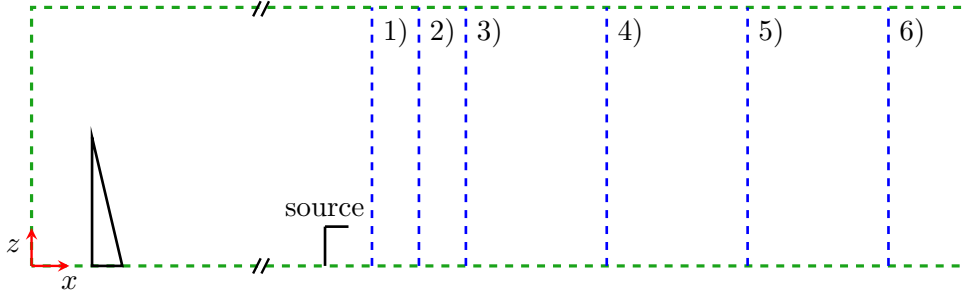


Figure 3.11: Vertical profiles of concentration. Six profiles was measured at: 1) 0.25 m, 2) 0.50 m, 3) 1.00 m, 4) 2.00 m, 5) 3.00 m and 6) 4.00 m from the source.

3.2.2 Boundary layer characteristics

The general characteristics of the [Nironi *et al.* \(2015\)](#) experiment, already presented above, are summarised in [Table 3.2](#). Here we focus on the analysis of the boundary layer characteristics and the methods for obtaining the values that allow to define numerically the boundary layer. Finally, we summarise our rigorous methodology to extract the LES inputs from the current experimental data and similar ones.

U_∞	5.0 m/s	Wind reference velocity
δ	0.70 m ÷ 0.80 m	BL height (δ_{99})
ν	$1.46 \times 10^{-5} \text{ m}^2/\text{s}$	Kinematic viscosity
Re	2.7×10^5	Reynolds number

Table 3.2: Characteristics of the experimental boundary layer.

Thanks to a preliminary post-processing, the hot wire anemometer is able to provide us the following data: the time t [s], the instantaneous flow velocity components u , v and w [m/s] and the instantaneous shear stresses uw and uv . Thanks to these data, it is possible to compute some statistics of the flow. The mean could be defined through the following general expression:

$$\bar{s} = \frac{1}{N} \sum_{j=1}^N s_j \quad (3.57)$$

where N is the number of samples in the time-series. Therefore, the mean velocity $\bar{\mathbf{u}}$ and the mean shear stress $\overline{u'w'}$ are computed. Higher order statistics could also be computed thanks to the instantaneous velocity signals.

The characterisation of the neutral atmospheric boundary layer of the [Nironi *et al.* \(2015\)](#) experiment could begin from the determination of the boundary layer (BL) height δ and the friction velocity u_* .

The BL height is figured out from the analysis of the $\overline{u'w'}$ profiles, which are shown in [Figure 3.12](#). It is observed that the boundary layer is not completely homogeneous along the experimental domain but it slowly continues to evolve. The criterion to establish the BL height is simply the height at which the mean shear stress $\overline{u'w'}$ begins to oscillate around zero. Therefore, the developed BL has a height of 0.70 m, 0.75 m and 0.80 m respectively at 6.00 m, 8.00 m and 10.00 m from the beginning of the test section. Moreover, as further evidence, the BL height δ (orange line) was plotted in [Figure 3.13](#). It shows that also \bar{u} and $\overline{u'v'}$ begins to oscillate around a constant value beyond this height.

The friction velocity u_* is the significant velocity scale in the turbulent boundary layer and depends on the nature of the surface and on the magnitude of the wind. So it is fundamental to estimate it. Since the surface stress equals the turbulent momentum flux in the air just

above the surface, u_* is representative of the turbulent wind fluctuations in the lower part of the atmosphere (Kaimal and Finnigan, 1994). There are many similar definitions of friction velocity that were compared by Weber (1999). It was chosen the definition found in Panofsky (1984), Garratt (1994) and Kaimal and Finnigan (1994). According to it, it is possible to write:

$$\tau_w = -\rho \overline{u'w'} = \rho u_*^2 \quad (3.58)$$

where τ_w is the shear stress at wall and ρ the density of the air. This definition assumes that the horizontal Reynolds stress vector $(-\rho \overline{u'w'}, -\rho \overline{u'v'})$ could be reduced to $(-\rho \overline{u'w'}, 0)$ when the u -axis is aligned with the mean wind. In the atmosphere, this assumption is not generally true (Weber, 1999). However, in the lower part of the boundary layer, the quantity $\overline{u'v'}$ is small compared to $\overline{u'w'}$, as shown by Figure 3.13. It is highlighted that, from $0 < z/\delta < 0.1$, $\overline{u'w'}$ changes so slowly that it could be considered effectively constant.

Consequently, the experimental data related to the Reynolds shear stress allows to compute the friction velocity thanks to Eq. (3.58), i.e. $u_* = (-\overline{u'w'})^{\frac{1}{2}}$. The friction velocity found is the result of the average of the experimental values of $\overline{u'w'}$ over all the data in the interval $0 < z/\delta < 0.1$. The latter region is delimited by the red line (“Av. region”) in Figure 3.14. This criterion lead to the friction velocity values that are 0.187 m/s at 6.0 m, 0.183 m/s at 8.0 m and 0.180 m/s at 10.0 m. Figure 3.14 illustrates the nondimensional $\overline{u'w'}/u_*$ profiles with respect to the nondimensional height z/δ . They were calculated thanks to the previously estimated values of u_* and δ . The plot probes the good approximation of u_* and δ , used for the nondimensional process.

In the lower part of the neutral boundary layer, the vertical profile of the mean velocity fits a logarithmic law, as predicted by the similarity theory (Tennekes and Lumley, 1972). The main length scale is z , the distance from the ground. It is needed to account the displacement effect due to the rough surface. The roughness displace the entire flow upwards. As shown by Equation 3.59, the logarithmic law is written including aerodynamic roughness z_0 and the displacement height d .

$$\frac{\bar{u}(z)}{u_*} = \frac{1}{\kappa} \ln \left(\frac{z + z_0 - d}{z_0} \right) \quad (3.59)$$

where u_* is the friction velocity, κ the von-Kármán coefficient and z_0 the aerodynamic roughness. The von-Kármán coefficient used in the current work is 0.40.

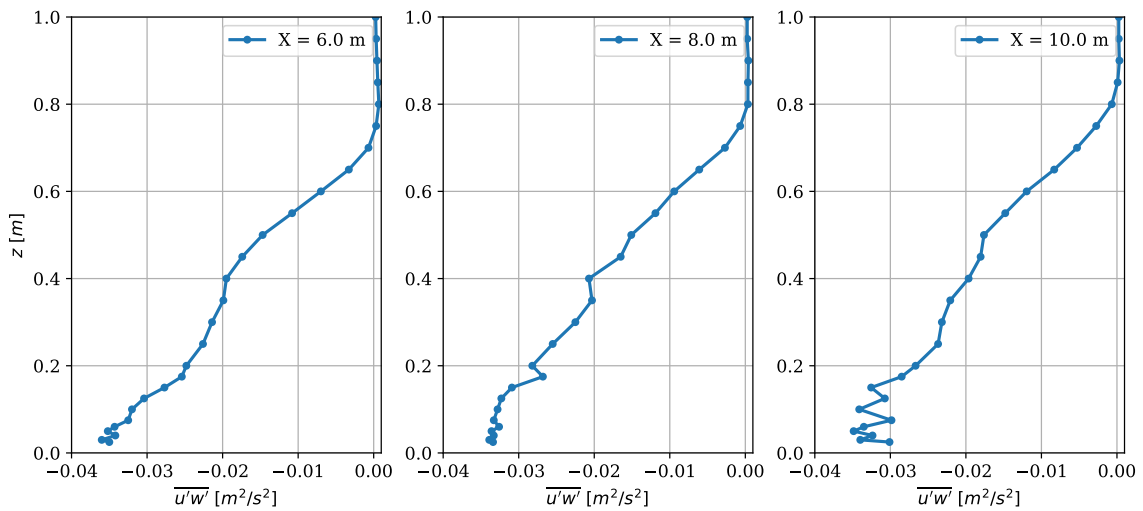


Figure 3.12: Reynolds shear stress $\overline{u'w'}$ for the three available profiles, which are respectively at 6.00 m, 8.00 m and 10.00 m from the beginning of the test section.

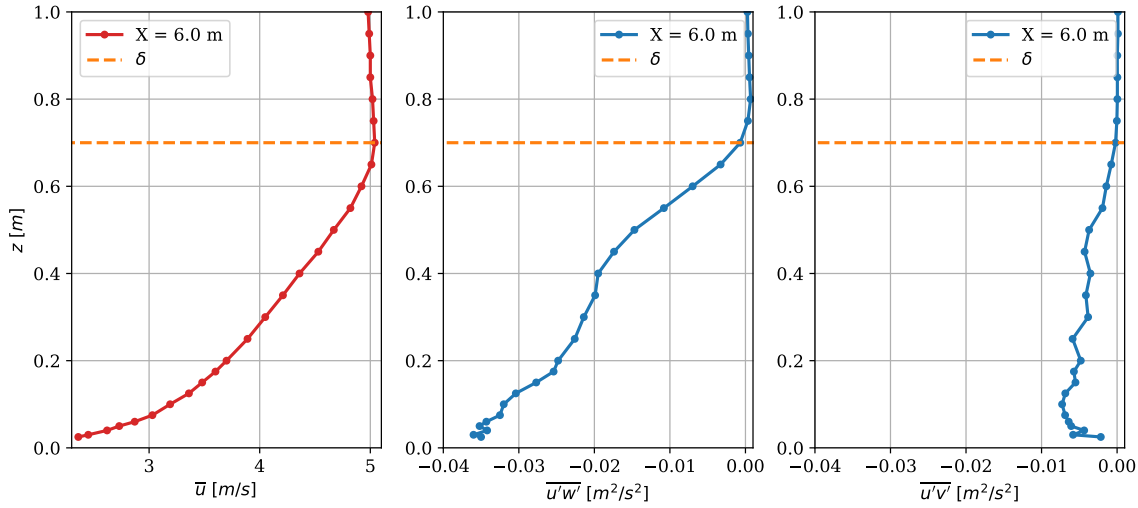


Figure 3.13: Streamwise mean velocity and Reynolds stress components ($\overline{u'w'}$ and $\overline{u'v'}$) profiles at 6.0 m from the beginning of the test section.

As predicted by the theory, and as shown in Figure 3.15, the Eq. (3.59) fits the velocity profile in a region that slightly exceeds the extent of the inertial region, i.e. $z/\delta < 0.25$. Otherwise, this region could be considered representative of the surface boundary layer (SBL). On the other hand, a good fit of the mean velocity profile along the whole turbulent boundary layer can be obtained thanks to a power-law of the type of Eq. (3.60).

$$\frac{\bar{u}(z)}{U_\infty} = \left(\frac{z-d}{\delta-d} \right)^n \quad (3.60)$$

Here, U_∞ is the free-stream mean velocity. In order to fit the experimental profile, n and d are the two values to optimise to best fit the velocity experimental profile, while δ is estimated as we have seen previously.

In order to compute the other characteristics of the BL, especially z_0 and d , the hot wire experimental data was fitted using the Eq. (3.59) and fixing the experimental friction velocity u_* . The fitting function, used in the current research, is an optimisation function from the

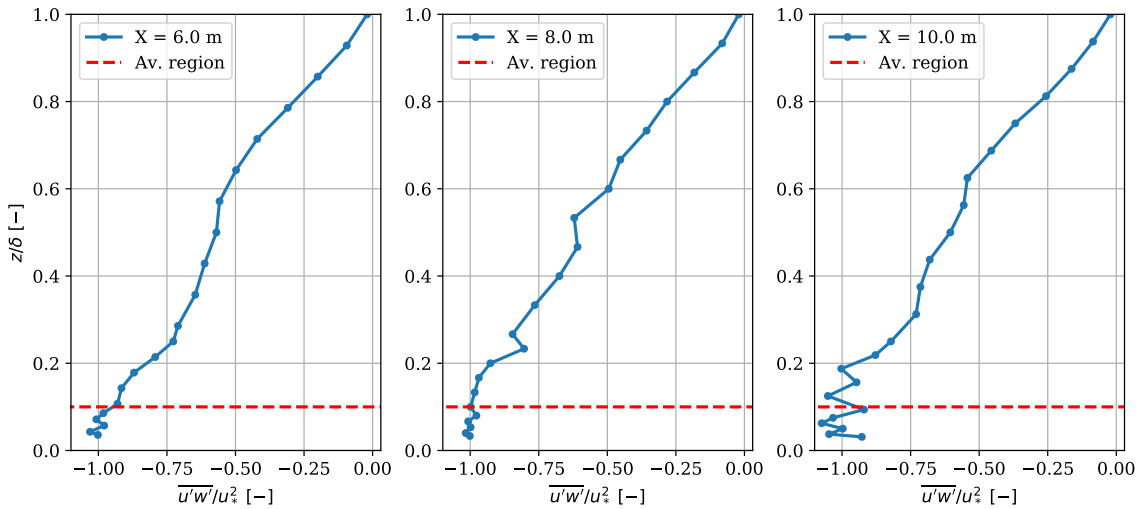


Figure 3.14: Nondimensional Reynolds shear stress for the three available profiles, which are respectively at 6.00 m, 8.00 m and 10.00 m from the beginning of the test section.

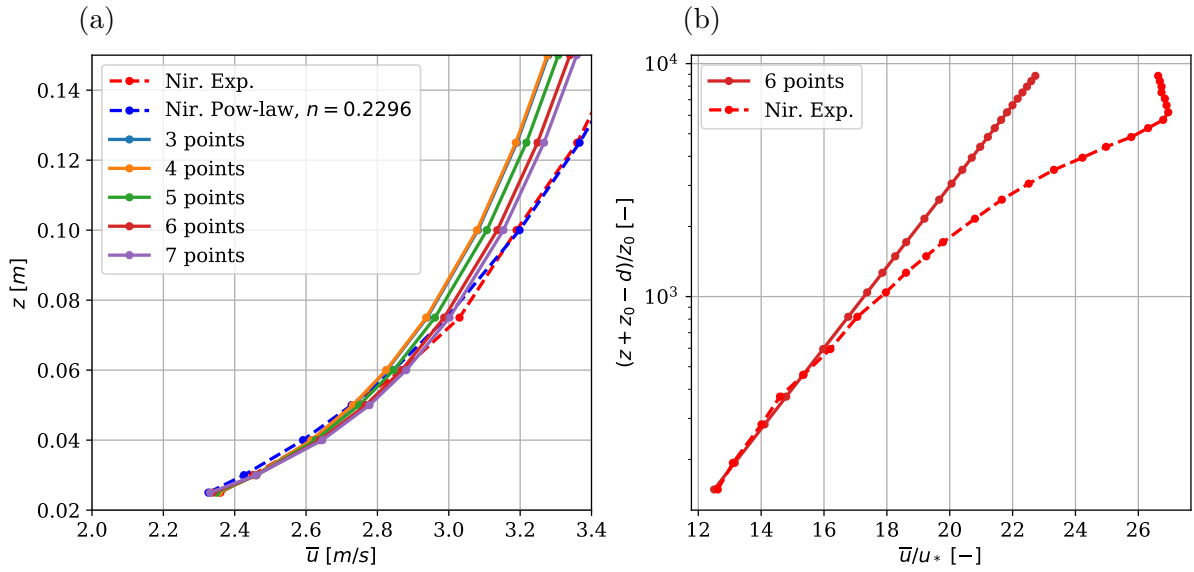


Figure 3.15: Mean velocity profiles at $x = 6$ m. The left figure (a) shows the Nironi experimental profile, the power-law profile and the 5 profiles used for the optimisation procedure with the Method 1. The right figure (b) employs a semi-logarithmic plot to compare the optimal profile (obtained with 6 points) and the Nironi experimental profile.

Python “scipy” library (i.e. `curve_fit`). Consequently, the variables to be optimised are z_0 and d . This is a method also used by Nironi (2013) and called the “Method 1”. It is important to estimate the friction velocity before proceeding with optimisation process. The latter process focused on the lower part of the boundary layer and was conducted using an increasing number of $\bar{u}(z)$ - z experimental pairs. A number of measurement points ranging between 3 and 7 have been used. For the profile at 6.0 m, the different graphical results are observed in Figure 3.15. The left-hand figure includes the Nironi experimental profile and the Nironi power-law profile with the exponential $n = 0.2394$. Moreover, the figure on the right shows the best fitting curve (using 6 points, i.e. at $z/\delta < 0.1$) together with the experimental data. The best fitting curve is obtained with 6 points and the optimal values are $z_0 = 1.119 \times 10^{-4}$ m and $d = 0.0085$ m. Repeating the procedure for the profiles at $x = 8.0$ m and $x = 10.0$ m, the following values was calculated: $z_0 = 1.111 \times 10^{-4}$ m and $d = 0.0094$ m for the first profile and $z_0 = 1.307 \times 10^{-4}$ m and $d = 0.0083$ m for the second. The graphical results for the latter profiles are shown in Figure 3.17 and Figure 3.18.

The boundary layer characteristics of the profile at $x = 6.00$ m is considered as the reference for our validation. The reason of this choice is due to the similarity with the values adopted by Nironi *et al.* (2015) and the position of the profile. The latter coincides with the position of the source and its characterisation is also useful to the nondimensional operation applied to the concentration field, as we will see in the next section (subsection 3.2.3). Therefore, from this moment on, the subsequent characteristics of the boundary layer will be referred to the experimental data at 6 m from the beginning of the test section.

Due to the fact that the logarithmic region is difficult to estimate from the mean velocity profiles, (Marusic *et al.*, 2013), it is preferable to use the profiles of the streamwise turbulence intensity (Marusic method), as explained in section 1.1.4. We need again an optimisation process to estimate the A_1 and B_1 coefficients of Eq. (1.48). The result of the optimisation is $A_1 = 1.40$ and $B_1 = 1.57$ for the $\overline{u'^2}$ profile. Thanks to this procedure, it is possible to identify the logarithmic region which roughly extends between 0.040 m and 0.100 m along the z -axis, as shown by Figure 3.16. Using wall units, the logarithmic region is located approximately in the interval $512 < z^+ < 1280$. This interval is also predicted by the range $3 Re_\tau^{1/2} < z^+ < 0.15 Re_\tau$

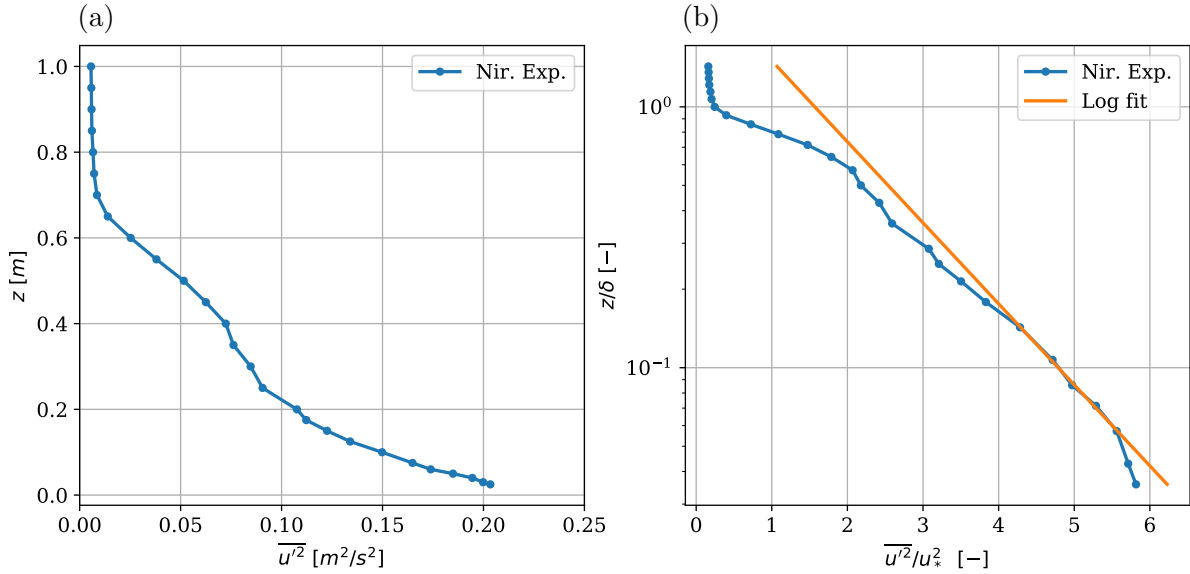


Figure 3.16: Streamwise turbulence intensity profile at $x = 6$ m. The left figure (a) shows the $\overline{u'^2}$ profile along the boundary layer. Whereas the right figure (b) illustrates the nondimensional profile $\overline{u'^2}$ and highlight the logarithmic region thanks to the “Log fit” curve.

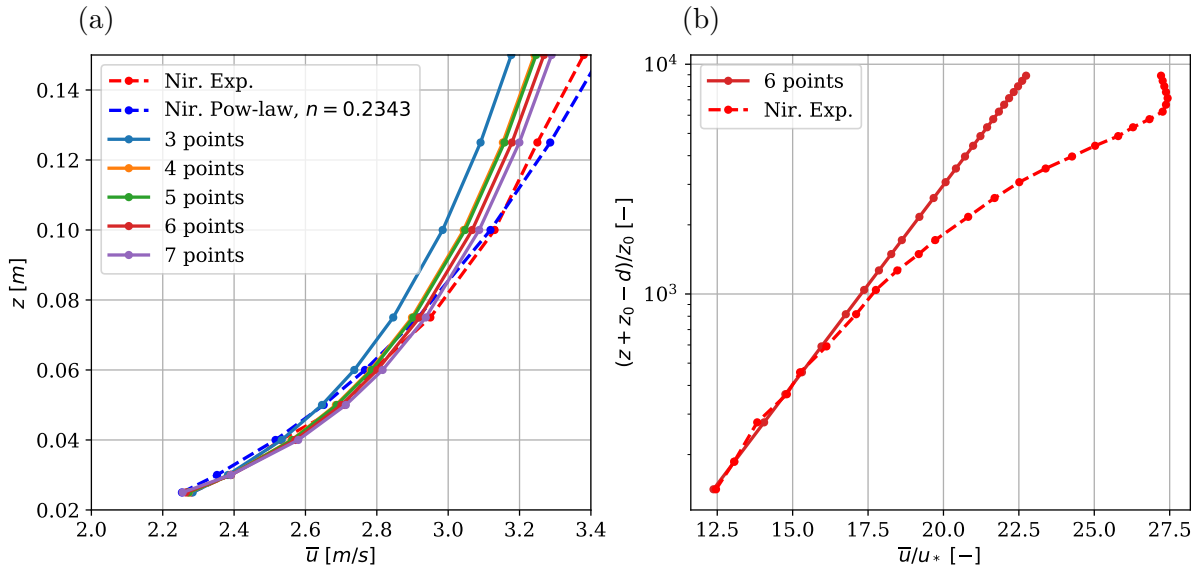


Figure 3.17: Mean velocity profiles at $x = 8$ m. The left figure (a) shows the Nironi experimental profile, the power-law profile and the 5 profiles used for the optimisation procedure with the Method 1. The right figure (b) employs a semi-logarithmic plot to compare the optimal profile (obtained with 6 points) and the Nironi experimental profile.

(Marusic relation) found by the work of [Marusic *et al.* \(2013\)](#) for high-Reynolds number flows. For our experiment, $Re_\tau \approx 9000$ and the logarithmic region results $284 < z^+ < 1350$. This makes us confident in the range found thanks to the experimental data.

Furthermore, the inertial subrange bounds could be estimated from the spectrum of wind field. Knowing the extension of the inertial subrange is fundamental to choose the mesh resolution for the numerical simulation. In fact, a generic rule states that the LES filter needs to be placed in the inertial subrange in order to have good performance of the LES model ([subsection 3.1.1](#)). In our case, the experimental data at the position (6.0, 0.0, 0.150) m, i.e. at the

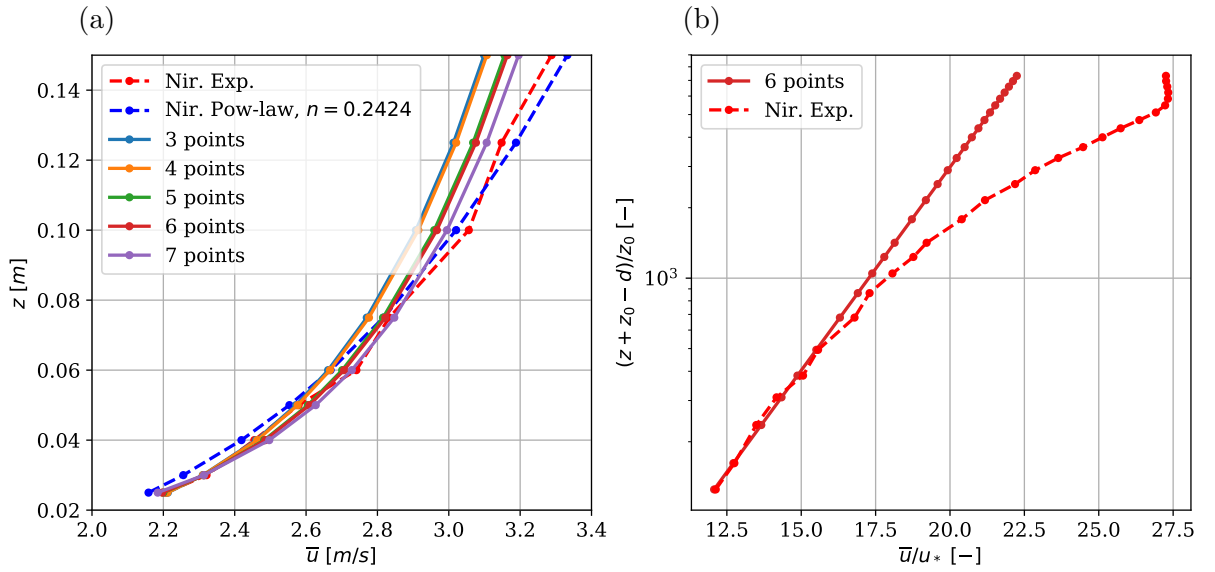


Figure 3.18: Mean velocity profiles at $x = 10$ m. The left figure (a) shows the Nironi experimental profile, the power-law profile and the 5 profiles used for the optimisation procedure with the Method 1. The right figure (b) employs a semi-logarithmic plot to compare the optimal profile (obtained with 6 points) and the Nironi experimental profile.

source position, are used to compute the spectrum of [Figure 3.19](#). The left-hand figure illustrates the spectrum $E(k)$ for the fluctuations u' , v' and w' together with the $-5/3$ -law curve, which identify the inertial subrange. The right-hand figure is used to define the bounds of the inertial subrange. This figure is a compensated spectrum, where $E(k)$ is multiplied by $k^{5/3}$, that is useful to identify the interested region. In fact, when the spectrum diverge from the central horizontal region, it means that the flow is in the energy region at left and in the viscous subrange at right. The regions are delimited respectively by k_c min and k_c max. This method estimates the extension of the inertial subrange between $9 < k < 200 \text{ m}^{-1}$.

Finally, to complete the BL characterisation, it is fundamental to compute also the bulk velocity U_{bulk} , defined by the following equation:

$$U_{\text{bulk}} \equiv \frac{1}{\delta} \int_0^\delta \bar{u}(z) dz \quad (3.61)$$

For the profile at 6.0 m, the bulk velocity is computed from the logarithmic profile with the optimisation parameters and it is equal to 3.62 m/s. As we will see in the [section 3.2.2](#), this velocity will be used to force the numerical flow.

The whole characterisation of the experimental boundary layer is summarised in [Table 3.3](#). It is important to highlight the the methods used to estimate the characteristics of the experimental boundary layer are not universal. Other methods exist and, unfortunately, some methods could estimate different values of the same characteristic. As we will see in more details below, this aspect is a source of uncertainties in the numerical simulation. It makes difficult to compare numerical and experimental results or even two different numerical simulations of the same phenomenon. In the current work, attempts have been made to adopt the same methods for characterising the boundary layer (experimental and numerical). Nevertheless, when it was not possible, it is remarked and discussed.

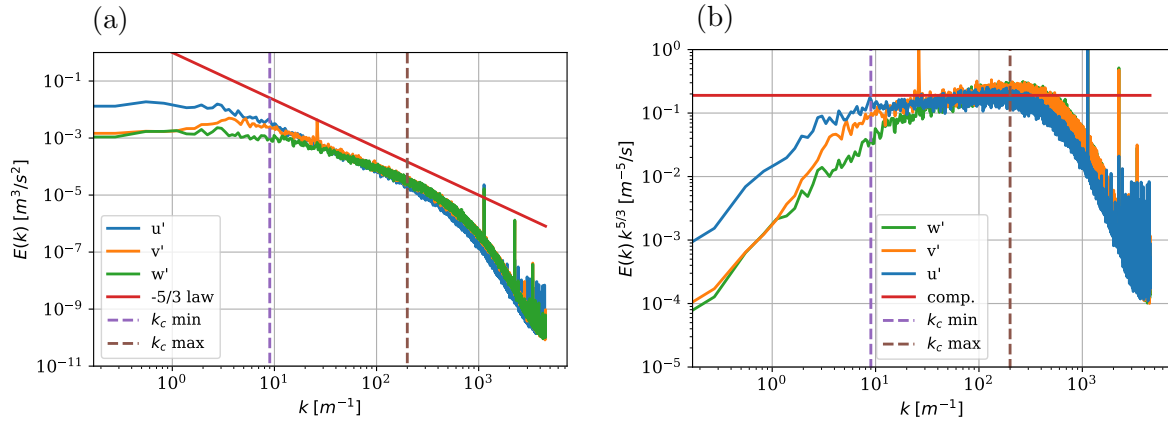


Figure 3.19: Velocity field spectrum for experimental data at $x = 6.0$ m, $y = 0.0$ m and $z = 0.152$ m. Figure (a) shows the spectrum of u' , v' and w' . Moreover, it illustrates the $-5/3$ law and the bounds of the inertial subrange, delimited by k_c min and max. Figure (b) compensates the spectrum and help to delimit the bounds of the inertial subrange.

	$x = 6$ m	$x = 8$ m	$x = 10$ m	Description
δ	0.70 m	0.75 m	0.80 m	BL height
u_*	0.187 m/s	0.183 m	0.181 m	Friction velocity
z_0	1.119×10^{-4} m	1.111×10^{-4} m	1.307×10^{-4} m	Aerodynamic roughness
d	8.5 mm	9.4 mm	8.3 mm	Displacement height
Log-region	$512 < z^+ < 1280$	$501 < z^+ < 1252$	$619 < z^+ < 1548$	Marusic et al. (2013) crit.
Inertial subrange	$9 < k < 200$	–	–	Spectrum crit.
U_{bulk}	3.62	–	–	Bulk velocity

Table 3.3: Complete characteristics of the experimental boundary layer at 3 different streamwise positions.

Extraction of LES inputs

The LES methodology adopted in this thesis, based on periodic simulations, mainly needs two parameters that can be derived from the experiments: z_0 and U_{bulk} . This could be considered as a first conclusion of the BL characterisation.

The first data is the aerodynamic roughness z_0 . The wall models, treated in [subsection 3.1.8](#), only need this input value. Moreover, it could be derived from experimental data, as pointed out in the previous section. We would like to emphasise that frictional velocity u_* is not an input but a result of the interaction between the wall model and the forcing of the flow.

Conversely, the precursor domain needs a force to generate and maintain the atmospheric flow throughout the duration of the simulation. Ultimately, this force is responsible for the pressure gradient. From the practical point of view, the flow is forced thanks to the `meanVelocityForce` OpenFOAM fvOption. According to the OpenFOAM User Guide, this option applies a force to maintain a user-specified volume-averaged mean velocity U_{bulk} , e.g. useful for channel flow cases. Currently it is available only to incompressible flows. U_{bulk} is expressed in continuous and discrete form in Eq. (3.62).

$$U_{\text{bulk}} = \frac{\int_0^H \bar{\mathbf{u}} \cdot \mathbf{n}_x dz}{\int_0^H dz} \approx \frac{\sum_i \bar{\mathbf{u}}_i \cdot \mathbf{n}_x \Delta z_i}{\sum_i \Delta z_i} \quad (3.62)$$

The force that maintain the volume-average mean velocity is applied through a pressure gradient, which value is correct at each time step. Therefore the second input is the U_{bulk} (or *Ubar* in OpenFOAM). This is deduced directly from the experimental velocity profile.

Thanks to these two inputs, it is possible to simulate a neutral atmospheric boundary layer. For our simulations, the inputs used are $z_0 = 1.119 \times 10^{-4}$ m and $U_{\text{bulk}} = 3.68$ m/s.

However, the experimental data also provide useful information to determine the size of the mesh and the dimension of the filter suitable for performing an accurate LES simulation ([subsection 3.4.1](#)). This is the second conclusion of the BL characterisation.

3.2.3 Concentration field characteristics

The concentration field is the result of the passive scalar dispersion throughout the atmospheric flow developed in the wind tunnel. This section introduces the experimental configuration and the concentration measures. The main statistics derived from the measured data are also illustrated. Consequently, it allows to obtain additional inputs and constraints for the LES simulations. The latter are examined in the final part of this subsection.

After a preliminary post-processing, the FID instrument could provide four data: the time t [s], the instantaneous concentration in parts per million [ppm], the ethane flow rate [l/h] and the air flow rate [l/h]. The experimental data was generated by a source located at $h_s = 152$ mm from the ground with a diameter of $\sigma_0 = 6$ mm. The choice is due to the fact that this configuration was judged to be more suitable for validating the LES methodology. In fact, based on a first consideration, the source is not so close to the ground and its diameter is large enough to be fairly simulated without extremely fine mesh around the source. Moreover, the experimental source is characterised by a constant emission.

Through an initial post-processing, the concentration is expressed in $[\text{kg}/\text{m}^3]$ and dimensionless. The constant mass flow rate of the source is a useful data to obtain the nondimensional instantaneous concentration. In fact, the nondimensional concentration is defined by the relation:

$$c^* \equiv \frac{c}{\Delta c} \quad (3.63)$$

where c is the instantaneous concentration in $[\text{kg}/\text{m}^3]$, $\Delta c = \bar{Q}/(\bar{U}_{\text{ref}} \delta^2)$, \bar{Q} is the mean mass flow rate of ethane injected at the source $[\text{kg}/\text{s}]$, \bar{U}_{ref} could be the free stream velocity or

another significant velocity. We have chosen the streamwise mean velocity at the source: $\bar{u}_s = 3.4896$ m/s. Whereas δ is the boundary layer height, it is equal to 0.70 m for our profiles. The nondimensional values allow to better compare the numerical and experimental results, which could have different mean mass flow rates at the source.

Passing to the concentration statistics, the nondimensional mean concentration \bar{c}^* is computed thanks to Eq. (3.57). On the other hand, the nondimensional root mean square (r.m.s.) concentration σ_c^* is given by:

$$\sigma_c^* = \sqrt{\left[\frac{1}{N} \sum_{j=1}^N (c_j^* - \bar{c}^*)^2 \right]} \quad (3.64)$$

where, similarly to Eq. (3.57), N is the number of samples in the time-series.

Transversal profiles of the mean concentration downwind the source are reported in Figure 3.20. Whereas, the vertical profiles are illustrated in Figure 3.21. The vertical profiles were measured on the plume axis, while the transversal profiles are measured at the source height.

The latter profiles are satisfactory reproduced by a Gaussian distribution (see Eq. (1.71)). In particular, the transversal profiles follow Eq. (3.65), while vertical profiles is reproduced by Eq. (3.66).

$$\bar{c}^*(x, y, h_s) = \frac{\bar{U}_{\text{ref}}}{\bar{U}_{\text{adv}}} \frac{\delta^2}{2\pi\sigma_y\sigma_z} \left[1 + \exp\left(-\frac{(2h_s)^2}{2\sigma_z^2}\right) \right] \exp\left(-\frac{y^2}{2\sigma_y^2}\right) \quad (3.65)$$

$$\bar{c}^*(x, 0, z) = \frac{\bar{U}_{\text{ref}}}{\bar{U}_{\text{adv}}} \frac{\delta^2}{2\pi\sigma_y\sigma_z} \left[\exp\left(-\frac{(z+h_s)^2}{2\sigma_z^2}\right) + \exp\left(-\frac{(z-h_s)^2}{2\sigma_z^2}\right) \right] \quad (3.66)$$

Here \bar{U}_{adv} is the advection velocity of the plume, while σ_y and σ_z are the plume spread respectively in y - and z -direction. The previous equations were used to fit the transversal and vertical mean concentration profiles of the experiment and obtain the plume spreads. The result of the fitting procedure is shown in Figure 3.24.

The intensity of concentration fluctuations at the source level is defined as:

$$i_c \equiv \frac{\sigma_c}{\bar{c}} \Big|_{y=0, z=h_s} \quad (3.67)$$

Observing the plot on the right in Figure 3.24, it is possible to observe that the downwind development of the intensity of concentration fluctuations decay. This is particularly true for the source considered (elevated source), for which the effects of source size are larger.

The previous characteristics and observations allow to set the numerical simulation. Moreover, the statistics are useful to compare and validate the LES methodology. They are also essential to interpreted the results, as we will see in section 3.4.

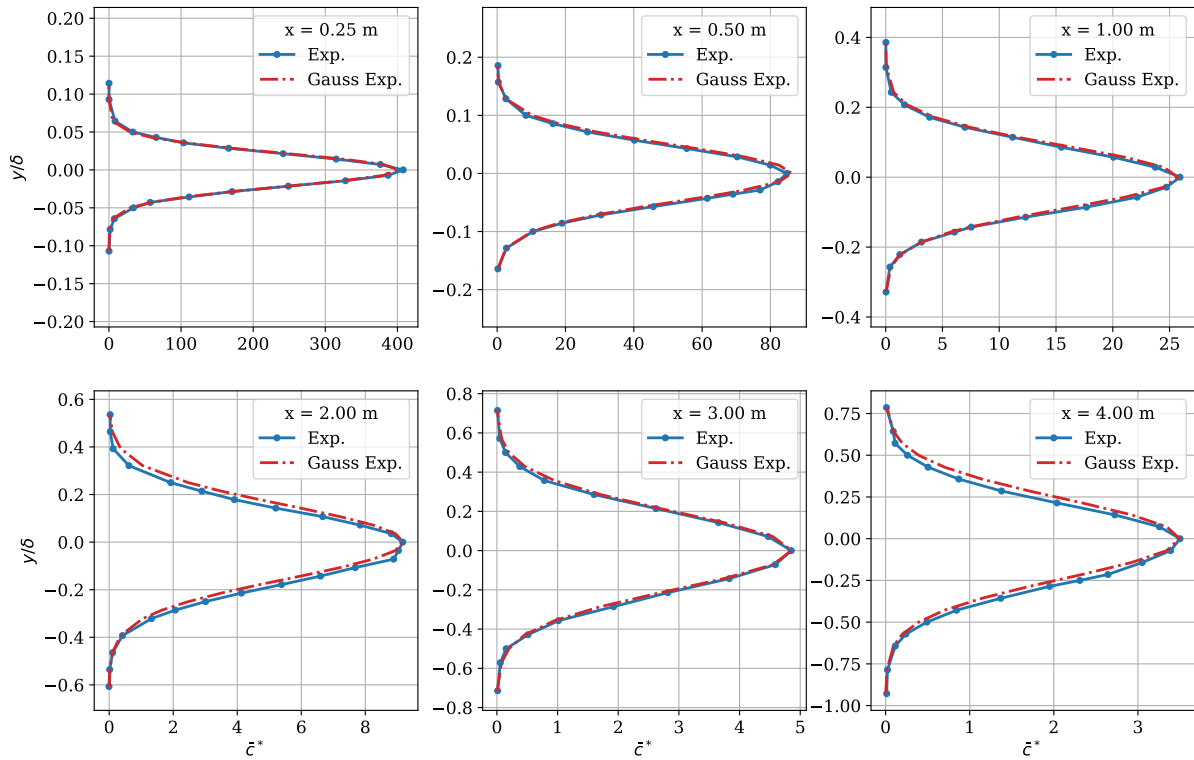


Figure 3.20: Horizontal profiles of nondimensional mean concentration at 6 distances downwind. The profiles are satisfactory fitted by a Gaussian distribution (Gauss Exp. – Eq. (3.65)). Profiles were measured at the source height $h_s = 0.152$ m.

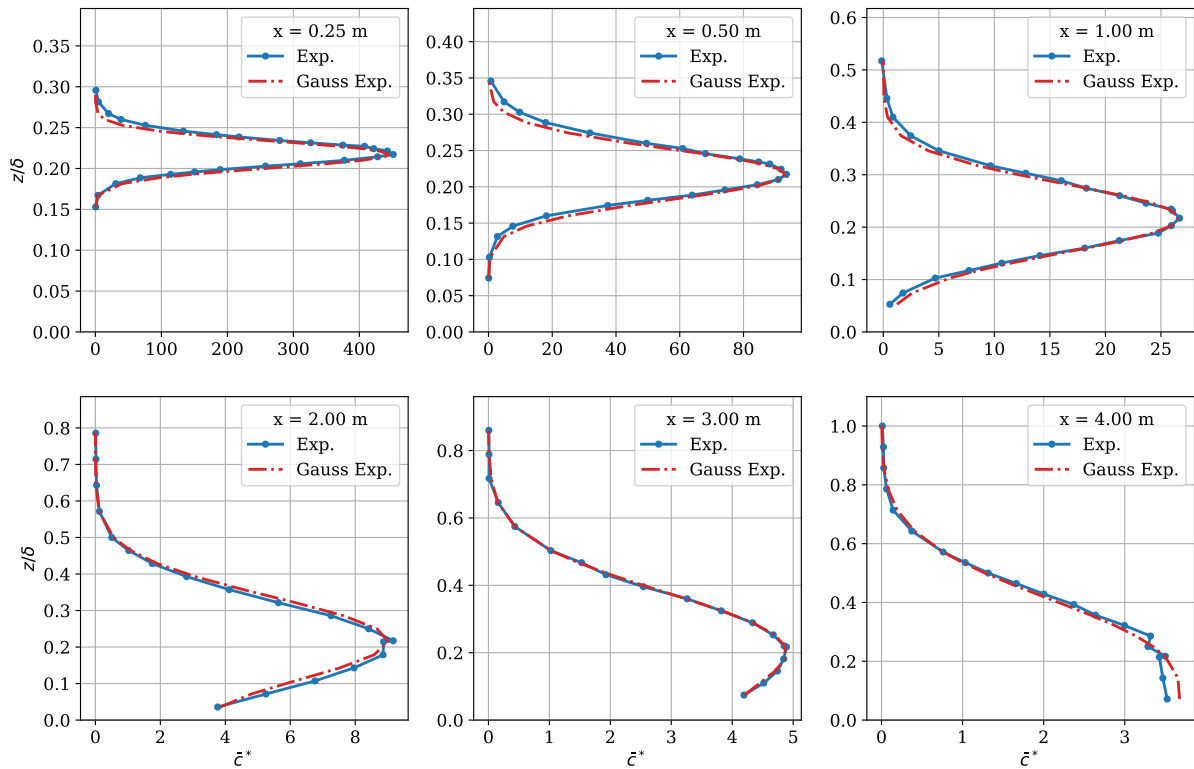


Figure 3.21: Vertical profiles of nondimensional mean concentration at 6 distances downwind. Profiles were measured at the plume axis.

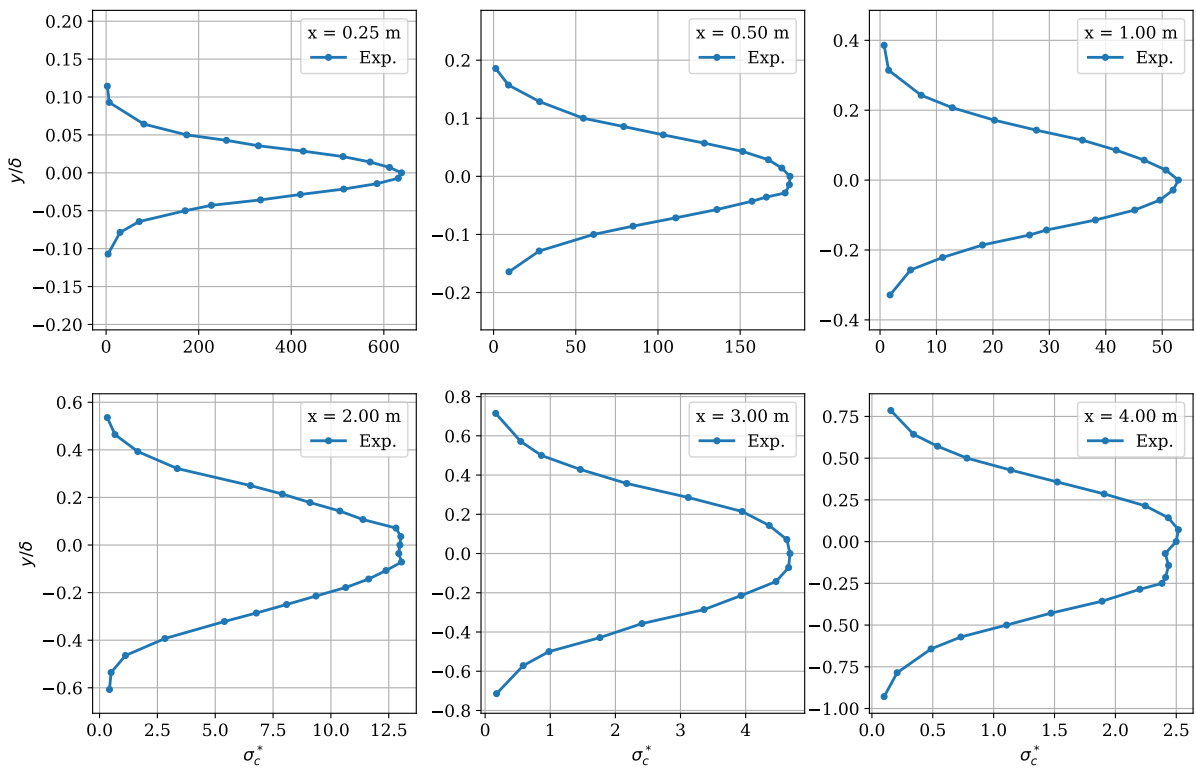


Figure 3.22: Horizontal profiles of nondimensional concentration standard deviation at 6 distances downwind. The profiles were measured at the source height $h_s = 0.152$ m.

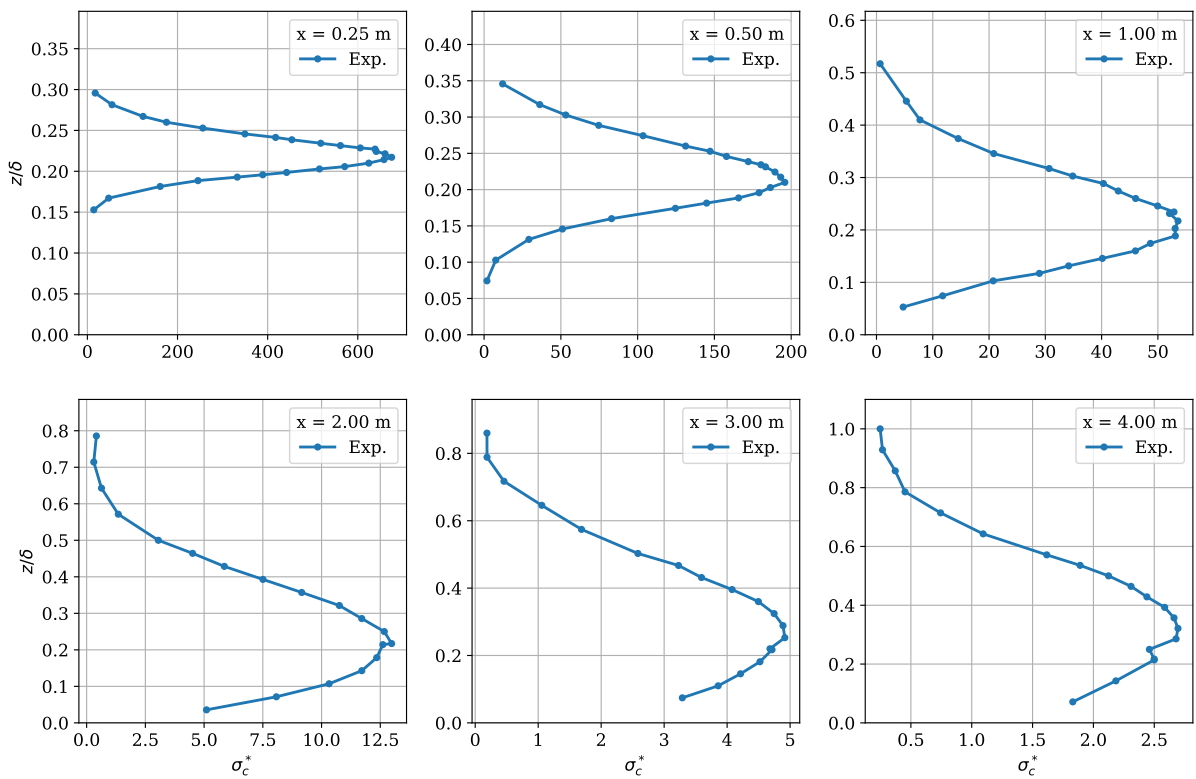


Figure 3.23: Vertical profiles of nondimensional concentration standard deviation at 6 distances downwind. The profiles were measured at the plume axis.

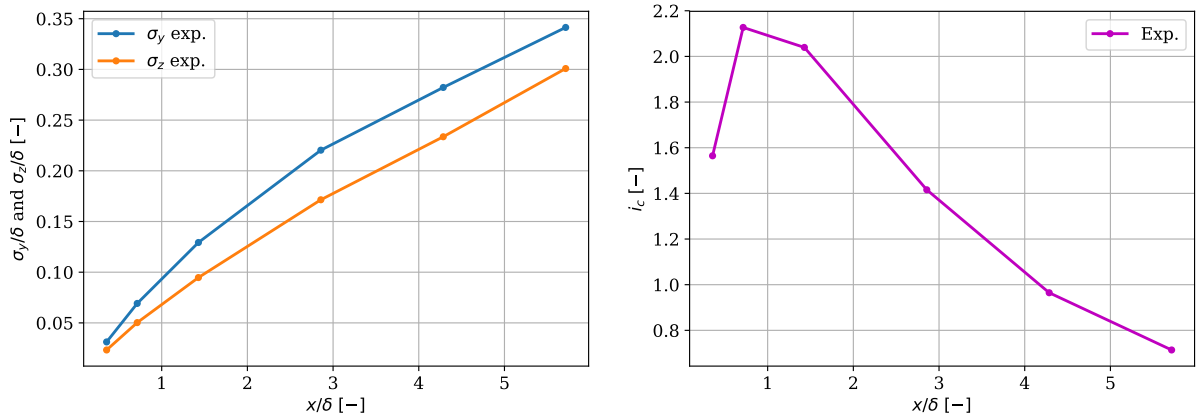


Figure 3.24: In the left-hand side figure, the experimental plume spreads σ_y and σ_z downstream the source are illustrated, while the figure on the right shows the development of the experimental intensity of concentration fluctuations i_c , defined in Eq. (3.67).

Extraction of LES inputs

In order to set the LES simulation, the characteristics of the source and the emissions are fundamental. These are the two main pieces of information that we can have with precision from the dispersion of a passive scalar in a wind tunnel experiment.

In the streamwise direction, the source is situated at 6.00 m (i.e. $x/\delta = 8.57$) from the beginning of the test section. Transversely, it is located at the center of the test section (i.e. $y/\delta = 0.00$). Whereas the source height is 0.152 m (i.e. $z/\delta = 0.22$) from the ground. The final useful information to characterise the source is its diameter, which is $\sigma_0 = 0.006$ m, i.e. $\sigma_0/\delta = 8.57 \times 10^{-3}$.

Information on the release data is usually required at each grid point and each time step for the numerical simulation. The experimental emission is characterised by a constant mass flow rate. Therefore, the numerical source could be considered as a cell or a group of cells that emits constantly over time. So, the mass flow rate is fixed as an arbitrary constant value. It is important to remember that the nondimensional operation allows to compare concentration fields having different mass flow rates at the source. Moreover, according to the “isokinetic” approach (see subsection 3.2.1), the velocity at the source is the velocity of the flow in that cell. It implies that numerical simulation needs to reproduce a wind velocity at the height of the source as similar as possible to the experiment.

The main characteristics derived from the dispersion of a passive scalar in the wind tunnel are summarised in Table 3.4. These characteristics are employed in the numerical setup and yield to some constrains and limits, as we will see in the next section.

x_s	6.00 m	Position of the source in x-coordinate
y_s	0.00 m	Position of the source in y-coordinate
z_s	0.152 m	Position of the source in z-coordinate
σ_0	0.006 m	Source diameter
\bar{Q}	0.001 kg/s	Arbitrary mass flow rate

Table 3.4: Characteristics of the experimental configuration for the dispersion phenomenon useful for setting up the numerical simulation.

3.3 Computational settings

This section is dedicated to the computational settings with the aim of making the LES methodology scientifically reproducible and questionable. The limits of the methods adopted are also discussed. In this way the criteria on which our methodology is based are explicitly expressed. Therefore, various concepts already treated will be recalled and, when necessary, those that have not yet been discussed will be presented.

The following subsections deal with the computational settings in the case of the LES simulation of the Nironi experiment, presented in the previous subsection. Firstly, the domain and the precautions to be taken into consideration when making its choice are discussed in [subsection 3.3.1](#). Then the mesh and its physical and numerical constraints are analysed in [subsection 3.3.2](#). The equations and the solvers employed are presented in [subsection 3.3.3](#), while the boundary conditions are illustrated in [subsection 3.3.4](#). Finally, [subsection 3.3.5](#) is dedicated to the numerical schemes used in our simulations.

3.3.1 Domains

In the current subsection, the types of domain adopted are listed together with the phenomenon that could determine their dimensions. Then, the size of the domain is discussed in a general way. Finally, we focused on the application of the constraints to the Nironi domain. In this way, we could define the criteria for determining the size of the domain.

Having chosen the precursor-successor method and the cyclic-dispersion method (see [subsection 3.1.7](#)), two domains are mainly employed. They have some similarities but also significant differences.

The precursor domain (PD) is focused on generating the inlet flow field of the successor domain. Therefore, its dimensions are principally constrained by the atmospheric flow to be simulated. In particular, the longitudinal and transversal dimensions need to satisfy the correct development of the turbulent structures, while the height of the domain is usually settled considering the height of the obstacles (e.g. buildings) and an appropriate height of the boundary layer in order to allow the development of the physical phenomena of interest. According to the previous considerations, it happens very often that the precursor domain has constraints on longitudinal and transversal dimensions that allow it to be smaller than the successor domain. This characteristic could be useful to reduce the computational time.

The successor domain (SD) is the domain dedicated to study the atmospheric dispersion and the influence of obstacles (e.g. buildings, vegetation, etc) on dispersion. Consequently, it is affected by the precursor domain constraints and more consistently by the obstacles. This domain could be bigger because the experimental domain or the industrial site have bigger dimensions and the dispersion phenomena could extend over long distances.

The cyclic-dispersion domain (CDD) has the same geometrical characteristics than the successor domain. The differences are mainly due to the boundary conditions applied, as we will see in [subsection 3.3.4](#).

In order to determine the size of the domain, [Sagaut \(2006\)](#) propose some basic rules for two classical building blocks of complex flows: the attached equilibrium boundary layer and the plane mixing layer. We are mainly interested to the first flow, which is presented below.

The main rules for determining the domain size are the following two:

- The first rule is based on the idea that the driving mechanisms, i.e. the events responsible for the turbulence production and mean profiles instabilities, must be correctly captured by the simulation to recover reliable results.
- Secondly, the size of the domain must be larger than the correlation length of the fluctuations, in each direction of space. A small domain could produce spurious couplings between the dynamics of the flow and the boundary conditions.

A precise domain size for simulations, as well as a value of mesh size or a number of grid points or cells and their distribution, are not available. These parameters depend on many others parameters, including numerical methods. The rules and constraints suggested are some commonly accepted ideas underlying the design of a large number of published works.

Equilibrium Boundary Layer

The boundary layer shows two different scalings, as described below:

- In the inner layer the viscous length δ_ν is important to describe the dynamics (see also [subsection 1.1.4](#)). The inner layer does not play an important role in the determination of the domain sizes. Nevertheless, it will be very important to the definition of the mesh, as discussed in [subsection 3.3.2](#).
- In the outer layer, the boundary layer thickness δ is the relevant scale. It contributes to determine the domain height H . In fact, the latter needs to be approximately equal to δ . Moreover, the large scales have a correlation length which scales with δ , and are advected in the streamwise direction at a speed roughly equal to $0.8U_\infty$ ([Sagaut, 2006](#)), where U_∞ is the free-stream velocity. As already mentioned, the domain sizes have to be larger than the correlation length of the fluctuations in each direction of space. Consequently the minimum domain sizes of 3δ to 5δ is required in the streamwise direction, while in the spanwise direction the minimum sizes are between 2δ and 3δ . Therefore, privileging the lower limit, it is possible to affirm that the domain must have streamwise and spanwise sizes greater than:

$$\frac{L}{\delta} > 3$$

$$\frac{W}{\delta} > 2$$

and the height is approximately:

$$\frac{H}{\delta} \approx 1$$

The defined sizes of the domain are considered as the physical criterion to simulate an atmospheric flow. This criterion is closely related to the statement that the domain sizes need to be larger than the correlation length of the fluctuations in each direction of space.

Nironi numerical domain

In the previous part, the physical criteria to determine the domain sizes were presented. Here, the practical criteria related to the dispersion phenomenon are illustrated. In fact, the dimension of the domain depends also on the physical phenomenon to be simulated. The two phenomena of interest are the neutral ABL and the dispersion of the passive scalar.

In order to numerically simulate the phenomena, three domain are available: the precursor and successor domain (PD and SD) and the cyclic-dispersion domain (CDD), for more details see [subsection 3.1.6](#). The PD aims to simulate only the atmospheric flow. So it is enough to respect the minimum dimensions suggested by the physical criterion to have an acceptable domain and economise on computational power. Considering $\delta = 0.70$ m, the nondimensional longitudinal L/δ and transversal size W/δ chosen are respectively 3.085 (i.e. $L = 2.160$ m) and 2.057 (i.e. $W = 1.440$ m). Whereas the nondimensional height H/δ is equal to 1.028 (i.e. $H = 0.720$ m). The height selected respects the height constraint (i.e. $H/\delta \approx 1$), being close to its value. On the other hand, the SD and CDD aims to simulate not only the atmospheric flow but also the

dispersion of the passive scalar. In this case, a strong constraint is given by the experimental concentration field to be simulated. Firstly, the longitudinal extension of the domain depends on the furthest data from the source. For the Nironi case, the farthest measurement points are situated at $x/\delta = 5.715$ from the source (see Figure 3.20 and Figure 3.21). Adding a space of $x/\delta = 1.485$ to separate the source and the furthest measurements from the inlet and outlet boundaries (especially important for the successor domain which is not periodic), the longitudinal extension of the domain is $L/\delta = 7.200$. Moreover, the transversal and vertical extension of the furthest experimental profiles are respectively $y/\delta = 1.571$ and $z/\delta = 0.928$. Consequently, the numerical domains could assume the following dimensions: $W/\delta = 2.057$ and $H/\delta = 1.028$.

The criteria illustrated here are schematically summarised by Figure 3.25 and Figure 3.26, while the chosen dimensions are illustrated in Table 3.5.

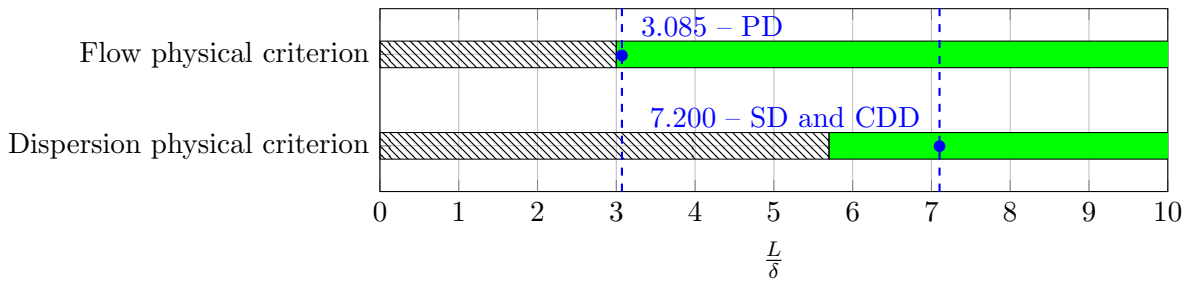


Figure 3.25: Graphic scheme to define the longitudinal dimension of the domain. The green region represents the region that respects the constraint.

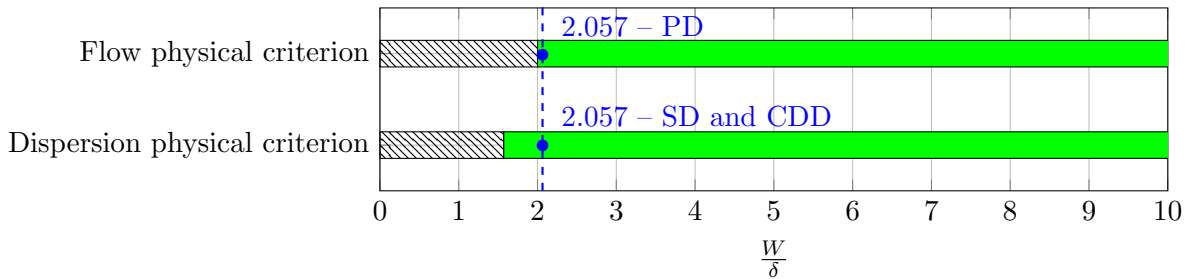


Figure 3.26: Graphic scheme to define the cross-section dimension of the domain. The green region represents the region that respects the constraint.

Precursor Domain (PD)	
$L/\delta = 3.085$	$L = 2.160$ m
$W/\delta = 2.057$	$W = 1.440$ m
$H/\delta = 1.028$	$H = 0.720$ m

Successor Domain (SD) and Cyclic-Dispersion Domain (CDD)	
$L/\delta = 7.200$	$L = 5.040$ m
$W/\delta = 2.057$	$W = 1.440$ m
$H/\delta = 1.028$	$H = 0.720$ m

Table 3.5: Nondimensional and dimensional sizes of numerical domains for Nironi case.

OpenFOAM domain

Entering in the more practical area dedicated to the use of the OpenFOAM, the 6 numerical boundaries presents 3 boundary types. It is pointed out in [Table 3.6](#) and [Table 3.7](#). `Cyclic` boundaries needs a neighbour, while `patch` and `wall` type not. Further the ground boundary employs a `wall` type, specific to solid surfaces. The main difference between the three domains is due to the inlet and outlet boundaries. We need a whole periodic domain in the PD and CDD because it is required to develop the turbulent flow. Whereas the SD, which is the domain used for complex dispersion studies, needs a simple inlet and outlet patch. In fact, it is desired that the passive scalar and the flow, both perturbed by the obstacles, leave the domain.

Boundary ID	Type	Additional information
inlet	<code>cyclic</code>	Neighbour: outlet
outlet	<code>cyclic</code>	Neighbour: inlet
side1	<code>cyclic</code>	Neighbour: side2
side2	<code>cyclic</code>	Neighbour: side1
ground	<code>wall</code>	
top	<code>patch</code>	

Table 3.6: Precursor Domain and Cyclic-Dispersion Domain boundaries and types.

Boundary ID	Type	Additional information
inlet	<code>patch</code>	
outlet	<code>patch</code>	
side1	<code>cyclic</code>	Neighbour: side2
side2	<code>cyclic</code>	Neighbour: side1
ground	<code>wall</code>	
top	<code>patch</code>	

Table 3.7: Successor Domain boundaries and types.

3.3.2 Meshes

In the current subsection, the criteria to define the mesh are treated. Moreover, the adopted meshes are listed and the characteristics of the chosen OpenFOAM mesh are presented.

In our LES methodology, the characteristics of the mesh are constrained by the filter size, the wall model, the passive scalar SGS model and the numerical source characteristics.

Firstly, it is important to remember that the LES filter need to be placed in the inertial subrange or in the dissipation range to correctly model the small scales and resolve the large scales. For the wind tunnel experiment, the inertial subrange was estimated in the interval: $9 \text{ m}^{-1} < k_c < 200 \text{ m}^{-1}$ ([subsection 3.2.2](#)), where k_c is the cut-off wave-number. It is defined according to a practical approach as:

$$k_c = \frac{1}{\Delta}$$

where $\Delta = (\Delta_x \Delta_y \Delta_z)^{1/3}$. This constraint prevents having a filter in the energy-containing range, but it does not prohibit having a filter in the dissipation range.

In order to apply the wall model correctly, the centre of the first cell adjacent to the wall must to be situated in the logarithmic region ([subsection 3.1.8](#)). According to the classical theory, the logarithmic region extends between $z^+ > 30$ and $z/\delta < 0.3$ ([subsection 1.1.4](#)). Nevertheless, more recent studies ([Marusic *et al.*, 2013](#)) have demonstrated that the logarithmic

region can be defined more precisely thanks to Re_τ or through the analysis of longitudinal turbulent fluctuations (all the details in [section 1.1.4](#)).

The third constraint is related to the SGS model adopted for the passive scalar equation ([subsection 3.1.13](#)). It is a simple model based on the subgrid Schmidt number Sc_{sgs} (or equivalently the subgrid Prandtl number), which is a common approach ([Xie *et al.*, 2004b](#); [Ardeshiri *et al.*, 2020](#)). According to [Sagaut \(2006\)](#), in the case of a high cut-off wave-number, i.e. beyond the inertial subrange, the diffusion term of the filtered governing equation of the passive scalar (Eq. [\(3.55\)](#)) may present problems. To remind, the latter term is:

$$\nabla \cdot [(D_c + D_{sgs}) \nabla \tilde{c}]$$

where D_c and D_{sgs} are respectively the molecular diffusivity and the subgrid turbulent diffusivity. The modelling closure adopted to determine D_{sgs} ([subsection 3.1.13](#)) imposes that the LES filter Δ needs to be placed in the inertial subrange. Otherwise, in cases where the velocity field is fully resolved (i.e. the filter is in the dissipation range) and the $Sc \gg 1$, ν_{sgs} goes to zero and consequently $D_{sgs} = 0$. However, the passive scalar spectrum presents a viscous-convective range at wave-number higher than the dissipation range of the velocity spectrum. So the viscous-convective range needs to be modelled, but it is not. This is a condition to avoid when using the current SGS closure model. On the other hand, if the velocity field is not fully resolved and the $Sc \ll 1$, it could happen that the inertial-diffusive range of the passive scalar spectrum is fully resolved and it would not need a model. However, $D_{sgs} \neq 0$ and so it contributes artificially in the diffusion term of the passive scalar equation. Concentrations may be lower due to an artificial disturbance of a term that should not be there. Finally, if $Sc \approx 1$ (as in our case), it is important to estimate the part of the passive scalar spectrum that need to be modelled with a specific SGS model. Therefore, in each of these cases it is important to make a comparison of the velocity and concentration spectra in order to choose the appropriate SGS model, because the model based on the Sc_{sgs} is not suitable for this case.

The numerical source represents the fourth constraint because the source dimension, the size of the cells and the number of cells used determine the accuracy of the numerical field and some expected variations between the statistics of the field. Firstly, the source dimension represents a considerable problem because it can have very small dimension in wind tunnel experiments. Therefore, if we want to proceed with the numerical simulation, it is necessary to adopt a larger numerical source which is suitable for the simulation. [Fackrell and Robins \(1982\)](#) and [Nironi *et al.* \(2015\)](#) have investigated the relation between the source size and the behaviour of the concentration statistics in wind tunnel experiments. A similar behaviour is to be expected numerically. If the numerical source is not of the same dimension than the experimental one (e.g. [Ardeshiri *et al.* \(2020\)](#) simulation), a direct consequence is that the concentration field statistics depend on the source size. Although the mean field is almost completely unaffected by the source dimension, the other statistics of higher order show strong source size dependence ([Nironi, 2013](#)). The mean field reports some difference only close to the source. Conversely, the source size influence extends to a considerable downwind distance for the higher order statistics. For the standard deviation σ_c^* of the concentration field, a strong dependence on the source size is visible near the source. The standard deviation for the smaller source is characterised by significantly higher values. The difference between the standard deviation of sources with different sizes decreases moving downwind and finally vanishes in the far field ([Nironi *et al.*, 2015](#)). Consequently, this constraint suggest that the dimension of the numerical source is the same of the experimental one. Otherwise, it is important to correctly interpreted the results.

Based on our current understanding, the number of cells used to define the numerical source and the size of the source cells lack a well-established criterion in works similar to ours ([Xie *et al.*, 2004a](#); [Ardeshiri *et al.*, 2020](#)). So it is in our interest to try to establish a criterion. Firstly, considering the source as an obstacle and following the tips of CFD user's guide manuals based on empirical tests, it can be established that the source discretisation needs at least 10 cells for

each direction in the two-dimensional space in which the source is defined. If the source is small, it implies very fine meshes as we will see below.

The combination of the previous physical and numerical constraints allow to define the criteria for meshes. Therefore, the criteria are based on 5 explicit constraints:

1. The LES filter, i.e. the dimension of the mesh, need to be placed in the inertial subrange (preferable) or in the dissipation range.
2. The first cell adjacent to the wall must be situated in the logarithmic region.
3. If a Sc_{sgs} approach is adopted to close the filtered passive scalar equation, the LES filter need to be placed in the inertial subrange.
4. If possible, the numerical source dimension needs to be the same dimension as the experimental one. Otherwise, the results must be interpreted based on the literature studies (e.g. [Nironi *et al.* \(2015\)](#)).
5. If possible, at least 10 cells should be used to define the numerical source.

For convenience, the 5 constraints are grouped into 4 mesh criteria. The constraints 1) and 2) define respectively the “LES filter” and the “Wall Model” criteria. The “SGS model” is defined by the constraint 3). Whereas the constraints 4) and 5) define the “Source” criterion.

Applying the mesh criteria to the Nironi experiment and considering an homogeneous mesh, [Figure 3.27](#) is obtained. It summarises the mesh criteria applied to the Nironi experiment and it will be useful for objectively evaluating the meshes adopted. In order to compare the constraints, a cell size in wall unit Δ^+ is employed. Therefore, thanks to the analysis of [subsection 3.2.2](#), the inertial subrange extends between $64 < \Delta^+ < 1422$. Thanks to the LES filter criterion, the inertial subrange and the dissipation range becomes an acceptable interval which respects the mesh criterion, i.e. $\Delta^+ < 1422$. The Wall Model criterion defines the log-region, which is constituted of three intervals because we have presented three approaches to determine its extension ([subsection 3.2.2](#)). In the current study, we consider the Marusic relation as the acceptable interval: $284 < \Delta^+ < 1350$ (i.e. something between the classical theory and the Marusic method, for details see [subsection 1.1.4](#)). The SGS model criterion considers the inertial subrange as the acceptable interval: $64 < \Delta^+ < 1422$. Finally, the Source criterion establishes the region of acceptability for the source. The experimental source diameter is $\Phi = 0.006$ m. Consequently $\Phi^+ = 76.8$ and $\Phi^+/10 = 7.68$. The latter value corresponds to 0.6 mm, which is extremely small. Unfortunately, in this case, the constraints 4) and 5) disagree because $\Phi^+/10$ is smaller than the other acceptable intervals. As a result, there is no interval that can satisfy all criteria.

Consequently, for the Nironi mesh, the acceptable region which almost completely meets the mesh criteria (i.e. 3 over 5 constraints are respected) is the log-region defined through the Marusic relation: $284 < \Delta^+ < 1350$. All the meshes found in this region respect the physical and numerical criteria on which the adopted models are based. Remember that this region of acceptability is conditioned to the interpretation of results in view of a larger numerical source.

ID	Δ^+	Δ_z^+	z_p^+
m24	352	308	154
m12	176	154	77
m06	88	77	39

Table 3.8: Cell sizes, cell heights and cell-centre heights adjacent to the wall in wall units.

According to similar works (e.g. [Xie *et al.* \(2004b\)](#); [Ardeshiri *et al.* \(2020\)](#)), three meshes have been chosen and they are resumed in [Table 3.9](#). The meshes are constituted by homogeneous

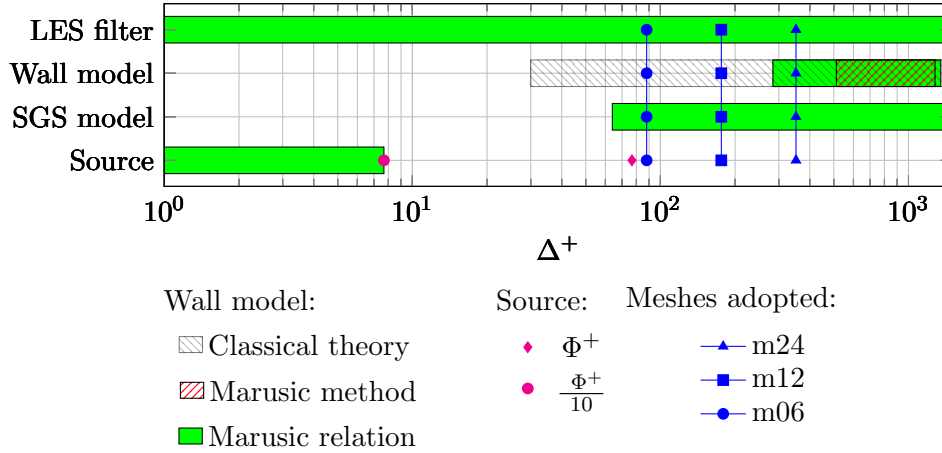


Figure 3.27: Mesh criteria.

hexahedral cells. The cells are regular on y - and z -coordinates, while it has a ratio of 1.5 with respect to the x -coordinate. This choice allows to have a regular mesh on the transverse and vertical plane, favouring dispersion (Ardeshiri *et al.*, 2020). Conversely, it is possible to have a coarse mesh in the x -coordinate without disadvantages for the dispersion and allowing to capture the longitudinal turbulent structures. The n_x , n_y and n_z are the number of cells respectively in x -, y - and z -coordinate. Therefore, the meshes m24, m12 and m06 have respectively 285 600, 2 284 800 and 18 278 400 cells. In order to include these meshes in Figure 3.27, the cell size in wall unit Δ^+ is computed for each mesh. The results are illustrated in Table 3.8 together with the cell heights z^+ and cell-centre heights adjacent to the wall z_p^+ in wall units.

The choice of the meshes was based on what was adopted by similar cases in the literature, in which even finer meshes were used, as previously mentioned. In fact, finer meshes are needed to respect the constraint 4) with an adequate representation of the source. Nevertheless, it implies the inadequacy of some fundamental models in our methodology (e.g. the wall model and the passive scalar modelling closure). Therefore, if we want to respect the mesh criteria, only the mesh m24 is appropriate. For this mesh, the numerical source adopted is bigger than the experimental one and only one cell is used to define it. These choices do not allow to respect the source criterion and will lead to the need for a careful interpretation of the results. Meshes m12 and m06 do not match the source criterion and the wall model criterion. So the interpretation of the results of these meshes needs even more attention. In order to evaluate the behaviour of the meshes that respect and that do not respect the criteria, these three meshes are analysed in subsection 3.4.1.

ID	$n_x \times n_y \times n_z$	Δ_x	Δ_y	Δ_z	k_c
m24	$140 \times 60 \times 34$	0.036 m	0.024 m	0.024 m	36.40 m^{-1}
m12	$280 \times 120 \times 68$	0.018 m	0.012 m	0.012 m	72.80 m^{-1}
m06	$560 \times 240 \times 136$	0.009 m	0.006 m	0.006 m	145.60 m^{-1}

Table 3.9: Characteristics of the Nironi case meshes.

OpenFOAM mesh

In OpenFOAM, the mesh was generated using the mesh generation utility, `blockMesh`. Consequently, the adopted mesh is made up of homogeneous hexahedral cells on the whole domain, as illustrated by [Figure 3.28](#).

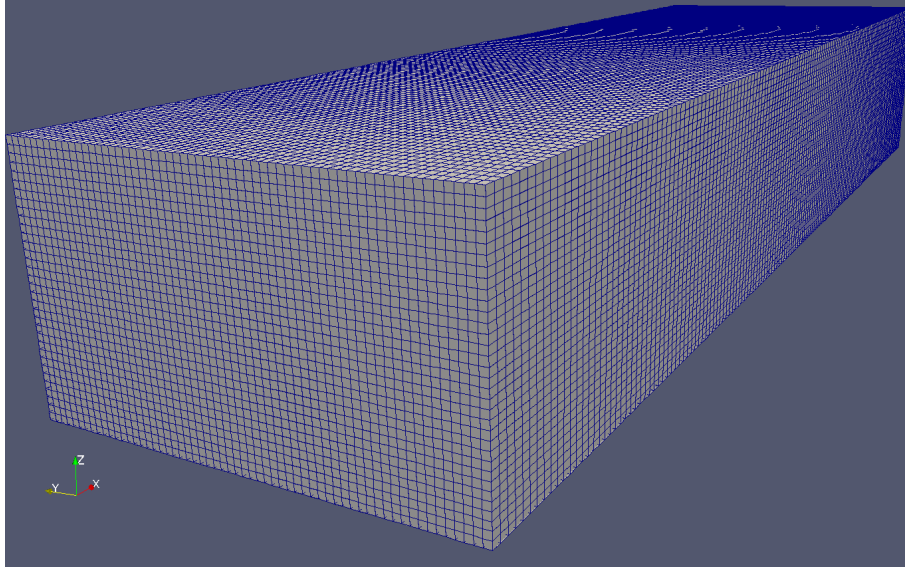


Figure 3.28: Generic mesh for Nironi case.

3.3.3 Equations and solver

The current section is dedicated to describe the solvers and the equations used to compute the wind field and the concentration field for the LES methodology using OpenFOAM.

The solver used to simulate the wind field, i.e. to solve the Navier-Stokes equations for the neutral SBL, is `pimpleFOAM` with some minimal modifications to allow the use of the wall models treated in [subsection 3.1.8](#). It is the PIMPLE version available in OpenFOAM. This algorithm is a transient solver for incompressible turbulent flow of Newtonian fluids ([Holzmann, 2016](#)). The algorithm of the solver merges two classical solvers: SIMPLE and PISO. SIMPLE is the acronym for Semi-Implicit Method for Pressure Linked Equations. It allows to couple the Navier-Stokes equations with an iterative procedure ([Patankar, 2018](#)). On the other hand, PISO is the acronym for Pressure-Implicit with Splitting of Operators and it is an efficient method to solve the Navier-Stokes equations in unsteady problems ([Issa, 1986](#)). Returning to the solver used here, a convenient way to think about the PIMPLE algorithm is to imagine it as a SIMPLE algorithm for every time step, where outer correctors are the iterations, and once converged will move to the next time step until the solution is complete. Better stability is obtained from PIMPLE over PISO for this reason, especially when dealing with large time steps where the maximum Courant number may consistently be above 1 or when the nature of the solution is inherently unstable.

For the LES methodology, it was needed to modify the `pimpleFOAM` solver to introduce the effect of the wall model. Therefore, the solver developed was named `ABLSolverLIA` (i.e. “ABL Solver for LES In Atmosphere”) and it is used to solve the continuity equation:

$$\nabla \cdot \mathbf{u} = 0 \quad (3.68)$$

and the momentum equation:

$$\frac{\partial \mathbf{u}}{\partial t} + \mathbf{u} \cdot \nabla \mathbf{u} - \nabla \cdot \mathbf{R} + \nabla \cdot \mathbf{R}_{\text{wall}} = -\nabla p + \mathbf{S}_u \quad (3.69)$$

where \mathbf{u} is the filtered velocity, p is the modified filtered pressure and \mathbf{R} is the stress tensor, which contains the dissipative term and the modelling closure. \mathbf{R}_{wall} is the stress tensor linked to the wall model and the \mathbf{S}_u is a momentum source. These expressions are equivalent to Eq. (3.4) and Eq. (3.13) presented in subsection 3.1.2.

The SGS stress tensor, which is included in the stress tensor \mathbf{R} , needs to be modelled to achieve the closure of the Navier-Stokes equations. The WALE model, described in subsection 3.1.5, was chosen because its characteristics are more suitable for carrying out a LES simulation with a rough and with complex geometries (Nicoud and Ducros, 1999).

The wall model wants to influence the tensor \mathbf{R} . In fact, it could be expressed as:

$$\nabla \cdot (\mathbf{R} + \mathbf{R}_{\text{wall}}) \quad (3.70)$$

Our wall model introduces a shear stress, typical of a rough wall, only in the wall patch. Moreover, it was found that it is important to fix the components parallel to wall of the velocity \mathbf{u}_{\parallel} in order to apply correctly the wall model. The component perpendicular to the wall is zero, while the other two components are approximated thanks to the gradients registered at the upper cells (Han *et al.*, 2016). This effect was introduced by the boundary condition `velocityABLWallFunction`. In this way, we arrive to the expression of \mathbf{R}_{wall} :

$$\mathbf{R}_{\text{wall}} = \begin{bmatrix} 0 & 0 & \tau_{13} \\ 0 & 0 & \tau_{23} \\ \tau_{13} & \tau_{23} & 0 \end{bmatrix} = \begin{bmatrix} 0 & 0 & \tau_{xz} \\ 0 & 0 & \tau_{xy} \\ \tau_{xz} & \tau_{xy} & 0 \end{bmatrix} \quad (3.71)$$

where the two components of the wall stress tensor are given by the wall model, as observed in subsection 3.1.10, subsection 3.1.11 and subsection 3.1.12.

Secondly, the solver used to simulate the concentration field is the `scalarTransportFOAM`. It is a basic solver which resolves a transport equation for a passive scalar, using a user-specified velocity field. In our case, the velocity field computed by the `ABLSolverLIA` is used. The passive scalar transport equation solved is:

$$\frac{\partial c}{\partial t} + \mathbf{u} \cdot \nabla c = +\nabla \cdot (D_{\text{eff}} \nabla c) + S_c \quad (3.72)$$

where c is the filtered passive scalar, D_{eff} is the effective diffusivity and S_c is the passive scalar source.

Similarly to Eq. (3.56), the effective diffusivity D_{eff} of the solver is composed by two terms:

$$D_{\text{eff}} = \alpha_l \nu + \alpha_t \nu_t$$

where α_l and α_t are two coefficients respectively related to the molecular diffusivity and turbulent diffusivity. In turbulent flows, like in our case, the turbulent diffusivity normally overwhelms the molecular diffusivity. Therefore, we focused on the estimation of the latter, leaving the OpenFOAM default value of the first. According to subsection 3.1.13, the turbulent diffusivity is none other than the SGS diffusivity D_{sgs} . Consequently:

$$\alpha_t = \frac{1}{S_{c_{\text{sgs}}}} = \frac{1}{Pr_{\text{sgs}}} \quad (3.73)$$

After some trials, the SGS Schmidt number $S_{c_{\text{sgs}}}$ was estimated equal to 0.25. In fact, the modelling closure adopted needs to estimate the appropriate value of $S_{c_{\text{sgs}}}$ for our simulation.

Finally, the solver could introduce a source thanks to the term S_c . Therefore, the OpenFOAM function `scalarSemiImplicitSource` is used to fix an arbitrary emission mass flow rate (i.e. 0.001 kg/s). Using this function, the passive scalar source is decomposed into an explicit S_e and a linearised implicit contributions:

$$S_c = S_e + S_i c \quad (3.74)$$

where the coefficient S_i needs to be less than or equal to zero. In our case, $S_e = 0.001 \text{ kg/s}$ and $S_i = 0$.

3.3.4 Boundary and initial conditions

Here we treat the boundary conditions and the initial conditions applied to the precursor, successor and cyclic-dispersion domain in OpenFOAM.

Table 3.10, Table 3.11 and Table 3.12 show the boundary conditions (BCs) and the initial conditions (ICs) of the five OpenFOAM input variables of the current simulations, i.e. the wind velocity \mathbf{u} , the modified pressure \mathbf{p} , the SGS viscosity \mathbf{nut} , the wall model stress tensor \mathbf{Rwall} and the passive scalar \mathbf{c} . The two boundary conditions specifically developed for the methodology are presented here. For an explanation of the standard boundary conditions, it is suggested to consult the OpenFOAM documentation.

The ground boundary condition employs the `velocityABLWallFunction` condition (developed together with the rough wall boundary condition) for \mathbf{u} . It fixes to zero the velocity normal to the wall surface. The specified surface total stress creates the surface drag useful to generate the velocity profile. However it is required to create an appropriate surface normal velocity gradient at $z_{p,1/2}$ level so that the SGS model has meaningful gradient to be used in its production term. It is highlighted that z_p is the height of the cell adjacent to the wall and $z_{p,1/2}$ is $z_p/2$ or the cell center height (if the cell is an hexahedron). Therefore, we compute the surface normal gradient at z_p level and use the same gradient at $z_{p,1/2}$ level. It is realised by specifying a surface parallel velocity that creates a surface normal gradient at $z_{p,1/2}$ equal to that at z_p .

The wall model is responsible of the generation of the surface shear stress at the ground boundary. In our simulations, the boundary condition related to the Wall Model (WM) (called `MasonCallenNeutral`, `ThomasWilliamsNeutral` or `XieElAlNeutral`) is applied thanks to the variable `Rwall` created only in order to introduce this effect (subsection 3.3.3).

The initial conditions (ICs) of the precursor domain (PD) and of the cyclic-dispersion domain (CDD) are 0 for all the variable. In fact, any IC between zero and the free-stream condition could be chosen for all variables. In fact, the flow of the PD is developed from a reasonable IC thanks to the forcing `meanVelocityForce` and the boundary conditions applied. At the end, this combination will develop the desired flow if all the parameters are correctly settled.

Conversely, the ICs of the successor domain (SD) are the flow developed in the precursor domain (PD) having reached the convergence of the wind field statistics. Indeed, the PD simulation is stopped only when the main statistics of the flow (i.e. principally mean velocity and standard deviation of fluctuations) reach a convergence interval which means that the flow is fully developed.

	\mathbf{u}	\mathbf{p}	\mathbf{nut}	\mathbf{Rwall}
inlet	cyclic	cyclic	cyclic	cyclic
outlet	cyclic	cyclic	cyclic	cyclic
side1	cyclic	cyclic	cyclic	cyclic
side2	cyclic	cyclic	cyclic	cyclic
ground	<code>velocityABLWallFunction</code>	<code>zeroGradient</code>	<code>zeroGradient</code>	WM
top	slip	<code>zeroGradient</code>	<code>zeroGradient</code>	<code>fixedValue</code>
I.C.	(0, 0, 0)	0	0	(0, 0, 0, 0, 0)

Table 3.10: Precursor Domain (PD) boundary conditions.

	u	p	nut	Rwall	c
inlet	timeVaryingMappedFixedValue	zeroGradient	calculated	cyclic	fixedValue
outlet	inletOutlet	fixedValue	calculated	cyclic	inletOutlet
side1	cyclic	cyclic	cyclic	cyclic	cyclic
side2	cyclic	cyclic	cyclic	cyclic	cyclic
ground	velocityABLWallFunction	zeroGradient	zeroGradient	WM	zeroGradient
top	slip	zeroGradient	zeroGradient	fixedValue	zeroGradient
I.C.	U (PD)	p (PD)	nut (PD)	Rwall (PD)	0

Table 3.11: Successor Domain (SD) boundary conditions.

	u	p	nut	Rwall	c
inlet	cyclic	cyclic	cyclic	cyclic	fixedValue
outlet	cyclic	cyclic	cyclic	cyclic	inletOutlet
side1	cyclic	cyclic	cyclic	cyclic	cyclic
side2	cyclic	cyclic	cyclic	cyclic	cyclic
ground	velocityABLWallFunction	zeroGradient	zeroGradient	WM	zeroGradient
top	slip	zeroGradient	zeroGradient	fixedValue	zeroGradient
I.C.	(0, 0, 0)	0	0	(0, 0, 0, 0, 0, 0)	0

Table 3.12: Cyclic-Dispersion Domain (CDD) boundary conditions.

3.3.5 Numerical schemes

In the current section, the OpenFOAM numerical schemes useful for our simulations are described and then the chosen schemes are specified.

From the numerical point of view, the Navier-Stokes equations and the transport of the passive scalar equation are discretised through a standard Gauss finite volume integration. Gaussian integration is based on summing values on cell faces, which must be interpolated from cell centres. For this purpose, a **linear** interpolation was primarily chosen.

In OpenFOAM, the **fvSchemes** dictionary in the **system** directory sets the numerical schemes for the simulations. Inside this directory, the sub-directory **gradSchemes** is used to set gradient terms. The default discretisation scheme that is used for gradient terms is **Gauss** and the interpolation scheme is **linear**. This combination, employed on our simulations, results into second order scheme.

The sub-directory **divSchemes** contains divergence terms, i.e. of the form $\nabla \cdot$, excluding Laplacian terms of the generic form $\nabla \cdot (\Gamma \nabla \cdot)$ (here Γ is a generic constant or coefficient). The current schemes includes both advective flux, e.g. $\nabla \cdot (\mathbf{U} c)$, where \mathbf{U} provides the advected flux, and other terms, that are often diffusive in nature, e.g. $\nabla \cdot \nu (\nabla \mathbf{U})^T$. The non-advective terms generally employ a **Gauss linear** scheme. In fact this was also our choice. It denotes a **Gauss** integration and a **linear** interpolation, that results into second order and unbounded behaviour.

The treatment of the advective term is more challenging in CFD and the options are more diversified. The keyword identifier for the advective terms are usually of the form **div(phi, ...)**, where **phi** usually denotes the (volumetric) flux of velocity on the cell faces for constant-density flows and the mass flux for compressible flow, e.g. **div(phi, U)** is the advective term of velocity or **div(phi, c)** is the advective term of the passive scalar. In this case, the schemes are all based on Gauss integration, using the flux **phi** and the advected field being interpolated to the cell faces by one of the selected schemes. Here, we focus on three of them:

- **linear**: second order, unbounded
- **upwind**: first-order bounded, typically too inaccurate to be recommended.

- **limitedLinear**: **linear** scheme that limits towards **upwind** in regions with gradients that change rapidly. It requires a coefficient, which varies between 0 and 1. The value 1 is strongest limiting. Conversely, it tends to **linear** as the coefficient tends to 0.

The advective divergence scheme used for the advective term of velocity is **Gauss linear**, i.e. a second order unbounded scheme. Conversely, for the passive scalar transport was used the **Gauss limitedLinear 0.2** scheme, so a second-order unbounded scheme.

Before dealing with the sub-directory **laplacianSchemes**, it is important to explain the **snGradSchemes** sub-directory that contains surface normal gradient terms because they are required to compute a Laplacian term using Gauss integration. A surface normal gradient is evaluated at a cell face. It is the component, normal to the face, of the gradient of values at the centres of 2 cells that the face connects. The basis of the gradient calculation at a face is to subtract the value at the cell centre on one side of the face from the value in the centre of the other side and divide by the distance. The calculation is a second order accurate for the gradient normal to the face, if the vector connecting the cell centres is orthogonal to the face, i.e. they are at right-angles. The **orthogonal** scheme makes this. Orthogonality requires a regular mesh. Nevertheless, our cases could present non-hexahedral cells which does not allow to use orthogonal scheme. Therefore, to maintain second-order accuracy, an explicit non-orthogonal correction can be added to the orthogonal component, known as the **corrected** scheme. It is the scheme adopted. For the Laplacian term, the **Gauss** scheme is the only choice of discretisation and it requires both an interpolation scheme for the diffusion coefficient, i.e. ν_{eff} or D_{eff} in our case, and a surface normal gradient scheme. The selection of these schemes determines a specific numerical behaviour for our simulations: unbounded, second order and conservative.

Finally the first time derivative ($\partial/\partial t$) scheme is specified in the **ddtSchemes** sub-directory. There are mainly 4 schemes: **Euler**, **localEuler**, **CrankNicholson ψ** and **backward**. The discretisation scheme chosen is the **backward** scheme, a second order implicit scheme.

3.3.6 Conclusions

In the current section, the computational setting for the LES methodology was defined. Together with it, a series of physical and numerical criteria have been developed and listed. They allow us to objectively evaluate our simulation, understanding the possible limits.

Therefore, after the overview of the LES simulation for the dispersion in the neutral SBL, the presentation and characterisation of the wind tunnel experiment to simulate and the computational setting based on the developed criteria, the next step is to combine all these concepts to concretely define the LES methodology. Finally, the methodology will be used to simulate the [Nironi \(2013\)](#) wind tunnel experiment and carry out the final process of numerical-experimental comparison and validation. The final section of this chapter, i.e. [section 3.4](#), is focused on this.

3.4 LES methodology, sensitivity study and results

In this part of the thesis, the aim is to simulate the neutral atmospheric boundary layer (ABL) and the atmospheric dispersion of a passive scalar through an LES approach and validate the results thanks to a wind tunnel experiment. In the previous sections, it was observed that numerical set-up needs physical and numerical criteria to properly choose the numerical parameters and to understand the quality and the limits of the choices made. These criteria are well known by the scientific community but are not always presented explicitly. The lack of explicit criteria can lead to confusion among researchers (above all between novice ones) who are interested in this branch. Therefore, the LES methodology developed aims not only to reproduce numerically the physical phenomena but also to make explicit the main criteria used to parametrise the numerical model.

The current methodology could be graphically summarised by the diagram presented in [Figure 3.29](#). Firstly, the input parameters need to be settled thanks to the experimental data related to the characteristics of the atmospheric flow and of the wall. Then the equations to solve an incompressible neutral ABL and the transport of a passive scalar are chosen. Consequently, a SGS model needs to be considered together with the passive scalar SGS model. Moreover, the roughness wall, typical of atmospheric flows, is not resolved but modelled. In this way, a wall model needs to be taken into account. Before to launch the simulation, it remains to choose an adequate mesh and appropriate numerical schemes.

In this process, that will lead to obtain a numerical resolution of the physical problem in question, it is our intention to emphasise the contribution of the current study to the determination of the inlet parameters, the implementation of the wall model and the explicit presentation of the physical criteria that determine the dimension of the domain and the resolution of the mesh.

Here the main contributions (marked by red in [Figure 3.29](#)) are resumed:

1. The determination of the numerical domain is conducted thanks to two types of physical criteria. The first is related to the flow and was fixed through the [Sagaut \(2006\)](#) suggestions. On the other hand, the second criterion concerns the physical characteristics of the dispersion plume. Considering and respecting the criteria, the three dimensions of the domain are fixed (i.e. length L , width W and height H). For more details, see [subsection 3.3.1](#)
2. Considering an homogeneous mesh, the determination of the proper mesh resolution is not trivial for the physical phenomena under analysis. In this case, four mesh criteria are involved. The first aims to establish the extension of the inertial subrange and the dissipation range thanks to the experimental spectrum of the turbulent fluctuations. This is the region where the LES filter needs to be placed for an adequate resolution of the large scales. The second criterion is focused on determining the extension of the logarithmic zone in the inner layer. This zone defines the mesh size acceptable to use a wall model (WM) based on the wall similarity hypothesis. The extension of the zone could be estimated thanks to classical theoretical considerations or to more recent [Marusic *et al.* \(2013\)](#) approach. The third criterion relates the SGS model adopted for filtered passive scalar equation and its range of validity. In fact, the model based on the subgrid Schmidt number is valid in the inertial subrange. Finally, the fourth criterion concerns the size of the mesh suitable for numerically representing the source of the passive scalar. It is important to consider the real dimension of the source and the appropriate dimension of the cells that surround it. In order to simulate correctly the passive scalar dispersion near the source, the cells need to be smaller than the size of the source (at least 10 times smaller). Indeed it is desired to reproduce the turbulent structures related to small scales, which contribute to dispersion. The latter criterion penalises the LES methodology when it is applied to

simulate the dispersion phenomenon in the wind tunnel at low Re number. However, in a real scenario, the four criteria find can be satisfied by a group of mesh sizes. For more detail, see [subsection 3.3.2](#).

3. The implementation of the wall model (WM) based on the wall similarity hypothesis was conducted because no LES rough wall model was available in the version of the CFD code adopted, i.e. OpenFOAM v1912. It mainly regards the implementation of a wall shear stress and velocity in the region adjacent to the wall. The effect of the first variable is introduced in the numerical solver by a variable which is added in the momentum equations. For more detail, see [subsection 3.3.3](#).

Finally, taking into consideration the validation process, the comparison of the results is conducted through the spatial and temporal statistics of the velocity field and the temporal statistics of the concentration fields. Moreover, we want to give some recommendations to present the results. The velocity field could be shown without any adimensionalisation. In fact, the numerical simulation can reproduce the wind tunnel experiment at the same scales. The Reynolds number of the SBL experiments are relatively low and the dimensions of the domain are reproducible numerically without similarities or other scaling operations. This choice make it easier to identify any errors resulting from non-compliance with physical and numerical criteria and to judge the reproducibility of the results. Furthermore, a nondimensional presentation of the results can mask some important errors and lead to a wrong interpretation of the numerical simulation. On the other hand, the concentration field needs a convenient adimensionalisation in order to compare the results and draw physical conclusions. In addition, it could advantage the identification of errors.

The comparison, the validation, the presentation and the discussion of the results are investigated in the current section. In [subsection 3.4.1](#), a sensitivity study is conducted in order to test the physical criteria adopted and support our choices. Firstly, a mesh sensitivity study is presented. Then, a wall model sensitivity study and an input sensitivity study are reported. The final part of the chapter is devoted to the comparison and validation of the velocity ([subsection 3.4.2](#)) and concentration ([subsection 3.4.3](#)) fields thanks to the [Nironi \(2013\)](#) wind tunnel experiment and the presentation of the resulting conclusions ([section 3.5](#)).

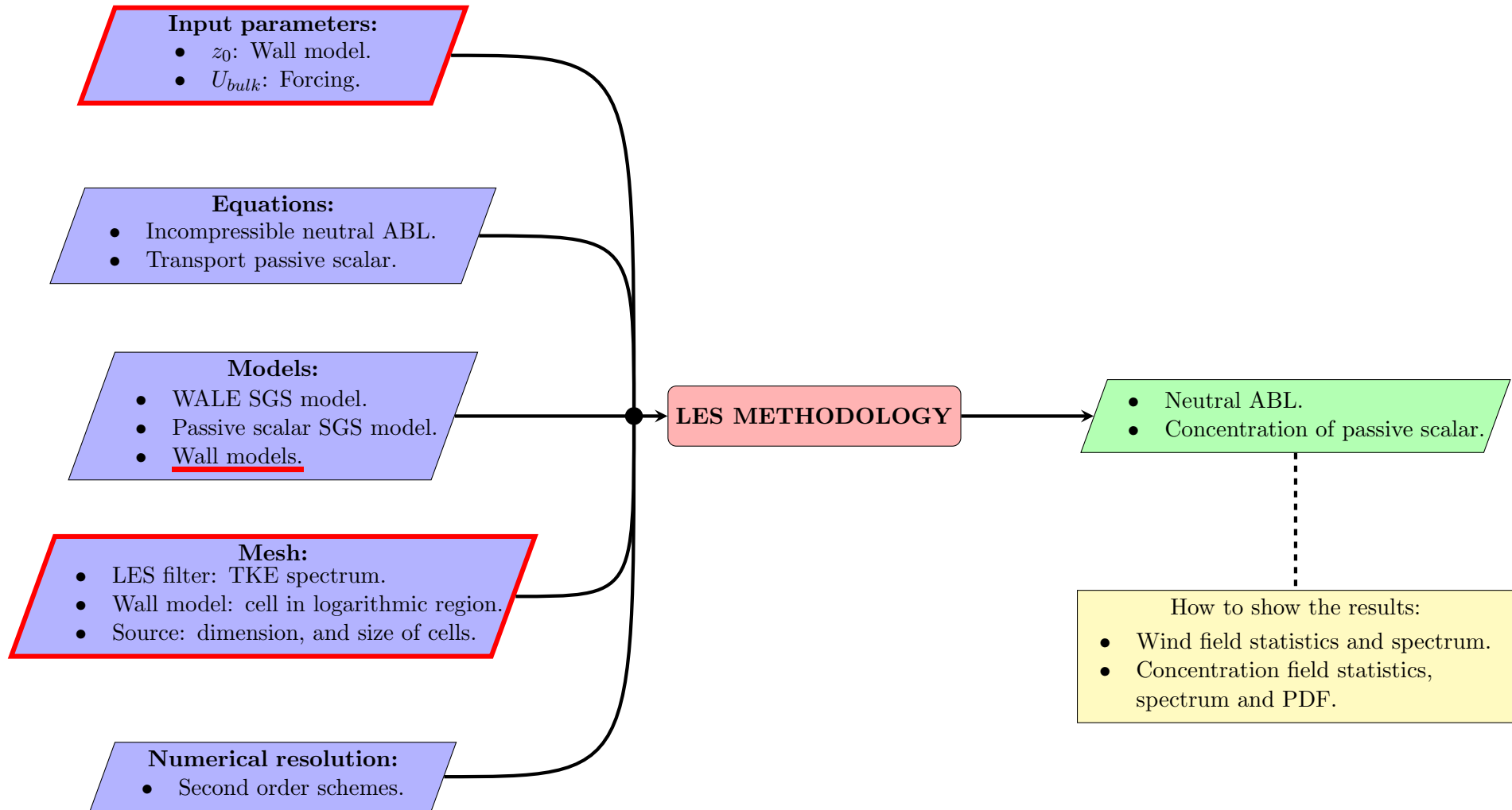


Figure 3.29: Overview of the LES methodology.

3.4.1 Sensitivity study

In the current subsection, three sensitivity studies are analysed:

- Mesh sensitivity study.
- Wall model sensitivity study.
- Input parameters sensitivity study.

The aim is to understand the impact of the main contributions of the methodology developed in the current thesis. Therefore at the beginning of each part, the parameters or characteristics of the simulation left unchanged and those that have been perturbed or modified will be specified. The effect of the perturbations on numerical simulations is analysed, while no physical and numerical interpretation will be dealt with below as this analysis will be reported in the next subsection.

Moreover, it is important to point out that the statistics of the numerical simulation presented here are the result of two steps. The first is the flow development step. According to it, the flow is allowed to develop until a condition in which velocity statistics no longer vary in the streamwise coordinate. After, we move to the second step, which concerns the sampling of the statistics. Only at the end, we could have a good quality of the statistics and be sure that the numerical atmospheric flow is well developed. The numerical results presented in the figures of this subsection are the result of a time-average ($\bar{}$) and a spatial-average ($\langle \rangle$). The latter average is computed along the cross-section of the domain.

Finally, the graphical results are supported by two statistics employed to evaluate the performance of the numerical simulation with respect to the experimental observations. This also allows to have a quantitative indicator of the errors of the LES methodology parameters when compared with the experimental data. These statistics are the Mean Relative Error (MRE) (here expressed in percentages) and the Root Mean Square Error (RMSE). They are computed thanks to the following expressions:

$$\text{MRE} = \frac{1}{N_s} \sum_{j=1}^{N_s} \left| \frac{y_j - \hat{y}_j}{y_j} \right| \quad (3.75)$$

$$\text{RMSE} = \sqrt{\frac{1}{N_s} \sum_{j=1}^{N_s} (y_j - \hat{y}_j)^2} \quad (3.76)$$

where y and \hat{y} are respectively the experimental and numerical statistics in comparison in the current study, where N_s is the number of samples analysed. For this performance analysis, it was decided to consider all the experimental points and their respective numerical values in the interval $z < 0.20$ m (i.e. $z/\delta < 0.285$). The aim is to consider the lower part of the boundary layer together with the region where the source is situated (i.e. $z_h = 0.152$ m). As better explained in the next subsection ([subsection 3.4.2](#)), this interval is chosen to compare the profiles because the experiment develops a neutral SBL only there. In fact, the limited length of the test section and the inlet conditions do not allow a complete development of desired boundary layer along the entire height of the domain.

Mesh sensitivity study

In the current part of the subsection, the mesh sensitivity is analysed. The aim is to study the influence of mesh size with respect to the whole numerical set-up. It was also desired to choose one of the analysed meshes to carry out the validation in depth.

In the cases analysed, the wall model used is the `ThomasWilliamsNeutral` model (Thomas and Williams, 1999). Whereas, the model inputs are the standard inputs extracted from the experimental data: $U_{\text{bulk}} = 3.68 \text{ m/s}$ and $z_0 = 1.119 \times 10^{-4} \text{ m}$. The three meshes studied are: m24, m12 and m06. The minimum cell dimension of these meshes is respectively 24 mm, 12 mm and 6 mm. As already mentioned, the ratio between x and z or x and y cell sizes is 1.5. Moreover, Table 3.13 resumes the dimensions of the wall adjacent cells in meters and in wall units for the meshes compared.

The Figure 3.30a and Figure 3.30b shows that finer meshes have a profile $\langle \bar{u} \rangle$ closer to the experimental profile. In fact, m06 profile matches better with experiment in the region close to the wall, while the other numerical profiles move away from the target. This result is supported by the MRE and RMSE values of Table 3.14a, which point out that m06 mesh has lower errors. An opposite behaviour is observed in the plot related to $\langle \bar{u}'w' \rangle$. Here, the coarser mesh is closer to the target in the region adjacent to the wall. According to Table 3.14b, lower errors are

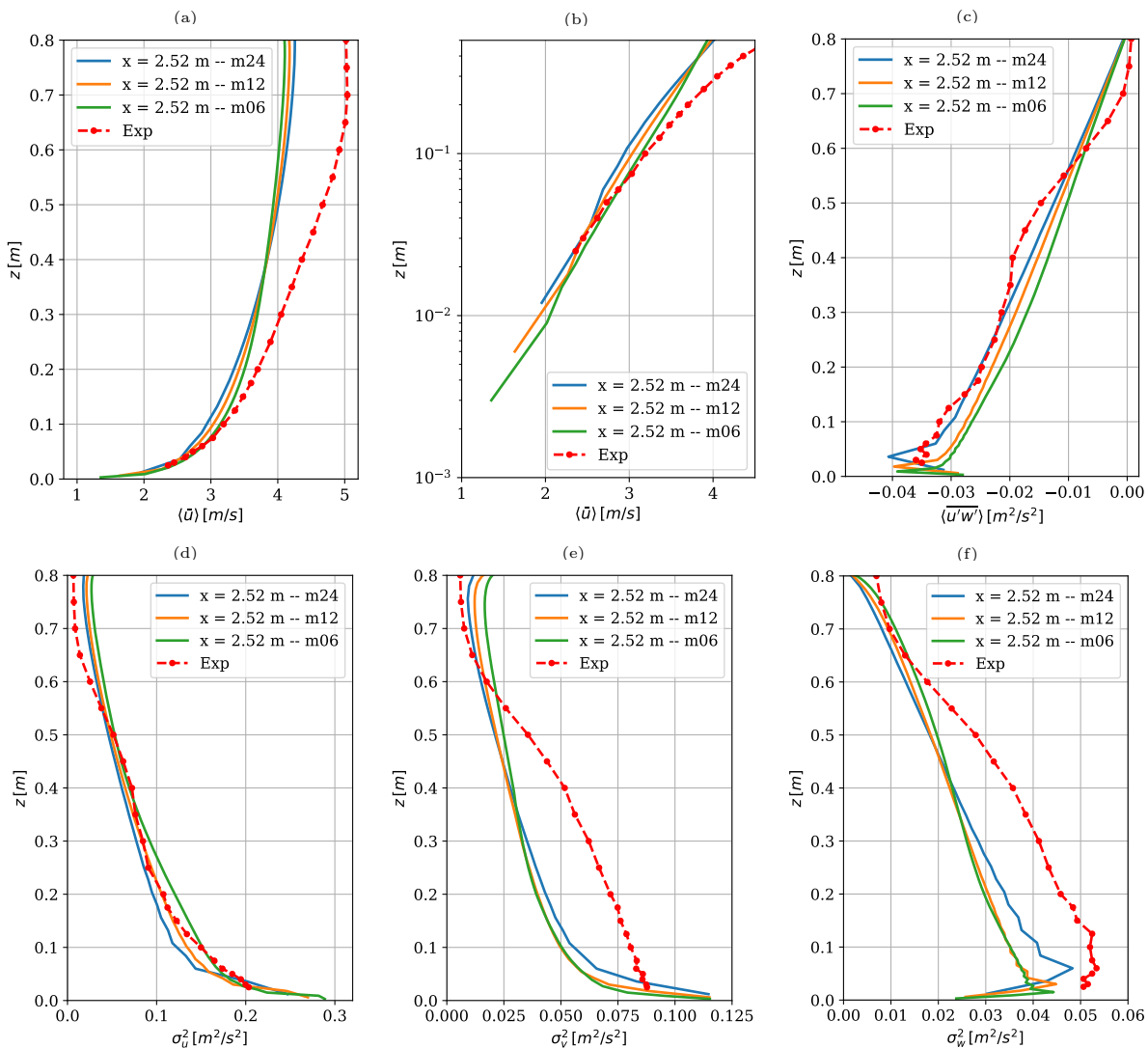


Figure 3.30: Profile statistics: Mesh sensitivity – U_{bulk} and z_0 reference.

	m24	m12	m06
Δ_x [m]	0.036	0.018	0.09
Δ_x^+	460	228	114
Δ_y [m]	0.024	0.012	0.006
Δ_y^+	308	144	78
Δ_z [m]	0.024	0.012	0.006
Δ_z^+	308	144	78

Table 3.13: Characteristics of the cell adjacent to the wall for the meshes in comparison.

reported by mesh m24. We have chosen to prefer this latter result because the wall model aims the reproduction of the friction velocity u_* , which is obtained from this profile through a linear regression. In fact, once the input parameters (i.e. z_0 and U_{bulk}) have been fixed, a specific value of u_* is expected. For the Nironi case, the target value of u_* is 0.187 m/s. The mesh m24 has reported a computational value of the friction velocity of 0.183 m/s. On the other hand, the meshes m12 and m06 have allowed to obtain respectively 0.176 m/s and 0.171 m/s. Finally, it is important to specify that the method to compute the friction velocity is based on a linear regression of the $\langle u'w' \rangle$ profiles. This procedure allows to extrapolate the value of $\langle u'w' \rangle$ at the wall.

Observing [Figure 3.30d-Figure 3.30f](#), the numerical profiles of σ_u^2 for the different meshes are centred on the experimental profile, while σ_v^2 and σ_w^2 are far from the desired result because the wall model is not able to reproduce these effects ([Thomas and Williams, 1999](#); [Xie et al., 2004b](#)). Considering the performance statistics ([Table 3.14c-Table 3.14e](#)), the σ_u^2 comparison shows that the meshes m12 and m06 have better performances w.r.t. m24 mesh. Nevertheless, the lower errors are registered by the m24 mesh for σ_v^2 and σ_w^2 .

The current comparison confirms that a finer mesh could degrade the accuracy of the results. In fact, the mesh m06 presents a profile $\langle u'w' \rangle$ and a value of u_* which are not satisfactory. Whereas, at the beginning we thought that a finer mesh would guarantee a better result. In fact, for an LES simulation without wall model, results are expected to improve with mesh refinement until they are unchanged and no longer affected by mesh refinement. The main reason of the behaviour observed in the current study is related to the wall model. The three meshes are characterised by a cell adjacent to the wall which are in the logarithmic region according to the classical theory ([Pope, 2000c](#)). Nevertheless, today we know that it is possible to estimate better the log-region following the [Marusic et al. \(2013\)](#) relation and method. In this case, mesh m06 is outside the log-region and could present problems linked to the violation

(a) $\langle \bar{u} \rangle$				(b) $\langle \overline{u'w'} \rangle$			
	m24	m12	m06		m24	m12	m06
MRE [%]	6.53	4.05	2.71	MRE [%]	4.82	9.78	14.51
RMSE [m s^{-1}]	0.2362	0.1634	0.1017	RMSE [m^2s^{-2}]	0.0021	0.0034	0.0047

(c) σ_u^2				(d) σ_v^2			
	m24	m12	m06		m24	m12	m06
MRE [%]	11.52	6.90	6.01	MRE [%]	23.91	32.41	33.93
RMSE [m^2s^{-2}]	0.0193	0.0137	0.0097	RMSE [m^2s^{-2}]	0.0209	0.0269	0.0276

(e) σ_w^2			
	m24	m12	m06
MRE [%]	20.54	27.88	29.97
RMSE [m^2s^{-2}]	0.0107	0.0145	0.0153

Table 3.14: Performance statistics for the mesh sensitivity case. Each sub-table shows the MRE and RMSE values for each flow field statistics under analysis.

of the validity criterion of the wall model. Only meshes m24 satisfy completely the criterion (for more details see [subsection 3.3.2](#)). This explains why the m24 mesh has better performance in the estimation of u_* and the finer mesh performance degradation. Although the m12 mesh does not fully respect the previously mentioned criteria but is very close to the boarder of the log-region defined with the Marusic relation, it will be taken into account in the following sensitivity studies and in the validation of the concentration field. In fact, a finer mesh would be more appropriate to dispersion. We need to find a balance between the validity criteria and the more appropriate mesh for dispersion, which represents our final goal. This choice will be discussed in more details in the following subsections.

Wall model sensitivity study

Here, the wall model sensitivity is analysed. The three wall models, introduced in [subsection 3.1.8](#), are compared in order to illustrate their influence on the methodology and choose the more appropriated wall model.

In the current study, the mesh m12 was chosen and the methodology inputs are: $U_{bulk} =$

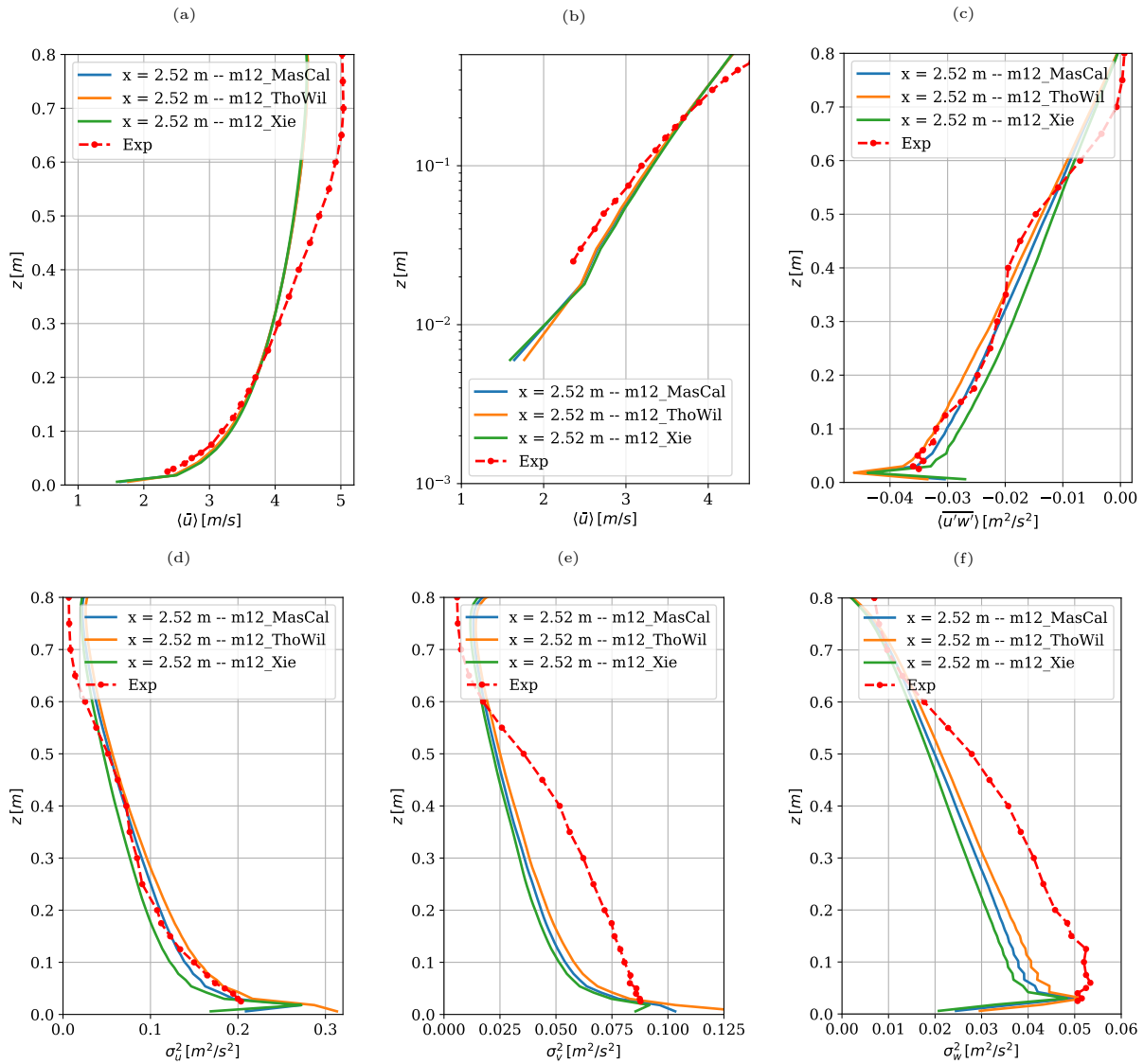


Figure 3.31: Profile statistics: Wall model sensitivity – U_{bulk} (+8% w.r.t. reference) and z_0 reference.

3.974 m/s (+8 % w.r.t. reference) and $z_0 = 1.119 \times 10^{-4}$ m. Although, mesh m12 does not fully respect the mesh criterion, explained in [subsection 3.3.2](#), it is close to the lower limit. However, as we will see in sensitivity study dedicated to the inputs, the mesh m12 can exhibit similar performance than mesh m24 thanks to minimal variations on the inputs (i.e. perturbation of 5 %). Moreover, mesh m12 is preferable to the dispersion of the passive scalar because smaller flow scales are resolved and the difference between the dimension of the numerical and experimental sources are less pronounced.

Therefore, the current sensitivity study analyses the following wall models:

- `MasonCallenNeutral` with the ID “MasCal”.
- `ThomasWilliamsNeutral` with the ID “ThoWil”.
- `XieElAlNeutral` with the ID “Xie”.

The profiles of the wind field statistics compared are taken at the same position, i.e. $x = 2.52$ m ($x/\delta = 3.6$), which corresponds to the middle of the domain. [Figure 3.31a](#) and [Figure 3.31b](#) show the similar behaviour of the streamwise mean velocity for all the wall models. This is confirmed by [Table 3.15a](#), which presents similar values of MRE and RMSE for the three wall models. On the other hand, [Figure 3.31c](#) highlights that there are some differences between the three cases for the Reynolds shear stress $\langle u'w' \rangle$. Both MasCal and ThoWil are closer to the experimental profile in the bottom part of the domain. Xie profile presents a good result but less accurate. [Table 3.15b](#) reflects this behaviour, e.g. the minimum MRE is reported by MasCal while the worst by Xie. In fact, Xie results move away from the target for $\langle u'w' \rangle$ and σ_u^2 profiles, see also [Figure 3.31d](#) and [Table 3.15c](#). A similar behaviour is reproduced in [Figure 3.31e](#) and [Figure 3.31f](#) but, as already mentioned, here the results are also influenced by the limits of the model. However, only Xie reports MRE values greater than 21 %. Whereas, the lower values of MRE and RMSE belong to ThoWil wall model.

In general, the performance of the three models are similar because they have a similar behaviour and are very close to the experimental profiles. For the following analyses and validation, the wall model `ThomasWilliamsNeutral` was chosen because, in our opinion, its physically considerations can be better explained by the theory of log-law and measurements.

(a) $\langle \bar{u} \rangle$				(b) $\langle u'w' \rangle$			
	MasCal	ThoWil	Xie		MasCal	ThoWil	Xie
MRE [%]	4.30	3.94	5.24	MRE [%]	4.19	5.79	9.44
RMSE [m s^{-1}]	0.1371	0.1266	0.1646	RMSE [$\text{m}^2 \text{s}^{-2}$]	0.0018	0.0025	0.0032

(c) σ_u^2				(d) σ_v^2			
	MasCal	ThoWil	Xie		MasCal	ThoWil	Xie
MRE [%]	7.59	6.45	14.62	MRE [%]	20.08	15.70	23.84
RMSE [$\text{m}^2 \text{s}^{-2}$]	0.0147	0.0180	0.0266	RMSE [$\text{m}^2 \text{s}^{-2}$]	0.0186	0.0148	0.0214

(e) σ_w^2			
	MasCal	ThoWil	Xie
MRE [%]	18.24	12.93	22.53435
RMSE [$\text{m}^2 \text{s}^{-2}$]	0.0104	0.0078	0.0125

Table 3.15: Performance statistics for the wall model sensitivity case. Each sub-table shows the MRE and RMSE values for each flow field statistics under analysis.

Input sensitivity study

In order to study the sensitivity of the LES methodology with respect to its inputs, the [Thomas and Williams \(1999\)](#) model and the m12 mesh were chosen. The inputs, extracted by the [Nironi et al. \(2015\)](#) experimental data, are considered as the reference inputs: $U_{\text{bulk}} = 3.68 \text{ m/s}$ and $z_0 = 1.119 \times 10^{-4} \text{ m}$.

In this section, our aim is to perturb the reference values of the inputs. In fact, as highlighted by [Table 3.16](#), the reference values of U_{bulk} and z_0 are perturbed through an intensity proportional to +5%, +8% and +10% of their original values. There is only a particular perturbation that considered the perturbation of $\ln(z_0)$ instead of z_0 . In this case, a perturbation of +10% is applied to $\ln(z_0)$. The perturbations adopted are only positive because the use of the m12 mesh and the reference inputs tends to underestimate the u_* value. Therefore, the present study also focuses on understanding whether it is possible to alleviate the underestimation of the friction velocity with an appropriate and justified combination of U_{bulk} and z_0 close to the reference values.

Four perturbed cases are considered, as resumed by [Table 3.16](#). The following parts of this subsection will present these cases. The perturbed input will be made explicit. Finally, some useful information will be exposed thanks to this sensitivity study.

ID	$U_{\text{bulk}} \text{ [m/s]}$	$z_0 \text{ [m]}$
P1	+5%, +8% and +10% w.r.t. ref.	Fixed ref. value
P2	+5%, +8% and +10% w.r.t. ref.	Fixed +5% w.r.t. ref.
P3	+5%, +8% and +10% w.r.t. ref.	Fixed +10% w.r.t. ref.
P4	Fixed +5% w.r.t. ref.	+5%, +8% +10% w.r.t. ref. and +10% of $\ln(z_0)$ ref.

Table 3.16: Table of perturbations of the input parameters U_{bulk} and z_0 .

Perturbation of U_{bulk}

Firstly, in the case P1, the $z_{\text{ref}} = 1.119 \times 10^{-4} \text{ m}$ is fixed and U_{bulk} is perturbed of +5%, +8% and +10% with respect to $U_{\text{bulk}} = 3.68 \text{ m/s}$. Respectively it results in $U5 = 3.86 \text{ m/s}$, $U8 = 3.97 \text{ m/s}$ and $U10 = 4.04 \text{ m/s}$.

Observing the bottom part of the domain, [Figure 3.32a](#) and [Figure 3.32b](#) illustrate that all the numerical profiles match with the experimental one. A better representation of the lower part of the profiles is obtained thanks to U8 or, especially, U5 profiles. In fact, they report the lower values of MRE and RMSE of [Table 3.17a](#). If considering the other figures, U5 achieves a better compromise between $\langle u'w' \rangle$ and $\langle \bar{u} \rangle$ profiles. In fact, it matches better all the experimental

(a) $\langle \bar{u} \rangle$					(b) $\langle \bar{u}'w' \rangle$				
	Ref	U5-R	U8-R	U10-R		Ref	U5-R	U8-R	U10-R
MRE [%]	4.48	2.47	3.94	5.24	MRE [%]	12.55	3.84	5.79	7.71
RMSE [m s^{-1}]	0.1825	0.0820	0.1266	0.1594	RMSE [$\text{m}^2 \text{s}^{-2}$]	0.0043	0.0017	0.0025	0.0030

(c) σ_u^2					(d) σ_v^2				
	Ref	U5-R	U8-R	U10-R		Ref	U5-R	U8-R	U10-R
MRE [%]	13.90	3.92	8.09	6.34	MRE [%]	34.05	25.83	22.08	20.43
RMSE [$\text{m}^2 \text{s}^{-2}$]	0.0231	0.0096	0.0163	0.0152	RMSE [$\text{m}^2 \text{s}^{-2}$]	0.0281	0.0222	0.0191	0.0177

(e) σ_w^2				
	Ref	U5-R	U8-R	U10-R
MRE [%]	31.32	21.00	16.70	14.72
RMSE [$\text{m}^2 \text{s}^{-2}$]	0.0161	0.0113	0.0093	0.0082

Table 3.17: Performance statistics for the P1 sensitivity case. Each sub-table shows the MRE and RMSE values for each flow field statistics under analysis.

profiles presented between Figure 3.32a and Figure 3.32d. Moreover, the values of MRE and RMSE reflect the previous statement (Table 3.17a-Table 3.17c). Only the results relative to σ_v^2 and σ_w^2 go against the trend but here the limits of the wall model are the cause of this behaviour.

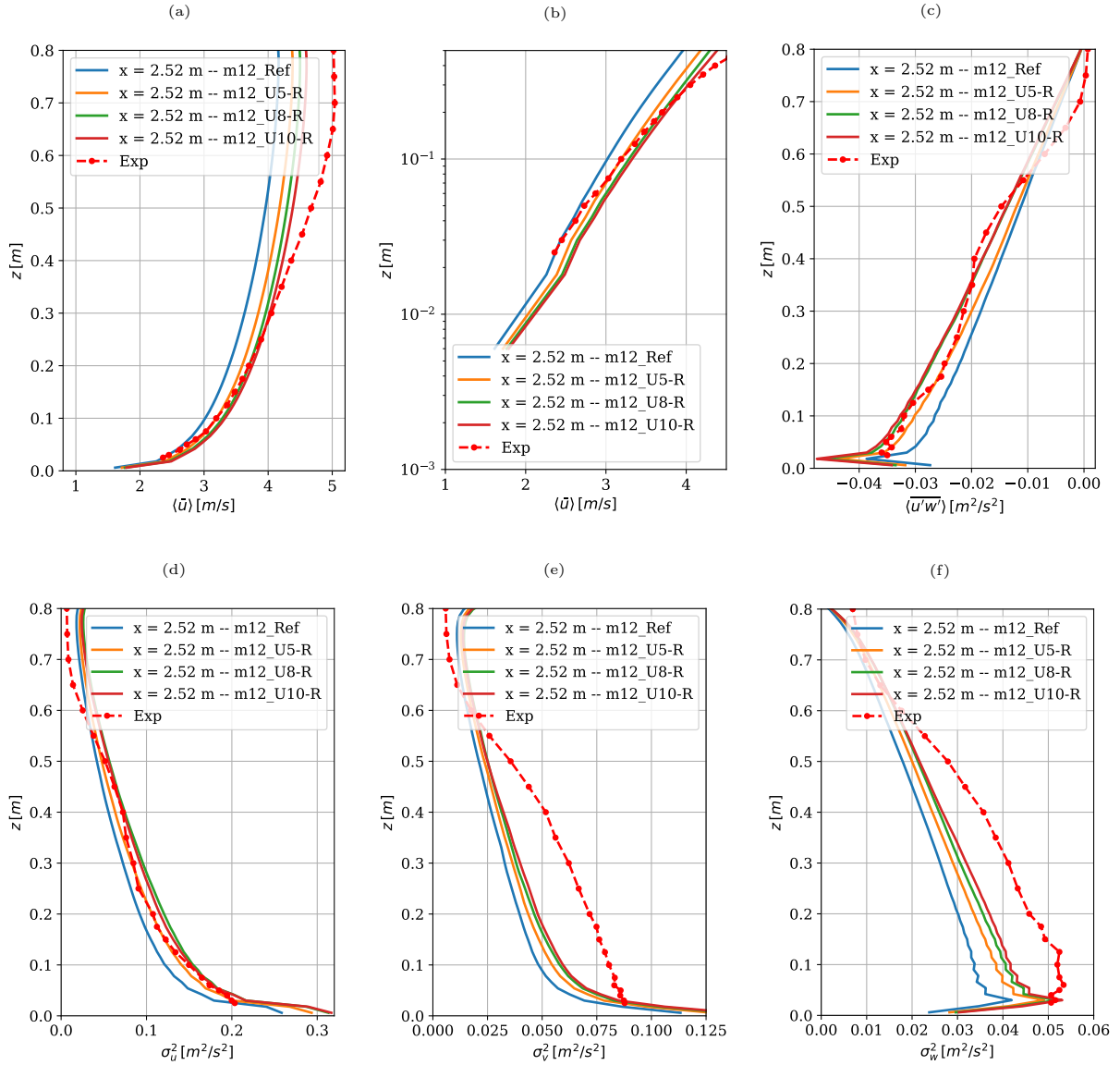


Figure 3.32: Profile statistics: U_{bulk} perturbed and z_0 fixed.

The case P2 takes into account $z_0 = 1.174 \times 10^{-4}$ m fixed, i.e. perturbed of +5% and identified by $z5$, and two perturbations of U_{bulk} : +5% and +10% with respect to $U_{bulk} = 3.68$ m/s. These two perturbations results into $U5 = 3.86$ m/s and $U10 = 4.04$ m/s, while $R = 3.68$ m/s.

Figure 3.33 shows that the profiles R - $z5$ does not match the experimental profiles as well as the perturbed cases. For $U5$ and $U10$ perturbations, $\langle \bar{u} \rangle$ profile is graphically in agreement with the experimental profile up to a height where the source is located. Nevertheless, the lower values of MRE and RMSE are reported by the cases R and $U5$. However, Figure 3.33c and Figure 3.33d point out that the perturbed profiles are able to better reproduce the trend of the experimental one for $\langle \overline{u'w'} \rangle$ and σ_u^2 profiles. The case $U5$ has minimum values of the performance statistics, as shown by Table 3.18b and Table 3.18c. Again the results relative to σ_v^2 and σ_w^2 have the same behaviour as in the P1 perturbation case.

(a) $\langle \bar{u} \rangle$				(b) $\langle \overline{u'w'} \rangle$			
	R-z5	U5-z5	U10-z5		R-z5	U5-z5	U10-z5
MRE [%]	4.07	2.28	5.53	MRE [%]	12.29	4.06	8.38
RMSE [m s^{-1}]	0.1711	0.0764	0.1664	RMSE [m^2s^{-2}]	0.0041	0.0016	0.0032

(c) σ_u^2				(d) σ_w^2			
	R-z5	U5-z5	U10-z5		R-z5	U5-z5	U10-z5
MRE [%]	16.51	4.83	8.82	MRE [%]	33.63	25.19	20.53
RMSE [m^2s^{-2}]	0.0263	0.0115	0.0184	RMSE [m^2s^{-2}]	0.0278	0.0217	0.0179

(e) σ_w^2			
	R-z5	U5-z5	U10-z5
MRE [%]	32.20	20.33	14.45
RMSE [m^2s^{-2}]	0.0165	0.0110	0.0081

Table 3.18: Performance statistics for the P2 sensitivity case. Each sub-table shows the MRE and RMSE values for each flow field statistics under analysis.

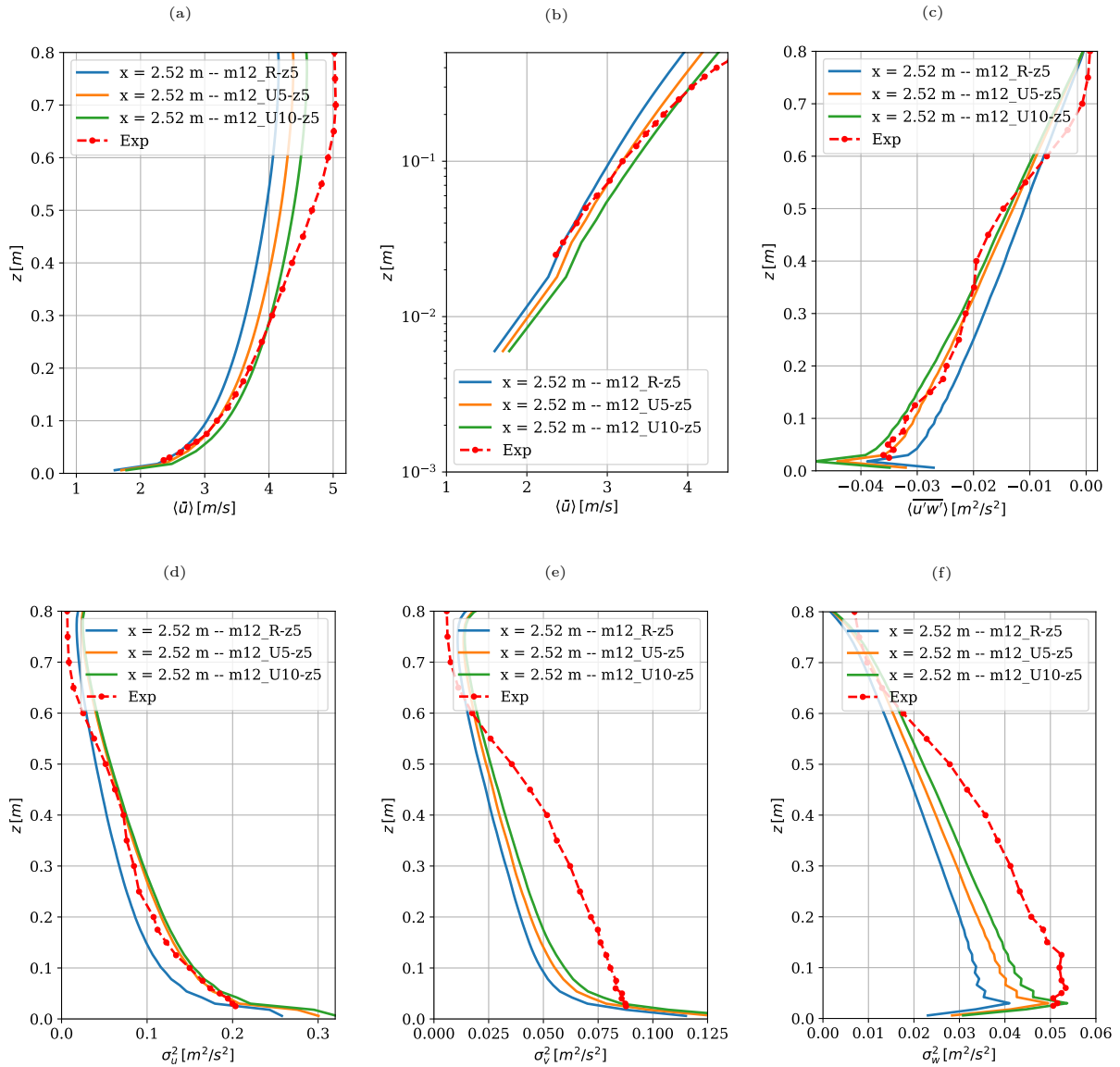
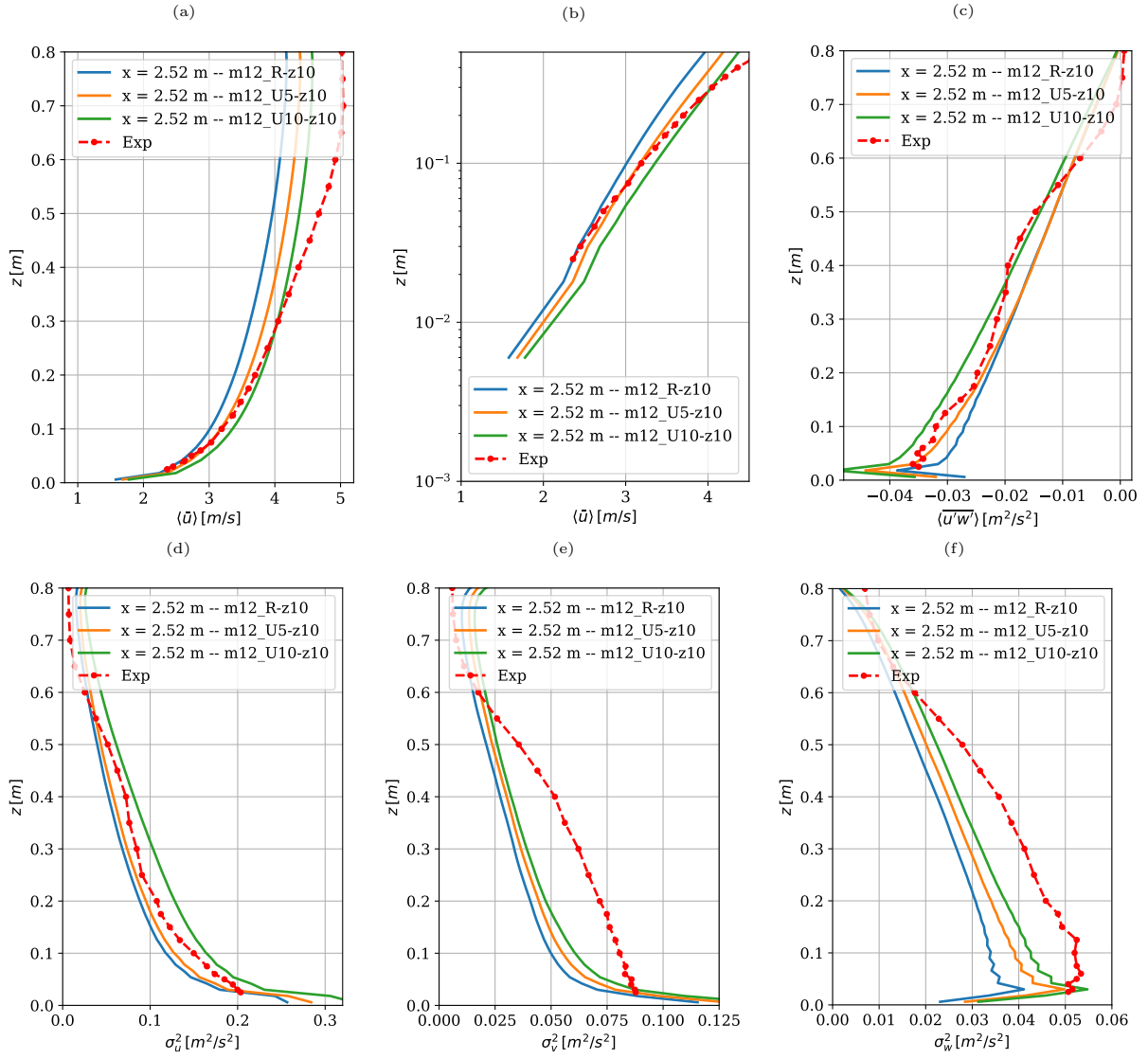


Figure 3.33: Profile statistics: U_{bulk} perturbed and $z_0 = 1.174 \times 10^{-4}$ m fixed.

Figure 3.34: Profile statistics: U_{bulk} perturbed and $z_0 = 1.230 \times 10^{-4}$ m fixed.

	(a) $\langle \bar{u} \rangle$			(b) $\langle \overline{u'w'} \rangle$		
	R-z10	U5-z10	U10-z10	R-z10	U5-z10	U10-z10
MRE [%]	4.72	2.19	6.00	11.06	4.92	11.33
RMSE [m s^{-1}]	0.1873	0.0729	0.1786	0.0038	0.0019	0.0040

	(c) σ_u^2			(d) σ_v^2		
	R-z10	U5-z10	U10-z10	R-z10	U5-z10	U10-z10
MRE [%]	5.79	10.93	14.93	32.48	25.17	19.55
RMSE [m^2s^{-2}]	0.0255	0.0175	0.0263	0.0269	0.0217	0.0172

	(e) σ_w^2		
	R-z10	U5-z10	U10-z10
MRE [%]	31.49	19.86	13.60
RMSE [m^2s^{-2}]	0.0162	0.0107	0.0076

Table 3.19: Performance statistics for the P3 sensitivity case. Each sub-table shows the MRE and RMSE values for each flow field statistics under analysis.

For the third case P3, the aerodynamic roughness is perturbed of +10% resulting into $z_0 = 1.230 \times 10^{-4}$ m. The latter is fixed over all the simulations, while U_{bulk} is perturbed of +5% and +10%. The bulk velocities are respectively $U5 = 3.86$ m/s and $U10 = 4.04$ m/s.

The comparison of the statistics tell us that the perturbation R -z10 and $U10$ -z10 underestimate or overestimate the experimental statistics, as we could observe from [Figure 3.34](#) and [Table 3.19](#). Therefore, the perturbation $U5$ -z10 presents better results matching the experimental profiles. Only the profile σ_u^2 of [Figure 3.34d](#) results unsatisfactory with respect to the cases presented in previous comparisons. This is confirmed by [Table 3.19c](#) which shows that case $U5$ -z10 has better performance statistics.

Considering an overview of all cases in which U_{bulk} is perturbed, we could consider that all the cases studied give acceptable results. In confirmation of this, if considering the statistic MRE of $\langle \bar{u} \rangle$, $\langle u'w' \rangle$ and σ_u^2 , it is less than 20%. Some cases could perform better than others but the difference is minimal.

Perturbation of z_0

The final comparison, i.e. case P4, is characterised by the $U_{\text{bulk}} = 3.843$ m/s fixed (+5% w.r.t. reference) and the perturbations of +5%, +10% with respect to the reference aerodynamic roughness $z_{\text{ref}} = 1.119 \times 10^{-4}$ m and +10% with respect to the $\ln(z_{\text{ref}})$. The aerodynamic roughness results into $R = z_{\text{ref}}$, $z5 = 1.174 \times 10^{-4}$ m, $z10 = 1.230 \times 10^{-4}$ m and $lz10 = 2.779 \times 10^{-4}$ m. The latter could be seen also as perturbation of +148% w.r.t. the reference value z_{ref} . Therefore, the latter is a big perturbation.

[Figure 3.35a](#) shows that there are not particular difference for the $\langle \bar{u} \rangle$ between the different numerical profiles. The performance statistics are similar, as illustrated by [Table 3.20a](#). A similar behaviour is observed for the other profiles, i.e. observed in [Figure 3.35c](#)-[Figure 3.35f](#) and [Table 3.20b](#)-[Table 3.20e](#). Only the high perturbed profile point out a completely different performance.

The previous considerations lead us to affirm that the methodology is insensitive to small perturbations of z_0 while it is only affected by high amplitude perturbations.

(a) $\langle \bar{u} \rangle$					(b) $\langle u'w' \rangle$				
	U5-R	U5-z5	U5-z10	U5-lz10		U5-R	U5-z5	U5-z10	U5-lz10
MRE [%]	2.47	2.28	2.19	2.21	MRE [%]	3.84	4.06	4.92	19.56
RMSE [m s^{-1}]	0.0819	0.0764	0.0729	0.0798	RMSE [$\text{m}^2 \text{s}^{-2}$]	0.0016	0.0016	0.0019	0.0064

(c) σ_u^2					(d) σ_v^2				
	U5-R	U5-z5	U5-z10	U5-lz10		U5-R	U5-z5	U5-z10	U5-lz10
MRE [%]	3.92	4.83	10.93	23.12	MRE [%]	25.83	25.18	25.17	15.06
RMSE [$\text{m}^2 \text{s}^{-2}$]	0.0096	0.0115	0.0175	0.0383	RMSE [$\text{m}^2 \text{s}^{-2}$]	0.0222	0.0217	0.0217	0.0132

(e) σ_w^2				
	U5-R	U5-z5	U5-z10	U5-lz10
MRE [%]	21.00	20.33	19.86	9.66
RMSE [$\text{m}^2 \text{s}^{-2}$]	0.0113	0.0110	0.0107	0.0052

Table 3.20: Performance statistics for the P4 sensitivity case. Each sub-table shows the MRE and RMSE values for each flow field statistics under analysis.

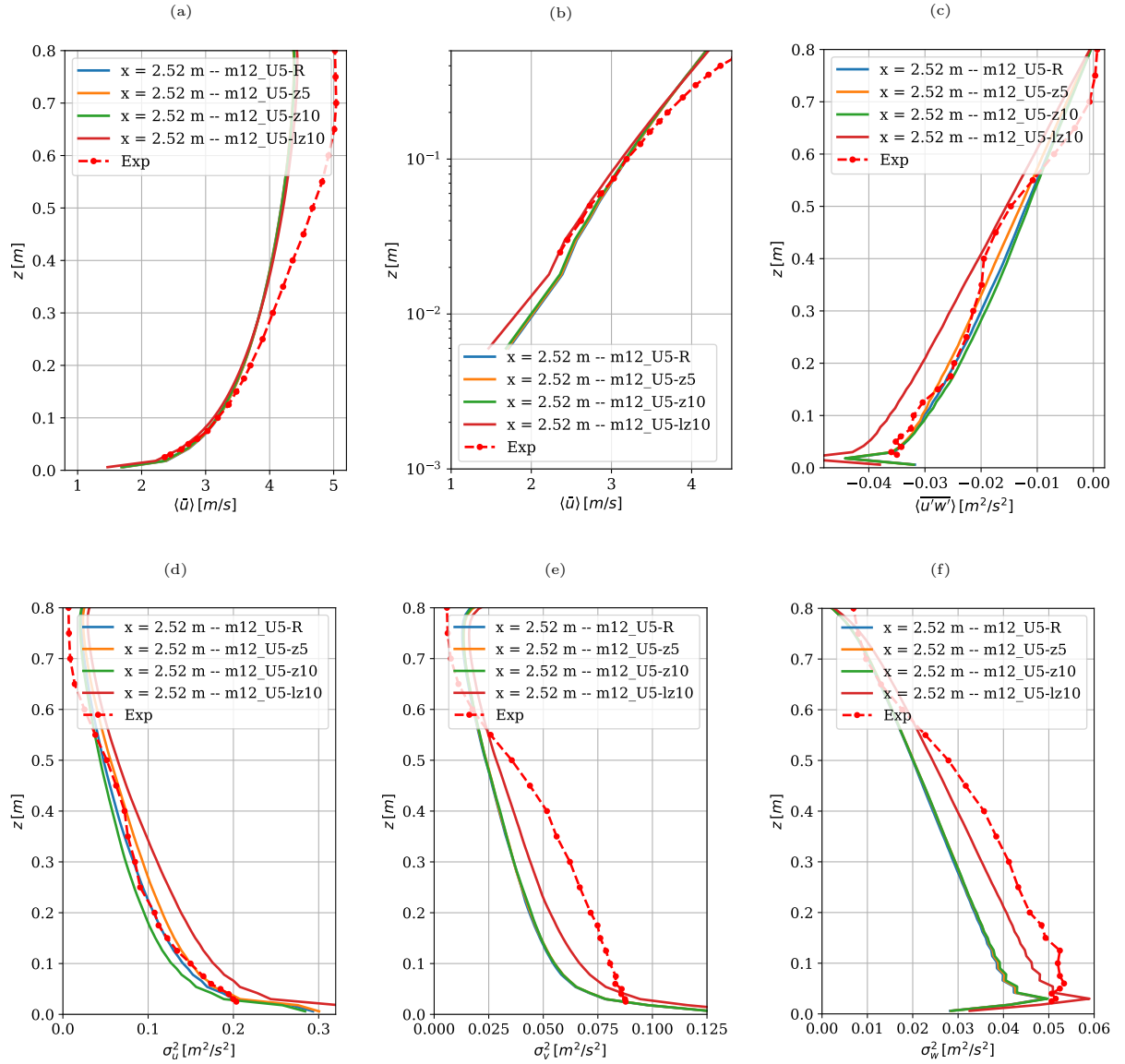


Figure 3.35: Profile statistics: $U_{bulk} = 3.843 \text{ m/s}$ fixed and z_0 perturbed.

Conclusion

The sensitivity study allows us to conclude that:

- The study of the mesh sensitivity highlights that fine meshes could degrade the results because they do not respect the criterion according to which the cell adjacent to the wall must be in the logarithmic zone of the boundary layer. Moreover, it is important to remember that the physical roughness size is 0.020 m . A cell smaller than the physical roughness does not have any physical meaning and violates the validity assumptions of the wall models employed in the current study. This is a problem typical of low-Reynolds number flows, as in the case of wind tunnels experiments.

Nevertheless, the intermediate mesh (i.e. m12) is chosen to continue the sensitivity studies and to the final comparison and validation. This choice was made to try to have a compromise between the performance of the flow field and of the passive scalar field of the LES simulation. In fact, finer meshes are more suitable for calculating the numerical simulation of dispersion.

- The sensitivity with respect to the three wall models analysed shows that all the models are capable to match the experimental statistics, though some of them shows better performances and lends better to physical interpretations.
- The perturbation of U_{bulk} influenced all the statistics analysed in this study. It could amplify or reduce the effect given by the joint perturbation of z_0 . Nevertheless, it is possible to consider that all the profiles match the trend of the experimental profiles. The only exception regards the statistics that cannot be reproduced due to the limits of the wall model family considered. This is the case of σ_v^2 and σ_w^2 .
- On the other hand, the perturbation of z_0 does not significantly influence the profile $\langle \bar{u} \rangle$, once the wall model, U_{bulk} and the type of mesh are fixed. In this case, only the other statistics are influenced by the perturbation. These statistics present acceptable behaviours as long as the perturbation is small.

3.4.2 Wind field comparison and validation

Thanks to the sensitivity study, it was possible to choose a single simulation case for validating the methodology. In fact, the case m12_U5-z5 was selected. The current simulation is slightly different than the one used for the sensitivity study. The main difference is due to the height of the numerical domain, which is $H = 0.726$ m, i.e. 1.028δ m. The mesh m12 is used, while the $U_{\text{bulk}} = 3.84$ m/s and $z_0 = 1.142 \times 10^{-4}$ m are adopted as inputs of the methodology. The latter inputs are both perturbed of +5% w.r.t. its reference values, i.e. 3.66 m/s and 1.088×10^{-4} m. Moreover, in this final case, the coefficient C_w of the SGS model, i.e. the WALE model, is modified. The value used in the sensitivity study was 0.325, which is the default value in OpenFOAM. Nevertheless, after a trial-and-error approach, here we employ $C_w = 0.495$ (subsection 3.1.5). This value helps to improve the lateral and vertical turbulent fluctuation. It means that it contributes to improve the wall model performance. The changes made on the final case are only the consequence of a greater familiarity with the methodology and the choice of the best possible parameters in compliance with the criteria introduced by the LES methodology and the limits found. The final aim is to have a flow field that allows the dispersion of the passive scalar in the best condition.

The domain used for the simulation is the cyclic-dispersion domain (CDD) because this domain could allow to save computational time and resources for dispersion (subsection 3.1.7). Thanks to preliminary studies on the development of the boundary layer and the convergence of statistics, the turbulent flow was developed in a simulation of 300 s with a time step of 0.0025 s and a maximum Courant number of 0.80. Whereas, the statistics are computed thanks to a subsequent simulation of 300 s with the same time step. The latter simulation was also used for the sampling procedure useful to compute the spectra. The computational time and resources required for the latter simulation are expressed in Table 3.21. Moreover, writing each time step to disk takes approximately 601 MB. It highlights how important it is to organise the results analysis procedure in advance. The storage space may not be enough if a large number of time steps are saved on the disk. This condition is even more critical in the case of complex simulations.

Physical time	CPU	Cores	Job time
300 s	Bi-Intel [®] Xeon [®] Intel [®] Gold 6226R @ 2.90GHz	64	11 h 10 m

Table 3.21: Computation time and resources for 300 s of simulation with 64 cores.

Moving on to the analysis of the results, Figure 3.36 presents the wind field statistics of the numerical and experimental vertical profiles. The numerical profiles are sampled at different distances from inlet boundary: $x = 6.00 \times 10^{-3}$ m, 1.26 m and 2.52 m (i.e. $x/\delta = 8.57 \times 10^{-3}$,

1.80 and 3.60). The numerical profile statistics are conserved along the domain. The cyclic boundary condition contributes to the optimal conservation of the profiles, as expected from precursor or cyclic-dispersion domain in a precursor-successor approach.

The validation of the wind field take place in the bottom part of the boundary layer. In fact, as already discussed in [subsection 3.2.2](#), the experimental velocity profile fits a logarithmic profile only in a region that slightly exceeds the extend of the inertial region, i.e. $z/\delta < 0.285$ or $z < 0.2$ m. This region, also known as surface boundary layer, is highlighted by the piece of experimental curve denoted as “Nir. Exp. Val.” in [Figure 3.36](#). Furthermore, it is important to highlight that a comparison between the numerical and experimental profiles on the whole boundary layer is not possible due to the way in which the experimental boundary layer is generated (see [Figure 3.37](#)). The test section of the wind tunnel has longitudinal limits that does not properly allow to develop a boundary layer without the support of the Irwin spires at the beginning of the test section. The latter contribute to accelerate the development of the boundary layer. Nevertheless, it could not reach the same numerical characteristics. In fact, the numerical boundary layer develops long enough (thanks to periodic boundary conditions)

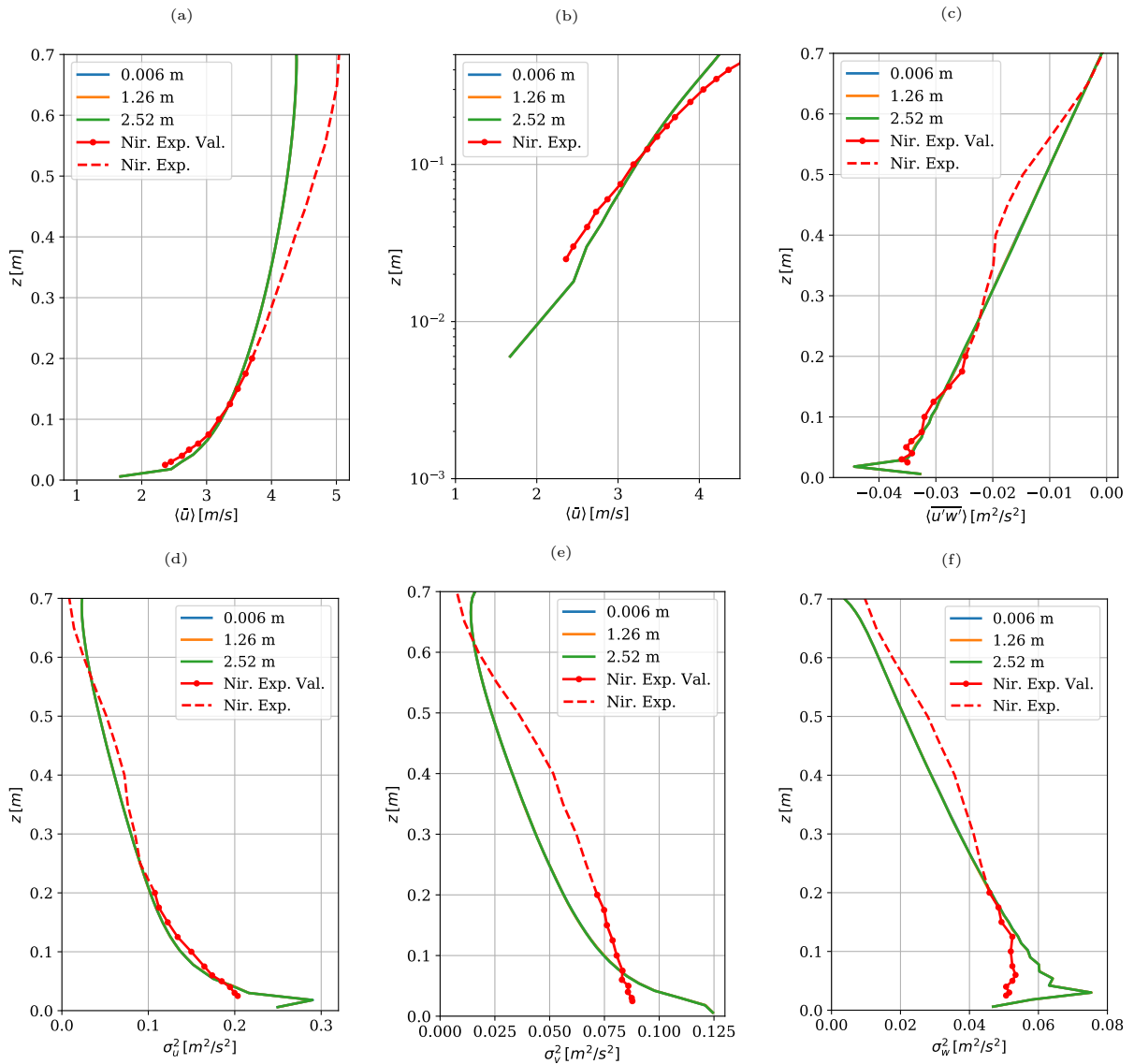


Figure 3.36: Wind field statistics of the final case and comparison with the [Nironi \(2013\)](#) experimental data. The validation of the methodology occurs for $z < 0.2$ m, i.e. $z/\delta < 0.285$.

	$\langle \bar{u} \rangle$	$\langle \overline{u'w'} \rangle$	σ_u^2	σ_v^2	σ_w^2
MRE	3.32 %	3.70 %	6.31 %	14.91 %	16.48 %
RMSE	0.1074 m s^{-1}	$0.0015 \text{ m}^2 \text{ s}^{-2}$	$0.0154 \text{ m}^2 \text{ s}^{-2}$	$0.0141 \text{ m}^2 \text{ s}^{-2}$	$0.0112 \text{ m}^2 \text{ s}^{-2}$

Table 3.22: Performance statistics for the final case.

to have a logarithmic streamwise mean velocity profile along the entire height of the domain (see Figure 3.36a). The experimental profile does not have the same characteristics but the logarithmic profile is developed in the region close to the wall, as previously cited and as we will see from the following comparison.

Figure 3.36 shows a good match between the numerical and experimental profiles in the bottom part of the boundary layer. Figure 3.36a and Figure 3.36b illustrate the mean wind profile $\langle \bar{u} \rangle$. The zoom in the logarithmic region underlines the expected result. Moreover, Figure 3.36c reports the mean Reynolds shear stress profile $\langle \overline{u'w'} \rangle$, which reproduces the experimental trend in the validation region and beyond it. This numerical profile allow to compute the friction velocity u_* , which is a result of the simulation and not an input, through a linear regression procedure. In the latter procedure, the bottom peak is not considered as it is judged as a numerical effect of the wall model. Consequently, the LES friction velocity is equal to 0.188 m/s , while the experimental one is 0.187 m/s . This result confirms the good performance of the wall model.

Then, Figure 3.36d illustrates the streamwise velocity variance σ_u^2 . The numerical and experimental profiles have a similar correspondence to that found for the shear stress profiles. Finally, the Figure 3.36e and Figure 3.36f highlight that the numerical profiles of the spanwise σ_v^2 and vertical velocity variance σ_w^2 tend to underestimate or overestimate the experimental profiles. The reason is related to the type of wall model adopted. In our case, Thomas and Williams (1999) wall model is not able to accurately simulate these profiles. Nevertheless, the C_w parameter adopted here has limited the errors of lateral and vertical turbulent fluctuations. If not alleviated, this particularity could determine a lower plume spread for the numerical simulation, as we will discuss in the next section.

The previous results are supported by the performance statistics computed in the lower part of the boundary layer (i.e. $z/\delta < 0.285$). Table 3.22 highlights the good performance of the simulation for the $\langle \bar{u} \rangle$, $\langle \overline{u'w'} \rangle$ and σ_u^2 profiles. Whereas higher errors are reported by σ_v^2 and σ_w^2 , but they are lower than the values registered in the sensitivity cases. The similar simulation in the sensitivity study, which used $C_w = 0.32$, has reported MRE values higher than 20 % (see Table 3.18) against 14.91 % and 16.48 % of the current simulation.

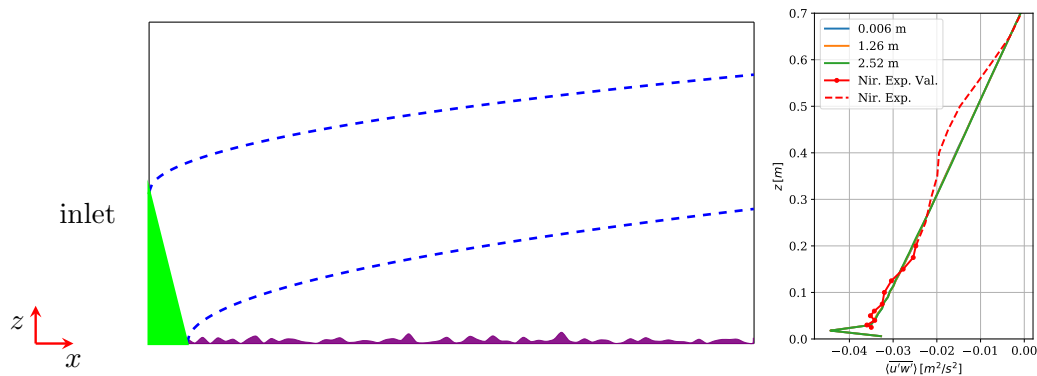


Figure 3.37: Sketch of the Irwin spire and roughness influence on the development of the experimental boundary layer.

Spectrum

A sample point was used to record the instantaneous velocity at a precise position and then compute the numerical spectrum. The position of the sample point is shown in Table 3.23. It corresponds to the position where the numerical source is located. In this way, the experimental spectra presented in subsection 3.2.2 could be compared with the current numerical spectra.

Figure 3.38 point out the spectrum $E(k)$ for the fluctuations u' , v' and w' together with the $-5/3$ -law curve, which identifies the inertial subrange. The spectrum of the streamwise fluctuations matches the experimental spectrum until the filter delimited by the cut-off wavenumber $k_c = 72.80 \text{ m}^{-1}$. Whereas the v' and w' spectrum reproduce their relative spectra less well. This behaviour is supported by the mean relative error (MRE) derived from the comparison of the integration of the numerical and experimental curves, shown in Table 3.24. As expected after the comparison of the flow statistics, $\text{MRE}[E(k)_u]$ presents a better performance with a value of 11.86 %, while the values of $\text{MRE}[E(k)_v]$ and $\text{MRE}[E(k)_w]$ exceed 20 %. Lastly, it is important to highlight that the numerical spectra respect the $-5/3$ -law as well as the experimental ones.

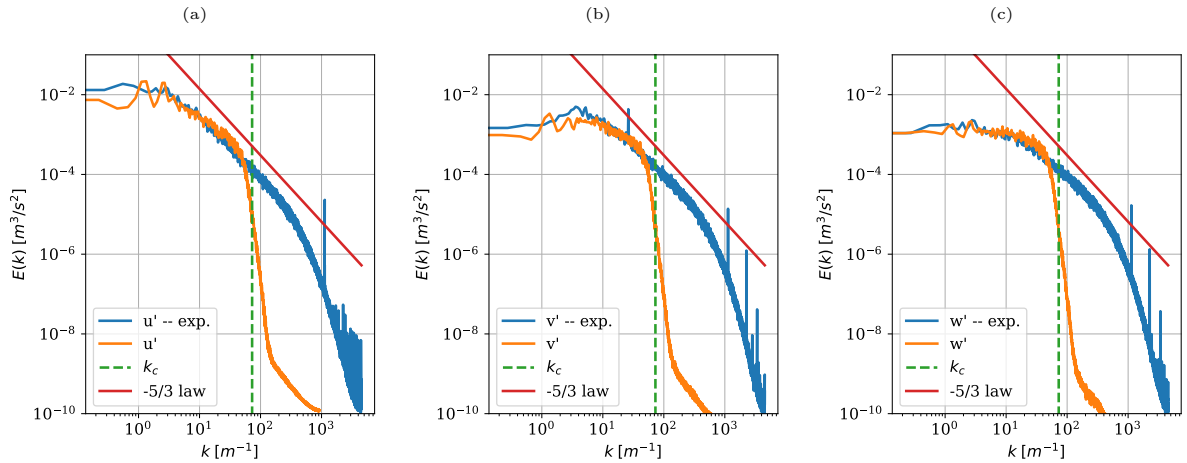


Figure 3.38: Velocity field spectrum for the case final comparison. Figure (a), (b) and (c) shows respectively the spectrum of u' , v' and w' . They illustrate also the $-5/3$ law and the cut-off wavenumber of the LES filter.

x_{sam}	0.747 m
y_{sam}	0.723 m
z_{sam}	0.152 m

Table 3.23: Point sample position, i.e. source position.

$\text{MRE}[E(k)_u]$	11.86 %
$\text{MRE}[E(k)_v]$	34.66 %
$\text{MRE}[E(k)_w]$	22.19 %

Table 3.24: Spectrum errors due to the comparison with experimental data for the three spectra.

3.4.3 Concentration field comparison and validation

In the current subsection, the numerical and experimental concentration fields are compared with the aim of validating the LES methodology. Therefore, the statistics of the concentration field, the spectrum of the concentration fluctuations and the probability density functions (PDFs) are analysed below.

As mentioned in the previous subsection, the domain used for the simulation is the cyclic-dispersion domain (CDD). Since the geometry of the experiment is simple being free of obstacles, this approach saves computational time (subsection 3.1.7). A simulation of 300 s with a time step of 0.001 s and a Courant number of 0.33 is conducted to compute the statistics and sampling the instantaneous field to derive the spectrum and the probability density functions (PDFs). This simulation requires higher computational time than the wind field simulation, as shown in Table 3.25. The main reason is the smaller time step and the use of more monitoring points which write each time step to the disk. In fact, writing each time step to disk takes approximately 726 MB, while the data generated for the monitoring points for the whole simulation is 360 MB.

Physical time	CPU	Cores	Job time
300 s	Bi-Intel® Xeon® Intel® Gold 6226R @ 2.90GHz	64	34 h 30 m

Table 3.25: Computational time and resources for 300 s of simulation with 64 cores.

Before to present the results, it is useful to recall the difficulties that we have not been able to overcome. Firstly, as mentioned in subsection 3.3.2, the mesh criteria is not fully respected. The constraints related to the dimension and the cell sizes of the source have been violated in the current simulation. The experimental source dimension is $\sigma_{0,\text{exp}} = 6$ mm, while the numerical one is $\sigma_{0,\text{m}12} = 12$ mm. For smaller sources, it implies that the high order statistics (e.g. the standard deviation σ_c^*) will have higher values close to the source. This difference should diminish moving downwind and finally vanish in the far field. Regarding the size of the source cell, the current simulation used only one cell to define the source. The related constraint suggests to use at least 10 cells to define the source. Nevertheless, following the previous constraint means violating other criteria (e.g. wall model, LES filter and SGS model criteria). Consequently, choosing to have only one cell implies that the flow at the scale of the source is not resolved and needs an interpretation.

In addition to previous consideration, the case chosen to simulate the wind field presents some limits related to the wall model. In fact, numerical σ_v^2 and σ_w^2 are not able to reproduce the experiment in the validation region (i.e. $z/\delta < 0.285$), while the other statistics match better the experimental results. Finally, it is important to consider that the SGS Schmidt number Sc_{sgs} chosen should be adapted to the simulation. An imprecise adaptation could play on the role that the SGS diffusivity D_{sgs} has in the far field.

In the following, two statistics of the concentration field are analysed: the mean concentration and the standard deviation. Then, spectrum of the concentration fluctuations in the far field is reported. The final part of this subsection is dedicated to the PDFs of the concentration field.

Mean concentration

The crosswind and vertical profiles of the mean concentration \bar{c} at various downwind distances are shown in Figure 3.39 and Figure 3.40. The downwind positions of the profiles are 0.25 m, 0.50 m, 1.00 m, 2.00 m, 3.00 m and 4.00 m (i.e. $x/\delta = 0.357, 0.714, 1.428, 2.857, 4.285$ and 5.714). The concentrations are adimensionalised, i.e. $c^* = c(\bar{u}_s \delta^2 / \bar{Q})$. As already mentioned, this process facilitates the comparison between numerical and experimental profiles.

Firstly, it is important to observe that the LES profiles are fitted with a Gaussian distribution of the type of Eq. (3.65) and Eq. (3.66) respectively for the crosswind and vertical profiles. A similar procedure was conducted for the experimental profiles in subsection 3.2.3. This fitting

procedure estimates also the plume spread σ_y and σ_z . The Gauss distribution could help to explain the overestimation of the maximum concentration of the \bar{c}^* profiles. In fact, it is inversely proportional to σ_y and σ_z (see Eq. (3.65) and Eq. (3.66)), which are underestimated.

In the far field, the LES simulation overestimates the experimental mean concentration field. One of the reasons for this behaviour is due to the trend of the vertical and transversal plume spreading, as shown by Figure 3.41. Both numerical plume spreads are underestimated in the far field. In large part, this could be explained by the mismatch between the numerical and experimental profiles of σ_v^2 and σ_w^2 (as observed in Figure 3.36e and Figure 3.36f). In fact, Eq. (1.64) shows the linear relation between the spreading σ_{x_i} and the velocity fluctuations σ_{u_i} in the same direction (subsection 1.1.5). Figure 3.41 shows that the experimental-numerical ratio of σ_v and σ_y are close in the far field. This could confirm that in the cross-section σ_v^2 is the main cause of the underestimation of the spread σ_y . A similar explanation is given for the σ_z spread.

Finally, in the region close to the source, the vertical and transversal profiles at $x = 0.25$ m underestimate the experimental profiles. This was predictable as the numerical source is represented with a coarse mesh. Nevertheless, up to the profiles at 2.00 m, the LES results reproduce well the progress of the experiment.

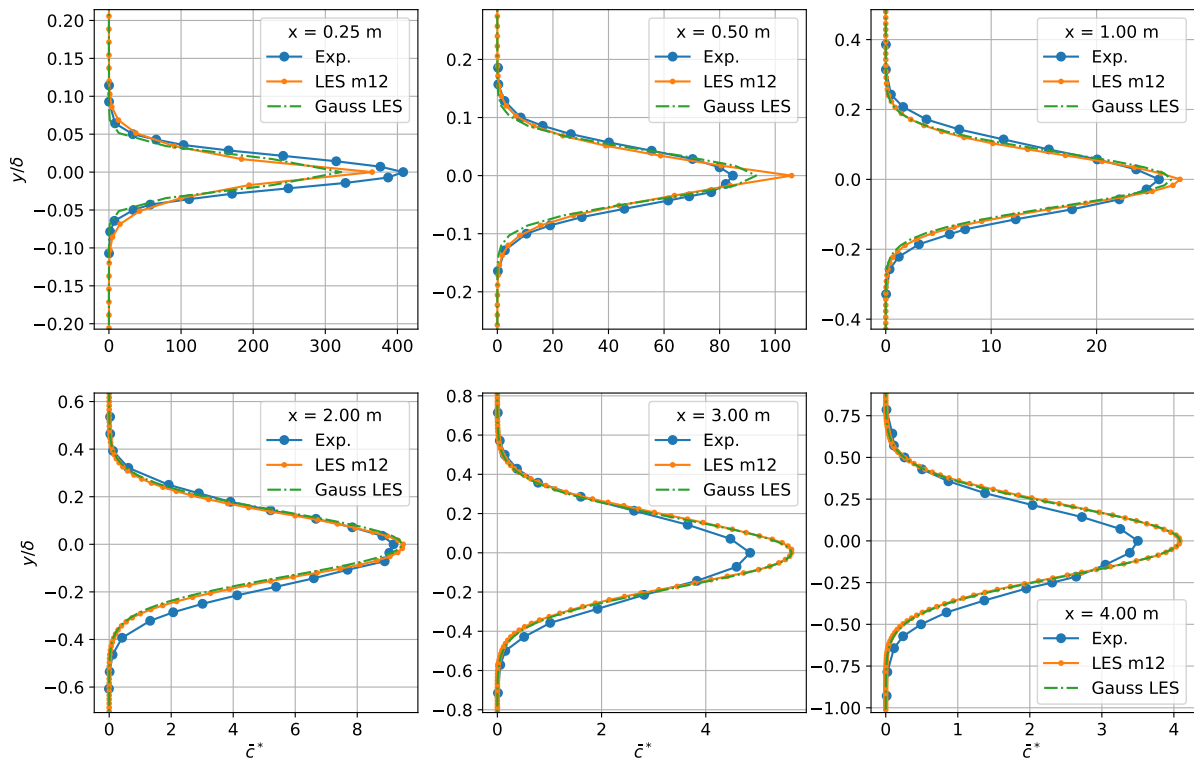


Figure 3.39: Crosswind profiles of nondimensional mean concentration for the m12.U5-z5 case. The profiles were measured and sampled at the source height $z/\delta = 0.217$. The numerical profiles were fitted with a Gaussian distribution of the type of Eq. (3.65).

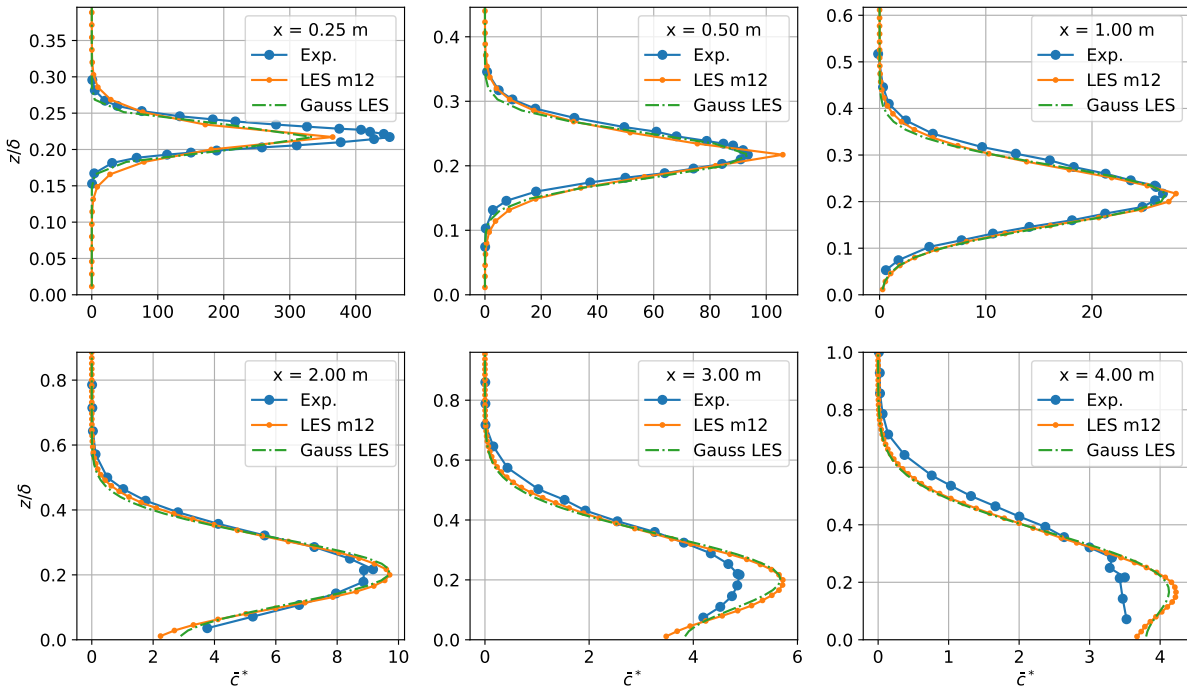


Figure 3.40: Vertical profiles of nondimensional mean concentration for the m12_U5-z5 case. The profiles were measured and sampled on the plume axis. The numerical profiles were fitted with a Gaussian distribution of the type of Eq. (3.66).

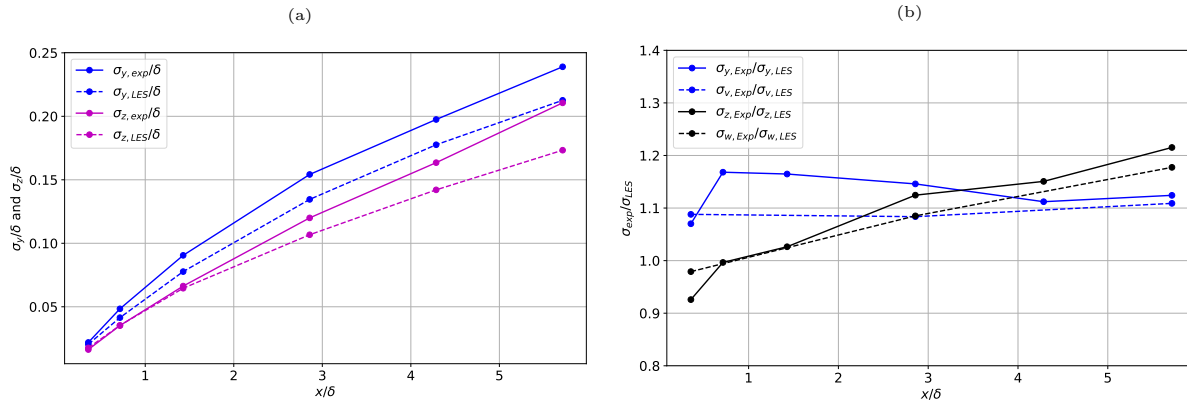


Figure 3.41: (a) Plume spread in transversal and vertical directions for LES and experiment. (b) σ_y , σ_z , σ_v and σ_w ratio between experiment and LES values.

Standard deviation

Figure 3.42 and Figure 3.43 illustrate the crosswind and vertical profiles of nondimensional concentration standard deviation σ_c^* for the LES case and the experimental case.

Here, one of the main reasons for the mismatch is the different dimension of the source. The experimental source is smaller than the numerical one. This explains the underestimation of the numerical transversal and vertical profiles of σ_c^* until $x = 2.00$ m, as observed from the Figure 3.42 and Figure 3.43. On the other hand, in the far field, the numerical standard deviation is closer to the experimental one. As already mentioned, a similar behaviour is presented by Nironi *et al.* (2015) when two sources of different diameter are compared. Similarly to our case, one source is double the other. The larger source has greater values of σ_c^* than the smaller one in the region close to the source, while the difference decreases in the far field.

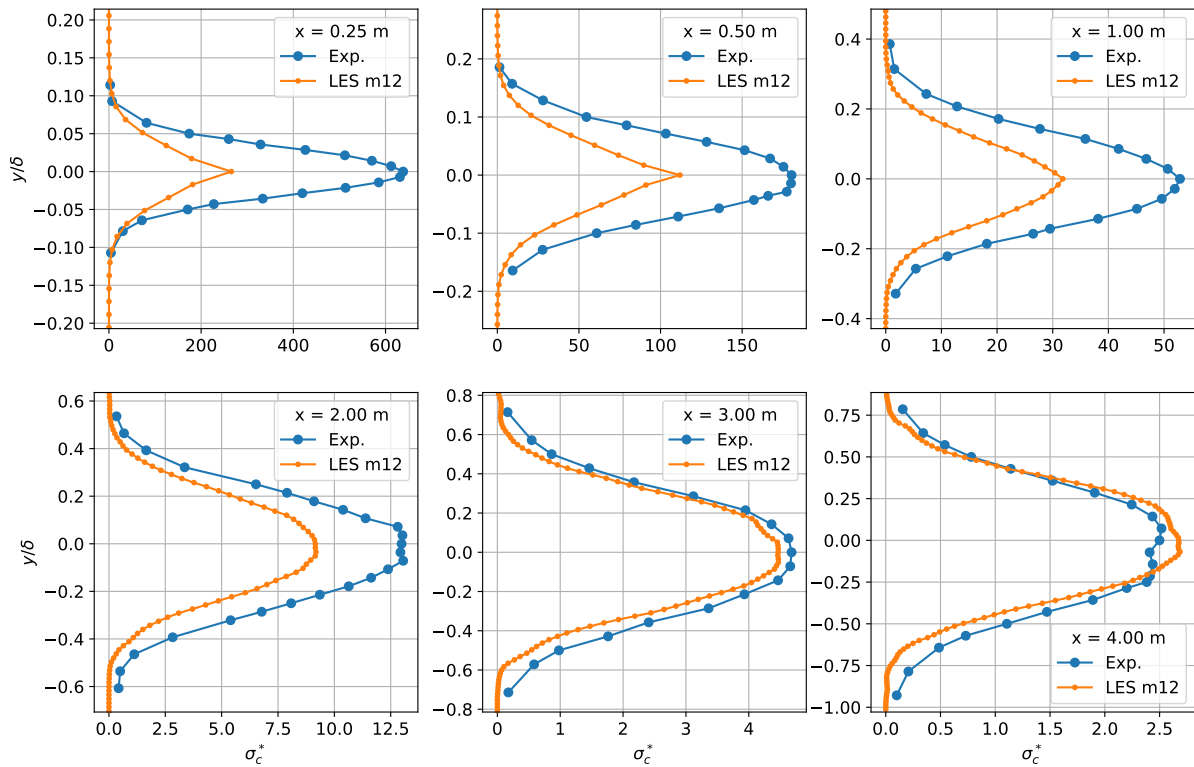


Figure 3.42: Crosswind profiles of nondimensional concentration standard deviation for the m12.U5-z5 case. The profiles were measured and sampled at the source height $z/\delta = 0.217$.

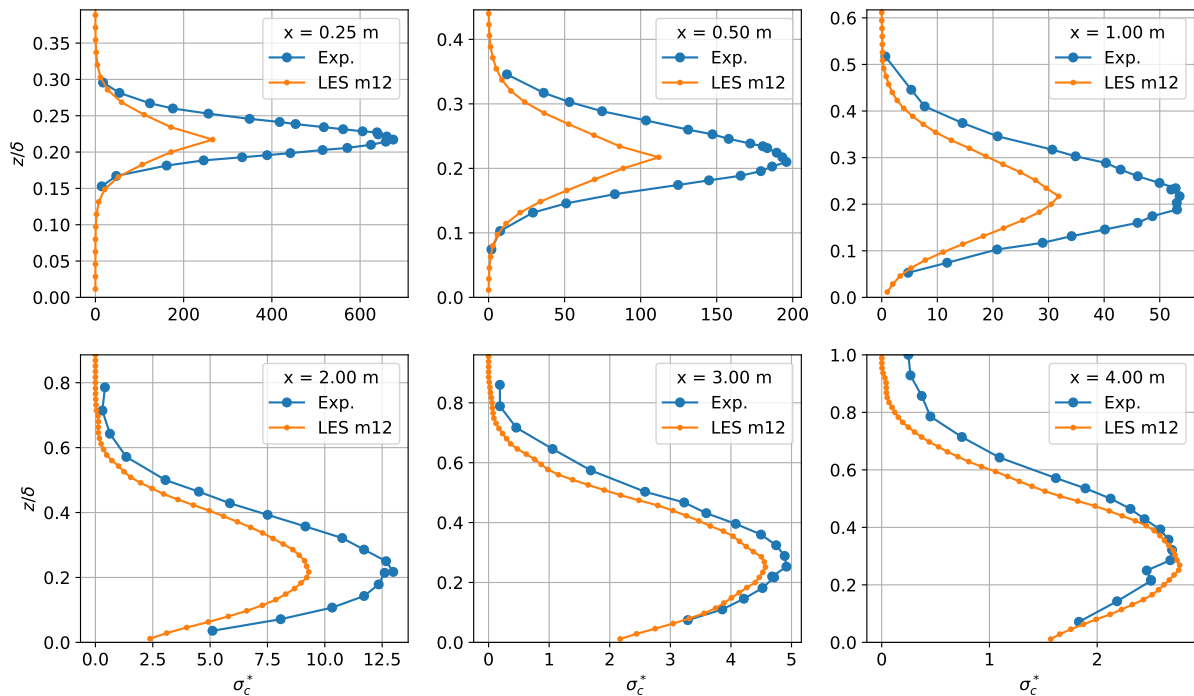


Figure 3.43: Vertical profiles of nondimensional concentration standard deviation for the m12.U5-z5 case. The profiles were measured and sampled on the plume axis.

Spectrum

The non dimensional spectrum of the concentration fluctuations, normalised as $E^* = E\delta/\sigma_c^2$ and as a function of $k\delta$, is shown in Figure 3.44 together with the LES and experimental fluctuations

signals over 60s. The position of the sampling point is presented in [Table 3.26](#). Therefore, the sampling point is located at 4.00 m (i.e. $x/\delta = 5.714$) from the source. The LES spectrum corresponds to the experimental one up to the cut-off wavenumber and the error of the spectrum is 11.61 %, see [Table 3.27](#). The error is not due to the difference between the spectra at the high wavenumbers. Conversely, the region is to be found in the most energetic region, i.e. at low wavenumber values.

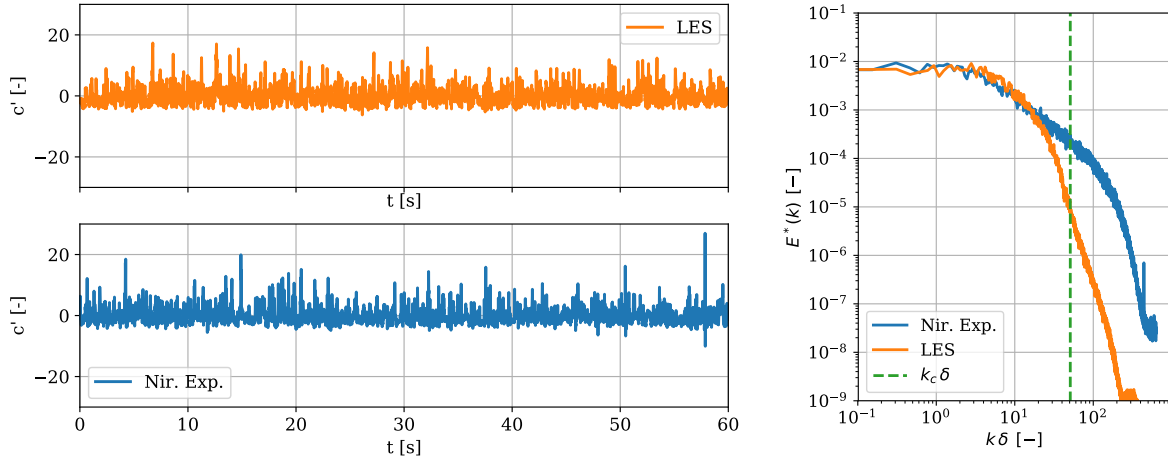


Figure 3.44: Experimental and LES concentration signal (a) and spectrum of concentration fluctuations (b) on the plume center line for the case m12_U5-z5 and the wind tunnel experiment. The sampling position is $x = 4.00$ m (i.e. $x/\delta = 5.714$).

x_{sam}	3.747 m	i.e. 4.00 m from the source.
y_{sam}	0.723 m	i.e. in the middle of the domain.
z_{sam}	0.152 m	

Table 3.26: Point sample position for the concentration spectrum.

$$\text{Err}[E(k)_c] \mid 11.61\%$$

Table 3.27: Concentration spectrum error.

Probability density function (PDF)

The experimental and numerical PDFs, computed thanks to sampling points situated on the plume centre-line and at the source height at various distance from the source, are presented in [Figure 3.45](#). In this figure, it is possible to observe the LES PDF, the Nironi experimental PDF and the Gamma distribution (Γ), which best fits the LES PDF.

The concentration PDF could be described by a family of one-parameter distribution with the following form ([Villermaux and Duplat, 2003](#)):

$$p(\chi, a) = \frac{a^a}{\Gamma(a)} \chi^{a-1} \exp(-a\chi) \quad (3.77)$$

where $\chi = c/\bar{c}$ is the normalised concentration. Therefore Eq. (3.77) depends on a single parameter a , which can be related to the concentration statistics through $a = \bar{c}^2/\sigma_c^2$.

The Gamma distribution is rather efficient in reproducing the shape modifications of the PDF when the distance from the source increase ([Yee and Skvortsov, 2011](#); [Orsi et al., 2021](#)).

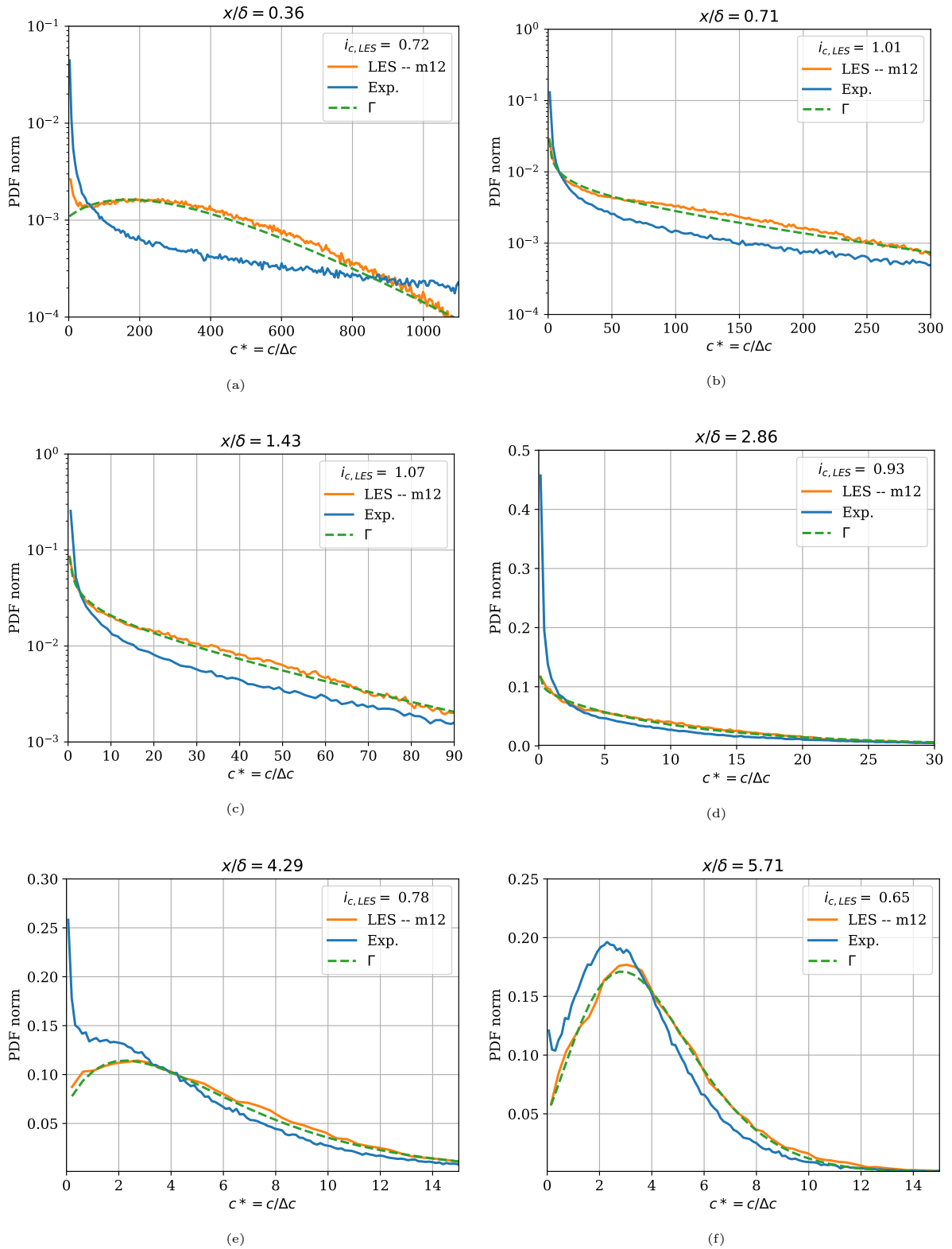


Figure 3.45: Comparison of numerical and experimental PDF plots at different distances from the source. The ordinate axis expresses a normalised PDF, given by $\text{PDF}/(N \Delta c^*)$, where Δc^* is the amplitude of concentration classes and N is the total number of classes on which the PDF is calculated. The plots show also the relation between the concentration fluctuation intensity i_c and the concentration PDF for the LES results.

An exponential-like shape is typical in the near field ($i_c > 1$), while a log-normal distribution with short tail is common in the intermediate field $i_c \approx 1$ and a Gaussian-like distribution in the far field ($i_c < 1$). It is interesting to highlight that this transition is entirely regulated by the value of the concentration fluctuation intensity i_c (Eq. (3.67)).

Therefore, the Gamma distribution is used to fit the numerical PDFs in Figure 3.45. As expected, numerical PDFs are capable of reproducing the experiment in the far field, particularly from $x/\delta = 2.86$ (i.e. 2.00 m). At the far field, the behaviour observed in previous analysis is confirmed by PDF. In fact the numerical mean concentration is overestimated, so the numerical PDF seems to be translated toward higher values.

On the other hand, the dimension of the numerical source and the size of its cells does not allow to simulate correctly the concentration field in the region close to the source. At $x/\delta = 0.36$ (i.e. 0.25 m), the meandering motion of the plume generates a high intermittency in the experimental case, which is traduced as a high probability to have zero concentrations. In this case, the intermittency is associated to the irregular alternation of zero and high values of concentrations registered by the monitoring point. For the numerical case, the intermittency is reduced because the source is bigger. This could be interpreted as a dispersion process more developed for the big source with respect to the small one.

Finally, it is important to highlight that the not accurate resolution of the concentration field close to the source leads to an incorrect shape of the PDF at $x/\delta = 0.36$ and an inappropriate value of i_c . At this distance from the source, the latter value is normally greater than one.

3.5 Conclusions

The current chapter is focused on the development of the LES methodology to simulate the dispersion of a passive scalar in a neutral surface boundary layer.

The first part is dedicated to introduce the LES approach applied to our objectives (section 3.1). A particular attention is dedicated to the SGS modelling, the modelling of a rough wall and the treatment of the boundary conditions. During the description of these concepts, some basis for defining the physical and numerical constraints that condition our simulations have been identified.

The second section (section 3.2) describes the wind tunnel experiment to simulate, i.e. the Nironi (2013) experiment. The characteristics of the wind and concentration fields of the experiment are essential to define the computational setting of the LES simulation. Moreover, how the LES methodology inputs can be extracted from the experiment are presented. Subsequently, section 3.3 is dedicated to make explicit the computational settings. The numerical and physical constraints identified are converted into the criteria that define our methodology. These criteria are also fundamental to understand the limits of the methodology and to interpret the results when it is not possible to respect all the criteria like in our case. The main criteria are related to the mesh definition. It is relevant because the flow field and the concentration field present conflicting requirements. For instance, the models employed (in agreement with works in literature) do not allow to work with fine meshes, which are largely preferable to study the dispersion phenomena close to small source typical of wind tunnel experiments. Therefore, some compromises were necessary to reach the final comparison and validation.

The LES methodology is summarised in the section 3.4. Particular attention is dedicated to the contribution made regarding the definition of the physical and numerical criteria to define the inputs, the domain and meshes and the wall model. Then sensitivity studies are conducted to highlight the effects of the criteria and of the methodology inputs. The results have also evidenced the compromise adopted to choose the case useful for the final comparison and validation. In this context, we have compared the LES simulation of the Nironi case with its respective experimental data. The comparison of the wind field yields to acceptable results. In fact, our methodology is capable to reproduce the experimental wind field in the bottom part

of the boundary layer (BL). Only the latter region, or a region similar, allows an acceptable comparison due to the experimental limitations (e.g. the approach adopted to develop the BL). On the other hand, the comparison of the concentration field presented more difficulties because the criteria not respected relates the source. These results are also conditioned by the SGS modelling adopted for the passive scalar transport equation. In fact, these modelling (usually adopted in previous works) are limited by the dimension of the filter that cannot be situated in the dissipation region. Similarly, the wall model limits the dimension of the cells adjacent to the wall, which needs to be placed in the logarithmic region. Consequently, if the source is positioned close to the ground, the criterion related to the wall model does not favour the accurate resolution of the source.

Therefore, although the case chosen is considered as a simple case because it represents a neutral boundary layer flow delimited by a rough wall and the dispersion phenomena is generated by a punctual source, it is not easy to describe numerically through a LES approach. It is possible to arrive to a final LES simulation only accepting the violation of some criteria and a compromise between some opposing conditions that allow to simulate correctly the wind field and the concentration field. Consequently, although the comparison revealed some issues, it can be concluded that the LES methodology is validated considering the appropriate interpretations of the results.

Numerically, some perspectives for improvement concern the use of different SGS models and wall models more adapted to treat smaller cells. Otherwise, it could be useful to simulate a LES which resolves the wall and improves the SGS model for the closure of the passive scalar. On the other hand, experimentally, it could be possible to increase the Re number, for example by increasing the velocity of the free-stream. Moreover, the choose of a larger source and further away from the wall could benefit the numerical-experimental comparison and enrich the experimental configurations studied. A sensitivity study of the dimension of the source and its position in the domain is beneficial for both numerical and experimental studies. Then, the development of experimental wind field may be improved to facilitate the comparison in this simple case. In this context, it is possible to affirm that doing more to improve the quality of results in this field of basic research can favour much more complex configurations of practical and industrial interest.

In fact, this study can be seen as a basis for studying more complex problems and geometries. The criteria defined here need to be adapted to study complex flows, like thermal stratified flows, or geometries which includes obstacles of different kinds. With this in mind, the LES methodology is applied to a real case. The test case to analyse is chosen in such a way that the current methodology can be adapted without adding extra models or criteria. This is the subject of the next chapter, dedicated to the TADI experiment.

Chapter 4

TADI: Real Scenario Case

4.1 Experiment description and case selection

Taking into account the numerous industrial risks in the oil and gas sector, safety plays a fundamental role. For this reason, the capacity to predict accidents is a priority.

Digital prevention represents a very useful tool to achieve safety ambitions. In this context, TADI project (**TotalEnergies Anomaly Detection Initiatives**; last access: January 18th, 2022) constitutes an innovative approach to optimise the management of the risks associated with gas leak. It combines three aspects, here presented:

- Early fault detection (e.g. equipment failure or gas leak) thanks to new-generation sensors, i.e. innovative optical or acoustic instruments. The latter contributes to rapidly detect the gas, quantify its concentration, identify the origin and indicate the gas flow rate. The sensors should provide real-time 3D visualisation of the hazard area.
- A system allowing real-time acquisition, processing and analysis of mass data. The aim is to transform the raw monitoring data into pertinent information about the anomaly identified.
- Data transform to control room operators in the form of diagnostic assessments and recommendations optimised by artificial intelligence as a decision-support tool.

From 2018, the TADI project has had its base of operation for testing and qualifying innovative technologies for gas leak detection and quantification. The site is part of the Lacq Pilot Platform (PPL) at the Platform for Experimental Research in Lacq (PERL) in France. The equipment used in the TADI facility allows to reproduce a wide variety of accident scenarios



Figure 4.1: TADI facility.

derived from field experience in controlled conditions (Figure 4.1). This infrastructure is unique in the world. This is due to its location in an industrial environment subject to EU SEVESO 3 regulations on major accident hazards. Furthermore, it is the only facility able to reproduce a wide range of gas leak flow rates, from 0.5 g/s to 300 g/s.

This facility has allowed to include new sensor technologies in a qualification program. Until today, three test programs have already been completed:

- One in June 2018 to test low-cost acoustic technologies for the safety monitoring of installations.
- Other two in October 2018 and October 2019 to evaluate several optical and acoustic technologies for remote gas detection-localisation-quantification using various deployment systems (e.g. ground-based, airborne, robot-mounted, drone, etc.) for emergency situations and safety surveillance.

The last test program concern our work. In fact, our aim in the current chapter is to apply the LES methodology in order to simulate a TADI test case and, subsequently, to use it to interpret and assimilate the measurements taken through optical technologies. It is important to highlight that the TADI case implies real scales, almost atmospheric neutral conditions, variability in the wind direction and presence of obstacles. These are the main difficulties to be faced, before to moving on to the final analysis of the results. The images generated by the optical instruments are reproduced numerically through the LES simulation and the implementation of a virtual camera. The numerical images should have the same characteristics of the experimental ones. It is fundamental to treat the signal and develop a method for the interpretation and assimilation of the results.

The current section is dedicated to illustrating the TADI experiment, choosing the most appropriate test case to simulate and describing the optical instrument employed in the case. Whereas the next section (section 4.2) presents the adaptation of the LES methodology to the TADI case and the numerical results obtained. Finally, section 4.3 develops an approach to interpret and assimilate the numerical and experimental results. Moreover, the preliminary results of this approach are exposed.

4.1.1 Case selection

The case to be simulated and subsequently used for the interpretation and assimilation of the experimental data needs to be chosen with care. The methodology developed in the previous chapter does not allow to treat complex experimental configurations, specifically with regard to atmospheric stability. Therefore, it was decided to identify a simple test case. The latter need to be mainly characterised by almost neutral atmospheric stability conditions and high pollutant emissions.

The October 2019 measurement campaign includes 17 tests, carried out over 3 days. Each test has a duration between 30 min to 60 min. Three species are examined (i.e. methane CH_4 , carbon dioxide CO_2 and ethane C_2H_6), emitted from different sources and regions of the TADI facility. The emissions vary from 0.5 g/s to 123 g/s, while the dimension of the source extends between 4 mm to 75 mm.

The meteorological conditions were monitored during the entire campaign. For this purpose, a fixed meteorological station (also known as “METEK sonic anemometer”) and a LIDAR were present on the site. The fixed monitoring station, situated at 2 m from the ground, allows to identify the cases which have stability condition almost neutral. Five cases were noted and their analysis is shown in Figure 4.3. Each plot shows the mean of the inverse of the Monin-Obukhov length L_{MO}^{-1} over the whole test and the 15 minutes average. All the cases have acceptable meteorological conditions. In fact, they are close to the neutral condition: $L_{MO}^{-1} \rightarrow 0 \text{ m}^{-1}$. The

case W40-05 was chosen because it presents an almost neutral condition in the last 15 minutes of the test and because its source has the larger diameter, i.e. 75 mm, and a flow rate of 30 g/s.

Then, considering the whole trend of the L_{MO}^{-1} of the case W40-05 (see Figure 4.4), it confirms that the last 15 minutes of the test shows neutral conditions. In particular, within the 15 minutes interval, an interval of almost 3 minutes is chosen to characterise the atmospheric boundary layer. The meteorological data obtained through the LIDAR instrument allow to have details of the wind velocity profile up to a height of 300 m. This allows to compute some characteristics of the boundary layer and obtain the LES methodology inputs (i.e. z_0 and U_{bulk}). Through an optimisation method (as done in subsection 3.2.2), it is possible to fit the experimental profile with the logarithmic law of Eq. (3.59). Figure 4.3 shows a match between the experimental profile and the logarithmic law up to about 50 m. The inputs of the LES methodology are reported in Table 4.1. The fixed meteorological station (i.e. the METEK sonic anemometer capable to measure $\overline{u'w'}$) reports a friction velocity u_* of 0.4829 m/s, while the value derived from the best fitting is 0.3723 m/s. The latter values was chosen as input of the numerical simulation together with its aerodynamic roughness z_0 and the METEK value is considered only as a comparison value. In fact, our methodology will simulate a logarithmic wind profile. The latter profile has also allowed to compute also the bulk velocity up to a height of 50 m and it is 5.88 m/s. Finally the mean wind direction was estimated thanks to the numerical data and the generation of the wind rose of Figure 4.5. The mean direction is equal to 331° and it is useful to orientate our numerical domain, as we will see in the next section. In order to better understand the configuration of the case W40-05, Figure 4.2 shows a vertical view of the TADI facility. Moreover, it is possible to observe the position of the source and the development of a possible plume.

The choice of the case W40-05 was also conditioned by the fact that it has 216.4s of optical measurements made thanks to the SIMAGAZ multispectral camera. The acquisition frequency of the available data is of 5 Hz. In the next subsection, this optical measurement and its measurements will be presented.

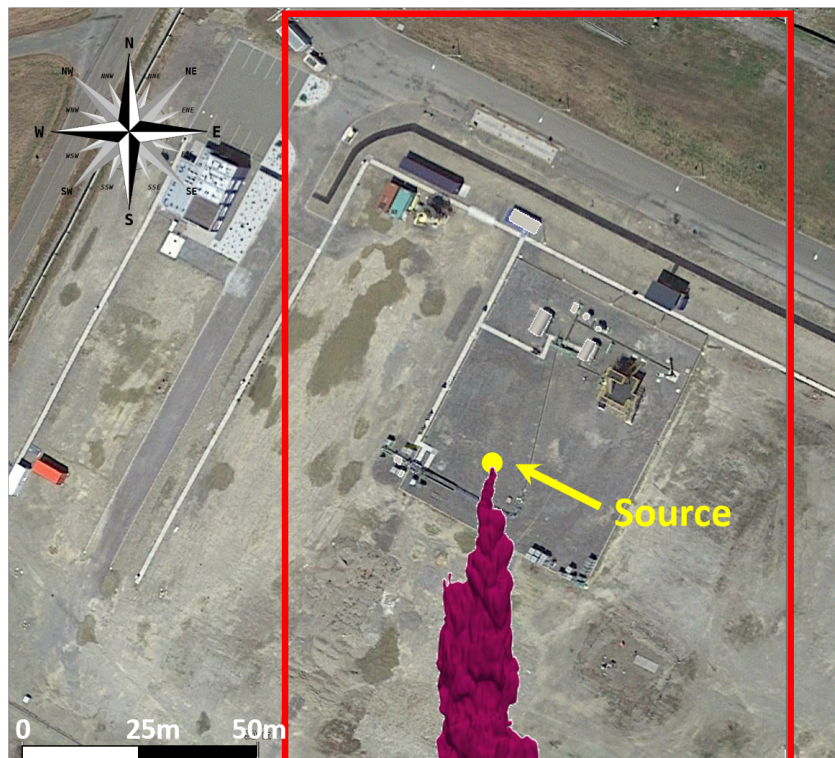


Figure 4.2: Plume in TADI site

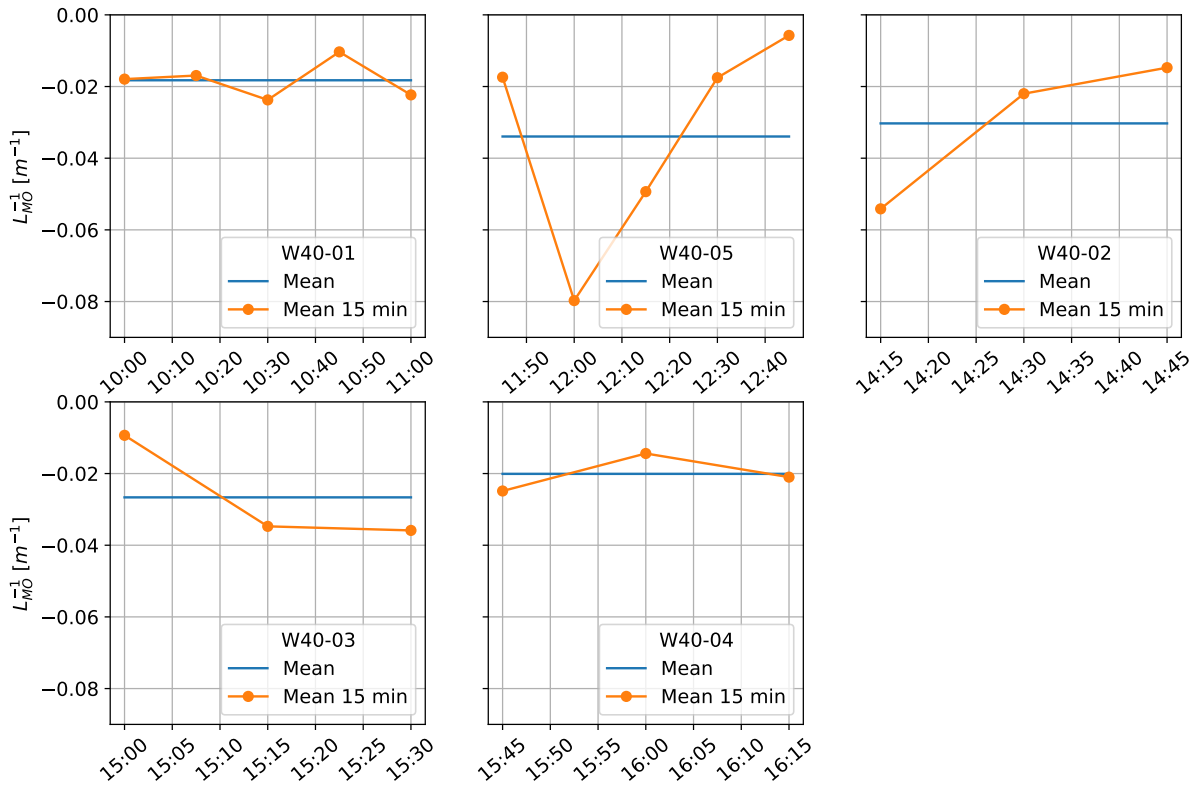


Figure 4.3: Inverse of the Monin-Obukhov length to identify neutral atmospheric conditions.

Time: 12:48:00 – 12:51:30	u_* METEK	u_*	z_0	U_{bulk}	Mean direction
W40-05	0.4829 m/s	0.3723 m/s	0.0372 m/s	5.88 m/s	331°

Table 4.1: Characteristics of W40-05 case in the time interval of 3 min and 30 s.

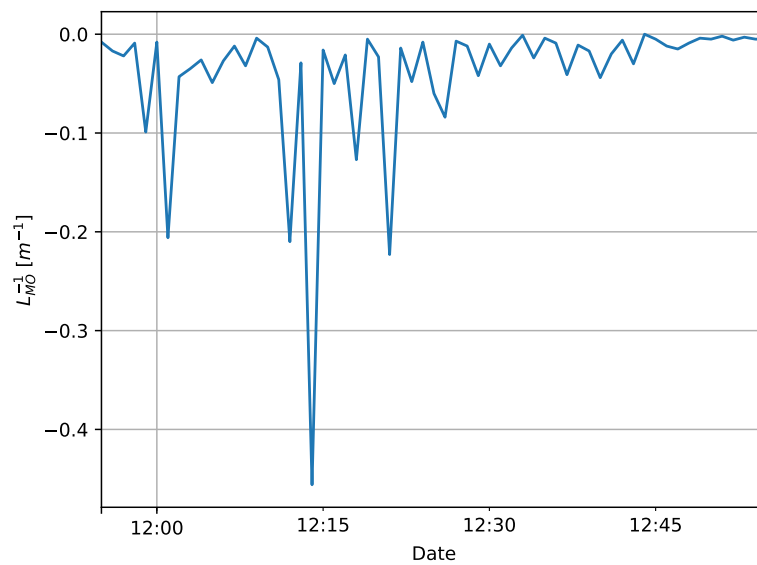


Figure 4.4: Inverse of the Monin-Obukhov length for the test W40-05.

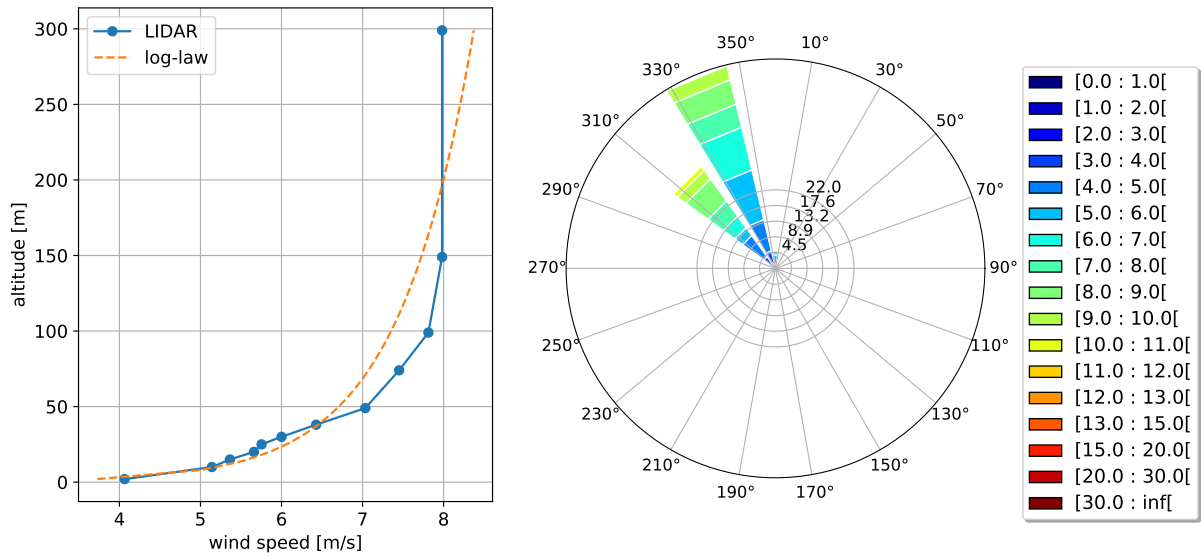


Figure 4.5: Test case W40-05 data. The left figure shows the LIDAR wind profile averaged over the 3 minutes and the logarithmic law that best fits it. In the right figure the wind rose obtained from LIDAR data is illustrated. The legend shows the color related to each wind field velocity class (expressed in [m/s]) employed by the wind rose.

4.1.2 Optical instrument

The optical instrument chosen to measure the concentration field is the SIMAGAZ camera. Their technical characteristics are presented here thanks to the information published in [Druart et al. \(2021\)](#) paper. Moreover, the procedure to generate a Column-Integrated Concentration (CIC) is introduced together with the data that can be derived from it.

The SIMAGAZ camera is based on the technology of cryogenic optics directly integrated in a standard Detector Dewar Cooler Assembly (DDCA). SIMAGAZ uses the LYNRED's state of the art architecture based on his cooled LW VGA format with a pixel pitch of 15 μ m and a RM3 cooler. Therefore, the outside view of the camera looks like a standard DDCA. Only the cold shield has been modified to integrate the optics. The optical part is simple made of a single array of lenses to produce 4 images of the scene on a single Focal Plane Array (FPA) and an array of filters to give the multispectral property of the camera, each filter being associated to a different optical channel. The MCT (Mercury-Cadmium-Telluride) infrared detector module offers high speed operation with a high sensitivity. Indeed, a Noise Equivalent Temperature Difference (NETD) has a mean value of 40 mK using band-pass filters with low FWHM and with an integration time of 5 ms and for a scene at around 20 °C. Consequently, the camera combine the advantages of have the following characteristics:

- Simple: only two major optical components are used.
- Cost effective: a single detector block is employed.
- Compact: the camera has the size of the detection block.
- Sensitive: a cryogenic infrared detector is used.
- High radioactive stability: the optics are at cryogenic temperature, limiting the background signal.

The main specifications of SIMAGAZ camera are summarised in [Table 4.2](#). SIMAGAZ data of the W40-05 case is available over 216.4s with a time step of 0.2s. Moreover, the camera

is mounted on a drone. It means that the position of the camera varies along the acquisition period. Therefore, the position is not precisely known. This adds a further difficulty when analysing the data and comparing it with the numerical case.

Detector type	Multispectral MCT
Image size for a sub-image	320x256 pixels with a pixel pitch of 15 m
Measurement rate	Up to 20 Hz
Volume of the core camera	1 L
Weight of the core camera	1.3 kg
Focal length	7 mm
Horizontal field of view	40 °
Vertical field of view	32 °
Sensitivity of methane leak flow rates	< 0.5 g/s

Table 4.2: SIMAGAZ specifications.

Many types of optical technologies exist. In a recent research in the sector, [Dinger *et al.* \(2018\)](#) study the turbulent dispersion of artificially released SO_2 puffs with UV cameras. The optical technique of this study helps to understand the procedure employed to generate the integrated concentration field which composes the SIMAGAZ images. Furthermore, it illustrates how to get more information and statistics from the images. In fact, it demonstrates that the turbulent dispersion parameters and emissions could be obtained from the experimental images, although with limitations.

The measurement of concentration with an hyper-spectral infrared camera is based on the differential absorption of specific wavelengths of infrared radiation by the the molecules of the pollutants of interest. Following the Beer–Lambert law, the attenuation of light along an optical path is proportional to the Column-Integrated Concentration (CIC) $C_{i,j}$, defined as:

$$C_{i,j}(\vec{m}, t) = \int_0^{s_{\max}} c(\vec{x}, t) ds \quad \text{with } s = \vec{x} \cdot \vec{m} \quad (4.1)$$

where \vec{x} is the coordinates vector. Assuming that the camera is at the origin O, \vec{m} is an unit vector in the direction of sight corresponding to one pixel and $c(\vec{x}, t)$ is the instantaneous concentration field (see [Figure 4.6](#)). By comparing the propagation of absorbed and unabsorbed wavelength and the differential intensities received on each pixel of a CCD sensor, the camera provides the integrated concentration $C_{i,j}$ along each direction of sight. An example of a picture of the instantaneous field of integrated concentration is represented on [Figure 4.7](#).

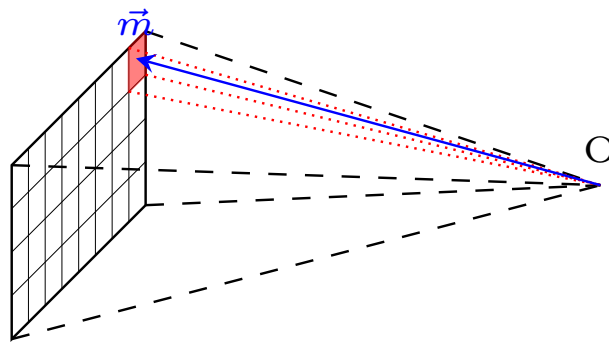


Figure 4.6: Diagram of the image taken by an optical instrument.

Different aspects of turbulent dispersion could be measured thanks to the CIC images, for instance: the total signal S_{tot} , the center of mass of the plume in the image plane or the spreading of the plume. This capacity is accentuated when images from different directions are

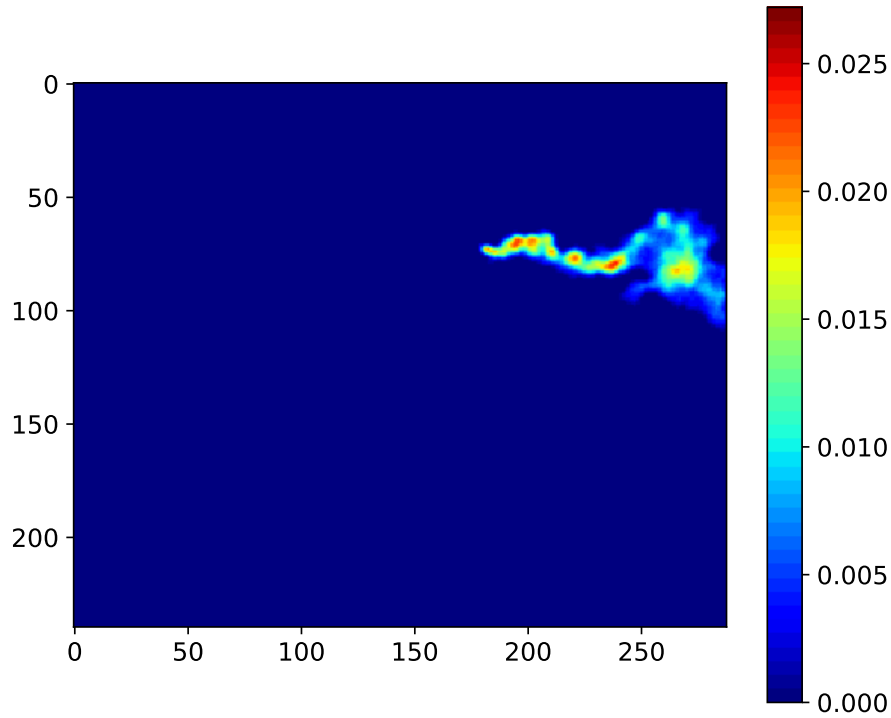


Figure 4.7: Instantaneous CIC field (expressed in $\text{kg} \cdot \text{m}^{-2}$) for the TADI case, obtained through the SIMAGAZ camera, with a resolution of 320x256 pixels.

available. In this case, it would be ideally possible to reconstruct in 3D the puff or plume under investigation. Every CIC images contain direct information about the position of the puff or plume and the spread projected to the image plane. Two discrete coordinate axis $i = [1, \dots, N_i]$ and $j = [1, \dots, N_j]$, which represent the image columns and rows, covers the image plane.

The [Dinger *et al.* \(2018\)](#) experience employs six UV cameras able to measure the total signal S_{tot} (i.e. the total mass in the image plane) of the puffs and the absolute dispersion, constituted by the sum of the variance of the centre of mass distribution and the variance of the concentration of the puff relative to its centre of mass. The total signal of the puff S_{tot} (also known, in statistical terms, as the zeroth moment of the CIC PDF) is expressed by Eq. (4.2).

$$S_{\text{tot}} = \sum_{i,j} C(i, j) \quad (4.2)$$

where $C(i, j)$ is the column-integrated concentration (CIC) at pixel (i, j) .

The passage from pixel measurements to physical measurement units is summarised here. A sketch of the field of view of two cameras from above is shown in [Figure 4.8](#). Firstly, it is important to define the apparent width of a pixel $s_p(d)$:

$$s_p(d) = s_i \cdot \frac{d}{f} \quad (4.3)$$

where s_i is the physical width of the pixel on the CCD (Charge-Coupled Device) sensor, d is the distance of the SO_2 puff to the camera and f is the focal length of the camera lens (distance between the lens and the CCD sensor). The use of two or more cameras help to find the distance d . In the experiment, the position of the centre of mass (CM) is reconstructed using the image of 3 cameras in order to reduce the uncertainties. The CM is the point in the global reference system which minimises the square distance to all lines and allow to find the relative distance from each camera.

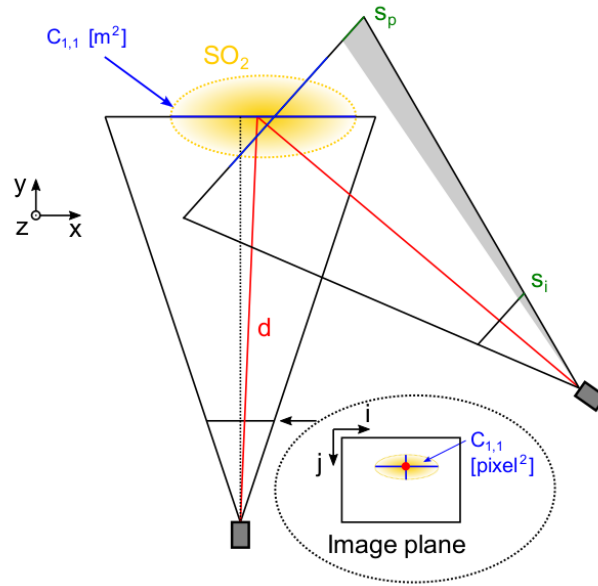


Figure 4.8: Sketch of the field of view of two cameras from above. Image from: [Dinger et al. \(2018\)](#).

When the puff's 3D extension is small with respect to the distance between the puff's CM and the camera, it is possible to neglect the puff's extension and assumes a constant scaling for the whole region of interest. Using the pixels' apparent area s_p^2 to scale the column-integrated concentration (CIC) images, it relates the image to the global reference system. Therefore the total mass M of a puff in the global reference system is given by:

$$M = s_p^2(d) S_{\text{tot}} \quad (4.4)$$

This approach is the same that need to be used to find the total mass for the CIC images for the SIMAGAZ camera. It reflects another of the limits of the available measures, that is, the fact of not having multiple cameras available at the same time. Consequently, the estimation of the flow rate of the source is impossible or requires additional assumptions about the position of the plume according to the camera.

4.2 LES simulation

After the choose of the TADI test case, the current section illustrates concisely the application of the LES methodology ([subsection 4.2.1](#)). Moreover, [subsection 4.2.2](#) presents the numerical results that help to judge and interpret the performance of the simulation.

4.2.1 Application of the LES methodology

In order to reproduce the TADI test case W40-05, the LES methodology developed in the previous chapter was used. Although we are aware that a more appropriate methodology is needed, the available methodology is tested in order to understand its limits face to a real scenario and design a better methodology in future.

The complexity of the phenomena to simulate yields to a different design of the domain and the mesh of the TADI case with respect to the wind tunnel case. Conversely, the numerical setting of the equations and solvers, of the boundary and initial conditions and of the numerical schemes is the same adopted for the Nironi case. They are considered appropriate to treat the

problem in a simple way. Consequently, the following part of this subsection is dedicated to treat the domain and the mesh.

Domain

The criteria to fix the domain dimensions, defined in subsection 3.3.1, are used here. For simplicity, the boundary layer height is considered equal to 50.4 m. This is the region where the logarithmic law reproduce better the LIDAR mean velocity profile. Further, the height of the domain was chosen so as to have a compact domain that allows to accurately simulate the phenomena close to the source because the optical measurements are concentrated in this area. In this way, the acceptable longitudinal and lateral dimensions are graphically represented in Figure 4.9 and Figure 4.10. The flow physical criterion depends on the height of the domain, while the dispersion physical criterion is chosen so as to respect the same limitations of the first criterion because the optical measurements are taken close to the source.

Consequently, in order to avoid complications and to save computational resources, the longitudinal and lateral dimensions of the domain were chosen in the lower limits. The dimensions of the domain are expressed in Figure 4.11. It also allows to enclose the TADI test section, which includes obstacles and sources and occupies an area of almost 2400 m² (i.e. ≈ 60 m x 40 m). The test section is graphically illustrated in Figure 4.12.

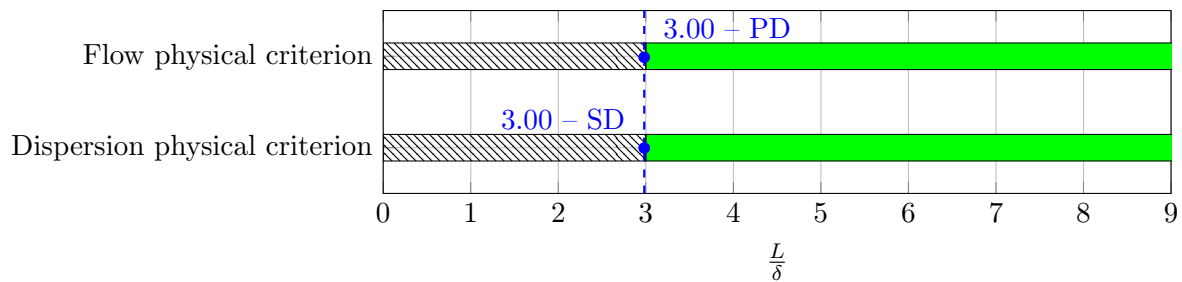


Figure 4.9: Graphic scheme to define the longitudinal dimension of the TADI domain.

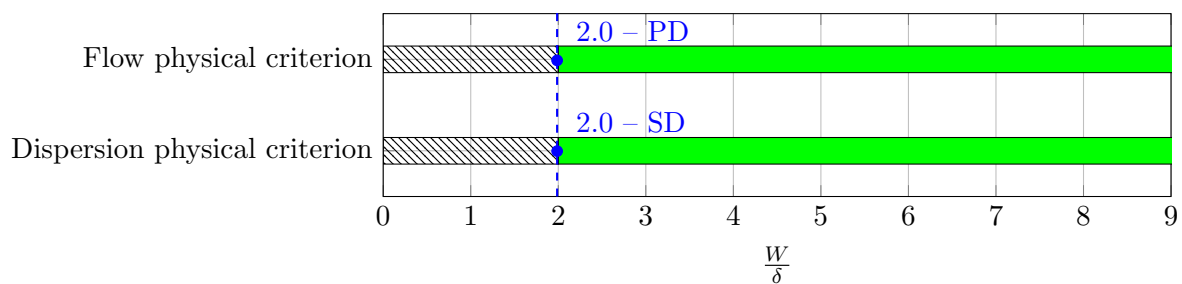


Figure 4.10: Graphic scheme to define the transverse dimension of the TADI domain.

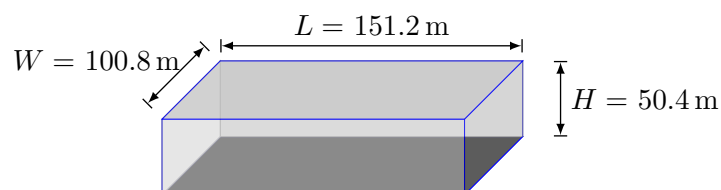


Figure 4.11: Dimensions of the precursor and successor domain of the TADI case.

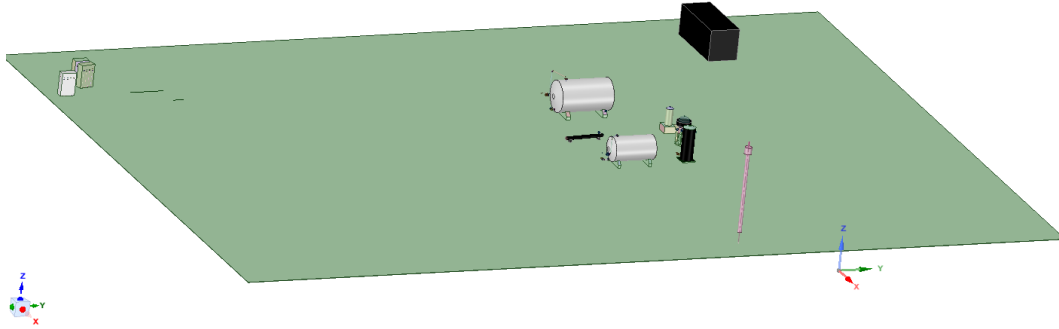


Figure 4.12: TADI test section.

Mesh

The mesh criteria developed in [subsection 3.3.2](#) are used here. As much as possible, the criteria were applied. Unfortunately, the data to compute the spectrum of the experimental wind field are not available. Consequently, the inertial subrange was not estimated, limiting our analysis.

According to our LES methodology ([subsection 3.3.2](#)), the characteristics of the mesh are constrained by the LES filter size, the wall model and the numerical source characteristic.

The LES filter needs to be placed in the inertial subrange or, if numerical resources allow it, in the dissipation range. It is important that it is not placed in the energy-containing range. Thanks to the experimental spectrum, the inertial subrange was estimated for the Nironi case. In the current case, it is not possible to estimate it because the available LIDAR data present a time step of 1 s. The time step is not considered fine enough to be able to calculate the spectrum. However, a scale analysis is used to try to estimate the range of the boundaries of the inertial subrange and of the energy-containing range. The length scale L_{EI} defines the lower boundary of the energy-containing range and it is defined as:

$$L_{EI} = \frac{1}{6} l_0 \approx \frac{1}{6} \kappa z$$

where κ is the von Kármán constant. If $\kappa = 0.4$ and $z = 10$ m, the $L_{EI} = 0.66$ m or in wall units $L_{EI}^+ = 16983$. On the other hand, the scale that marks the boundary between the inertial subrange and the dissipation range is L_{DI} . It is defined as:

$$L_{DI} = 60\eta \approx 60 \left(\frac{\nu^3}{\varepsilon} \right)^{\frac{1}{4}} = 60 \left(\frac{\nu^3 \kappa z}{u_*^3} \right)^{\frac{1}{4}}$$

where η is the Kolmogorov scale and ε is the dissipation rate. This approximation yields to $L_{DI} = 0.042$ m (i.e. $L_{DI}^+ = 1071$), for $z = 10$ m and $u_* = 0.3723$ m/s. These scales give us an idea of the possible scales involved and help us understanding the validity of our methodology.

Moving to the wall model constraint, it is required that the first cell adjacent to the wall must be situated in the logarithmic region. According to the classical theory, the logarithmic region extends between $z^+ > 30$ and $z/\delta < 0.3$. Whereas, the “Marusic method” is not applicable because the appropriate data are not available. Nevertheless, being the Re number equal to almost 22.2×10^6 (i.e. a high Re number), the “Marusic relation” is valid. Therefore, the logarithmic region could be estimated in the interval: $3 \text{Re}_\tau^{1/2} < z^+ < 0.15 \text{Re}_\tau$. In our case, $\text{Re}_\tau = 1.2 \times 10^6$. So the previous interval extends between $3386 < z^+ < 119158$. These two estimations of the logarithmic region are illustrated in the [Figure 4.13](#).

The third constraint concerns the SGS model, which is valid in the inertial subrange, e.g. $1071 < \Delta^+ < 16983$. This is the interval in which we are going to work in order to use a

reasonable amount of resources.

The fourth constraint is related to the numerical source. Although we cannot count with the direct estimation of the inertial subrange, it is possible to interpret this criterion through-out comparison between the characteristics of the current source and those of the Nironi case. For simplicity, it was decided to consider a numerical source which is the double of the source dimension of the TADI case. It means that $\Phi_{\text{LES}} = 0.15$ m, while $\Phi_{\text{exp}} = 0.075$ m. In this case, two cells were used to define the source. The experimental source in wall units and the tenth of its value (i.e. $\Phi^+/10$) are illustrated in Figure 4.13. Both are situated in the logarithmic region. This is not possible for the Nironi case. Moreover, thanks to the previous scale analysis, it is possible to observe that the source dimension is located in the inertial subrange. Whereas if 10 cells are used to discretise the numerical source in each direction of the plane in which the source is defined, it is likely that the SGS closure of the passive scalar is not appropriated because the cells would be in the dissipation range but this needs to be confirmed by measurements. In any case, thanks to an appropriate computational power, sources of the order of centimetres can be simulated in real scenarios. Unlike the wind tunnel case, the source criterion does not represent a major obstacle for real scenario simulations, like TADI case.

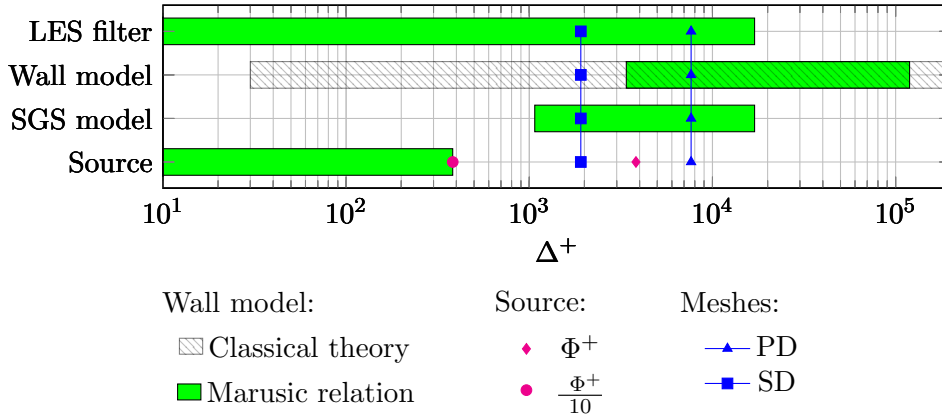


Figure 4.13: TADI mesh criteria.

The precursor-successor approach was used to carry out the simulation. Therefore two meshes are used. Their characteristics are resumed in Table 4.3 and Table 4.4. The successor domain presents more refinement levels and, consequently, a finer mesh is used in the zones where the obstacles and the source are situated. The smallest cell size for the two meshes are represented in Figure 4.13. The mesh of the precursor domain (PD) is situated in the logarithmic region defined by the Marusic relation. Therefore, the wall model respects the mesh criterion. Whereas, the mesh of the successor domain (SD) is in the logarithmic region defined according to the Classical theory. Nevertheless, this is not a problem because the cells that apply the wall model have the same dimensions of the SD cell adjacent to the wall, i.e. $\Delta_z = 0.30$ m. Finally, thanks to the scale analysis, it is possible to observe that both the meshes are situated in the inertial subrange.

For the TADI case, the meshes are constituted by a mix of principally homogeneous hexahedral cells and to a lesser extend from other types of cells, e.g. prisms and polyhedral cells. The latter are used to define the obstacles and buffer regions between two refinement levels. In the hexahedral regions, the cells are regular on y - and z -coordinates, while it has a ratio of 1.5 with respect to the x -coordinate. The two meshes employed have respectively 3 259 872 and 4 802 632 cells.

Finally, it is possible to affirm that the LES methodology seems to be more easily applicable to a real case because the larger scales allow compliance with the mesh criteria without the need for any kind of compromise.

Levels - Δ_z	h_{lv1}
Level 0	1.2 m
Level 1	0.6 m
Level 2	0.3 m

Table 4.3: Precursor domain mesh at the different refinement levels.

Levels - Δ_z	h_{lv1} or region
Level 0	1.2 m
Level 1	0.6 m
Level 2	0.3 m
Level 3	0.15 m
Level 4	0.075 m

Table 4.4: Successor domain mesh at the different refinement levels.

OpenFOAM mesh

The mesh is generated thanks to the OpenFOAM `snappyHexMesh` tool. An example of the mesh resulted is shown in [Figure 4.14](#). The obstacles and the source are discretised with the level 4 of mesh refinement, while the level 3 is used as a buffer region between the refinement level 2 and 4.

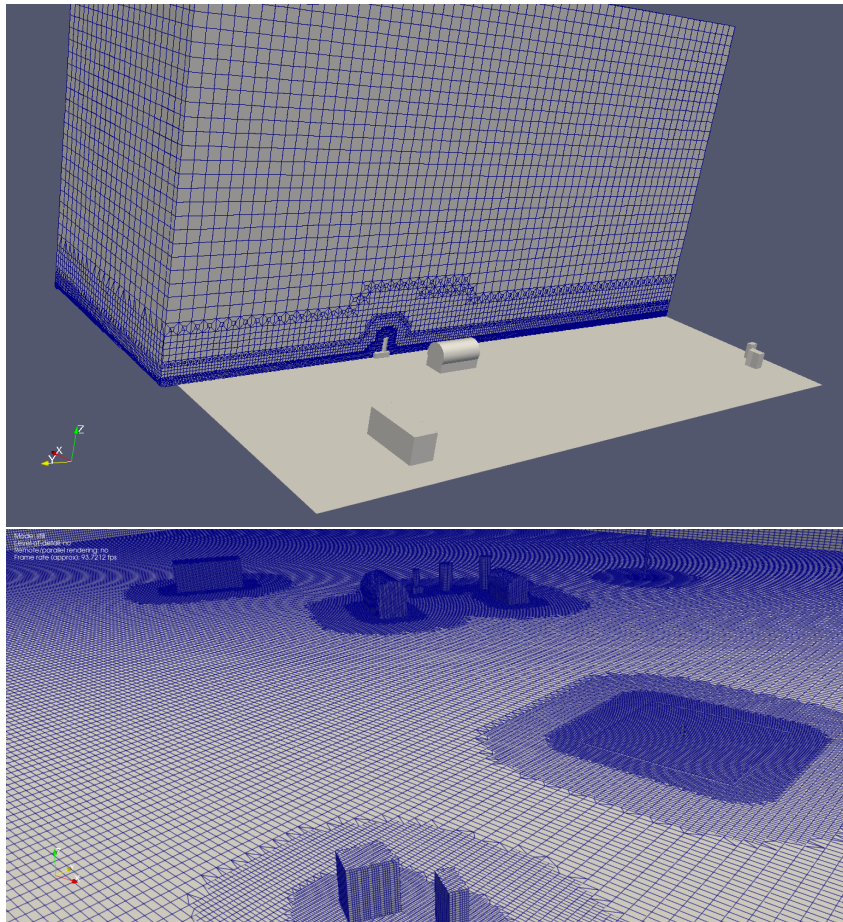


Figure 4.14: TADI mesh.

4.2.2 Simulation results

According to the precursor-successor approach, firstly the precursor domain is used to develop the turbulent flow and generate the statistics that allow to understand the performance of the simulation. This simulation is similar to Nironi case because there are no obstacles in the domain. Subsequently, the same domain is used to sample the instantaneous velocity at the inlet surface in order to generate the inlet conditions of the successor domain. Lastly the successor domain, which contains the main obstacles of the TADI test section, is used to simulate the dispersion of a passive scalar and generate results similar to images of optical instruments.

In the precursor domain, a simulation of 10 000 s with a time step of 0.05 and a maximum Courant number of 0.90 is conducted. The numerical resources used are presented in [Table 4.5](#).

On the other hand, the concentration field is simulated in the latter 300 s with a time step of 0.001 s. The resources employed are resumed in [Table 4.6](#). The high job time is due to a higher number of cells, a smaller time step used and writing procedure to save data compactly. Moreover, writing each time step into the disk takes approximately 1.6 GB. Again this point out how important it is to organise the results analysis procedure in advance.

As remarked here, these simulations are very expensive in terms of computational power. Consequently, they were performed thanks to the availability of TotalEnergies supercomputers: *Pecan* in Houston, USA and *PangeaII* in Pau, France.

Physical time	CPU	Cores	Job time
10 000 s	Intel® Xeon® E5-2670 @ 2.60GHz	120	20 h

Table 4.5: Computational time and resources for 10 000 s of simulation with 120 cores for the development of the boundary layer in the precursor domain with a mesh of 3 259 872 cells.

Physical time	CPU	Cores	Job time
300 s	Intel® Xeon® E5-2670 @ 2.60GHz	192	1 day 14 h

Table 4.6: Computational time and resources for 300 s of simulation with 196 cores for the dispersion simulation in the successor domain with a mesh of 4 802 632 cells.

Wind field

Figure 4.15 shows the statistics of the numerical wind field at different distances from the inlet boundary in the precursor simulation. The profiles are sampled at the inlet (0.15 m) and at two distances in the middle of the domain, i.e. 37.80 m and 75.60 m or in nondimensional coordinates x/δ at 0.756 and 1.512.

The LES mean velocity $\langle \bar{u} \rangle$ matches the experimental profile obtained from the LIDAR instrument, as observed in Figure 4.15a. This is the only comparison made between the numerical and experimental profiles because the data to compare the other statistics are not available. On the other hand, it is possible to compare the numerical friction velocity u_* and the experimental one. For the LES, it is possible to use a linear regression of the profile $\langle \bar{u}'w' \rangle$ to estimate the friction velocity (as made for the Nironi case in subsection 3.4.2). Consequently, the LES friction velocity is 0.3535 m/s. It is close to the experimental value, which is 0.3723.

Outside of the experimental comparison, Figure 4.15b, Figure 4.15d and Figure 4.15e highlight the effect of the mesh refinement levels. The interface between the levels generates some

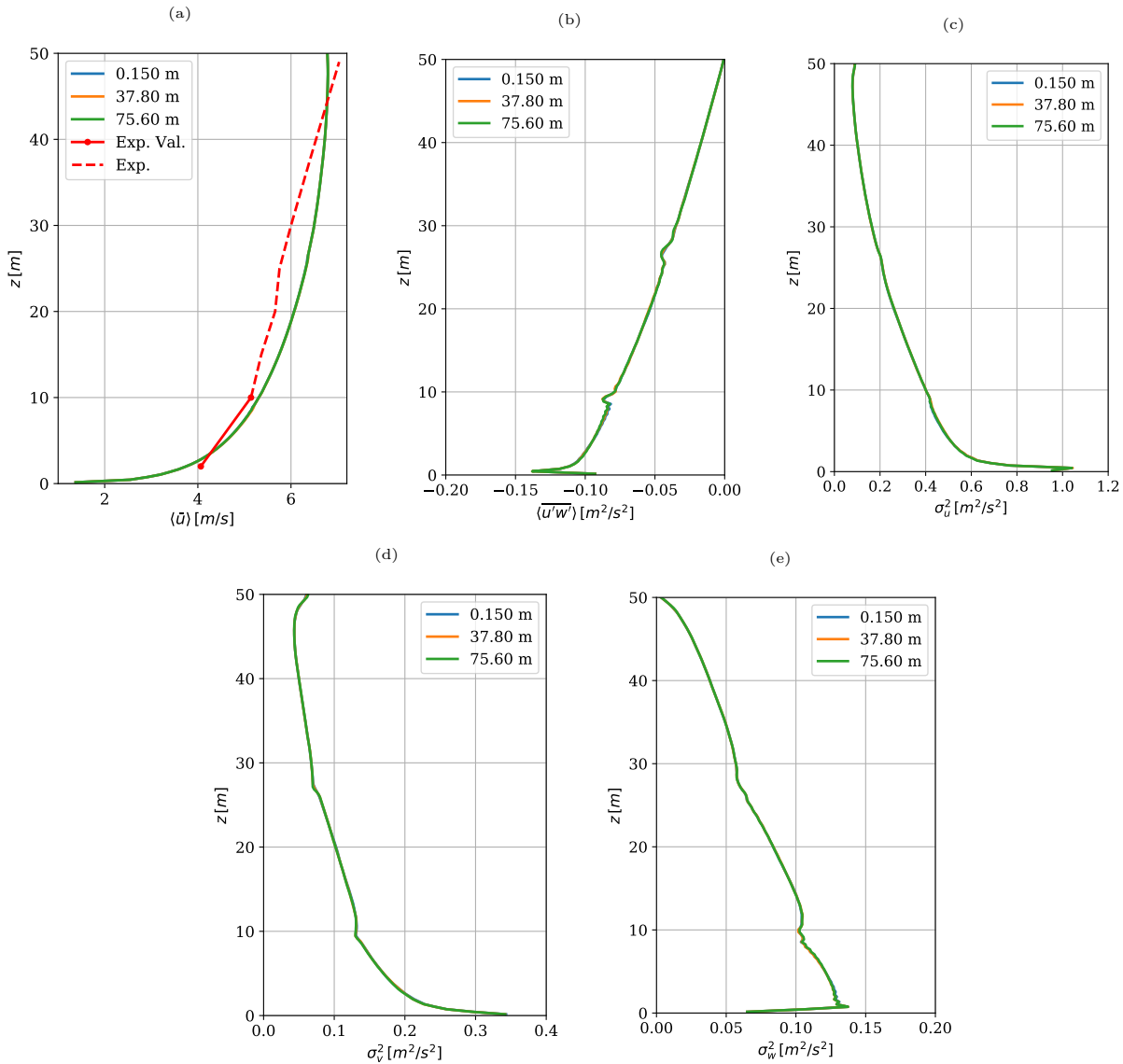


Figure 4.15: Wind field statistics of the TADI case. The mean velocity of the wind field is compared with the TADI experimental data obtained with LIDAR. In this case, the validation of the methodology occurs for $z < 10$ m, i.e. $z/\delta < 0.285$.

oscillations in the statistic profiles. It would be interesting to analyse better this kind of effects.

The comparison between the experimental and numerical wind fields is acceptable with respect to the parameters compared. Nevertheless, in a real case, this comparison need to be improved. For instance, velocity fluctuations data should be better extracted from the raw LIDAR data.

Concentration field

In order to simulate the concentration field of the TADI case, the position of the numerical source that generates the concentration field is expressed in [Table 4.7](#). A constant mass flow rate is applied and it is equal to 0.03 kg/s. While the integrated concentration field for the experimental case is acquired thanks to the SIMAGAZ instrument, the numerical simulation needs to use a numerical method to generate a LES image through a virtual camera. The latter needs to generate a CIC of the instantaneous passive scalar capable to reproduce the experimental results. Therefore, the virtual camera is placed in a region of the numerical domain where the drone flies. Its position is pointed out in [Table 4.8](#). Unfortunately this position introduces uncertainties because in the real case the drone moves but we do not know its exact position. To implement the virtual camera, the behaviour of the optical instruments was taken into account, as we will see in the following section.

The instantaneous CIC field image, obtained from the LES simulation, is shown in [Figure 4.16](#). The next section is focused on the interpretation and assimilation of the numerical CIC images.

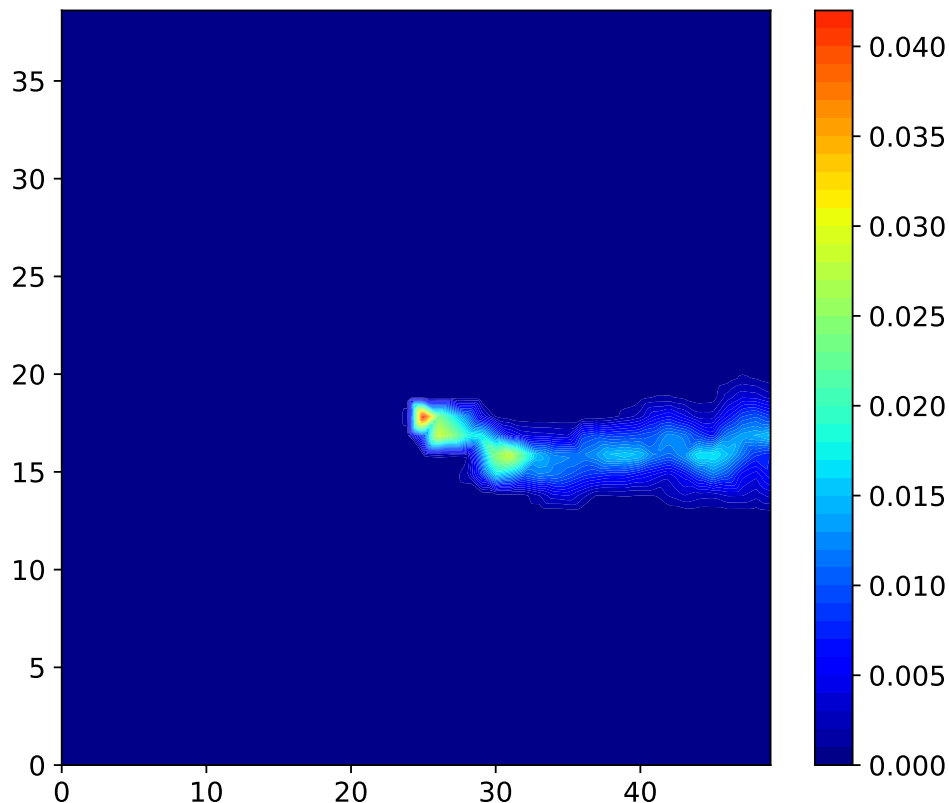


Figure 4.16: CIC field for the LES simulation with a resolution of 50x40 pixels and expressed in kg/m^2 .

x_s	92.175 m
y_s	41.475 m
z_s	0.592 m

Table 4.7: Source position in the numerical domain.

x_d	100.175 m
y_d	16.475 m
z_d	8.000 m

Table 4.8: Virtual camera position in the numerical domain.

4.3 Data interpretation and assimilation

4.3.1 Methodology for the source emission estimation from optical measurements

In this subsection, we propose a new approach to analyse optical measurements data in order to estimate the source emission rate. This approach will be evaluated using the LES concentration field to produce an emulation of images of column integrated concentration and to apply the methodology to estimate the source release rate. The validation of this approach can allow to give useful advice to the producers and developers of optical instruments for the estimation of emissions.

Consider the camera setup illustrated on [Figure 4.6](#). The angle of view of the camera is $\Delta\theta$ in the horizontal direction and $\Delta\varphi$ in the vertical direction. If the number of pixels is $N_\theta \times N_\varphi$, the corresponding angular resolutions are $\delta\theta = \Delta\theta/N_\theta$ and $\delta\varphi = \Delta\varphi/N_\varphi$. One can define the integrated mass \mathcal{M}_i corresponding to the solid angle $\delta\theta \delta\varphi$ by the equation:

$$m_{ij}(t) = \delta\theta \delta\varphi \int_0^{r_{\max}} c(\vec{x}(r, \vec{s}_{ij}), t) r^2 dr \quad (4.5)$$

If the distance R between the camera and the plume axis is large according to the plume width (or standard deviation) in the direction of sight of the camera, one can assume that the non-zero values of concentration in the integral correspond to distances r so that $|r - R| \ll R$. Consequently, the integrated mass corresponding to each image pixel can be related to the integrated concentration by:

$$m_{ij}(t) = \delta\theta \delta\varphi R^2 \int_0^{r_{\max}} c(\vec{x}(r, \vec{s}_{ij}), t) dr = \delta\theta \delta\varphi R^2 \mathcal{C}_{i,j}(t) \quad (4.6)$$

The total mass of pollutant on a vertical cross section, normal to the plume axis, in an horizontal angular opening of $\delta\theta$, is:

$$\mathcal{M}_i(t) = \sum_{j=1}^{N_\varphi} m_{ij}(t) \quad (4.7)$$

[Figure 4.17](#) and [Figure 4.18](#) show the relation between the horizontal profile of the cross-section integrated mass $\mathcal{M}_i(t)$ and the integrated mass m_{ij} image.

[Figure 4.19](#) illustrates the horizontal profile of the cross-section integrated mass $\mathcal{M}_i(t)$ as a function of the horizontal angle of view θ , for different times. One can notice the horizontal translation of the curve due to the advection process. Using this observation, it is possible to estimate the advection velocity of the plume by a maximisation of the auto-correlation:

$$R(\mathcal{M}_{i+\delta i}(t), \mathcal{M}_i(t + \delta t)) \quad \text{where} \quad R(x, y) = \frac{\overline{(x - \bar{x})(y - \bar{y})}}{\sqrt{\overline{(x - \bar{x})^2} \overline{(y - \bar{y})^2}}} \quad (4.8)$$

The instantaneous angular velocity of the plume (velocity seen from the camera point of view) can be calculated from the shift δi that maximises R :

$$\omega(t) = \frac{\delta i \delta \theta}{\delta t} \quad (4.9)$$

The crossing duration t_{tot} of the domain is the time needed by the plume to cross the field of view of the camera. It can be evaluated by the condition:

$$\int_{t-t_{\text{tot}}(t)}^t \omega(t) dt = \Delta \theta \quad (4.10)$$

During the crossing duration t_{tot} , the mass of pollutant transported by the atmospheric flow is approximately the total mass M_{tot} in the field of view, i.e.:

$$M_{\text{tot}}(t) = \sum_{i=1}^{N_\theta} \mathcal{M}_i(t) \quad (4.11)$$

Finally, in a steady state, the mass of pollutant transported per unit of time has to be balanced by the emission rate of the source:

$$Q_{\text{src}} = \frac{M_{\text{tot}}(t)}{t_{\text{tot}}(t)} \quad (4.12)$$

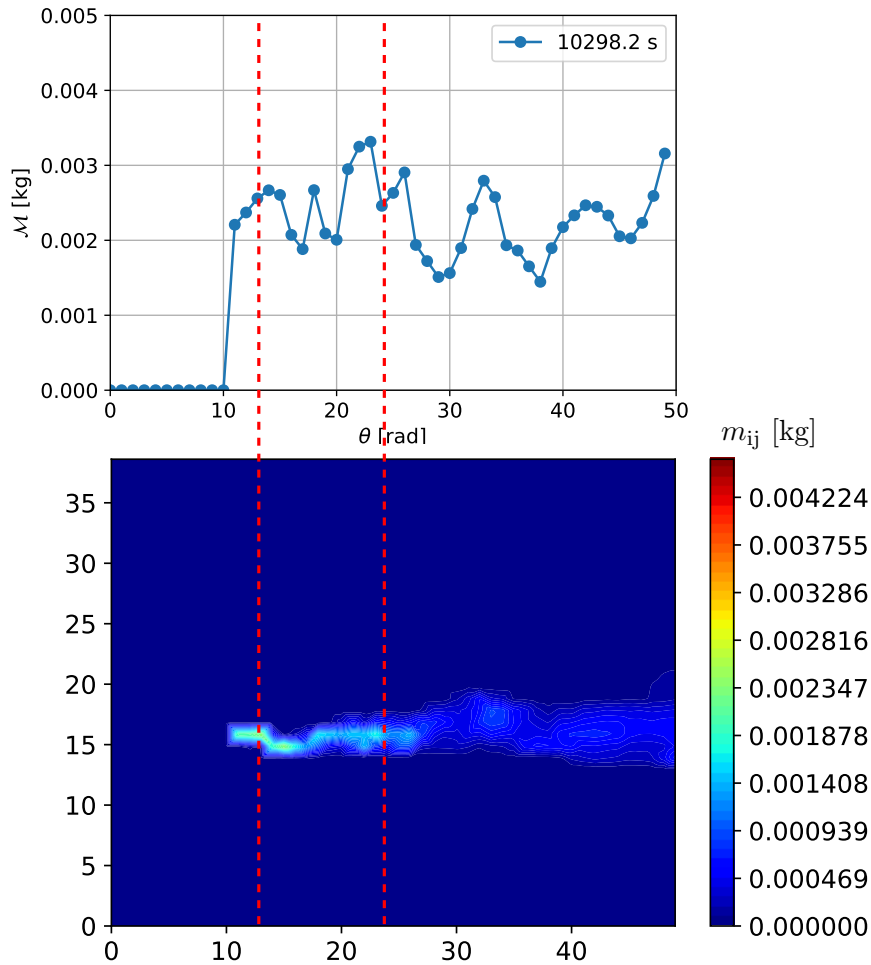


Figure 4.17: Relation between the profile of the cross-section integrated mass $\mathcal{M}_i(t)$ and the integrated mass m_{ij} image.

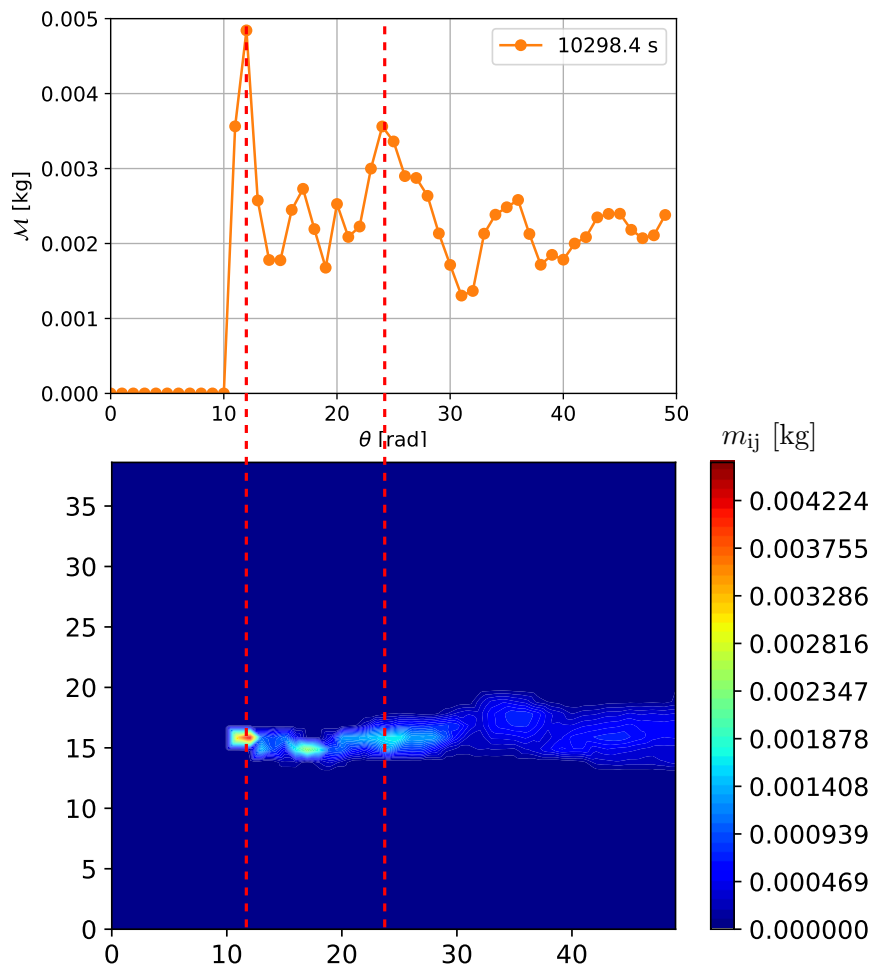


Figure 4.18: Relation between the profile of the cross-section integrated mass $\mathcal{M}_i(t)$ and the integrated mass m_{ij} image at a different time step.

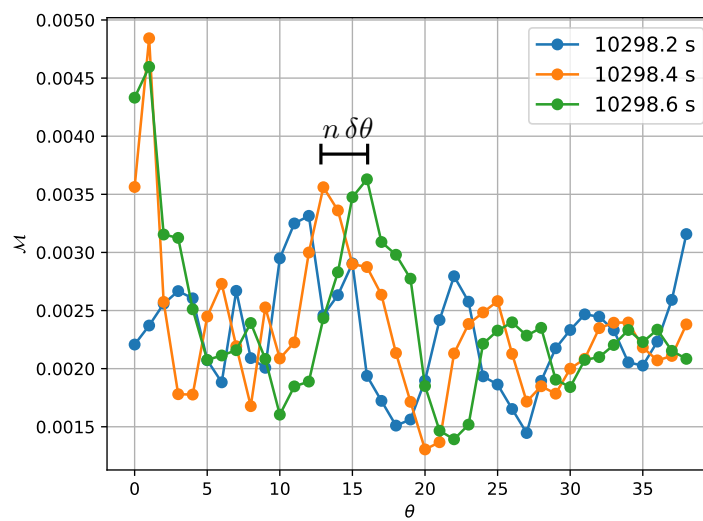


Figure 4.19: Cross-section integrated mass for different times.

4.3.2 Evaluation of the methodology

The previous approach has been implemented and the test on the LES concentration field has been started. Unfortunately we did not have enough time to analyse the performance of the approach in-depth and be able to present the results in an appropriate way. Nevertheless, we conducted a first test thanks to the Nironi case. For this case, the reference emission rate value is: $Q_{\text{exp}} = 1.00 \text{ g/s}$. Whereas the value estimated is: $Q_{\text{LES}} = 0.94 \text{ g/s}$. Figure 4.20 illustrates some images used to evaluate the current methodology in an area close to the source. The whole interval employed is of 2 s, i.e. 80 frames. This preliminary result is encouraging.

Finally, we believe that it can make an important contribution in the treatment of images generated by optical instruments, not only from a numerical point of view but also by providing advice for making measurements with a different post-processing techniques.

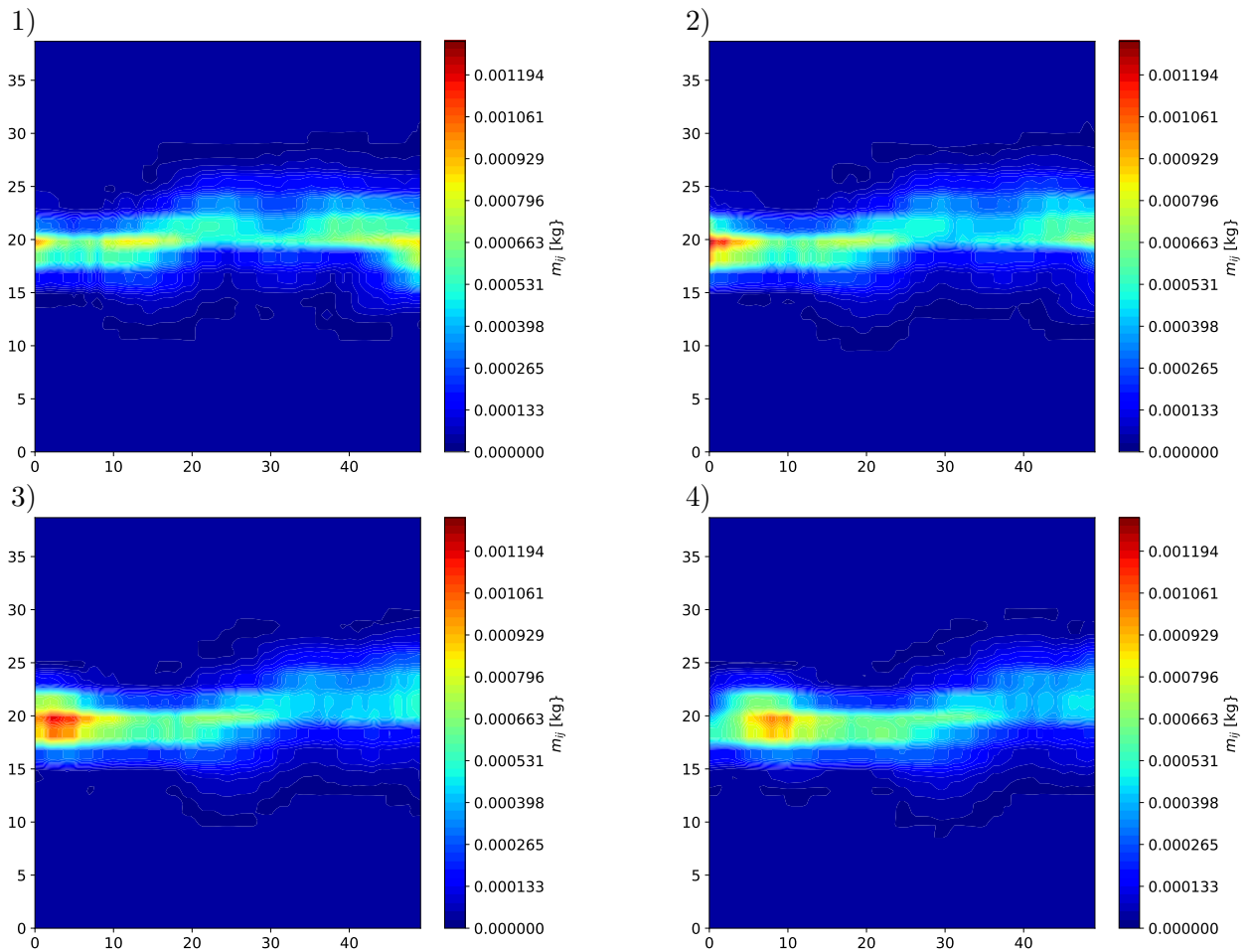


Figure 4.20: Images used to estimate the LES emission rate. The time step is 0.025 s.

4.4 Conclusions

In the current chapter, our LES methodology was applied to a real scenario, i.e. the TADI case. Although a simple case was chosen, TADI case implies real scales, almost atmospheric neutral conditions, variability in the wind direction and presence of obstacles. Therefore the adaptation of the LES methodology was not simple. Nevertheless, for some aspects, it proved to be more suitable for simulation real cases. In fact, the mesh criterion is easily respected. The wind and concentration field are simulated but a more accurate experimental-numerical comparison is necessary.

In order to interpret and assimilate the CIC images generated by the SIMAGAZ camera during the TADI tests, an LES simulation was used to reproduce the concentration field and a numerical approach was implemented to generate numerical CIC images and estimate the source release rate. We believe that this approach can provide encouraging results so its consolidation and validation are one of the first things to do in the future.

Conclusions and perspectives

Conclusions

The final aim of the thesis is to interpret and assimilate the results of optical measurements of pollution thanks to the numerical simulation of the atmospheric dispersion. The experimental data, describing a complex physical process, is characterised by a high sampling frequency and a strong level of fluctuations. Therefore, a numerical approach capable to capture not only the mean state of turbulent flow and of plume dispersion but also its higher moments is preferable, i.e. the Large-Eddy Simulation (LES) approach.

The strategy of the work was based on a gradual increment of physical and numerical difficulties. After the state of the art of the atmospheric flow and dispersion phenomena, a simple case study was chosen, i.e. the dispersion of the passive scalar in a surface boundary layer under neutral conditions. This case study was designed in order to develop a progressively more complex simulation methodology. So firstly a simple turbulence modelling strategy was adopted such as the Reynolds-Average Navier Stokes (RANS). In this way, it was possible to face with one big source of uncertainties: the boundary conditions, e.g. inflow profiles, ground roughness and others. Although decades of studies, the issue derived from the appropriate application of the boundary conditions is still open due to the extremely complexity of the ABL. Moreover, the equilibrium of the turbulence model coefficients adds to difficulties. Some cases from the literature are reproduced to understand the problem and apply the solutions suggested. These numerical simulations have allowed to become familiar with this kind of difficulties and to observe the evolution of the solutions proposed in the literature with respect to the current CFD codes. An inter-comparison work with different codes and boundary conditions has been performed and compared with previous published studies. The main result is that the actual commercial or open-source codes used in engineering allow to simulate the chosen case study without ad-hoc modifications of the boundary conditions or of the turbulence model coefficients.

Subsequently a more complex turbulence modelling strategy is adopted. It is the Large-Eddy Simulation (LES). After the presentation of the concepts useful to our purposes, the same simple case was adopted but here a wind tunnel experiment was coupled in order to compare and validate the numerical results. For this purpose, it was necessary to develop a LES methodology which establishes some physical and numerical criteria useful for adopting an appropriate computational setting and interpreting the results. In fact, it was found that even if the case is simple, it is not possible to apply all the necessary criteria. In particular the criteria related to the mesh and to the SGS model for the closure of the passive scalar transport equation warns us that the numerical configuration, taken from other studies of the literature, are not the most suitable and can present difficult issues. Therefore, the LES methodology was validated thanks to the application of some compromises and with the correct interpretation of the results.

Finally, the acquired knowledge is used to simulate a real scenario, i.e. a test case of the TotalEnergies Anomaly Detection Initiatives (TADI) project. The LES methodology previously developed was adapted in the best possible way to a simple real case. It was selected a test case that reproduces approximately a neutral surface boundary layer. The application of the

mesh criterion proved to be encouraging. Unlike the case in the wind tunnel, the constraints linked to the source are more easily respected and without particular compromises thanks to the larger scales considered. Although the energy and dissipation scales need to be estimated more accurately, the scale analysis allows to affirm that the models applied are suitable for the TADI case. The numerical results of the wind field were compared with the LIDAR velocity profile and with the friction velocity derived from it. This comparison shows encouraging performance but a more accurate comparison of the numerical and experimental turbulent statistics is necessary. Aware of the limits, the numerical results of the concentration field were compared with the images of the multispectral camera SIMAGAZ. It is not possible to compare each instantaneous field because the results are unsteady and such a comparison of two different realisations has no sense. Conversely, the comparison of some characteristics of the column-integrated concentrations (CIC) are more interesting. The total mass and the mass flow rate of the source could be estimated thanks to the CIC images. We wanted to estimate these values but due to time constraints it was not possible to further develop the method.

Perspectives

The LES methodology developed in the current thesis was firstly applied to simulate a wind tunnel experiment. The comparison of the numerical and experimental results has allowed to validate the methodology but with some limitations. In fact, the mesh criterion is not fully satisfied and some compromises are needed. In order to improve the LES methodology validation, the following perspectives must be considered:

- A better choice or development of SGS models and rough wall models.
- A different configuration of the wind tunnel experiment. A different technique to develop the turbulent boundary layer as well as a high Re number could benefit the validation and enrich the experimental study. Likewise, a more appropriate positioning of the source relative to the wall or a larger source size may allow for easier comparison of results.
- If adequate computational resources are available, an accurate simulation of the wall region would be considered without the use of any wall model.

In the future, it is important to complicate the study case. In this perspective, the LES methodology needs to take into account stratification effects as well as a better modelling of the obstacles. Moreover, the variability of the wind direction is important to treat. Finally, the dispersion of other types of species need to be considered, e.g. heavy or chemical reactive gases.

The numerical approach developed to treat the Column-Integrated Concentration (CIC) field has not been properly tested. Therefore, the validation and the optimisation of this technique need to be completed. The possible practical implications should be taken into account.

Finally, it is important to highlight that the simplicity of the case considered should not mislead anyone who approaches to solve this type of case study. In fact, the complexity of the numerical modelling is also present in the determination of the parameters that characterise the flow and the concentration field. Today a universal approach that allows to determine the flow characteristics does not exist. For instance, a different method to estimate the friction velocity could yield to different performance of the LES simulation. In the same way, the numerical source dimension and discretisation should be determined by more widely diffused criteria. Our work did not start with the aim of defining these kind of criteria. Nevertheless, we would like to underline the attempt to define criteria for LES modeling that will hopefully be more explicitly used by the scientific community.

Appendix A

A.1 Wall function for rough surfaces

According to [subsection 1.1.4](#) and OpenFOAM v1812 source codes, if it is desired to model a turbulent wall-bounded flow in which the wall roughness effects are considered to be significant, it is possible include the wall roughness effects through the law-of-the-wall modified for roughness. In the current section, the practical procedure to obtain a wall function for rough surfaces is presented.

Experiments in roughened pipes and channels indicate that the mean velocity distribution near rough walls, when plotted in usual semi-logarithmic scale, has the same slope ($1/\kappa$) but a different intercept (additive constant ΔB in the log-law). Thus, the law-of-the-wall for mean velocity modified for roughness has the form of Eq. (A.1).

$$u^+ = \frac{1}{\kappa} \ln(Ez^+) - \Delta B \quad (\text{A.1})$$

where:

$$\Delta B = \frac{1}{\kappa} \ln(f_r)$$

Here, f_r is a roughness function that quantifies the shift of the intercept due to roughness effects. In general, ΔB depends on the type (uniform sand, rivets, threads, ribs, mesh-wire, etc) and size of the roughness. There is no universal roughness function valid for all types of roughness. For a sand-grain roughness and similar types of uniform roughness elements, however, ΔB has been found to be well corrected with the non-dimensional roughness height:

$$K_s^+ = \rho K_s \frac{u_*}{\mu} = K_s \frac{u_*}{\nu}$$

where K_s is the physical roughness height. Analysis of experimental data shows that the roughness function is not a single function of K_s^+ , but takes different forms depending on the K_s^+ value ([Cebeci and Bradshaw, 1977](#)). Three different regions could be recognised:

- Hydro dynamically smooth:

$$K_s^+ < 2.25$$
$$\Delta B = 0$$

- Transitional

$$2.25 < K_s^+ \leq 90$$
$$\Delta B = \frac{1}{\kappa} \ln \left[\frac{K_s^+ - 2.25}{87.75} + C_s K_s^+ \right] \sin[0.4258 \ln(K_s^+ - 0.811)]$$

where C_s is the roughness constant:

$$C_s \simeq 0.5$$

- Fully rough

$$K_s^+ > 90$$

$$\Delta B = \frac{1}{\kappa} \ln(1 + C_s K_s^+)$$

The roughness parameter $\Delta B(K_s^+)$ represents a downward shift of the logarithmic velocity profile. The choice of K_s value depends of the modelling strategy. In the case of a wall with uniform sand-grain roughness, the height of the sand-grain could be taken and assigned to K_s . For a non-uniform sand-grain, however, the mean diameter (D_{50}) would be a more meaningful roughness height. For other types of roughness, an equivalent sand-grain roughness height could be used for K_s . Franke *et al.* (2004) illustrates that the relation between the aerodynamic roughness z_0 and the roughness height K_s could be given by:

$$K_s = \frac{E}{C_s} z_0 \quad (\text{A.2})$$

The empirical parameter E is almost 9.793 while the roughness constant C_s could assume a value between 0 and 1. A roughness height K_s of zero corresponds to smooth wall. On the other hand, for the roughness to take effect, K_s must be different from zero.

Choosing a proper roughness constant C_s is mainly imposed by the given roughness. The default roughness constant ($C_s = 0.5$) was determined so that, when employed the k - ε model, it reproduces resistance data of Nikuradse (1933) for pipes roughened with tightly-packed, uniform sand-grain roughness. It is necessary to adjust the roughness constant when it is wanted to model departs from uniform sand-grain. For instance, there is some experimental evidence that, for non uniform sand-grain, ribs, and wire-mesh roughness a higher value ($C_s = 0.5 \sim 1.0$) is more adequate. Unfortunately, a clear guideline for choosing C_s for arbitrary types of roughness does not exist. The Fluent manual suggests also to make sure that the distance from the wall to the centroid of the wall-adjacent cell has to be greater than K_s in order to obtain good performances. It is because having a mesh size such that the wall-adjacent cell is smaller than the roughness height is not physically meaningful. Nevertheless, as it is illustrated in section 2.2, it is shown that, for RANS simulations, it is true that conceptually the results of the smaller cells are not physically meaningful but numerically the results are correct. The wall function used is able to give good first cell values in order to maintain the inlet profiles that have been developed with a roughness effect.

Whereas it is not possible to control the code source of Fluent to understand the approach adopted, OpenFOAM uses an approach based on velocity/shear-stress relation. The approach is confirmed by the examination of the source codes. So, in OpenFOAM, the shear-stress could be defined as:

$$\tau = \rho \nu_{\text{total}} \frac{\partial u}{\partial z} \quad (\text{A.3})$$

Assuming $\tau = \tau_{\text{wall}}$, the wall shear-stress τ_w could be conveniently implemented via an effective wall viscosity $\nu_{\text{eff,wall}}$:

$$\tau_w = \rho \nu_{\text{eff,wall}} \frac{u_p}{z_p} \quad (\text{A.4})$$

where:

$$\nu_{\text{eff,wall}} = \nu + \nu_t$$

The manipulation of Eq. (A.1) bring to Eq. (A.5), as shown here:

$$u^+ = \frac{1}{\kappa} \ln \left(\frac{E z^+}{f_r} \right)$$

$$\begin{aligned}\frac{u_p}{u_*} &= \frac{1}{\kappa} \ln\left(\frac{E z^+}{f_r}\right) \\ \frac{u_p \rho u_*}{\tau_w} &= \frac{1}{\kappa} \ln\left(\frac{E z^+}{f_r}\right) \\ \tau_w &= \frac{\rho \kappa u_* u_p}{\ln\left(\frac{E z^+}{f_r}\right)} = \rho u_*^2 = \text{const}\end{aligned}\quad (\text{A.5})$$

Mixing Eq. (A.4) and Eq. (A.5) we obtain the relation of ν_t (Eq. (A.6)) implemented in OpenFOAM in the *nutkRoughWallFunction* boundary condition.

$$\begin{aligned}\rho \nu_{\text{eff,wall}} \frac{u_p}{z_p} &= \frac{\rho \kappa u_* u_p}{\ln\left(\frac{E z^+}{f_r}\right)} \\ \nu + \nu_t &= \frac{\kappa \nu z^+}{\ln\left(\frac{E z^+}{f_r}\right)} \\ \nu_t &= \nu \left[\frac{\kappa z^+}{\ln\left(\frac{E z^+}{f_r}\right)} - 1 \right]\end{aligned}\quad (\text{A.6})$$

In the following part of this section, the *nutkRoughWallFunction* will be presented in mathematical terms according the source code of OpenFOAM. The expression of ν_t implemented in the current wall function is illustrated in Eq. (A.7).

$$\nu_t = \nu \left[\frac{\kappa z^+}{\ln[\max(\bar{E} z^+, 1 + 1\text{E-}04)]} - 1 \right] \quad (\text{A.7})$$

where:

$$\bar{E} = \begin{cases} E & \text{if } K_s^+ \leq 2.25 \\ \frac{E}{f_r} & \text{if } K_s^+ > 2.25 \end{cases} \quad (\text{A.8})$$

and:

$$f_r = \begin{cases} 1 + C_s K_s^+ & \text{if } K_s^+ \geq 90 \\ \left[\frac{K_s^+ - 2.25}{87.75} \right]^{\sin(0.4258 \ln(K_s^+) - 0.811)} & \text{if } K_s^+ < 90 \end{cases} \quad (\text{A.9})$$

It is important to remark that the friction velocity u_* is needed to compute z^+ . In RANS cases, the turbulence model allows to compute u_* . For instance, the k - ε model computes the friction velocity thanks to the following expression:

$$u_* = C_\mu^{\frac{1}{4}} k^{\frac{1}{2}}$$

where C_μ is a coefficient of the current model and k is the turbulent kinetic energy.

A.2 WALE model development

The authors of the model (Nicoud and Ducros, 1999) have proposed to define a new operator \overline{OP} in Eq. (3.35). The main properties that characterise this new operator are two. Firstly, it is a function of both the strain and rotation rates and then its value goes to zero at the wall. Another important property is that the operator should guarantee that ν_{sgs} does not change if the reference frame is translated or rotated. Therefore, an invariant tensor representative of turbulent activity needs to be chosen. As seen for Smagorinsky model, a good choice for representing the turbulent fluctuations at the length scale Δ is the velocity gradient tensor $\tilde{g}_{ij} = \partial\tilde{u}_i/\partial x_j$. The latter model employs the second invariant of the symmetric part of this tensor, i.e. \tilde{S}_{ij} . As already treated, this approach presents some drawbacks.

The approach of the developers of the model to obtain a better operator is based on considering the trace-less symmetric part of the square of the velocity gradient tensor, shown in:

$$\mathcal{S}_{ij}^d = \frac{1}{2}(\tilde{g}_{ij}^2 + \tilde{g}_{ji}^2) - \frac{1}{3}\delta_{ij}\tilde{g}_{kk}^2 \quad (\text{A.10})$$

where $\tilde{g}_{ij}^2 = \tilde{g}_{ik}\tilde{g}_{kj}$ and δ_{ij} is the Kronecker symbol.

In order to consider the effects of vorticity, it is fundamental to add $\tilde{\Omega}$. It is the anti-symmetric part of $\tilde{\mathbf{g}}$ and is defined in Eq. (A.11).

$$\tilde{\Omega}_{ij} = \frac{1}{2} \left(\frac{\partial\tilde{u}_i}{\partial x_j} - \frac{\partial\tilde{u}_j}{\partial x_i} \right) \quad (\text{A.11})$$

The tensor defined by Eq. (A.10) could be reformulated in terms of $\tilde{\mathbf{S}}$ and $\tilde{\Omega}$ as illustrated by Eq. (A.12).

$$\mathcal{S}_{ij}^d = \tilde{S}_{ik}\tilde{S}_{kj} + \tilde{\Omega}_{ik}\tilde{\Omega}_{kj} - \frac{1}{3}[\tilde{S}_{mn}\tilde{S}_{mn} - \tilde{\Omega}_{mn}\tilde{\Omega}_{mn}] \quad (\text{A.12})$$

By construction, the trace of \mathcal{S}_{ij}^d is zero. Further, its second invariant is still finite and proportional to $\mathcal{S}_{ij}^d\mathcal{S}_{ij}^d$. Using Eq. (A.12), the Cayley-Hamilton theorem of linear algebra and assuming incompressibility, an equivalent expression is obtained, as shown by Eq. (A.13).

$$\mathcal{S}_{ij}^d\mathcal{S}_{ij}^d = \frac{1}{6}(S^2S^2 + \Omega^2\Omega^2) + \frac{2}{3}S^2\Omega^2 + 2IV_{S\Omega} \quad (\text{A.13})$$

where:

$$S^2 = \tilde{S}_{ij}\tilde{S}_{ij}, \quad \Omega = \tilde{\Omega}_{ij}\tilde{\Omega}_{ij}, \quad IV_{S\Omega} = \tilde{S}_{ik}\tilde{S}_{kj}\tilde{\Omega}_{jl}\tilde{\Omega}_{li}$$

The relation of Eq. (A.13) is able to identify turbulence structures with either strain rate, rotation rate or both. Moreover, pure shear flow implies that the invariant is null. A consequence is that the laminar to turbulent transition could be reproduced by this model which is another advantage with respect to the Smagorinsky model.

In the near wall region, i.e. $z \simeq 0$, the invariant $\mathcal{S}_{ij}^d\mathcal{S}_{ij}^d$ does not behave like $O(z^3)$ but like $O(z^2)$. Therefore, it is necessary to adjust the dimension of the operator and guarantee that it is well conditioned numerically. For this reason, the operator \overline{OP} is represented by the ratio $\overline{OP}_1/\overline{OP}_2$, as shown in Eq. (3.36).

Bibliography

- Aboshosha, H., Bitsuamlak, G., El Damatty, A., 2015. Les of abl flow in the built-environment using roughness modeled by fractal surfaces. *Sustainable Cities and Society* 19, 46–60.
- Adrian, R.J., 2007. Hairpin vortex organization in wall turbulence. *Physics of Fluids* 19, 041301.
- Ardeshiri, H., Cassiani, M., Park, S.Y., Stohl, A., Pisso, I., Dinger, A.S., 2020. On the convergence and capability of the large-eddy simulation of concentration fluctuations in passive plumes for a neutral boundary layer at infinite reynolds number. *Boundary-Layer Meteorology* 176, 291–327.
- de Arellano, J.V.G., Dosio, A., Vinuesa, J.F., Holtslag, A.A., Galmarini, S., 2004. The dispersion of chemically reactive species in the atmospheric boundary layer. *Meteorology and Atmospheric Physics* 87, 23–38.
- Axtmann, G., Rist, U., 2016. Scalability of openfoam with large eddy simulations and dns on high-performance systems, in: *High Performance Computing in Science and Engineering '16*. Springer, pp. 413–424.
- Baklanov, A., 2000. Application of cfd methods for modelling in air pollution problems: possibilities and gaps, in: *Urban Air Quality: Measurement, Modelling and Management*. Springer, pp. 181–189.
- Balasubramanian, S., Louvar, J.F., 2002. Study of major accidents and lessons learned. *Process Safety Progress* 21, 237–244.
- Bank, W., for Health Metrics, I., Evaluation, 2016. The cost of air pollution: Strengthening the economic case for action.
- Ben Salem, N., Soulhac, L., Salizzoni, P., Marro, M., 2014. Pollutant source identification in a city district by means of a street network inverse model. *International Journal of Environment and Pollution* 55, 50–57.
- Bey, I., Jacob, D.J., Yantosca, R.M., Logan, J.A., Field, B.D., Fiore, A.M., Li, Q., Liu, H.Y., Mickley, L.J., Schultz, M.G., 2001. Global modeling of tropospheric chemistry with assimilated meteorology: Model description and evaluation. *Journal of Geophysical Research: Atmospheres* 106, 23073–23095.
- Blocken, B., Stathopoulos, T., Carmeliet, J., 2007. Cfd simulation of the atmospheric boundary layer: wall function problems. *Atmospheric environment* 41, 238–252.
- Bocquet, M., Elbern, H., Eskes, H., Hirtl, M., Žabkar, R., Carmichael, G., Flemming, J., Inness, A., Pagowski, M., Pérez Camaño, J., *et al.*, 2015. Data assimilation in atmospheric chemistry models: current status and future prospects for coupled chemistry meteorology models. *Atmospheric chemistry and physics* 15, 5325–5358.
- Bozon, N., Mohammadi, B., 2009. Gis-based atmospheric dispersion modelling. *Applied Geomatics* 1, 59–74.

- Brandt, J., Christensen, J., Frohn, L., 2002. Modelling transport and deposition of caesium and iodine from the chernobyl accident using the dream model. *Atmospheric Chemistry and Physics* 2, 397–417.
- Briggs, G.A., 1973. Diffusion estimation for small emissions. *Atmospheric turbulence and diffusion laboratory* , 83.
- Buckingham, E., 1914. On physically similar systems; illustrations of the use of dimensional equations. *Physical review* 4, 345.
- Businger, J.A., 1982. *Equations and Concepts*. Springer Netherlands, Dordrecht. pp. 1–36.
- Cancelli, C., Boffadossi, M., Salizzoni, P., 2006. *Fluidodinamica ambientale: Turbolenza e dispersione*. Otto Editore.
- Cebeci, T., Bradshaw, P., 1977. *Momentum transfer in boundary layers*. Washington .
- CFX 5.7, 2004. *ANSYS CFX User’s Guide*. Ansys Inc. Canonsburg, PA, USA .
- Chai, T., Draxler, R., Stein, A., 2015. Source term estimation using air concentration measurements and a lagrangian dispersion model—experiments with pseudo and real cesium-137 observations from the fukushima nuclear accident. *Atmospheric Environment* 106, 241–251.
- Chapman, D.R., Kuhn, G.D., 1986. The limiting behaviour of turbulence near a wall. *Journal of Fluid Mechanics* 170, 265–292.
- Cheng, W., Liu, C.H., 2011. Large-eddy simulation of flow and pollutant transports in and above two-dimensional idealized street canyons. *Boundary-Layer Meteorology* 139, 411–437.
- Cimorelli, A.J., Perry, S.G., Venkatram, A., Weil, J.C., Paine, R.J., Wilson, R.B., Lee, R.F., Peters, W.D., Brode, R.W., 2005. *Aermod: A dispersion model for industrial source applications. part i: General model formulation and boundary layer characterization*. *Journal of applied meteorology* 44, 682–693.
- Coudon, T., Nguyen, C.V., Volta, P., Grassot, L., Couvidat, F., Soulhac, L., Gulliver, J., Mancini, F.R., Fervers, B., Salizzoni, P., 2021. Retrospective modeling of no₂ and pm₁₀ concentrations over the lyon metropolitan area (france), 1990–2010—performance evaluation, exposure assessment and correlation between pollutants. *Atmosphere* 12, 239.
- Deardorff, J., Willis, G., 1984. Groundlevel concentration fluctuations from a buoyant and a non-buoyant source within a laboratory convectively mixed layer. *Atmospheric Environment* (1967) 18, 1297–1309.
- Deardorff, J.W., *et al.*, 1970. A numerical study of three-dimensional turbulent channel flow at large reynolds numbers. *J. Fluid Mech* 41, 453–480.
- Di Mare, L., Klein, M., Jones, W., Janicka, J., 2006. Synthetic turbulence inflow conditions for large-eddy simulation. *Physics of Fluids* 18, 025107.
- Di Sabatino, S., Buccolieri, R., Pulvirenti, B., Britter, R., 2008. Flow and pollutant dispersion in street canyons using fluent and adms-urban. *Environmental Modeling & Assessment* 13, 369–381.
- Diamond, M.L., de Wit, C.A., Molander, S., Scheringer, M., Backhaus, T., Lohmann, R., Arvidsson, R., Bergman, Å., Hauschild, M., Holoubek, I., *et al.*, 2015. Exploring the planetary boundary for chemical pollution. *Environment international* 78, 8–15.

- Dinger, A.S., Stebel, K., Cassiani, M., Ardeshiri, H., Bernardo, C., Kylling, A., Park, S.Y., Pisso, I., Schmidbauer, N., Wasseng, J., *et al.*, 2018. Observation of turbulent dispersion of artificially released so 2 puffs with uv cameras. *Atmospheric Measurement Techniques* 11, 6169–6188.
- Driest, E.V., 1956. On turbulent flow near a wall. *Journal of the aeronautical sciences* 23, 1007–1011.
- Druart, G., Foucher, P.Y., Doz, S., Watremez, X., Jourdan, S., Vanneau, E., Pinot, H., 2021. Test of simagaz: a lwir cryogenic multispectral infrared camera for methane gas leak detection and quantification, in: *Algorithms, Technologies, and Applications for Multispectral and Hyperspectral Imaging XXVII*, International Society for Optics and Photonics. p. 117270G.
- Duynkerke, P., 1988. Application of the ϵ - ϵ turbulence closure model to the neutral and stable atmospheric boundary layer. *Journal of the atmospheric sciences* 45, 865–880.
- Dyer, A., 1974. A review of flux-profile relationships. *Boundary-Layer Meteorology* 7, 363–372.
- Dyer, A., Garratt, J., Francey, R., McIlroy, I., Bacon, N., Hyson, P., Bradley, E.F., Denmead, O., Tsvang, L., Volkov, Y., *et al.*, 1982. An international turbulence comparison experiment (itce 1976). *Boundary-Layer Meteorology* 24, 181–209.
- EEA, 2020. Air quality in europe — 2020 report. Publications Office of the European Union; European Environment Agency.
- ESDU, 1982. Strong Winds in the Atmospheric Boundary Layer. Part 1: hourly-mean wind speeds. Engineering Sciences Data Unit Item 82026.
- European-Parliament, Council-EU, 2008. Directive 2008/50/ec of the european parliament and of the council of 21 may 2008 on ambient air quality and cleaner air for europe. Official Journal of the European Union .
- Fackrell, J., Robins, A., 1982. Concentration fluctuations and fluxes in plumes from point sources in a turbulent boundary layer. *Journal of Fluid Mechanics* 117, 1–26.
- Ferziger, J., 1993. Subgrid scale modelling, in: B Galperin and S Orszag (eds.) *Large-Eddy Simulation of Complex Engineering and Geophysical Flows*. Cambridge University Press, pp. 37–54.
- Flack, K.A., Schultz, M.P., Shapiro, T.A., 2005. Experimental support for townsend’s reynolds number similarity hypothesis on rough walls. *Physics of Fluids* 17, 035102.
- Flores, F., Garreaud, R., Muñoz, R.C., 2013. Cfd simulations of turbulent buoyant atmospheric flows over complex geometry: Solver development in openfoam. *Computers & Fluids* 82, 1–13.
- Fluent 6.1, 2003. ANSYS Fluent User’s Guide. Ansys Inc. Lebanon, NH, USA .
- Foken, T., 2006. 50 years of the monin–obukhov similarity theory. *Boundary-Layer Meteorology* 119, 431–447.
- Fossum, H.E., Reif, B.P., Tutkun, M., Gjesdal, T., 2012. On the use of computational fluid dynamics to investigate aerosol dispersion in an industrial environment: a case study. *Boundary-layer meteorology* 144, 21–40.
- Franke, J., Hirsch, C., Jensen, A., Krüs, H., Schatzmann, M., Westbury, P., Miles, S., Wisse, J., Wright, N., 2004. Recommendations on the use of cfd in predicting pedestrian wind environment, in: *Cost action C*.

- Gant, S., Kelsey, A., 2012. Accounting for the effect of concentration fluctuations on toxic load for gaseous releases of carbon dioxide. *Journal of Loss Prevention in the Process Industries* 25, 52–59.
- Garcia-Menendez, F., Odman, M.T., 2011. Adaptive grid use in air quality modeling. *Atmosphere* 2, 484–509.
- Garratt, J., 1980. Surface influence upon vertical profiles in the atmospheric near-surface layer. *Quarterly Journal of the Royal Meteorological Society* 106, 803–819.
- Garratt, J.R., 1994. The atmospheric boundary layer. *Earth-Science Reviews* 37, 89–134.
- Gee, D., Grandjean, P., Hansen, S.F., MacGarvin, M., Martin, J., Nielsen, G., Quist, D., Stanners, D., *et al.*, 2013. Late lessons from early warnings: science, precaution, innovation .
- George, W.K., 2006. Recent advancements toward the understanding of turbulent boundary layers. *AIAA journal* 44, 2435–2449.
- Gifford, F.A., 1976. Turbulent diffusion-typing schemes: A review .
- Goricsán, I., Balczó, M., Balogh, M., Czáder, K., Rákai, A., Tonkó, C., 2011. Simulation of flow in an idealised city using various cfd codes. *International journal of Environment and Pollution* 44, 359–367.
- Grell, G.A., Peckham, S.E., Schmitz, R., McKeen, S.A., Frost, G., Skamarock, W.C., Eder, B., 2005. Fully coupled “online” chemistry within the wrf model. *Atmospheric Environment* 39, 6957–6975.
- Gryning, S.E., Batchvarova, E., Brümmner, B., Jørgensen, H., Larsen, S., 2007. On the extension of the wind profile over homogeneous terrain beyond the surface boundary layer. *Boundary-Layer Meteorology* 124, 251–268.
- Gualtieri, C., Angeloudis, A., Bombardelli, F., Jha, S., Stoesser, T., 2017. On the values for the turbulent schmidt number in environmental flows. *Fluids* 2, 17.
- Han, Y., Stoellinger, M., Naughton, J., 2016. Large eddy simulation for atmospheric boundary layer flow over flat and complex terrains, in: *Journal of Physics: Conference Series*, IOP Publishing. p. 032044.
- Hanna, S.R., Briggs, G.A., Hosker Jr, R.P., 1982. Handbook on atmospheric diffusion. Technical Report. National Oceanic and Atmospheric Administration, Oak Ridge, TN (USA
- Hargreaves, D., Wright, N.G., 2007. On the use of the $k-\epsilon$ model in commercial cfd software to model the neutral atmospheric boundary layer. *Journal of Wind Engineering and Industrial Aerodynamics* 95, 355–369.
- Haszpra, T., 2016. Time-reversibility in atmospheric dispersion. *Atmosphere* 7, 11.
- Högström, U., 1990. Analysis of turbulence structure in the surface layer with a modified similarity formulation for near neutral conditions. *Journal of the atmospheric sciences* 47, 1949–1972.
- Holmes, N.S., Morawska, L., 2006. A review of dispersion modelling and its application to the dispersion of particles: an overview of different dispersion models available. *Atmospheric environment* 40, 5902–5928.
- Holzmann, T., 2016. Mathematics, numerics, derivations and openfoam®. Loeben, Germany: Holzmann CFD .

- Horiuti, K., 1985. Large eddy simulation of turbulent channel flow by one-equation modeling. *Journal of the Physical Society of Japan* 54, 2855–2865.
- Van der Hoven, I., 1957. Power spectrum of horizontal wind speed in the frequency range from 0.0007 to 900 cycles per hour. *Journal of Atmospheric Sciences* 14, 160–164.
- Huang, S., Li, Q., Wu, J., 2010. A general inflow turbulence generator for large eddy simulation. *Journal of Wind Engineering and Industrial Aerodynamics* 98, 600–617.
- Hultmark, M., Vallikivi, M., Bailey, S.C.C., Smits, A., 2012. Turbulent pipe flow at extreme reynolds numbers. *Physical review letters* 108, 094501.
- Hutchins, N., Chauhan, K., Marusic, I., Monty, J., Klewicki, J., 2012. Towards reconciling the large-scale structure of turbulent boundary layers in the atmosphere and laboratory. *Boundary-layer meteorology* 145, 273–306.
- Irvine, M., Gardiner, B., Hill, M., 1997. The evolution of turbulence across a forest edge. *Boundary-Layer Meteorology* 84, 467–496.
- Irwin, H., 1981. The design of spires for wind simulation. *Journal of wind engineering and industrial aerodynamics* 7, 361–366.
- Issa, R.I., 1986. Solution of the implicitly discretised fluid flow equations by operator-splitting. *Journal of computational physics* 62, 40–65.
- Jarrin, N., Benhamadouche, S., Laurence, D., Prosser, R., 2006. A synthetic-eddy-method for generating inflow conditions for large-eddy simulations. *International Journal of Heat and Fluid Flow* 27, 585–593.
- Jeong, H., Han, M., Hwang, W., Kim, E., 2008. Application of data assimilation to improve the forecasting capability of an atmospheric dispersion model for a radioactive plume. *Annals of Nuclear Energy* 35, 838–844.
- Jiménez, J., 2004. Turbulent flows over rough walls. *Annu. Rev. Fluid Mech.* 36, 173–196.
- Johansson, C., Smedman, A.S., Högström, U., Brasseur, J.G., Khanna, S., 2001. Critical test of the validity of monin–obukhov similarity during convective conditions. *Journal of the atmospheric sciences* 58, 1549–1566.
- Jones, W., Launder, B.E., 1972. The prediction of laminarization with a two-equation model of turbulence. *International journal of heat and mass transfer* 15, 301–314.
- Kaimal, J.C., Finnigan, J.J., 1994. *Atmospheric boundary layer flows: their structure and measurement*. Oxford university press.
- Katata, G., Chino, M., Kobayashi, T., Terada, H., Ota, M., Nagai, H., Kajino, M., Draxler, R., Hort, M., Malo, A., *et al.*, 2015. Detailed source term estimation of the atmospheric release for the fukushima daiichi nuclear power station accident by coupling simulations of an atmospheric dispersion model with an improved deposition scheme and oceanic dispersion model. *Atmospheric chemistry and physics* 15, 1029–1070.
- Kim, J., Moin, P., 1989. Transport of passive scalars in a turbulent channel flow, in: *Turbulent Shear Flows* 6. Springer, pp. 85–96.
- Kim, J., Moin, P., Moser, R., 1987. Turbulence statistics in fully developed channel flow at low reynolds number. *Journal of fluid mechanics* 177, 133–166.

- Kim, Y., Castro, I.P., Xie, Z.T., 2013. Divergence-free turbulence inflow conditions for large-eddy simulations with incompressible flow solvers. *Computers & Fluids* 84, 56–68.
- Kline, S.J., Reynolds, W.C., Schraub, F., Runstadler, P., 1967. The structure of turbulent boundary layers. *Journal of Fluid Mechanics* 30, 741–773.
- Kolmogorov, A., 1942. Equations of turbulent motion of an incompressible fluid, *izv. acad. sci., ussr. Physics* 6, 2.
- Kolmogorov, A.N., 1941. The local structure of turbulence in incompressible viscous fluid for very large reynolds numbers. *Cr Acad. Sci. URSS* 30, 301–305.
- Krogstad, P.Å., Antonia, R., 1994. Structure of turbulent boundary layers on smooth and rough walls. *Journal of Fluid Mechanics* 277, 1–21.
- Krogstad, P.Å., Antonia, R., Browne, L., 1992. Comparison between rough-and smooth-wall turbulent boundary layers. *Journal of Fluid Mechanics* 245, 599–617.
- Kundu, P.K., Cohen, I.M., Dowling, D.R., 2012a. Chapter 12 - turbulence, in: *Fluid Mechanics (Fifth Edition)*. fifth edition ed.. Academic Press, Boston, pp. 541–620.
- Kundu, P.K., Cohen, I.M., Dowling, D.R., 2012b. Chapter 9 - boundary layers and related topics, in: *Fluid Mechanics (Fifth Edition)*. fifth edition ed.. Academic Press, Boston, pp. 361–419.
- Kylling, A., Ardeshiri, H., Cassiani, M., Dinger, A.S., Park, S.Y., Pizzo, I., Schmidbauer, N., Stebel, K., Stohl, A., 2020. Can statistics of turbulent tracer dispersion be inferred from camera observations of so₂ in the ultraviolet? a modelling study. *Atmospheric Measurement Techniques* 13, 3303–3318.
- Launder, B., Spalding, D., 1972. *Mathematical models of turbulence* academic press. New York .
- Launder, B.E., Sharma, B., 1974. Application of the energy-dissipation model of turbulence to the calculation of flow near a spinning disc. *Letters in heat and mass transfer* 1, 131–137.
- Lee, B.X., Kjaerulf, F., Turner, S., Cohen, L., Donnelly, P.D., Muggah, R., Davis, R., Realini, A., Kieselbach, B., MacGregor, L.S., *et al.*, 2016. Transforming our world: implementing the 2030 agenda through sustainable development goal indicators. *Journal of public health policy* 37, 13–31.
- Lee, X., 2018. *Fundamentals of boundary-layer meteorology*. volume 256. Springer.
- Leelőssy, Á., Lagzi, I., Kovács, A., Mészáros, R., 2018. A review of numerical models to predict the atmospheric dispersion of radionuclides. *Journal of environmental radioactivity* 182, 20–33.
- Leelőssy, Á., Molnár, F., Izsák, F., Havasi, Á., Lagzi, I., Mészáros, R., 2014. Dispersion modeling of air pollutants in the atmosphere: a review. *Central European Journal of Geosciences* 6, 257–278.
- Leonard, A., 1975. Energy cascade in large-eddy simulations of turbulent fluid flows, in: *Advances in geophysics*. Elsevier. volume 18, pp. 237–248.
- Leuzzi, G., Amicarelli, A., Monti, P., Thomson, D.J., 2012. A 3d lagrangian micromixing dispersion model lagflum and its validation with a wind tunnel experiment. *Atmospheric environment* 54, 117–126.

- Li, X.X., Liu, C.H., Leung, D.Y., 2008. Large-eddy simulation of flow and pollutant dispersion in high-aspect-ratio urban street canyons with wall model. *Boundary-Layer Meteorology* 129, 249–268.
- Lilly, D.K., 1967. The representation of small-scale turbulence in numerical simulation experiments. *IBM Form* , 195–210.
- Lilly, D.K., 1992. A proposed modification of the germano subgrid-scale closure method. *Physics of Fluids A: Fluid Dynamics* 4, 633–635.
- Lund, T.S., Wu, X., Squires, K.D., 1998. Generation of turbulent inflow data for spatially-developing boundary layer simulations. *Journal of computational physics* 140, 233–258.
- Mahrt, L., 1986. On the shallow motion approximations. *Journal of Atmospheric Sciences* 43, 1036–1044.
- Managi, S., Guan, D., 2017. Multiple disasters management: Lessons from the fukushima triple events. *Economic Analysis and Policy* 53, 114–122.
- Marro, M., Salizzoni, P., Soulhac, L., Cassiani, M., 2018. Dispersion of a passive scalar fluctuating plume in a turbulent boundary layer. part iii: Stochastic modelling. *Boundary-layer meteorology* 167, 349–369.
- Martin-Martínez, S., Viguera-Rodríguez, A., Gómez-Lázaro, E., Molina-García, A., Muljadi, E., Milligan, M., 2012. Wind power variability and singular events. *Advances in Wind Power* , 285–304.
- Marusic, I., McKeon, B.J., Monkewitz, P.A., Nagib, H.M., Smits, A.J., Sreenivasan, K.R., 2010. Wall-bounded turbulent flows at high reynolds numbers: recent advances and key issues. *Physics of Fluids* 22, 065103.
- Marusic, I., Monty, J.P., Hultmark, M., Smits, A.J., 2013. On the logarithmic region in wall turbulence. *Journal of Fluid Mechanics* 716.
- Mason, P., Callen, N., 1986. On the magnitude of the subgrid-scale eddy coefficient in large-eddy simulations of turbulent channel flow. *Journal of Fluid Mechanics* 162, 439–462.
- Mason, P.J., Thomson, D.J., 1992. Stochastic backscatter in large-eddy simulations of boundary layers. *Journal of Fluid Mechanics* 242, 51–78.
- Mathews, E., 1987. Prediction of the wind-generated pressure distribution around buildings. *Journal of Wind Engineering and Industrial Aerodynamics* 25, 219–228.
- Mathey, F., Cokljat, D., Bertoglio, J.P., Sergent, E., 2006. Assessment of the vortex method for large eddy simulation inlet conditions. *Progress in Computational Fluid Dynamics, An International Journal* 6, 58–67.
- Meeder, J., Nieuwstadt, F., 2000. Large-eddy simulation of the turbulent dispersion of a reactive plume from a point source into a neutral atmospheric boundary layer. *Atmospheric Environment* 34, 3563–3573.
- Mejia Estrada, J., Donnat, L., Duclaux, O., Lamaison, G., Soulhac, L., 2019. Review and inter-comparisons of parameterizations and boundary conditions for rans and les cfd simulations of atmospheric flow and dispersion, in: *19th Conference on Harmonisation within Atmospheric Dispersion Modelling for Regulatory Purposes*. <https://www.harmo.org/conference.php?id=19>.

- Mikkelsen, T., Alexandersen, S., Astrup, P., Champion, H., Donaldson, A., Dunkerley, F., Gloster, J., Sørensen, J., Thykier-Nielsen, S., 2003. Investigation of airborne foot-and-mouth disease virus transmission during low-wind conditions in the early phase of the uk 2001 epidemic. *Atmospheric chemistry and physics* 3, 2101–2110.
- Millikan, C.B., 1939. A critical discussion of turbulent flow in channels and circular tubes, in: *Proc. 5th Int. Congress on Applied Mechanics* (Cambridge, MA, 1938), Wiley. pp. 386–392.
- Moin, P., Kim, J., 1982. Numerical investigation of turbulent channel flow. *Journal of fluid mechanics* 118, 341–377.
- Mole, N., Jones, C., 1994. Concentration fluctuation data from dispersion experiments carried out in stable and unstable conditions. *Boundary-layer meteorology* 67, 41–74.
- Molnar Jr, F., Szakaly, T., Meszaros, R., Lagzi, I., 2010. Air pollution modelling using a graphics processing unit with cuda. *Computer Physics Communications* 181, 105–112.
- Monin, A.S., Obukhov, A.M., 1954. Basic laws of turbulent mixing in the surface layer of the atmosphere. *Contrib. Geophys. Inst. Acad. Sci. USSR* 151, e187.
- Mosca, S., Graziani, G., Klug, W., Bellasio, R., Bianconi, R., 1998. A statistical methodology for the evaluation of long-range dispersion models: an application to the etex exercise. *Atmospheric Environment* 32, 4307–4324.
- Mukha, T., Rezaeiravesh, S., Liefvendahl, M., 2018. A library for wall-modelled large-eddy simulation based on openfoam technology. *arXiv preprint arXiv:1807.11786* .
- Muñoz-Esparza, D., Sauer, J.A., Shin, H.H., Sharman, R., Kosović, B., Meech, S., García-Sánchez, C., Steiner, M., Kniewel, J., Pinto, J., *et al.*, 2020. Inclusion of building-resolving capabilities into the fasteddy® gpu-les model using an immersed body force method. *Journal of Advances in Modeling Earth Systems* 12, e2020MS002141.
- Nakayama, H., Jurcakova, K., Nagai, H., 2013. Development of local-scale high-resolution atmospheric dispersion model using large-eddy simulation. part 3: turbulent flow and plume dispersion in building arrays. *Journal of Nuclear Science and Technology* 50, 503–519.
- Nakayama, H., Nagai, H., 2009. Development of local-scale high-resolution atmospheric dispersion model using large-eddy simulation part 1: turbulent flow and plume dispersion over a flat terrain. *Journal of nuclear science and technology* 46, 1170–1177.
- Nicoud, F., Ducros, F., 1999. Subgrid-scale stress modelling based on the square of the velocity gradient tensor. *Flow, turbulence and Combustion* 62, 183–200.
- Nikuradse, J., 1933. *Strömungsgesetze in rauhen rohren*, forschungshefte 361. Rapport technique 1292.
- Nironi, C., 2013. Concentration fluctuations of a passive scalar in a turbulent boundary layer. Ph.D. thesis. Ecole Centrale de Lyon.
- Nironi, C., Salizzoni, P., Marro, M., Mejean, P., Grosjean, N., Soulhac, L., 2015. Dispersion of a passive scalar fluctuating plume in a turbulent boundary layer. part i: Velocity and concentration measurements. *Boundary-layer meteorology* 156, 415–446.
- Obukhov, A., 1946. Turbulence in an atmosphere with a non-uniform temperature, *trudy inst. Theor. Geofiz. AN SSSR* 1, 95–115.
- Okaze, T., Mochida, A., 2017. Cholesky decomposition-based generation of artificial inflow turbulence including scalar fluctuation. *Computers & Fluids* 159, 23–32.

- Orsi, M., Soulhac, L., Feraco, F., Marro, M., Rosenberg, D., Marino, R., Boffadossi, M., Salizzoni, P., 2021. Scalar mixing in homogeneous isotropic turbulence: A numerical study. *Physical Review Fluids* 6, 034502.
- O'Sullivan, J., Archer, R., Flay, R., 2011. Consistent boundary conditions for flows within the atmospheric boundary layer. *Journal of Wind Engineering and Industrial Aerodynamics* 99, 65–77.
- Paeschke, W., 1937. Experimentelle untersuchungen zum rauhigkeits-und stabilitatsproblem in der boden-nahen luftschicht. *Beitrage z. Phys. d. freien Atmos.* 24, 163–189.
- Panofsky, H.A., 1984. Atmospheric turbulence. Models and methods for engineering applications. 397.
- Parente, A., Gorlé, C., van Beeck, J., Benocci, C., 2011a. A comprehensive modelling approach for the neutral atmospheric boundary layer: consistent inflow conditions, wall function and turbulence model. *Boundary-layer meteorology* 140, 411–428.
- Parente, A., Gorlé, C., Van Beeck, J., Benocci, C., 2011b. Improved $k-\epsilon$ model and wall function formulation for the rans simulation of abl flows. *Journal of wind engineering and industrial aerodynamics* 99, 267–278.
- Paris-Agreement, 2015. Paris agreement, in: Report of the Conference of the Parties to the United Nations Framework Convention on Climate Change (21st Session, 2015: Paris). Retrieved December, HeinOnline. p. 2017.
- Parker, S., Kinnersley, R., 2004. A computational and wind tunnel study of particle dry deposition in complex topography. *Atmospheric Environment* 38, 3867–3878.
- Pasquill, F., 1961. The estimation of the dispersion of windborne material. *Met. Mag.* 90, 33.
- Patankar, S.V., 2018. Numerical heat transfer and fluid flow. CRC press.
- Perry, S.G., 1992. Ctdmpls: A dispersion model for sources near complex topography. part i: Technical formulations. *Journal of Applied Meteorology and Climatology* 31, 633–645.
- Philips, D., Rossi, R., Iaccarino, G., 2013. Large-eddy simulation of passive scalar dispersion in an urban-like canopy. *Journal of Fluid Mechanics* 723, 404.
- Piomelli, U., 1999. Large-eddy simulation: achievements and challenges. *Progress in Aerospace Sciences* 35, 335–362.
- Piomelli, U., Balaras, E., 2002. Wall-layer models for large-eddy simulations. *Annual review of fluid mechanics* 34, 349–374.
- Piomelli, U., Ferziger, J., Moin, P., 1987. Models for large-eddy simulations of turbulent channel flows including transpiration. report tf-32.
- Poletto, R., Craft, T., Revell, A., 2013. A new divergence free synthetic eddy method for the reproduction of inlet flow conditions for les. *Flow, turbulence and combustion* 91, 519–539.
- Pope, S.B., 2000a. Large-eddy simulation. Cambridge University Press. p. 558–640.
- Pope, S.B., 2000b. PDF methods. Cambridge University Press. p. 463–557.
- Pope, S.B., 2000c. Turbulent flows. IOP Publishing.
- Pope, S.B., 2000d. Wall flows. Cambridge University Press. p. 264–332.

- Povinec, P., Sýkora, I., Gera, M., Holý, K., Brest'áková, L., Kováčik, A., 2013. Fukushima-derived radionuclides in ground-level air of central europe: a comparison with simulated forward and backward trajectories. *Journal of Radioanalytical and Nuclear Chemistry* 295, 1171–1176.
- Prandtl, L., 1925. 7. bericht über untersuchungen zur ausgebildeten turbulenz. *ZAMM-Journal of Applied Mathematics and Mechanics/Zeitschrift für Angewandte Mathematik und Mechanik* 5, 136–139.
- Prandtl, W., 1905. Ueber complexe verbindungen des fünfwerthigen vanadins mit vierwerthigen elementen. *Berichte der deutschen chemischen Gesellschaft* 38, 1305–1310.
- Raskob, W., Hugon, M., Andronopoulos, S., Davakis, E., Bartzis, J., Kovalets, I., 2010. Rodos meteorological pre-processor and atmospheric dispersion model dipcot: a model suite for radionuclides dispersion in complex terrain. *Radioprotection* 45, S77–S84.
- Raupach, M.R., Antonia, R.A., Rajagopalan, S., 1991. Rough-wall turbulent boundary layers. *Applied Mechanics Reviews* .
- Richards, P., Hoxey, R., 1993. Appropriate boundary conditions for computational wind engineering models using the $k-\epsilon$ turbulence model. *Journal of Wind Engineering and Industrial Aerodynamics* , 145–153.
- Richards, P., Norris, S., 2011. Appropriate boundary conditions for computational wind engineering models revisited. *Journal of Wind Engineering and Industrial Aerodynamics* 99, 257–266.
- Richards, P., Quinn, A., Parker, S., 2002. A 6 m cube in an atmospheric boundary layer flow-part 2. computational solutions. *Wind & structures* 5, 177–192.
- Robins, A., AG, R., 1979. The development and structure of simulated neutrally stable atmospheric boundary layers .
- Robins, A., Castro, I., Hayden, P., Steggel, N., Contini, D., Heist, D., Taylor, T.J., 2001. A wind tunnel study of dense gas dispersion in a stable boundary layer over a rough surface. *Atmospheric environment* 35, 2253–2263.
- Rockström, J., Steffen, W., Noone, K., Persson, Å., Chapin, F.S., Lambin, E.F., Lenton, T.M., Scheffer, M., Folke, C., Schellnhuber, H.J., *et al.*, 2009. A safe operating space for humanity. *nature* 461, 472–475.
- Rodi, W., Constantinescu, G., Stoesser, T., 2013. Large-eddy simulation in hydraulics .
- Rossi, R., Iaccarino, G., 2009. Numerical simulation of scalar dispersion downstream of a square obstacle using gradient-transport type models. *Atmospheric Environment* 43, 2518–2531.
- Rotta, J., 1951. Statistische theorie nichthomogener turbulenz. *Zeitschrift für Physik* 129, 547–572.
- Rotta, J., 1962. Turbulent boundary layers in incompressible flow. *Progress in aerospace sciences* 2, 1–95.
- Saffman, P.G., 1970. A model for inhomogeneous turbulent flow. *Proceedings of the Royal Society of London. A. Mathematical and Physical Sciences* 317, 417–433.
- Sagaut, P., 2006. Large eddy simulation for incompressible flows: an introduction. Springer Science & Business Media.

- Saunier, O., Mathieu, A., Didier, D., Tombette, M., Quélo, D., Winiarek, V., Bocquet, M., 2013. An inverse modeling method to assess the source term of the fukushima nuclear power plant accident using gamma dose rate observations. *Atmospheric Chemistry and Physics* 13, 11403–11421.
- Schumann, U., 1975. Subgrid scale model for finite difference simulations of turbulent flows in plane channels and annuli. *Journal of computational physics* 18, 376–404.
- Segersson, D., 2017. A tutorial to urban wind flow using openfoam. *Proceedings of CFD with OpenSource Software* .
- Sergent, E., 2002. Vers une méthode de couplage entre la simulation des grandes échelles et les modèles statistiques. *Ecole Centrale de Lyon* .
- Shin, K.J., Nakakido, R., Horie, S., Managi, S., 2016. The effects of community attachment and information seeking on displaced disaster victims' decision making. *PloS one* 11, e0151928.
- Smagorinsky, J., 1963. General circulation experiments with the primitive equations: I. the basic experiment. *Monthly weather review* 91, 99–164.
- Smirnov, A., Shi, S., Celik, I., 2001. Random flow generation technique for large eddy simulations and particle-dynamics modeling. *J. Fluids Eng.* 123, 359–371.
- Soberanis, M.E., Mérida, W., 2015. Regarding the influence of the van der hoven spectrum on wind energy applications in the meteorological mesoscale and microscale. *Renewable Energy* 81, 286–292.
- Soulhac, L., Salizzoni, P., Cierco, F.X., Perkins, R., 2011. The model sirane for atmospheric urban pollutant dispersion; part i, presentation of the model. *Atmospheric environment* 45, 7379–7395.
- Spalart, P., Allmaras, S., 1994. A one-equation turbulence model for aerodynamic flows. [arXiv:https://arc.aiaa.org/doi/pdf/10.2514/6.1992-439](https://arc.aiaa.org/doi/pdf/10.2514/6.1992-439).
- Speziale, C.G., Abid, R., Anderson, E.C., 1992. Critical evaluation of two-equation models for near-wall turbulence. *AIAA journal* 30, 324–331.
- Steffen, W., Crutzen, P., McNeill, J., 2007. Theanthropocene: arehumans now overwhelming the great forces of nature? *A Journal of the Human Environment* 36, 614–621.
- Steffen, W., Richardson, K., Rockström, J., Cornell, S.E., Fetzer, I., Bennett, E.M., Biggs, R., Carpenter, S.R., De Vries, W., De Wit, C.A., *et al.*, 2015. Planetary boundaries: Guiding human development on a changing planet. *Science* 347.
- Stohl, A., Forster, C., Frank, A., Seibert, P., Wotawa, G., 2005. The lagrangian particle dispersion model flexpart version 6.2. *Atmospheric Chemistry and Physics* 5, 2461–2474.
- Stull, R.B., 2012. An introduction to boundary layer meteorology. volume 13. Springer Science & Business Media.
- Sykes, R.I., Henn, D., 1992. Large-eddy simulation of concentration fluctuations in a dispersing plume. *Atmospheric Environment. Part A. General Topics* 26, 3127–3144.
- Tabor, G.R., Baba-Ahmadi, M., 2010. Inlet conditions for large eddy simulation: A review. *Computers & Fluids* 39, 553–567.
- Tamura, T., 2008. Towards practical use of les in wind engineering. *Journal of Wind Engineering and Industrial Aerodynamics* 96, 1451–1471.

- Tanaka, K., Managi, S., 2016. Impact of a disaster on land price: evidence from fukushima nuclear power plant accident. *The Singapore Economic Review* 61, 1640003.
- Taylor, G.I., 1921. Diffusion by continuous movements. *Proceedings of the london mathematical society* 2, 196–212.
- Tennekes, H., 1984. Similarity relations, scaling laws and spectral dynamics, in: *Atmospheric turbulence and air pollution modelling*. Springer, pp. 37–68.
- Tennekes, H., Lumley, J.L., 1972. *A 1st course in turbulence*. The MIT Pres .
- Tewari, M., Kusaka, H., Chen, F., Coirier, W.J., Kim, S., Wyszogrodzki, A.A., Warner, T.T., 2010. Impact of coupling a microscale computational fluid dynamics model with a mesoscale model on urban scale contaminant transport and dispersion. *Atmospheric Research* 96, 656–664.
- Thomas, T., Williams, J., 1999. Generating a wind environment for large eddy simulation of bluff body flows. *Journal of Wind Engineering and Industrial Aerodynamics* 82, 189–208.
- Thykier-Nielsen, S., Deme, S., Mikkelsen, T., 1999. Description of the atmospheric dispersion module rimpuff. Riso National Laboratory, PO Box 49.
- Tian, L., Zhao, N., Wang, T., Zhu, W., Shen, W., 2018. Assessment of inflow boundary conditions for rans simulations of neutral abl and wind turbine wake flow. *Journal of Wind Engineering and Industrial Aerodynamics* 179, 215–228.
- Townsend, A., 1980. *The structure of turbulent shear flow*. Cambridge university press.
- Troen, I., Lundtang Petersen, E., 1989. *European wind atlas* .
- Uberoi, M.S., 1956. Effect of wind-tunnel contraction on free-stream turbulence. *Journal of the Aeronautical Sciences* 23, 754–764.
- United-Nations-Environment-Programme, 2017. *Towards a pollution-free planet: Background report*. United Nations Environment Programme.
- Vasaturo, R., Kalkman, I., Blocken, B., van Wesemael, P., 2018. Large eddy simulation of the neutral atmospheric boundary layer: performance evaluation of three inflow methods for terrains with different roughness. *Journal of Wind Engineering and Industrial Aerodynamics* 173, 241–261.
- Veloudis, I., Yang, Z., McGuirk, J., Page, G., Spencer, A., 2007. Novel implementation and assessment of a digital filter based approach for the generation of les inlet conditions. *Flow, Turbulence and Combustion* 79, 1–24.
- Vendel, F., 2011. *Modélisation de la dispersion atmosphérique en présence d’obstacles complexes: application à l’étude de sites industriels*. Ph.D. thesis. Ecole Centrale de Lyon.
- Vendel, F., Lamaison, G., Soulhac, L., Volta, P., Donnat, L., Duclaux, O., Puel, C., 2010. Modelling diabatic atmospheric boundary layer using a rans cfd code with k-epsilon turbulence closure, in: *13th Conference on Harmonisation within Atmospheric Dispersion Modelling for Regulatory Purposes*.
- Venetsanos, A., Bartzis, J., Würtz, J., Papailiou, D., 2003. Display-2: a two-dimensional shallow layer model for dense gas dispersion including complex features. *Journal of hazardous materials* 99, 111–144.

- Venkatesan, R., Mathiyarasu, R., Somayaji, K., 2002. A study of atmospheric dispersion of radionuclides at a coastal site using a modified gaussian model and a mesoscale sea breeze model. *Atmospheric Environment* 36, 2933–2942.
- Villiermaux, E., Duplat, J., 2003. Mixing is an aggregation process. *Comptes Rendus Mécanique* 331, 515–523.
- Von Kármán, T., 1930. Mechanische ahnlichkeit und turbulenz. *Math.-Phys. Klasse* .
- Wang, K., Zhang, Y., Jang, C., Phillips, S., Wang, B., 2009. Modeling intercontinental air pollution transport over the trans-pacific region in 2001 using the community multiscale air quality modeling system. *Journal of Geophysical Research: Atmospheres* 114.
- Weber, R.O., 1999. Remarks on the definition and estimation of friction velocity. *Boundary-Layer Meteorology* 93, 197–209.
- Wilcox, D., 2001. Turbulence modeling-an overview, in: 39th Aerospace Sciences Meeting and Exhibit, p. 724.
- Wray, A., Hunt, J., 1989. Algorithms for classification of turbulent structures. Cambridge University Press, Cambridge, UK.
- Wu, X., 2017. Inflow turbulence generation methods. *Annual Review of Fluid Mechanics* 49, 23–49.
- Xie, Z., Hayden, P., Voke, P.R., Robins, A.G., 2004a. Large-eddy simulation of dispersion: comparison between elevated and ground-level sources. *Journal of Turbulence* 5, 031.
- Xie, Z., Voke, P.R., Hayden, P., Robins, A.G., 2004b. Large-eddy simulation of turbulent flow over a rough surface. *Boundary-layer meteorology* 111, 417–440.
- Xie, Z.T., Castro, I.P., 2008. Efficient generation of inflow conditions for large eddy simulation of street-scale flows. *Flow, turbulence and combustion* 81, 449–470.
- Yamane, F., Ohgaki, H., Asano, K., 2011a. Nuclear power-related facilities and neighboring land price: A case study on the mutsu-ogawara region, japan. *Risk Analysis: An International Journal* 31, 1969–1994.
- Yamane, F., Ohgaki, H., Asano, K., 2011b. Social factors affecting economic welfare of the residents around nuclear power plants in japan. *Energy Procedia* 9, 619–629.
- Yang, X.I., Meneveau, C., 2016. Recycling inflow method for simulations of spatially evolving turbulent boundary layers over rough surfaces. *Journal of Turbulence* 17, 75–93.
- Yang, Y., Gu, M., Chen, S., Jin, X., 2009. New inflow boundary conditions for modelling the neutral equilibrium atmospheric boundary layer in computational wind engineering. *Journal of Wind Engineering and Industrial Aerodynamics* 97, 88–95.
- Yee, E., Kosteniuk, P., Chandler, G., Biltoft, C., Bowers, J., 1993a. Recurrence statistics of concentration fluctuations in plumes within a near-neutral atmospheric surface layer. *Boundary-layer meteorology* 66, 127–153.
- Yee, E., Kosteniuk, P., Chandler, G., Biltoft, C., Bowers, J., 1993b. Statistical characteristics of concentration fluctuations in dispersing plumes in the atmospheric surface layer. *Boundary-Layer Meteorology* 65, 69–109.
- Yee, E., Skvortsov, A., 2011. Scalar fluctuations from a point source in a turbulent boundary layer. *Physical Review E* 84, 036306.

Yoshizawa, A., 1982. A statistically-derived subgrid model for the large-eddy simulation of turbulence. *The Physics of Fluids* 25, 1532–1538.

Zhang, X., 2009. Cfd simulation of neutral abl flows. Risø National Laboratory for Sustainable Energy, Technical University of Denmark, Roskilde, Denmark .